Gravitational lensing by x-ray luminous galaxy clusters

Smith, Graham Peter

Gravitational Lensing by X-ray Luminous Galaxy Clusters

Graham Peter Smith

Department of Physics
University of Durham

August 2002

A thesis submitted to the University of Durham in accordance with the regulations for admittance to the degree of Doctor of Philosophy.

ABSTRACT

Since the discovery that the large-scale dynamics of galaxy clusters are dominated by dark matter, cosmologists have aspired to measure the spatial distribution of dark matter and identify its nature. Gravitational lensing, especially employing the *Hubble Space Telescope (HST)* has emerged as the tool-of-choice for mapping dark matter. Standing on the shoulders of the pioneering 1990's, this thesis is the first homogeneous lensing study of clusters with *HST*. We measure the mass and structure of an objectively-selected sample of X-ray luminous clusters at a single epoch ($z \sim 0.2$). We present *HST* observations of ten clusters ($L_X \geq 8 \times 10^{44}$[0.1–2.4 keV] erg s^{-1}) and use the numerous gravitationally-lensed features in these data to constrain a detailed model of the central regions ($r \sim 500$ kpc) of each cluster. Our models provide an unprecedented view of cluster morphology, revealing that 60% of the sample contain significant substructure. *Chandra* X-ray observations confirm this is a signature of dynamical immaturity, and show that the mean temperature of the intra-cluster medium of the morphologically complex clusters is $\sim$ 25% higher than their regular siblings. This offset results in a critical, and previously unexplored, systematic uncertainty in the use of clusters to normalise the mass power spectrum. We also use the detailed morphology of the clusters to constrain the nature of dark matter. We then exploit the clusters as gravitational telescopes, using ground-based near-infrared imaging to construct a sample of 60 gravitationally magnified Extremely Red Objects (EROs), a population that is believed to harbour important clues on the formation epoch and mechanism of massive galaxies. This unique sample overcomes the faintness of EROs ($R \gtrsim 23$, $K \gtrsim 18$) to uncover a wealth of morphological, photometric and spectroscopic evidence of diversity in both passively evolving and dusty active EROs. Coupled with our deep number counts (to $K \sim 22$), these observations provide important new constraints on competing theoretical models of galaxy formation.

PREFACE

The work presented in this thesis was carried out between 1999 and 2002 while the author was a research student under the supervision of Dr. Ian Smail and Dr. Richard Bower, in the Department of Physics at the University of Durham.

The overall programme of research, of which this study is a part, is an international collaboration, between the author, Dr. Ian Smail (University of Durham), Dr. Jean-Paul Kneib (Observatoire Midi-Pyrénées, Toulouse, France), Dr. Harald Ebeling (Institute for Astronomy, University of Hawaii, USA) and Dr. Oliver Czoske (Institut für Astrophysik und Extraterrestrische Forschung, Bonn, Germany). Prior to the commencement of the author's studies in Durham, Kneib, Smail & Ebeling applied for and were awarded 24 orbits of *Hubble Space Telescope* time to observe a sample of X-ray luminous galaxy clusters. This thesis describes the analysis and interpretation of these data. The gravitational lens models, which lie at the heart of this work, were constructed using a method based on the modelling techniques developed by Kneib (1993).

The major part of the work presented in this thesis is the author's own except where noted explicitly in the text, and summarised below:

- Dr. P. Mazzotta (Durham) reduced the *Chandra* data presented in §3.
- Dr. J.-P. Kneib constructed the lens model of A 2218 in §3.
- Dr. O. Czoske reduced the ground-based optical data described in §4.
- Dr. H. Ebeling conducted the spectroscopic observations described in §4.
- Dr. V.R. Eke (Durham) coded the temperature function model described in §4.
- Dr. R.J. Ivison (Astronomy Technology Centre, Edinburgh) and Dr. A.C. Edge (Durham) assisted with the near-infrared observations described in §5.
- Prof. R.S. Ellis and Dr. T. Treu (California Institute of Technology, USA) observed ERO J164023 with the Keck-II telescope (§6).

This work has not been submitted for any degree, diploma or other qualification at any other university. A full list of publications submitted by the author during the three year period of study towards this PhD is provided overleaf. A number of the results described in this thesis have appeared in papers 1, 3, 4, 6 and 8 from this list.

PUBLICATION LIST

Refereed Papers

[8] Smith G.P., Edge A.C., Eke V.R., Nichol R.C., Smail I., Kneib J.-P., 2002, ApJL, submitted, astro-ph/0211186

[7] Dunlop J.S., McLure R.J., Yamada T., Kajisawa M., Peacock J.A., Mann R.G., Hughes D.H., Aretxaga I., Muxlow T.W.B., Richards A.M.S., Dickinson M., Ivison R.J., Smith G.P., Smail I., Serjeant S., Almaini O., Lawrence A., 2002, MNRAS, submitted, astro-ph/0205480

[6] Smith G.P., Smail I., Kneib J.-P., Davis C.J., Takamiya M., Ebeling H., Czoske O., 2002, MNRAS, 333, L16-20

[5] Balogh M.L., Smail I., Bower R.G., Ziegler B.L., Smith G.P., Davies R.L., Gaztelu A., Kneib J.-P., Ebeling H., 2002, ApJ, 566, 123-136

[4] Smith G.P., Smail I., Kneib J.-P., Czoske O., Ebeling H., Edge A.C., Pello R., Ivison R.J., Packham C., Le Borgne J.-F., 2002, MNRAS, 330, 1-16

[3] Smith G.P., Treu T., Ellis R., Smail I., Kneib J.-P., Frye B.L., 2001, ApJ, 562, 635-640

[2] Smail I., Kuntschner H., Kodama T., Smith G.P., Packham C., Fruchter A.S., Hook R.N., 2001, MNRAS, 323, 839-849

[1] Smith G.P., Kneib J.-P., Ebeling H., Csozke O., Smail I., 2001, ApJ, 552, 493-503

Conference Proceedings

Smith G.P., 2001, To appear in "A New Era in Cosmology" (ASP Conference Proceedings), eds. T. Shanks and N. Metcalfe, astro-ph/0201236

Smith G.P., Smail I., Kneib J.-P., Czoske O., Ebeling H., 2000, Poster Contribution to the Third Birmingham Workshop on Galaxy Evolution

Circulars and Communications

Chaty S., Haswell C.A., Smith G.P., Smail I., Hynes R.I., IAUC 7389, 3, 2000

CONTENTS

LIST OF FIGURES

LIST OF TABLES

ACKNOWLEDGMENTS

I acknowledge financial support from the Particle Physics and Astronomy Research Council. The research described in this thesis would also not have been possible without the dedication and skills of numerous computing and observatory staff, many of whom I have not met. I thank all of these people, especially Alan Lotts and Chris Davis for their efforts.

There are many things for which I should thank my advisor Ian Smail. In the last three years I have appreciated his ability to combine the big picture view of a budding "pundit" with detailed practical help and advice when I needed it. Beyond that, I keep an eye on the rain forests, simply say a big thank you. Special thanks also go to Jean-Paul Kneib for teaching me about gravitational lensing and freely sharing his lens modelling software. I also appreciate the warm hospitality that Jean-Paul and his family extended to me during my many adventures in Toulouse. Alastair Edge has been a constant source of support during my time in Durham; I thank him for many things, including a family man's perspective on astronomy.

Many other astronomers have, sometimes unwittingly, helped and inspired me during the last three years. I thank: Michael Balogh, Carlton Baugh, John Blakeslee, Richard Bower, Sarah Bridle, Shaun Cole, Warrick Couch, Oliver Czoske, Roger Davies, Jim Dunlop, Harald Ebeling, Richard Ellis, Vincent Eke, Rob Ivison, Harald Kuntschner, John Lucey, Pasqualle Mazzotta, John Mulchaey, Bob Nichol, John Peacock, Roser Pelló, Ray Sharples and Tommaso Treu.

I have been privileged to be taught by some excellent physics teachers over the years. It is with great pleasure that I thank Derek Fry for his encouragement over many years, both at school, and in more recent years as I emerged from the business world to resume my studies. I also thank: the late Henry Allinson, Paul Davis, the late Ron Hill, Peter Hodgson, Tony Lynas-Gray, the late Bruce Patchett, John Singleton and Ken Woodgate. Joining forces with Derek to support my return to academia were Paul Murdin, Chris Wray and Suzanne McDowell. I thank these people for the diverse and important roles that they played.

Returning to Durham and astronomy, my fellow inmates in Room 6 deserve much praise for surviving my company. I thank Eugenio Barrio, Mike Beasley, Andrew Benson,

John Helly and Colin Wilson for their humour and tolerance. I also owe a debt of gratitude to Kevin Pimblett, for being Ian's first graduate student. Other people who have helped me to enjoy the last three years include Nathan Courtney, Dajana Dzanovic, Fiona Hoyle, Peder Norberg, Marc Vallbe, David Wilman and doubtless others who I have carelessly forgotten to mention.

I am inspired and sustained by my friends, who all deserve a medal! I thank Richard McDermid, for champagne and cigars; Chris Power, cameraman extraordinaire; Chris Addy, for enduring twenty-three years; Chris Brockwell, a fellow escapee and a fine friend; Ricky Paul, for surviving and joining the exodus; Stu Jarrold for not really understanding, but being my friend anyway; Lyn Morris for hospitality in Hong Kong.

I am deeply indebted to Robert and Margaret, my parents, for their love, patience and faith in me, even when at my lowest ebb. Much love and gratitude also go to Josephino, Andy, Anna, Oliver, Ronald, Dorothy, Edna and Kenneth, for their love and support over many years and their contributions to who and where I am today. I also thank Lisa and Karl-Werner for embarking on two unexpected adventures to the North-East of England and for welcoming me into their home in Bötzingen – vielen Dank ihr Zwei! Coffee and words of encouragement from René, Carmen and Elena are also greatly appreciated.

Ironically, this thesis would not have been finished so promptly without the birth of my daughter Olivia in April 2002. It is well-known in my family that I am not great at getting up in the morning, so 6am breakfast with Olivia has worked wonders in this department! Olivia's birth, smiles and nappies also remind me often that astronomy is not the most important thing in life.

Finally, the most important person in my life. After writing tens of thousands of words in this thesis, I find myself short of words to thank an extraordinary woman called Michaela Müller. A simple, yet heartfelt "thank you" seems barely adequate for the enormous support and patience that I have, at times, barely deserved from Michaela during the last few years. I am privileged that she chooses to be my lover, friend and wife.

As every flower fades and as all youth
Departs, so life at every stage,
So every virtue, so our grasp of truth,
Blooms in its day and may not last forever.
Since life may summon us at every age
Be ready, heart, for parting, new endeavour,
Be ready bravely and without remorse
To find new light that old ties cannot give.
In all beginnings dwells a magic force
For guarding us and helping us to live.

Serenely let us move to distant places
And let no sentiments of home detain us.
The Cosmic Spirit seeks not to restrain us
But lifts us stage by stage to wider spaces.
If we accept a home of our own making,
Familiar habit makes for indolence.
We must prepare for parting and leave-taking
Or else remain the slaves of permanence.

Even the hour of our death may send
Us speeding to fresh and newer spaces,
And life may summon us to newer races.
So be it heart: bid farewell without end.

Stages,
from The Glassbead Game, by Hermann Hesse

To Michaela

1 INTRODUCTION

1.1 Lambert's "Dark Regents"

Humankind has studied the Universe as revealed by its luminous material (i.e. stars) for many millenia. However, we can only speculate whether ancient observers considered whether the Universe may contain significant quantities of non-luminous material or "dark matter". In the eighteenth century Johan Lambert was one of the first to postulate that dark matter may exist and indeed may dominate the gravitational physics of the Universe. This remarkable man* wrote a series of "Cosmological Letters" in which he speculated, among other things, that astronomical systems may be dominated by massive non-luminous bodies, or "dark regents", as he called them (Lambert 1761). He went on to suggest how such invisible material might be detected observationally, proposing that the reflection of star-light from the surface of the dark bodies may reveal their presence.

Nearly two hundred years after Lambert's letters, the presence of dark matter was detected observationally by Zwicky (1933). Whilst the dark matter particle itself has yet to be detected, it is clear that it does not reflect light. However, we now know that, as light from distant galaxies traverses dense concentrations of dark matter, the path of this light is deflected on its journey toward Earth. This deflection of light by matter has become known as gravitational lensing, and has become a powerful tool of observational cosmologists.

The principal aim of this thesis is to study the distribution of dark matter using observations of gravitational lensing by galaxy clusters. We begin by summarising the empirical evidence and theoretical arguments that together comprise the standard cosmological model within which this work is conducted (§1.2). We also review the development of extragalactic observational astronomy, leading to

*Despite completing a mere six years of formal schooling, Lambert later became a member of the Berlin Academy of Sciences.

the discovery that galaxy clusters are dominated by dark matter (§1.3). We then introduce gravitational lensing (§1.4) and explain how this phenomenon can be applied to answer fundamental questions about galaxy clusters, dark matter and the evolution of galaxies (§1.5). Finally, we design an experiment to exploit lensing by clusters to tackle these issues (§1.6) and state the scope and objectives of this thesis (§1.7). Unless otherwise stated, we assume throughout this thesis that $H_0 = 50\ \mathrm{km\,s^{-1}Mpc^{-1}}$ and that the Universe is flat with $q_0 = 0.5$, however these assumptions have very little impact on the majority of our conclusions. When this is not the case, we quantify the impact.

1.2 Standard Cosmological Model

We briefly review the empirical evidence and theoretical arguments that comprise the standard cosmological model. This model describes our current understanding of the origin and content of the Universe, and as such provides the context within which the experiment described in this thesis was performed. Our treatment is deliberately brief, and we refer the interested reader to the numerous texts on this subject (e.g. Peacock 1999) for more detailed explanation and background information.

1.2.1 The Big Bang

When formulating his General Theory of Relativity, Einstein (1917) believed the Universe to be static (i.e. neither expanding nor contracting), and thus introduced the "cosmological constant" in his quest for a static solution to his field equations. However, Hubble & Humason (1931) showed that galaxies are receding from the Milky Way (MW), and that their recessional velocities are proportional to their distances from the MW. This was the first observational evidence for the expansion of the Universe.

Simple thermodynamic arguments imply that if the Universe used to be smaller, then it was also hotter in the past. Gamow (1949) realised that the early stages of an expanding universe would have been so hot that the dynamics of the early expansion

must have been dominated by the energy density of thermal radiation rather than by matter. This led to the prediction that as the Universe expanded and cooled, the matter and radiation would fall out of thermodynamic equilibrium, leaving a background of black-body radiation that would have cooled to approximately $5K$ by the present day (Alpher & Herman 1950).

The microwave remnant of the "Big Bang" (as it had now become known) was detected observationally by Penzias & Wilson (1965). NASA's Cosmic Background Explorer (COBE) confirmed that the microwave background follows the predicted blackbody spectrum with a radiation temperature of $T = 2.728 \pm 0.002K$ (Fixsen et al. 1996). Further early support for the Big Bang model came from the nucleosynthesis calculations of Hoyle & Tayler (1964). At that time it was known that the cosmic abundance of Helium (24% by mass) was too high to be explained by stellar nucleosynthesis. Hoyle & Tayler calculated that the abundance of Helium could be explained by primordial nucleosynthesis.

1.2.2 Isotropy and Homogeneity

Interpretation of the observed expansion of the Universe rests on the Friedman-Le Maître expanding solutions of Einstein's field equations (Friedman 1922, 1924; Le Maître 1927). These solutions describe a perfectly isotropic (the same in all directions) and homogeneous (constant density) universe. For empirical evidence of isotropy and homogeneity, we turn again to COBE, which revealed that the root-mean-square (rms) fractional temperature fluctuations in the microwave background on scales of 7° are at the level of 10^{-5} (Bennett et al. 1996). The Universe is thus isotropic to one part in 100,000 on the largest scales observed. If we also adopt the Copernican argument that we are not privileged observers, then we further conclude that the Universe is both isotropic and homogeneous (see Peacock (1999) for a discussion of these arguments).

Robertson (1936) and Walker (1935) showed independently that the geometry of space-time in an isotropic and homogeneous universe is described by the following equation which is generally known as the Robertson-Walker metric:

$$c^2 d\tau^2 = c^2 dt^2 - R^2(t) \left(\frac{dr^2}{1 - kr^2} + r^2 d\psi^2 \right) \tag{1.1}$$

where $d\tau$ is the proper time interval measured between two distant events, dt is the proper time interval between these two events measured by an observer at rest with respect to the local matter distribution, and the spatial component has been decomposed into a time-dependent scale factor $R(t)$ that accounts for the expansion of the Universe and a time-independent "co-moving" term that contains radial (r) and transverse (ψ) components.

Cosmological models that describe an expanding, isotropic and homogeneous universe are thus commonly referred to as Friedman-Robertson-Walker (FRW) models. An important feature of FRW models is that the global geometry of the Universe is linked directly to the mean density of matter. This is conveniently expressed in terms of the curvature of the Universe k (see equation 1.1) and the mean density of the Universe Ω in units of the "critical density" $\rho_c = 3H^2/8\pi G$. If $\Omega > 1$, then the Universe is a gravitationally bound system and will ultimately re-collapse. The geometry of such a universe is closed and satisfies $k = 1$. In contrast, if $\Omega < 1$ then the Universe is un-bound and will expand for ever, with an open geometry i.e. $k = -1$. Finally, a universe with $\Omega = 1$ neither expands for ever nor re-collapses. Instead it asymptotes to zero expansion velocity and is spatially flat i.e. $k = 0$.

1.2.3 Inflation

Although measurements of the matter content of the Universe differ in their details, there is broad consensus that the mean density of the Universe is of order the critical density, i.e. the Universe is approximately flat. This result conflicts with the standard Big Bang model, in which the mean density Universe is always driven away from that required for flatness. This implies that just after the Big Bang, the Universe must have been extremely close to the critical density, thus introducing a requirement to "fine-tune" the initial conditions. The isotropy of the microwave background also causes a problem for the standard Big Bang model. The finite speed of light limits the physical scale over which thermal equilibrium could be reached at the epoch of de-coupling (i.e. when the background radiation last interacted with matter) to scales much smaller than the current horizon. A further, related uncertainty is the origin of the small observed fluctuations in the microwave

background.

Guth (1981) proposed a solution to the flatness and horizon problems which also offers a natural explanation of the microwave fluctuations. His theory of inflation postulates a period of exponential growth shortly after the Big Bang that is driven by a scalar field. This expansion drives the mean density of the Universe very close to unity, and expands small regions of the Universe over which thermal equilibrium has been reached to scales in excess of the current horizon. This process also naturally produces tiny density perturbations in the early Universe as a result of quantum fluctuations in the scalar field. These small-scale fluctuations would then be expanded to cosmological scales by inflation.

1.2.4 Dark Matter

In §1.3 we describe evidence that the material content of the Universe is dominated by mysterious, invisible matter that has become known as "dark matter". The simplest possible explanation of dark matter is that it consists of baryons that have not been incorporated into stars. There is strong evidence that such baryonic dark matter does exist in the form of brown dwarfs, planets, and black holes (see Carr 1994 for a comprehensive review of baryonic dark matter). However primordial nucleosynthesis calculations, together with modern estimates of the Hubble parameter (e.g. Freedman et al. 2001) strongly indicate that only a small fraction of the dark matter can be baryonic (Walker et al. 1991).

Broadly speaking two forms of non-baryonic dark matter have been postulated: hot dark matter (HDM) and cold dark matter (CDM). HDM consists of particles such as a massive ($\sim 30\,\mathrm{eV}$) neutrino species that moved at relativistic velocities when they de-coupled from the primordial plasma. In contrast, CDM candidates are massive weakly interacting particles such as the proposed gravitinos or photinos, and the less massive axions with similar dynamical behaviour. The greater mass of CDM particles means that they would become non-relativistic before they de-couple from the radiation field in contrast to HDM.

These differences between HDM and CDM lead to differing predictions for the clustering properties of dark matter and the fluctuations in the microwave back-

ground. For example, the relativistic velocities of HDM particles enable them to "free-stream" out of growing density perturbations in the early Universe, in contrast to CDM particles which become trapped in these primordial potential wells. HDM dominated universes therefore contain less structure than CDM universes on small scales (i.e. masses below $\sim 10^{16}$ $M_{\odot}$ – Bond, Efstathiou & Silk 1980). Simulations by White, Frenk & Davis (1983) and Davis et al. (1985) also reveal that the clustering scale of CDM more faithfully reflects the clustering of observed galaxies than that of HDM.

In summary, CDM is very successful at explaining the large-scale distribution of matter in the Universe. However, this theory faces a number of important challenges on the scales of galaxies and clusters of galaxies. We defer discussion of these challenges to §1.5.2, and now turn our attention to galaxy clusters and the role that gravitational lensing can play in studying these massive systems.

1.3 Dark Matter in Galaxy Clusters

In the eighteenth century it was known that the night sky contains fuzzy and extended objects; these objects were originally named "nebulae", indeed Wright (1750) and Kant (1755) speculated that the nebulae might actually be stellar systems comparable with our own Milky Way (MW). The status of the nebulae as systems either internal or external to the MW was resolved when Hubble (1925) identified a Cepheid variable star[†] in the Andromeda nebula (or galaxy as we now refer to it), thus enabling him to measure the distance to this system and confirm its extragalactic status. Hubble's pioneering measurement of the distance to the Andromeda galaxy opened the frontiers of extragalactic research.

It was also clear to eighteenth century astronomers that galaxies are not randomly distributed on the sky. Their positions are correlated, and there are areas of sky where the galaxy density is noticeably higher or lower than average. Associations of galaxies range from groups that contain a few members through to the most

[†]Cepheid variable stars have a well defined period-luminosity relationship which allows astronomers to deduce the distance to such stars from measurements of the period and the relative magnitude of the star.

massive clusters that contain thousands of galaxies. The first written reference to clusters of galaxies is probably that of the French astronomer Messier (1784) who noticed the exceptional concentration of galaxies in the Virgo constellation. William Herschel also commented on the tendency of galaxies to cluster on the sky, and in particular mentioned what we now refer to as the Coma cluster: *"that remarkable collection of many hundreds of nebulae which are to be seen in what I have called the nebulous stratum of Coma Berenices"* (Herschel 1785).

In the course of his life, Herschel recognised several other nearby clusters and groups of galaxies, such as Leo, Ursa Major, Hydra and NGC1469 (Herschel 1811). Today, we know of several thousand clusters; for example, Abell's (1958) catalogue lists 2,712 clusters north of $\delta = -20°$ and away from the Galactic plane (see also Abell, Corwin & Olowin 1989). Employing less strict selection criteria, Zwicky et al. (1968) identified 9,134 clusters north of $\delta = -3°$.

Zwicky (1933) used spectroscopic observations of cluster galaxies and the virial theorem to show that the galaxies in the Coma cluster (Fig. 1.1) and other rich clusters move so fast that the clusters require $\sim$ 10–100 times more mass to keep the galaxies in bound orbits than could be accounted for by the luminous galaxies alone. This was the first indication that there is invisible mass, or "dark matter", in at least some objects in the Universe. When X-ray telescopes became available (Byram, Chubb & Friedman 1966; Bradt et al. 1967; Gursky et al. 1971a & b; Kellogg et al. 1972), it was discovered that clusters are also powerful X-ray emitters. Their X-ray luminosities fall in the range $(10^{43}$–$10^{45})$ erg s^{-1}, rendering them the most luminous X-ray sources in the sky. This X-ray emission is best explained by thermal bremsstrahlung (free-free radiation) from a hot, dilute plasma with temperatures in the range $(10^7$–$10^8)$K and electron number densities of $n_e \sim 10^{-3}$cm^{-3}. Based on the assumption that this intra-cluster gas is in hydrostatic equilibrium, the X-ray temperature and flux can be used to estimate the cluster mass. Typical results *approximately* (i.e. up to a factor of $\sim$ 2) agree with the mass estimates derived from the kinematics of cluster galaxies (Zwicky 1933), with the mass of the intra-cluster gas accounting for $\sim$ 15% of the total cluster mass. The X-ray emission thus *independently* confirms the existence of dark matter in galaxy clusters.

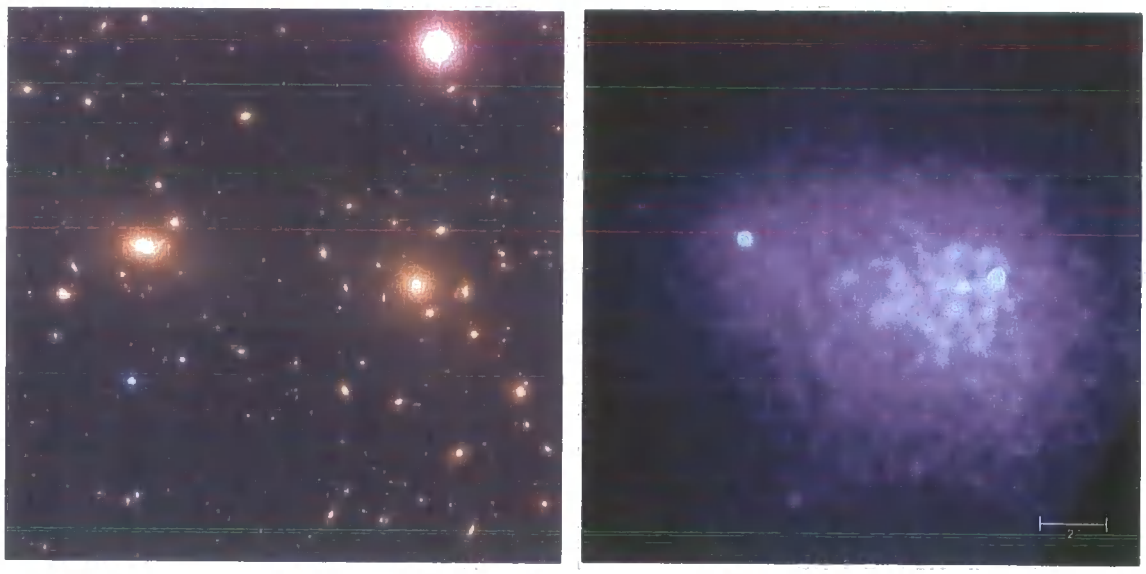

Figure 1.1: The central $17' \times 17'$ of the Coma cluster of galaxies. The left panel shows an optical image of the cluster, revealing numerous cluster elliptical galaxies, including two dominant galaxies that suggest that this cluster is undergoing a merger. The right panel presents *Chandra* observations of the same cluster. A similar bi-modal structure can be seen in the X-ray data as in the optical; the majority of the X-ray emission comes from diffuse gas that permeates the space between the cluster galaxies. However, neither the galaxies nor the X-ray emitting gas dominate the mass of the clusters such as Coma. "Dark matter", so-called because it does emit light was discovered in 1939 by Zwicky to dominate the mass of galaxy clusters. Image Credits: http://chandra.harvard.edu/photo/2002/0150/index.html

1.4 Gravitational Lensing by Galaxy Clusters

Gravitational lensing by galaxy clusters was first observed in the late-1980's and subsequently emerged as a powerful probe of the distribution of mass in galaxy clusters. In contrast to the methods described in §1.3, the deflection of light by mass depends on the *total* projected mass density (i.e. luminous and dark matter) of the lens. Lensing therefore does not rely on any assumptions regarding virialisation of the cluster, hydrostatic equilibrium between the intra-cluster gas and the underlying gravitational potential, nor the intrinsic shape of the total mass distribution. Gravitational lensing is therefore a direct observational tracer of dark matter.

1.4.1 Historical Perspective

Gravitational lensing, the deflection of light by massive bodies, is a consequence of the General Theory of Relativity (Einstein 1911; 1915). Newton (1704) had speculated about the deflection of light, however it was Soldner (1804) who calculated

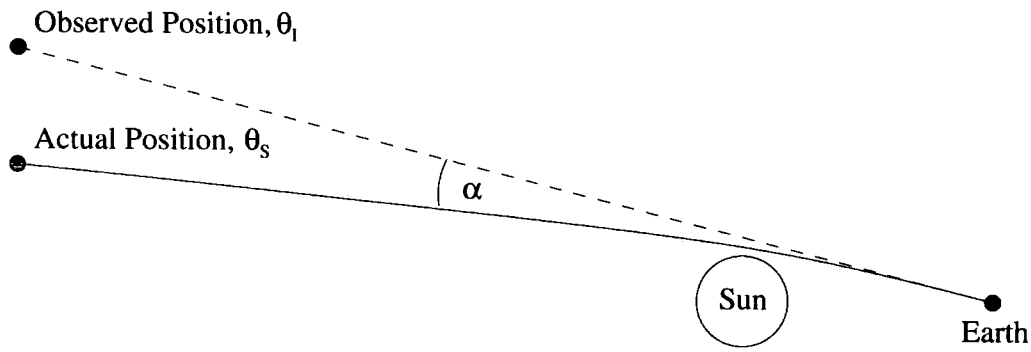

Figure 1.2: Schematic diagram of the deflection of light by the Sun. The light from a distant star grazes the limb of the Sun and is deflected by a small angle α. Treating the Sun as a point mass, Einstein showed that this angle is proportional to the mass of the Sun and inversely proportional to the distance of closest approach between the light path from the star to the observer and the centre of the Sun. Einstein's predictions were spectacularly confirmed by a team of British scientists lead by Eddington during the total solar eclipse of 1919.

the magnitude of the deflection due to the Sun, assuming that light consists of material particles and using Newtonian gravity. When Einstein (1915) applied the full field equations of General Relativity, he discovered that the deflection angle should be twice the value calculated by Soldner. Specifically, Einstein predicted that the deflection angle caused by a point mass is given by the following formula:

$$\alpha = \frac{4GM}{c^2\xi} \tag{1.2}$$

where M is the mass of the deflecting body, G is Newton's gravitational constant, c is the speed of light in vacuo and the light passes the deflector at a distance ξ. Using this formula, Einstein went on to predict that a light ray which tangentially grazes the surface of the Sun is deflected by $1.75''$. Observational confirmation arrived when the apparent shift of stars close to the limb of the Sun was measured during the 1919 total solar eclipse (Fig. 1.2; Dyson, Eddington & Davidson 1920). This quantitative agreement between prediction and observation was one of the first pieces of evidence in support of the General Theory of Relativity.

A year after the dramatic solar eclipse measurements, Eddington (1920) noted that in some cases, it might be possible for multiple light-paths to connect a source with an observer, implying that gravitational lensing can give rise to multiple images of a single source. Chowlson (1924) considered the creation of fictitious double stars by gravitational lensing of stars by stars, but did not comment on whether

the phenomenon could actually be observed. Einstein (1936) discussed the same problem and concluded that there is little chance of observing strong lensing by stellar-mass lenses because the separation of the images on the sky would be too small to be resolved by an optical telescope.

In contrast, Zwicky (1937a) pointed out that a galaxy-mass lens could split images of background sources by a large enough angle to be observed. At that time galaxies were commonly believed to have masses of $\sim 10^9$ $M_\odot$, however Zwicky (1933) had applied the virial theorem to the Virgo and Coma clusters of galaxies and had estimated a mean galaxy mass of $\sim 4 \times 10^{11}$ $M_\odot$. Zwicky (1937b) argued that the deflection of light by galaxies would have three important astrophysical applications:

- to provide further tests of General Relativity;
- to magnify distant galaxies which would otherwise remain undetected;
- to measure precisely the mass of the lensing galaxies.

Zwicky's latter two points continue to drive much of extragalactic gravitational lensing studies to the present day. However, over forty years passed before multiple gravitational images were first observed by Walsh, Carswell & Weymann (1979), when they confirmed that the double quasar QSO 0957+561A,B actually consists of two images (A and B) of the same quasar that is lensed by a foreground galaxy (Fig. 1.3).

On larger scales, the idea of gravitational lensing by galaxy clusters had been considered theoretically before the discovery of QSO 0957+561, however it was not until the late-1980's that it entered the observational realm. The breakthrough came with the discovery of giant blue luminous arcs in the centre of the galaxy clusters A 370 and Cl 2244−02 (Soucail et al. 1987a; Lynds & Petrosian 1989). Paczyński (1987) proposed that the arcs are the images of background galaxies that are strongly distorted and elongated by the gravitational lens effect of the foreground cluster. This interpretation was confirmed when the first arc redshifts were measured and found to be significantly greater than that of the clusters (Soucail 1987b). The ability of massive clusters of galaxies to form strongly distorted,

Figure 1.3: *HST* image of the double quasar QSO 0957+561. The faint halo just above the lower image comes from the galaxy that is gravitationally lensing the light from this distant quasar and producing two images of it. The discovery by Walsh, Carswell & Weymann (1979) that these are two images of the same quasar was the first observation of strong gravitational lensing. Image credit: http://www.astr.ua.edu/keel/agn/q0957.html

multiple images of faint distant galaxies has become known as "strong lensing" (Fig. 1.4).

Shortly after these discoveries, Fort et al. (1988) detected a number of weakly distorted galaxy images in the cluster A 370. They also interpreted these "arclets" as distorted images of background galaxies, but on a weaker level than the luminous giant arc in the same cluster. The redshift determination of one arclet by Mellier et al. (1991) provided early support for this interpretation (see also Tyson et al. 1990; Kochanek 1990; Miralda-Escudé 1991). The study of galaxy clusters using weakly distorted images of faint background galaxies has become known as "weak lensing" (Fig. 1.4).

At the beginning of the 1990's, gravitational lensing by galaxy clusters was therefore a new and exciting opportunity to study galaxy clusters and the distant galaxies that they magnify. However, to interpret robustly these new observational data and thus obtain accurate astrophysical measurements, it was essential to develop new modelling and analysis techniques. The techniques that emerged in the ensuing years fall broadly under two headings: parametric and non-parametric techniques.

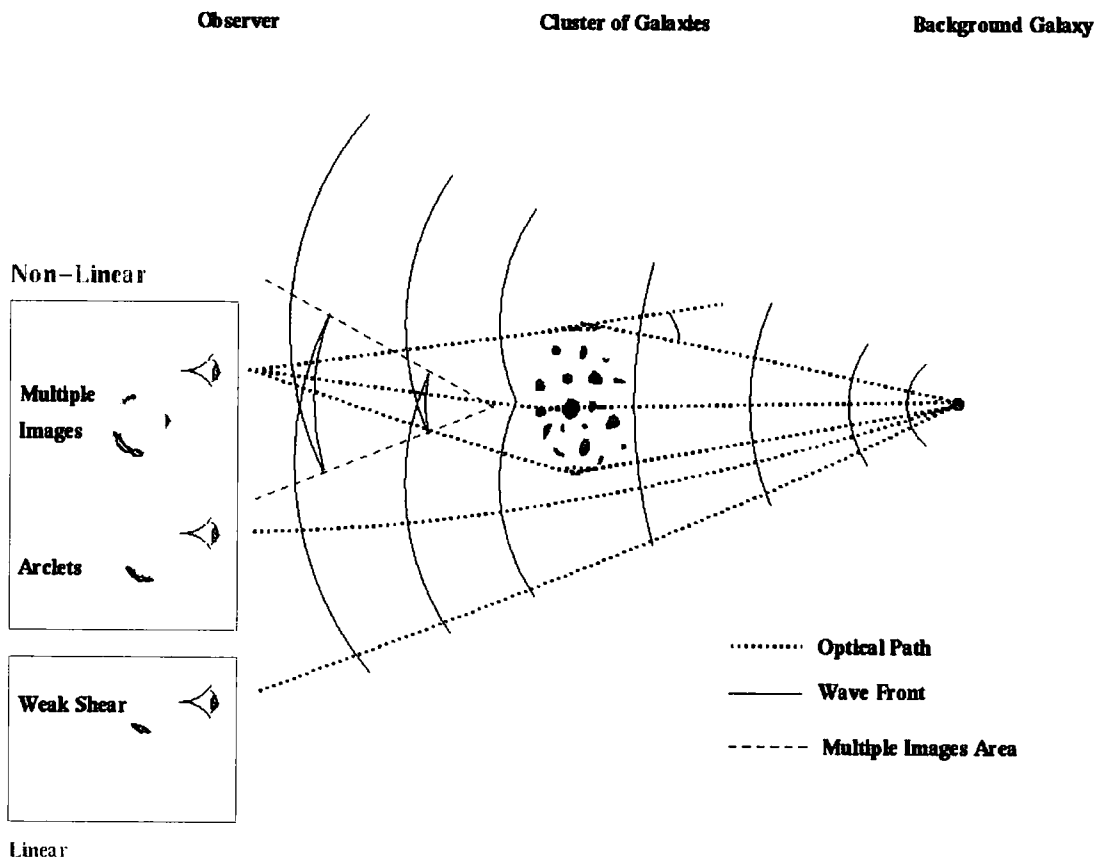

Figure 1.4: Schematic diagram of the strong (non-linear) and weak (linear) lensing regimes of gravitational lensing by galaxy clusters. Light-paths that pass close to the centre of the cluster lens are deflected by the relatively strong gravitational potential of the cluster, and in some cases multiple light-paths can connect an observer with a distant galaxy. At slightly larger radii, the deflection of the light-path is still non-linear, leading to quite strong distortion of the images of distant galaxies. At larger radii still, the deflection is so weak that it can only be studied on a statistical basis by averaging over the images of many faint galaxies. This is called the linear regime, or weak lensing. Figure Credit: Dr. Jean-Paul Kneib, Observatoire Midi-Pyrénées, Toulouse, France.

1.4.2 Parametric Techniques

Significant effort was invested in the development of parametric techniques during the 1990's. Pre-eminent among these techniques was that developed by Dr. Jean-Paul Kneib (Kneib 1993; Kneib et al. 1993; Mellier et al. 1993; Kneib et al. 1994; Kneib et al. 1995), with which one can reconstruct a detailed map of the total cluster mass from the multiple-images observed in their central regions[‡].

Kneib's method uses the position, shape, relative flux and redshift of multiple-images of background galaxies to constrain an analytic description of the mass distribution in the cluster lens. These analytic mass maps comprise a superposition of mass components that are associated with the likely concentrations of mass in the cluster. Conceptually, therefore, this method consists of solving equations of the form:

$$\theta_{\rm S} = \theta_{\rm I}{}^{j} - \alpha(\theta_{\rm I}{}^{j})\, f(z_{\rm L}, z_{\rm S}, \Omega_{\rm o}, \Lambda_{\rm o}, H_{\rm o}) \tag{1.3}$$

where $\theta_{\rm S}$ is the position on the sky that the lensed galaxy would have in the absence of the foreground lens, $\theta_{\rm I}{}^{j}$ is the observed position on the sky of the jth image of the lensed galaxy, α is the angle through which the light-ray from the source to the observer is deflected and f is a function of the redshift of the lens ($z_{\rm L}$) and the source ($z_{\rm S}$) and the geometry ($\Omega_{\rm o}$, $\Lambda_{\rm o}$) and speed of expansion ($H_{\rm o}$) of the Universe. Equation 1.2 shows that α is related to the mass of the lens, and so in essence the method involves finding the analytic mass distribution that is the best fit to the observed image positions, constrained by the identification of several images as arising from the same source.

Despite encouraging early progress in developing these modelling techniques, the accuracy of the resulting mass maps was limited by the spatial resolution of the ground-based observations upon which they were based (FWHM$\sim 1''$). A major improvement arrived with the *Hubble Space Telescope (HST)* which, even in its aberrated state, provided a significant improvement in spatial resolution over the ground-based observations (e.g. Smail 1993; Fig. 1.5). Most strikingly, after

[‡]We adopt and extend the methods developed by Kneib (1993), and explain the relevant theory and the details of this approach in §2. Here we provide a brief overview of the method.

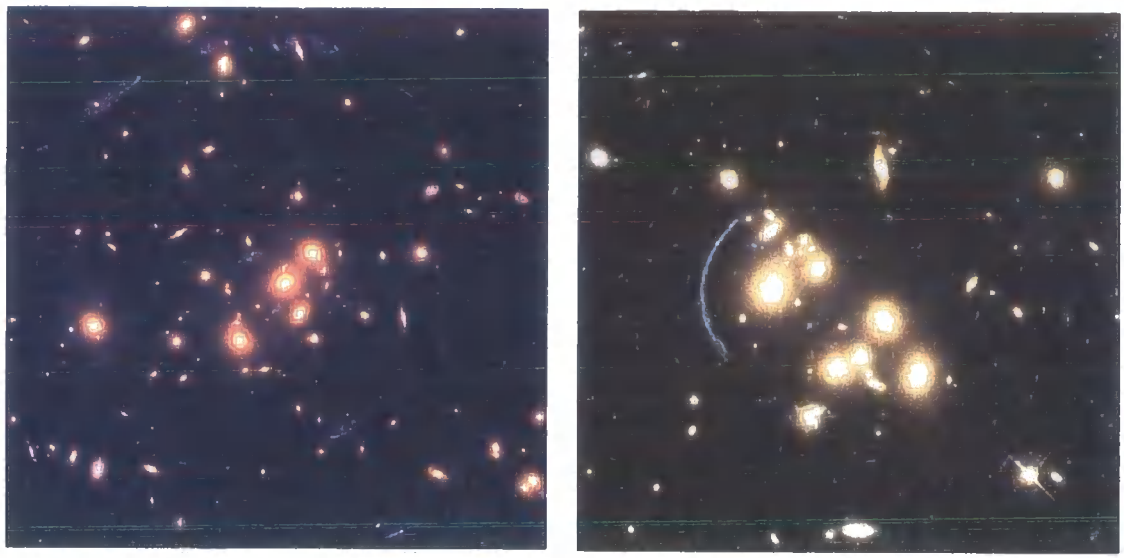

Figure 1.5: The superlative spatial resolution of *HST* reveals several striking multiple-image systems in Cl 0024+16 ($z = 0.39$; left panel) and Cl 2244−02 ($z = 0.33$; right panel), two of the first clusters to be observed following the correction of the *HST* optics. Five images of a blue background galaxy are visible around the center of Cl 0024+16 (3 at the top, 1 at the bottom and 1 in the centre of the frame). The semi-circular blue arc seen left of centre in Cl 2244−02 has been spectroscopically identified as a z=2.235 galaxy, at the time the highest redshift 'normal' galaxy known. Image Credits: http://star-www.dur.ac.uk:80/~irs/astronomy.html.

correction of the aberrated optics, the superlative resolution (FWHM $\sim 0.15''$) of *HST* observations of A 2218 ($z = 0.17$) enabled Kneib et al. (1996) to identify numerous new faint, lensed features in the crowded core of this galaxy cluster. These new data enabled Kneib et al. to improve dramatically the precision of their previous modelling of this cluster (Kneib et al. 1995).

In summary, mass maps derived from parametrised models based on *HST* observations of strong lensing provide the most direct and detailed view of the spatial distribution of matter in the centers ($r \lesssim 0.5$ Mpc) of these massive systems.

1.4.3 Non-parametric Techniques

In contrast to the parametric techniques described above, non-parametric methods are generally applied to weak-lensing data[§], and can thus in principal probe the mass distribution in galaxy clusters on scales of $r \sim 0.5$–10 Mpc. The field of weak

[§]We also note that Abselsalam et al. (1998) developed a non-parametric approach for application to strong lensing data; this method has only been applied to three clusters in the literature and therefore we do not consider it any further.

lensing by galaxy clusters began to flourish when Kaiser & Squires (1993 – hereafter KS93) showed that a statistical analysis of the distortion of background galaxies by a foreground cluster lens can be used to reconstruct a parameter-free map of the cluster surface mass density. In summary, this method involves constructing a shear map by averaging in cells the ellipticity and orientation of the weakly sheared faint galaxy images to calculate the local shear γ on a grid, and then convolving this shear map with a complex kernel $\mathcal{D}^*$ to recover the projected surface mass density:

$$\kappa(\theta) - \kappa_o = \frac{1}{\pi} \int d^2\theta' \, \Re \left[\mathcal{D}^*(\theta - \theta') \gamma(\theta) \right] \tag{1.4}$$

where κ is the projected mass density of the cluster, κ_o is an additive constant, the integral extends over the full projected spatial extent of the cluster and γ is the smoothed shear-field[¶]. From an observational point of view, this method suffers from several problems because observational data have finite spatial extent, equation 1.4 only holds in the low density limit (i.e. $\gamma \ll 1$ and $\kappa \ll 1$) and this method only determines the cluster mass distributions upto an additive constant (κ_o). These problems have been addressed to some extent with the advent of panoramic CCD cameras with fields of view of a substantial fraction of a square degree, and numerous modifications and additions to the KS93 formalism (e.g. Seitz & Schneider 1995; van Kampen 1998; Dye & Taylor 1998).

Nevertheless, two fundamental limitations continue to plague cluster mass-maps based on weak-lensing analyses: their noise properties are difficult to quantify and they have limited spatial resolution ($\gtrsim 30''$). As a result, weak-lensing mass-maps are prone to spurious detections and noise artefacts masquerading as cluster substructure (e.g. Fahlman et al. 1994; Smail et al. 1995a; Marshall et al. 2002). Other non-parametric techniques such as maximum likelihood and maximum entropy methods (e.g. Bridle et al. 1998) claim to provide a more tractable error analysis. However, crucially, they do not improve upon the poor spatial resolution of KS93-based methods. The limited spatial resolution of weak lensing studies arises

[¶]This technique is not employed in the experiment described in this thesis; we therefore refer the reader to Kaiser & Squires (1993) or a suitable review article for a detailed derivation and explanation of this formula (e.g. Narayan & Bartelmann 1996; Mellier 1999; Bartelmann & Schneider 2000).

because the method relies on a sparsely sampled field of faint galaxy images that have a random distribution of intrinsic shapes and alignments. The width of the smoothing filter used in the construction of the all-important shear map therefore places a hard lower limit on the spatial resolution of the resulting mass maps. Weak lensing mass maps therefore cannot be used to track the distribution of dark matter on scales of $\lesssim 100$ kpc.

In response to these issues, an interesting trend has recently emerged: KS93-based methods are increasingly used simply to visualise cluster mass distributions in a qualitative manner, and the detailed analysis of the cluster mass distributions places increasing reliance on fitting parametrised models (e.g. singular isothermal sphere models) to the radial shear profile (e.g. Smail et al. 1995a; King, Clowe & Schneider 2002; Dahle et al. 2002a). The appeal of these parametrised methods is the simplicity of the error treatment which enables the statistical significance of the results to be estimated robustly. This same attraction also applies to parametrised models based on strong-lensing observations described in §1.4.2, with the added advantage that strong-lensing-based methods do not rely on a smoothed shear field, and thus enjoy vastly superior spatial resolution.

We return to Gravitational Lensing in §2 when we describe the theoretical framework relevant to multiple-imaging by clusters and explain our lens modelling methodology.

1.5 Applications of Cluster Lensing

We discuss key applications of gravitational lensing by galaxy clusters, concentrating on the following three areas: the mass and structure of galaxy clusters, testing the cold dark matter (CDM) paradigm and clusters as gravitational telescopes.

1.5.1 The Structure of Galaxy Clusters

Galaxy clusters are currently believed to form through the hierarchical merging of smaller mass units (e.g. Frenk et al. 1990). Indeed, by the early-1990's there was clear evidence in both optical and X-ray pass-bands that a substantial fraction of

clusters exhibit internal substructure and are not all dynamically relaxed systems (e.g. Geller & Beers 1982; Dressler & Shectman 1988; West & Bothun 1990; Forman & Jones 1990). At around this time it was also noted that the growth and hence morphology of clusters is connected with the underlying cosmology, especially the value of Ω_o, the matter density of the Universe (Gunn & Gott 1972; Peebles 1980; Richstone, Loeb & Turner 1992; Evrard et al. 1993). Significant effort was therefore invested during the 1990's in attempts to quantify cluster morphology, largely using data from X-ray satellites such as *Einstein* and *ROSAT* (e.g. Mohr et al. 1995; Buote & Tsai 1995, 1996; Jones & Forman 1999). These pioneering works relied on relatively crude measurements derived from the low-resolution X-ray data that was available at the time. They also assumed that the X-ray morphology of the clusters was a fair tracer of the underlying mass distribution. It was therefore difficult to interpret these results beyond making broad estimates of the fraction of clusters that contain substructure. In contrast, a strong test of the prevalence of cluster substructure would go beyond mere identification of its possible existence, and make precise, quantitative, measurements of the amount of substructure without relying on assumptions about the nature and physical properties of the cluster material.

Today, high precision parametric lens models based on *HST* imaging observations (e.g. Kneib et al. 1996; §1.4.2) and the new generation of high-resolution X-ray observatories (*Chandra* and *XMM-Newton*) are a powerful combination with which to investigate the structure of galaxy clusters (e.g. Mazzotta et al. 2002) and the relative contributions of dark and luminous matter. The spatially resolved spectroscopic capability of these new X-ray observatories also means that we can study the temperature structure of clusters and relate these measurements to the structure of the underlying gravitational potential as determined from lensing studies. In summary, the superlative resolution of modern space-based observatories in conjunction with the lens modelling and analysis techniques developed in the 1990's place us at the brink of major breakthroughs in our understanding of the detailed physics of galaxy clusters.

1.5.2 Testing the Cold Dark Matter Paradigm

The currently popular CDM paradigm of structure formation makes a number of predictions about the observable properties of the Universe (see Primack 2002 for a recent review). These predictions are generally in excellent agreement with observations on large scales ($\gg$ 1 Mpc; e.g. Bahcall et al. 1999), however they appear to conflict with a number of observations on smaller scales ($\lesssim$ 1 Mpc). For example, numerical simulations that follow the development of structure in dark matter only universes predict that the density profile ($\rho(r)$, where ρ is the three dimensional matter density and r is the radial direction) of clusters contains a central cusp, and that this cusp is shallower than isothermal[‖] i.e. $\rho \propto r^{-\alpha}$ with $\alpha \sim 1.0$–1.6 (Navarro, Frenk & White 1997; Moore et al. 1998; Ghinga et al. 2001; Power et al. 2002). The simulations also predict that the shape of the density profile is independent of the mass of the system. Detailed observational investigation of the density profiles of real astrophysical systems across a range of masses is required to test these predictions. Gravitational lensing by galaxy clusters provides an important opportunity to address this question at the high-mass end of the spectrum of collapsed astrophysical objects. It appears from analysis of Cl 0024+16 (Tyson et al. 1998) that, at least in one cluster, the dark matter density profile is flat in the central region. Clearly a systematic gravitational study of a sample of clusters is required to test the reliability of this claim.

The numerical simulations referred to above all assume that dark matter particles do not interact with each other, indeed the predicted central density cusp stems largely from this assumption. This collisionless picture appears to conflict with several pieces of evidence on galaxy-scales. Specifically, dwarf irregular galaxies appear to have low density cores (Moore 1994; Flores & Primack 1994; de Blok & McGaugh 1997; Dalcanton & Bernstein 1999) with much shallower profiles than predicted by the simulations, and observations of the Local Group of galaxies reveal less than 100 galaxies (Mateo 1998) while the simulations (Klypin et al. 1999; Moore et al. 1999) and analytical theory (Bond et al. 1991; Bower 1991; Lacey & Cole 1993) predict that there should be $\sim 1,000$ discrete dark matter halos within

[‖]The density profile of an isothermal mass distribution goes as $\rho \propto r^{-2}$.

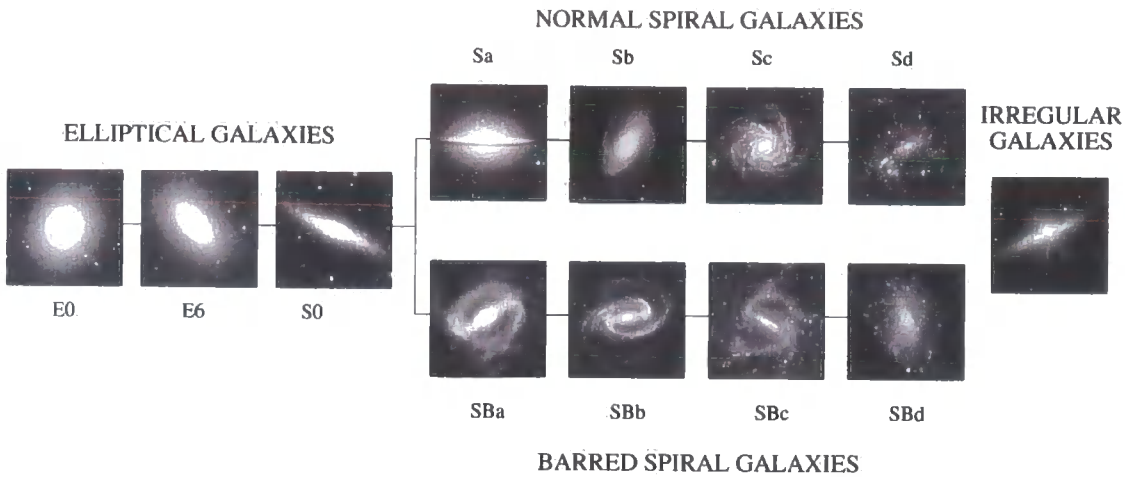

Figure 1.6: The classical "tuning fork" diagram that Hubble used to classify the morphologies of galaxies. Image Credits: http://www.astr.ua.edu/preprints/white/gal_tuningfrk.html

the Local Group. Spergel & Steinhardt (2000) proposed that these issues could be resolved if dark matter is self-interacting. Such a modification to the physical properties of dark matter should have measurable effects on the distribution of matter in galaxy clusters (e.g. removal of the central density cusp, and more spherical clusters). Galaxy clusters are therefore an important laboratory in which to study the fundamental properties of dark matter and gravitational lensing has a vital role to play in this investigation.

1.5.3 Clusters as Gravitational Telescopes

Following Hubble's (1925) pioneering observations of the Andromeda galaxy (§1.3), we now estimate that there are $\sim 10^{10}$ galaxies in the observable Universe. Despite the enormity of this number, Hubble found that the morphologies of local galaxies can be classified into four main morphological types: ellipticals, normal spirals, barred spirals and irregular galaxies (Fig. 1.6).

Hubble's classification scheme prompts the question: *"why do galaxies look like this?"*; this question continues to drive galaxy formation and evolution studies to the present day. Given the finite speed of light, one approach to answering this question is to study galaxies at greater and greater look-back-times with the aim of identifying evolutionary trends that may provide clues to when and how present-day galaxies acquired their familiar elliptical and spiral structures. Unfortunately,

several effects conspire to make it increasingly difficult to apply this approach to more distant galaxies. The signal-to-noise ratio achievable in such observations therefore decreases with increasing redshift, and this approach becomes more and more expensive, whilst the bias towards the most luminous systems also increases.

Gravitational lensing offers a partial solution to these problems, because the cores of massive galaxy clusters at intermediate redshift ($z \sim 0.2$–1) act as powerful gravitational lenses and thus provide a magnified view of the galaxies that lie behind them. As we explain in more detail in §2, this magnification increases the solid-angle subtended by the background galaxy whilst conserving its surface brightness. Lensing therefore increases both the sensitivity and the spatial resolution of observations of high-redshift galaxies. Galaxy clusters have therefore been used as natural zoom lenses to study systematically several populations of high-redshift galaxies, including "faint blue galaxies" (e.g., Kneib et al., 1996; see also Ellis 1997 for a review) and extragalactic sub-millimetre sources (e.g., Smail, Ivison & Blain 1997a; Smail et al. 2002a). A number of individual sources have also been discovered serendipitously and studied in this way (e.g. Hammer & Rigaut 1989 ; Ebbels et al. 1996; Franx et al. 1997; Seitz et al. 1998; Pelló et al. 1999; Ellis et al. 2001).

A key feature of these studies is that the lens magnification enables intrinsically low-luminosity galaxies at remote epochs to be observed and studied in great detail. Gravitational lensing therefore has an important role to play in filling the many gaps in our understanding of how and when both luminous and the more typical and numerous sub-luminous galaxies form and how they subsequently evolve.

Extremely Red Objects

One class of distant galaxy that may benefit from the enhanced sensitivity provided by a gravitational lens is Extremely Red Objects (EROs). These galaxies are defined by their very red optical/near-infrared colours (e.g. $(R - K) \geq 5.3$) and typically have K–band magnitudes of $K \gtrsim 18$. Since their discovery in pioneering near-infrared imaging observations (Elston et al. 1988, 1989, 1991; McCarthy et al. 1992; Eisenhardt & Dickinson 1992; Graham et al. 1994; Hu & Ridgway 1994; Dey et al.

1995), they have intrigued cosmologists, but their extreme properties have so far escaped detailed, systematic investigation.

The optical faintness of EROs ($R \gtrsim 23$) and the lack of near-infrared multi-object spectrographs have combined to severely limit the number of spectroscopic identifications. However, the available spectra indicate that EROs comprise two broad classes of system: galaxies with evolved stellar populations at $z \gtrsim 1$ (e.g. Dunlop et al. 1996; Soifer et al. 1999; Liu et al. 2000) and dust-reddened starbursts at similar and higher redshifts (e.g. Graham & Dey 1996; Dey et al. 1999; Smail et al. 1999a). These two classes of EROs may represent different phases in the formation and evolution of a single family of high redshift galaxies: massive ellipticals. However, rival galaxy formation theories (pure luminosity evolution and hierarchical clustering) predict very different formation epochs for such galaxies. The former predicts formation at high redshift in what is traditionally known as the "monolithic collapse" scenario (e.g. Eggen et al. 1962; Larson 1975; Tinsley & Gunn 1976) followed by subsequent passive evolution. The latter predicts formation through the merging of disk galaxies at $z \lesssim 1$ (e.g. White & Frenk 1991; Kauffmann et al. 1993, 1996; Baugh et al. 1996; Cole et al. 1996, 2000). To understand more about the nature of these galaxies requires spectroscopic study. Such observations are extremely challenging, even with 10–m class telescopes; consequently, only a handful of EROs have been spectroscopically identified and studied in detail to date (e.g. Dey et al. 1999; Pierre et al. 2001; Afonso et al. 2001).

In summary, the properties of EROs, particularly, their redshift distribution and spectral characteristics, are crucial tests of galaxy formation theories. Many groups are therefore currently investigating different aspects of the ERO population using a variety of observational approaches, for example: wide-field imaging surveys (Thompson et al. 1999; Daddi et al. 2000a; Roche et al. 2002), morphological studies (Treu et al. 1999; Moriondo et al. 2000), searches for over-densities around radio-loud active galactic nuclei (AGN) (Willott, Rawlings & Blundell 2000; Chapman, McCarthy & Persson 2000; Cimatti et al. 2000, Hall et al. 2001), deep K–band number counts (Barger et al. 1999; McCracken et al. 2000; Corbin et al. 2000), searches for optically faint radio (Smail et al. 2002b), sub-mm (Smail et al. 1999a;

Mohan et al. 2002) and X-ray (Cowie et al. 2001; Alexander et al. 2001; Brusa et al. 2002) counterparts, photometric redshift studies (Fontana et al. 1999; Firth et al. 2002), optical spectroscopy of bright EROs (Cimatti et al. 2002) and studies of faint field spheroidals (Menanteau et al. 1999).

Clearly, the lens amplification afforded by a sample of massive foreground clusters would increase the detected flux from EROs that lie behind the lenses, thus increasing the probability of successful spectroscopic identifications. A sample of gravitationally lensed EROs therefore promises to drive this field forward.

1.6 Survey Design

Previous studies of gravitational lensing by galaxy clusters have concentrated on individual clusters selected because of their prominent arcs (e.g. Kneib et al. 1993, 1994, 1995, 1996; Mellier et al. 1993; Smail et al. 1996; Allen et al. 1996; Tyson et al. 1998; Kneib et al. 1999; Cohen et al. 2002), larger samples of clusters selected because they were previously well-studied (e.g. Smail et al. 1997b; Hoekstra 1998) and ground-based searches for elongated structures that paid limited attention to whether such arcs are truly multiply-imaged (e.g. Luppino et al. 1999). Regardless of the merits of any individual work, two factors have resulted in the poorly defined cluster selection criteria typical of these surveys. First, with the emergence of cluster lensing as a field of study at the beginning of the 1990's, came a need to develop new analysis and modelling techniques (§1.4.2 & §1.4.3); developmental activities necessarily concentrated on clusters that exhibit high signal-to-noise signatures of gravitational lensing. Second, studies that exploit data from over-subscribed observatories such as *HST* have understandably made the most of existing datasets that may not have been constructed with an objective study of cluster lensing in mind. The net result is that we now have a powerful armoury of modelling and analysis techniques at our disposal, however these techniques have yet to be applied in a systematic manner to objectively selected cluster samples. In summary, it is time to move on from the developmental years of the 1990's and to begin the systematic exploitation of cluster lensing to investigate fundamental questions about the

formation and evolution of galaxy clusters and distant galaxies.

The overall aim of our survey is to analyse the distribution of dark and luminous matter in an objectively selected sample of galaxy clusters. Ideally we would investigate large numbers of clusters across a broad range of redshifts and masses, however we adopt a more realistic approach and limit the initial phase of our survey to the most massive systems at a single epoch. The design and execution of our survey is somewhat circular in that gravitational lensing is the tool of choice for measuring cluster masses and yet we wish to study a mass-selected sample. In the absence of mass-selected cluster catalogues from which to construct our sample, X-ray selected cluster catalogues (Gioia et al. 1990; Ebeling et al. 1998, 2000; DeGrandi et al. 1999) are best suited to selecting well-defined samples of massive clusters. X-ray selection also influences our choice of epoch at which to study clusters because the completeness of currently available X-ray catalogues typically falls off dramatically beyond $z \sim 0.3$ (although see Ebeling, Edge & Henry 2001). We therefore adopt $z = 0.2$ as the nominal epoch of our cluster sample.

We select ten of the most X-ray luminous clusters ($L_{\rm X} \geq 8 \times 10^{44}$ erg s^{-1}, 0.1–2.4 keV) in a narrow redshift slice at $0.17 < z < 0.25$, with line-of-sight reddening of $E(B-V) \leq 0.1$ from the XBACs sample (X-ray Brightest Abell-type Clusters; Ebeling et al. 1996). We also ensure that our sample spans the full range of X-ray properties (morphology, central galaxy line emission, cooling flow rate, core radius) found in much larger X-ray selected samples (e.g. Peres et al. 1998; Crawford et al. 1999). We list our cluster sample in Table 1.1.

A comprehensive study of this cluster sample requires both strong and weak lensing analyses to probe the dark matter distribution on scales spanning $\sim$ 10–1,000 kpc** from the centre of each cluster. Indeed, the strong lensing analysis of the central region of each cluster will be the fundamental cornerstone of the whole survey, as it will deliver the absolute calibration of the combined strong and weak lensing mass maps. We also complement the lensing analysis with X-ray observations of each cluster with *XMM-Newton* and exploit archival *Chandra* observations that offer higher spatial resolution in the central regions. Finally, an extensive

**In the cosmology adopted throughout this thesis, $1'' \equiv 4.2$ kpc at $z = 0.2$.

Table 1.1: Sample Selection

Cluster	Co-ordinates of Central Galaxy α, δ (J2000)	Selection Criteria (Ebeling et al. 1996) Redshift	$E(B-V)$	L_X [0.2–2.4 keV] (10^{44} erg s^{-1})
A 68	00 37 06.81 +09 09 24.0	0.255	0.093	8.4 ± 2.3
A 209	01 31 52.53 −13 36 40.5	0.209	0.019	13.8 ± 2.3
A 267	01 52 41.97 +01 00 26.2	0.230	0.025	13.3 ± 2.8
A 383	02 48 03.38 −03 31 45.7	0.187	0.033	8.0 ± 2.4
A 773	09 17 53.37 +51 43 37.2	0.217	0.015	12.5 ± 2.1
A 963	10 17 03.57 +39 02 49.2	0.206	0.015	10.2 ± 1.9
A 1763	13 35 20.10 +41 00 04.0	0.228	0.009	14.2 ± 2.1
A 1835	14 01 02.05 +02 52 42.3	0.253	0.030	38.3 ± 5.4
A 2218	16 35 49.22 +66 12 44.8	0.171	0.024	9.0 ± 0.8
A 2219	16 40 19.82 +46 42 41.5	0.228	0.024	19.8 ± 2.2

spectroscopic survey of the cluster galaxies will probe the galaxy dynamics of each cluster.

The observatory of choice for strong-lensing observations of galaxy clusters is *HST* (§1.4.2). As part of our survey, eight clusters have been observed through the F702W filter using the WFPC2 camera onboard *HST* during Cycle 8 (A 68, A 209, A 267, A 383, A 773, A 963, A 1763 and A 1835). We draw similar observations of the remaining two clusters in our sample from the *HST* archive (A 2218, A 2219). Homogeneous F702W imaging with the WFPC2 camera is therefore available for all ten clusters.

1.7 Thesis Scope and Objectives

This thesis concentrates on the detailed mass distribution in the inner 1 Mpc of the clusters, which can be well constrained by models constructed from multiple-

image systems observed in their central regions. We thus build the foundation for subsequent analysis of the panoramic weak-lensing, X-ray and spectroscopic datasets. The objectives of this thesis are as follows:

- to construct a detailed lens model of each cluster;
- to use these models to measure the mass and structure of each cluster;
- to probe the dynamical maturity of the clusters using a joint lensing and X-ray analysis;
- to test key predictions of the standard CDM-based cosmological model using the properties of the lens models;
- to exploit the cluster lenses as gravitational telescopes and construct a sample of gravitationally lensed EROs;
- to investigate the nature of these EROs and also to test rival theories of galaxy formation.

We summarise the content of each chapter:

Chapter 2, Gravitational Lensing Theory and Modelling

We explain the theoretical background required to interpret multiply-imaged galaxies, and explain our lens modelling methodology. We aim to provide an intuitive grasp of relevant physical phenomena, underpinned with key equations, numerical examples and simple illustrative models.

Chapter 3, The Lens Models and The Structure of Clusters

We present *HST* observations of the whole cluster sample, and use them, in conjunction with ground-based spectroscopy to construct detailed lens models. We analyse the distribution of mass in the clusters and compare our cluster mass and substructure measurements with independent constraints from archival *Chandra* and *ROSAT* observations.

Chapter 4, Implications for Cold Dark Matter

We exploit the lens models to investigate key predictions of and alternatives to the popular CDM paradigm, including the inner slope of the cluster density profile, self-interacting dark matter and the normalisation of the matter power spectrum.

Chapter 5, A Search for Gravitationally Lensed EROs

We complement the optical *HST* data with deep, high-resolution near-infrared imaging from the United Kingdom Infrared Telescope (UKIRT). Using our cluster sample as a suite of ten powerful gravitational telescopes, we construct a sample of 60 gravitationally lensed EROs. We compare our sample with the predictions of rival theoretical predictions and suggest possible modifications to these theories.

Chapter 6, The Diversity of EROs

We study two of the brightest EROs in our sample. Near-infrared spectroscopy reveals ERO J164023 to be a starburst-Seyfert galaxy at $z = 1.05$, and ERO J003707 to be an Sa galaxy at $z = 1.60$. These two galaxies provide dramatic evidence of the diversity of EROs.

Chapter 7, Conclusions

We briefly summarise the conclusions of the thesis and suggest fruitful avenues for future study.

2 GRAVITATIONAL LENSING THEORY AND MODELING

Prior to engaging in the detailed analysis and gravitational lens modelling (§3), we review the theoretical ingredients of our lens models (§2.1), and explain our modelling methodology (§2.2). We summarise the key points of this chapter in §2.3.

2.1 Theoretical Essentials

We explain the basic equations of gravitational lensing as they relate to lensing by clusters. Our aim is to cover the theoretical background to a depth required to achieve an intuitive grasp of gravitational lensing as a physical process. We therefore avoid detailed mathematical derivations in favour of physical arguments and simple illustrative models wherever possible. Much of this section is based on the treatments of Schneider, Ehlers & Falco (1992), Kneib (1993) and Narayan & Bartelmann (1996); we refer the interested reader to these works for additional theoretical details.

2.1.1 Working Assumptions

The propagation of light in arbitrary curved spacetimes is a complex theoretical problem. Fortunately, for almost all cases of relevance to gravitational lensing, we can make a number of simplifying assumptions:

A Perturbative Approach – In common with the majority of cosmological research, we assume that the Universe is homogeneous and isotropic on large scales. This means that we can treat the matter inhomogeneities which deflect light as local perturbations. We therefore think of the light path from a source, past a lens to an observer as comprising three regions: first, the light passes unperturbed from the source to a point close to the lens; second, the light path is deflected (i.e. per-

turbed) by the lens; third, the light again travels unperturbed to the observer. We quantify this assumption using the example of a massive galaxy cluster at $z = 0.2$ that deflects light from a distant galaxy at $z = 1$. The distance from observer to lens and from lens to source are both $\sim$ 1 Gpc, i.e. approximately 2–3 orders of magnitude greater than the typical dimension of a galaxy cluster ($\sim$ 5 Mpc). Thus the portion of the total light path in which deflection occurs is a very small fraction of the total source-observer distance.

Weak, stationary gravitational fields – We consider the physics required to describe the deflection of light in the vicinity of the lens. We assume that the spacetime local to the lens is flat, and that it is weakly perturbed by the Newtonian gravitational potential of the lens. This is justified if the gravitational potential of the lens Φ is small, $|\Phi| \ll c^2$, and if the peculiar velocity v of the lens is small, $v \ll c$. Returning to our example of a cluster at $z = 0.2$, light from a distant galaxy that is observed $\sim 5''$ from the centre of the cluster has experienced a Newtonian potential of $|\Phi| \sim 10^{-5}c^2 \ll c^2$ at its closest approach to the centre of the cluster, assuming the cluster to have a mass of $\sim 10^{13}$ $M_\odot$ interior to a $5''$ radius around the centre of mass. Cluster peculiar velocities are also known to be $\sim 10^3$ km s$^{-1} \ll c$.

Thin lens approximation – Extending the perturbative approach, we replace the three-dimensional mass distribution in the lens with a two-dimensional mass sheet, orthogonal to the line of sight. The plane of the mass sheet is commonly called the "lens plane", and we characterise the mass sheet by its surface-mass density:

$$\Sigma(\vec{\xi}) = \int \rho(\vec{\xi}, l) dl \tag{2.1}$$

where $\vec{\xi}$ is a two-dimensional vector in the lens plane and l is the line-of-sight co-ordinate.

Small deflection angles – The angular separation of multiple images of distant galaxies from the centre of the foreground galaxy cluster lens is typically $\lesssim 30''$. The typical deflection angle is therefore of the same order of magnitude as this angular separation, and the small angle approximation applies (i.e. $\theta \simeq sin\theta \simeq tan\theta$). This approximation is crucial to the derivation of the "lens equation", which enables us

to relate observations of multiple images in the cores of galaxy clusters to the details of the mass distribution in the lens.

2.1.2 The Lens Equation

Fig. 2.1 shows the geometry of a typical cluster lens system. A light ray from a source S is deflected by an angle $\vec{\alpha}$ and reaches the observer O. The angle between the (arbitrarily chosen) optic axis and the true source position is $\vec{\theta_S}$, and the angle between the optic axis and the image I is $\vec{\theta_I}$. Using simple geometry, we can write down a relationship between the source and image positions and the deflection angle:

$$\vec{\theta_S} = \vec{\theta_I} - \frac{D_{LS}}{D_{OS}} \vec{\alpha}(\vec{\theta_I}) \tag{2.2}$$

In general, the lens equation is non-linear, and so it is possible to have multiple values of $\vec{\theta_I}$ for a single $\vec{\theta_S}$; we illustrate this phenomenon with the images I_1, I_2 and I_3 in Fig. 2.1 and show an example of multiple images of faint background observed through the core of A 2218, a massive clusters at $z = 0.17$ in Fig. 2.2.

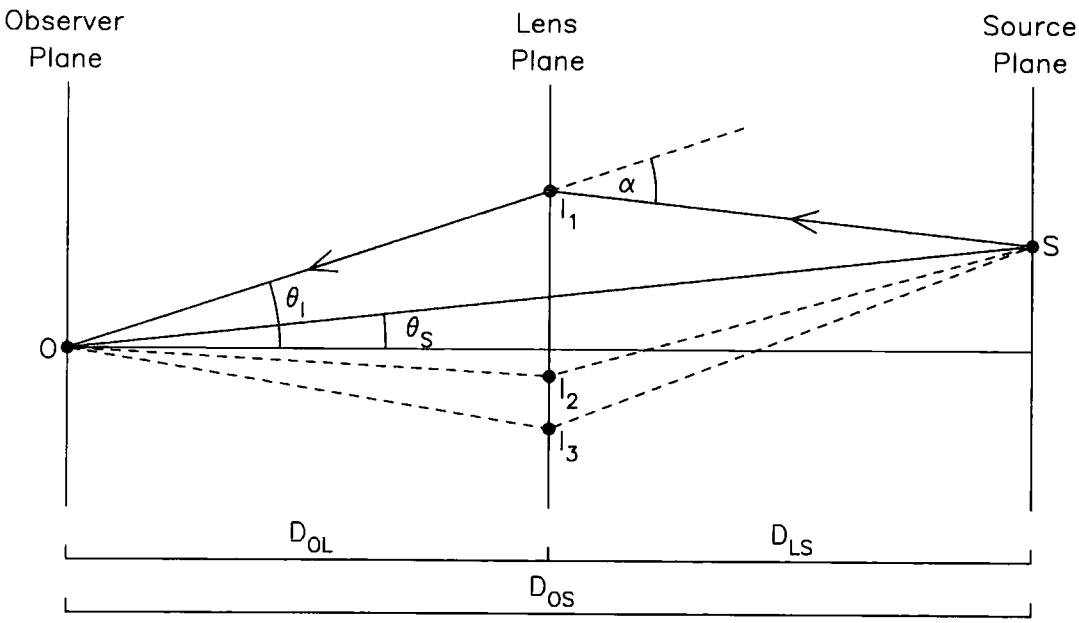

Figure 2.1: Optical diagram of a typical cluster lens; three images I_1, I_2 and I_3 of a single source S and formed.

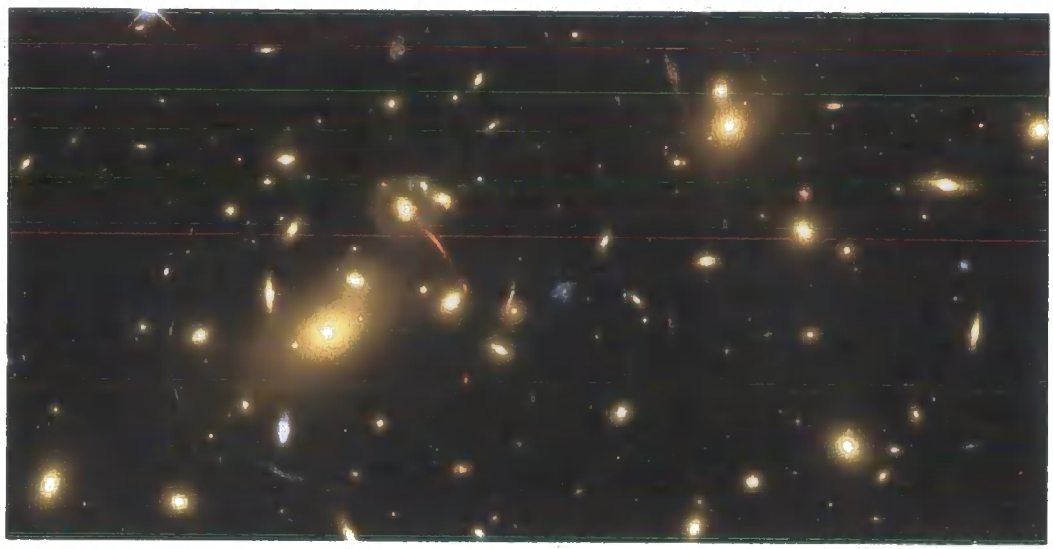

Figure 2.2: A 2218 ($z = 0.17$) is arguably the best studied galaxy cluster lens. This true colour BVI–band view from *HST* reveals numerous multiply-imaged galaxies in this central 300 kpc $\times$ 600 kpc region. Image credit: NASA and the ERO Team (Andrew Fruchter, Sylvia Baggett, Richard Hook and Zoltan Levay), http://oposite.stsci.edu/pubinfo/pr/2000/08/index.html.

2.1.3 Fermat's Principle

To obtain information about the mass distribution in a gravitational lens, we need to solve the lens equation. High resolution observations with *HST* furnish the image positions, $\vec{\theta_{\rm I}}$; identification of several images of the same background galaxy allow us to constrain several values of $\vec{\theta_{\rm I}}$ to a single value of (the as yet unknown) $\vec{\theta_{\rm S}}$. The other quantity in the lens equation is the deflection angle, $\vec{\alpha}$, which links $\vec{\theta_{\rm I}}$ and $\vec{\theta_{\rm S}}$. We apply Fermat's principle to derive an expression for the deflection angle in terms of the two-dimensional Newtonian potential of the lens, $\phi(\vec{\theta_{\rm I}})$.

In a weak gravitational field, a photon emitted by the source S at time $t = 0$, deflected by the thin lens L, arrives at the observer O at t_a, where t_a is given by (Schneider, Ehlers & Falco 1992):

$$t_a = c^{-1} \int (1 - \frac{2\Phi}{c^2}) dl = \frac{l}{c} - \frac{2}{c^3} \int \Phi dl \tag{2.3}$$

where Φ is the three dimensional Newtonian potential of the lens and l is the distance traveled by the photon. Concentrating on the right-hand-side of Equation 2.3 and neglecting high-order terms in $\vec{\theta_{\rm I}}$ and $\vec{\theta_{\rm S}}$, we can write l as:

$$l = l_{OI} + l_{IS} = D_{\rm OL} + \frac{D_{\rm OL}\vec{\theta_{\rm I}}^2}{2} + D_{\rm LS} + \frac{(D_{\rm OL}\vec{\theta_{\rm I}} - D_{\rm OS}\vec{\theta_{\rm S}})^2}{2\, D_{\rm LS}} \tag{2.4}$$

We also write the integral of the Newtonian potential along the line of sight as a projected two-dimensional potential:

$$\int \Phi dl = \phi(\vec{\xi}) = {D_{\rm OL}}^2\, \phi(\vec{\theta_{\rm I}}) \tag{2.5}$$

Substituting Equations 2.4 and 2.5 into Equation 2.3, we obtain (upto an additive constant):

$$ct_a(\vec{\theta_{\rm I}}, \vec{\theta_{\rm S}}) = \frac{(D_{\rm OL}\vec{\theta_{\rm I}} - D_{\rm OS}\vec{\theta_{\rm S}})^2}{2\, D_{\rm LS}} + \frac{D_{\rm OL}{\vec{\theta_{\rm I}}}^2}{2} - \frac{2\, {D_{\rm OL}}^2\, \phi(\vec{\theta_{\rm I}})}{c^2} \tag{2.6}$$

Applying Fermat's Principle, the light paths that connect observer and source are stationary points on the time arrival surface described by $t_a(\vec{\theta_{\rm I}})$, i.e. they satisfy $\vec{\nabla}_{\vec{\theta_{\rm I}}} t_a(\vec{\theta_{\rm I}}) = \vec{0}$. Differentiating 2.6, therefore yields the requirement that:

$$\frac{(D_{\rm OL}\vec{\theta_{\rm I}} - D_{\rm OS}\vec{\theta_{\rm S}})}{D_{\rm LS}} + \vec{\theta_{\rm I}} - \frac{2\, D_{\rm OL}}{c^2}\vec{\nabla}_{\vec{\theta_{\rm I}}}\phi(\vec{\theta_{\rm I}}) = 0, \tag{2.7}$$

which reduces to the following expression for the deflection angle $\vec{\alpha}$ in terms of the projected Newtonian potential of the lens:

$$\vec{\alpha}\,(\vec{\theta_{\rm I}}) = \frac{2\, D_{\rm OL}}{c^2}\vec{\nabla}_{\vec{\theta_{\rm I}}}\phi(\vec{\theta_{\rm I}}) = \frac{D_{\rm OS}}{D_{\rm LS}}\vec{\nabla}_{\vec{\theta_{\rm I}}}\varphi(\vec{\theta_{\rm I}}) \tag{2.8}$$

Where φ is called the lensing potential and is defined as $\varphi = (2D/c^2)\phi$, with $D = (D_{\rm OL}D_{\rm LS}\,/\,D_{\rm OS})$. Combining Equation 2.2 and 2.8, we can write the lens equation as a gradient mapping from the source to image plane:

$$\vec{\theta_{\rm S}} = \vec{\theta_{\rm I}} - \vec{\nabla}_{\vec{\theta_{\rm I}}}\varphi(\vec{\theta_{\rm I}}) \tag{2.9}$$

We can see from Equation 2.9 that knowledge of $\vec{\theta_{\rm I}}$ and multiple-image identifications enable us to place constraints on φ, and thus on the projected mass density of the lens.

2.1.4 Critical Density

The projected mass density of gravitational lenses is often described in terms of the "critical density", $\Sigma_{\rm crit}$, of the lens. We use Poisson's equation to relate the lensing potential to the surface density of the lens and thus to define $\Sigma_{\rm crit}$:

$$\vec{\nabla}^2_{\vec{\theta_I}}\varphi = \frac{2D}{c^2}\vec{\nabla}^2_{\vec{\theta_I}}\phi = \frac{2D}{c^2}4\pi G\Sigma = 2\frac{\Sigma}{\Sigma_{\rm crit}} = 2\kappa(\vec{\theta_I}) \tag{2.10}$$

where $\kappa(\vec{\theta_I}) = \Sigma(\vec{\theta_I})/\ \Sigma_{\rm crit}$ is called the convergence and we define $\Sigma_{\rm crit}$, the critical surface density to be:

$$\Sigma_{\rm crit} = \frac{c^2}{4\pi G}\frac{1}{D} \tag{2.11}$$

The Laplacian of the lens potential is therefore directly related to the surface density of the lens, and this is often written in terms of the dimensionless mass density κ, which measures the strength of the lens in units of $\Sigma_{\rm crit}$.

We explain the relevance of this convenient parameterisation to strong lensing studies using the example of a singular isothermal sphere (SIS). The projected Newtonian potential of a SIS is given by:

$$\phi(\vec{\theta_I}) = \frac{2\pi\ {\sigma_o}^2}{D_{\rm OL}}|\vec{\theta_I}| \tag{2.12}$$

from which the deflection angle can be simply shown to be:

$$\vec{\alpha}\ (\vec{\theta_I}) = \frac{2\ D_{\rm OL}}{c^2}\vec{\nabla}_{\vec{\theta_I}}\phi(\vec{\theta_I}) = \frac{4\pi\ {\sigma_o}^2}{c^2}\frac{\vec{\theta_I}}{|\vec{\theta_I}|} \tag{2.13}$$

The absolute value of the deflection angle, $|\vec{\alpha}|$, is therefore independent of image-plane position, $|\vec{\theta_I}|$. We illustrate this in Fig. 2.5 where we plot $|\vec{\alpha}|$ versus $|\vec{\theta_I}|$ as the solid heavy line. The dashed lines show several different values of $|\vec{\theta_S}|$. The intersections of the dashed lines with the thick solid line represent solutions of the lens equation, and thus demonstrate in graphical form the ability of a gravitational lens to form multiple images of single source.

When $|\vec{\theta_S}| = 0$, the circular symmetry of the lens results in the images forming a ring centred on the centre of the lens at $|\vec{\theta_I}| = \theta_{\rm E}$, where $\theta_{\rm E}$ is the Einstein radius of the lens and the ring is called an Einstein ring. If $0 < |\vec{\theta_S}| < \theta_{\rm E}$ then multiple solutions of the lens equation are still found (Fig. 2.3), however if $|\vec{\theta_S}| > \theta_{\rm E}$, then only one solution is found and strong lensing does not occur. The radius $\theta_{\rm E}$ therefore has a special significance in determining whether a lens produces multiple images of any given source. We substitute $|\vec{\theta_S}| = 0$, $|\vec{\theta_I}| = \theta_{\rm E}$ and $|\vec{\alpha}|$ from 2.13 into the lens equation to obtain the following expression for $\theta_{\rm E}$:

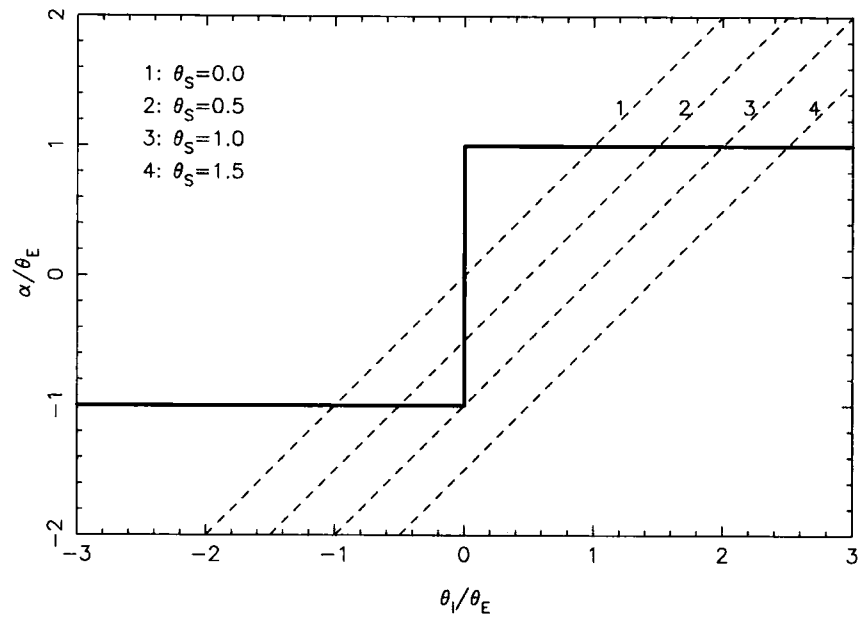

Figure 2.3: Deflection angle diagram for a SIS mass distribution. The thick solid line shows the deflection angle as a function of image plane position; a unique property of this mass distribution is that $|\vec{\alpha}|$ is independent of $|\vec{\theta_I}|$. The dashed lines show four different values of $|\vec{\theta_S}|$ and the intersection of these lines with the thick line define the positions of the images formed by the lens for the various source positions. From this diagram it is clear that if $|\vec{\theta_S}| > \theta_E$, then just one image is observed; if $|\vec{\theta_S}| \leq \theta_E$, then three images are formed.

$$\theta_E = \frac{4\pi\ {\sigma_o}^2}{c^2}\frac{D_{OL}}{D_{OS}} \tag{2.14}$$

The mean surface density mass within this radius can be found by integrating the surface density of the lens:

$$\Sigma(<\theta_E) = \frac{1}{\pi\ {\theta_E}^2}\int_0^{\theta_E}\Sigma(\theta)2\pi\theta d\theta \tag{2.15}$$

Using $\Sigma(\theta) = {\sigma_o}^2/(2G\,D_{OL}\theta)$, the surface density of a SIS, and integrating gives:

$$\Sigma(<\theta_E) = \frac{{\sigma_o}^2}{G\ D_{OL}\theta_E} = \frac{c^2}{4\pi G}\frac{1}{D} = \Sigma_{crit} \tag{2.16}$$

The importance of Σ_{crit} is now obvious: multiple-imaging occurs when the projected density of the lens exceeds the critical density and the source is sufficiently well aligned behind that super-critical region (see also Subramanian & Cowling 1986 and Schneider, Ehlers & Falco 1992).

2.1.5 Lens Magnification

The multiple-images produced by a super-critical gravitational lens are magnified and distorted relative to the "un-lensed" appearance of the source. Specifically, the solid angle of a light bundle is distorted by the deflection and, because the total photon number is conserved, this alters the flux of the images relative to the un-lensed flux of the source. Consider an infinitesimal source with surface brightness I_ν (where ν is the observed frequency), which, in the absence of the gravitational deflection, subtends a solid angle $d\omega_S$ on the sky. The (monochromatic) flux from the source is therefore:

$$S_{\nu,S} = I_\nu d\omega_S \tag{2.17}$$

If the light bundle undergoes a deflection, the solid angle of the image, $d\omega_I$, will differ from $d\omega_S$. Since the light deflection changes neither ν nor I_ν, the observed flux of the image is:

$$S_{\nu,I} = I_\nu d\omega_I \tag{2.18}$$

Therefore, the light deflection changes the flux of the observed image relative to the unlensed flux of the source by a factor of:

$$|\mu| = \frac{S_{\nu,I}}{S_{\nu,S}} = \frac{d\omega_I}{d\omega_S} = \frac{d^2\vec{\theta}_I}{d^2\vec{\theta}_S} \tag{2.19}$$

which is independent of the frequency of the deflected radiation. This underlines an important feature of gravitational lensing: the gravitational deflection of light is achromatic.

The magnification factor $\mu(\vec{\theta}_I)$ can therefore be obtained from the determinant of the Jacobian matrix of the lensing transformation between source- and image-planes:

$$J(\vec{\theta}_I) = \frac{\partial\,\vec{\theta}_S}{\partial\,\vec{\theta}_I} \qquad \mu(\vec{\theta}_I) = \frac{1}{\det J(\vec{\theta}_I)} \tag{2.20}$$

The image at $\vec{\theta}_I$ of an infinitesimally small source is thus brightened or dimmed by a factor $|\mu(\vec{\theta}_I)|$. The magnification factor, $\mu(\vec{\theta}_I)$ can also be positive or negative,

depending on the sign of $\det J(\vec{\theta_{\rm I}})$; the corresponding images are said to have either positive or negative parity. We discuss the parity of gravitationally lensed images in §2.1.7.

Substituting Equation 2.9 into Equation 2.20 we obtain the following expression for J:

$$J(\vec{\theta_{\rm I}}) = \frac{\partial\,\vec{\theta_{\rm S}}}{\partial\,\vec{\theta_{\rm I}}} = \delta_{ij} - \frac{\partial^2\varphi(\vec{\theta_{\rm I}})}{\partial\,\theta_{{\rm I}i}\,\partial\,\theta_{{\rm I}j}} \tag{2.21}$$

where δ_{ij} is the identity matrix. This equation shows that the matrix of the second partial derivatives of the potential $\varphi(\vec{\theta_{\rm I}})$ (i.e. the Hessian matrix of $\varphi(\vec{\theta_{\rm I}})$) describes the deviation of the lens mapping from the identity mapping. For convenience we introduce the following notation:

$$\varphi_{ij} \equiv \frac{\partial^2\varphi(\vec{\theta_{\rm I}})}{\partial\,\theta_{{\rm I}i}\,\partial\,\theta_{{\rm I}j}} \tag{2.22}$$

Since the Laplacian of $\varphi(\vec{\theta_{\rm I}})$ is twice the convergence (Equation 2.10), we can write:

$$\kappa = \frac{1}{2}(\varphi_{11} + \varphi_{22}) = \frac{1}{2} tr\varphi_{ij} \tag{2.23}$$

and we use two further linear combinations of φ_{ij} to define the shear, $\gamma = (\gamma_1^2 + \gamma_2^2)^{1/2}$, as follows:

$$\gamma_1(\vec{\theta_{\rm I}}) = \frac{1}{2}(\varphi_{11} - \varphi_{22}) \qquad \gamma_2(\vec{\theta_{\rm I}}) = \varphi_{12} = \varphi_{21} \tag{2.24}$$

These definitions enable us to write the Jacobian as:

$$J = \begin{pmatrix} 1-\kappa-\gamma_1 & -\gamma_2 \\ -\gamma_2 & 1-\kappa+\gamma_1 \end{pmatrix} = (1-\kappa)\begin{pmatrix} 1 & 0 \\ 0 & 1 \end{pmatrix} - \begin{pmatrix} \gamma_1 & \gamma_2 \\ \gamma_2 & -\gamma_1 \end{pmatrix} \tag{2.25}$$

The physical meaning of the terms "convergence" and "shear" are clear from this equation. Convergence acting alone causes an isotropic focusing of the light rays leading to an isotropic magnification of the source. The source is mapped onto an image of the same shape but larger size. Shear introduces anisotropy into the lens mapping, and distorts the observed images of background galaxies.

2.1.6 Critical Lines and Caustics

From Equation 2.20 we can see that those positions in the image plane that satisfy $\det J(\vec{\theta_{\rm I}}) = 0$ will suffer infinite amplification. These positions generally fall on continuous curves that are called critical lines. Under the lens mapping, the critical curves transform to another set of curves in the source plane that are called caustics. In Fig. 2.4 we show typical critical curves and caustics for a number of different potentials.

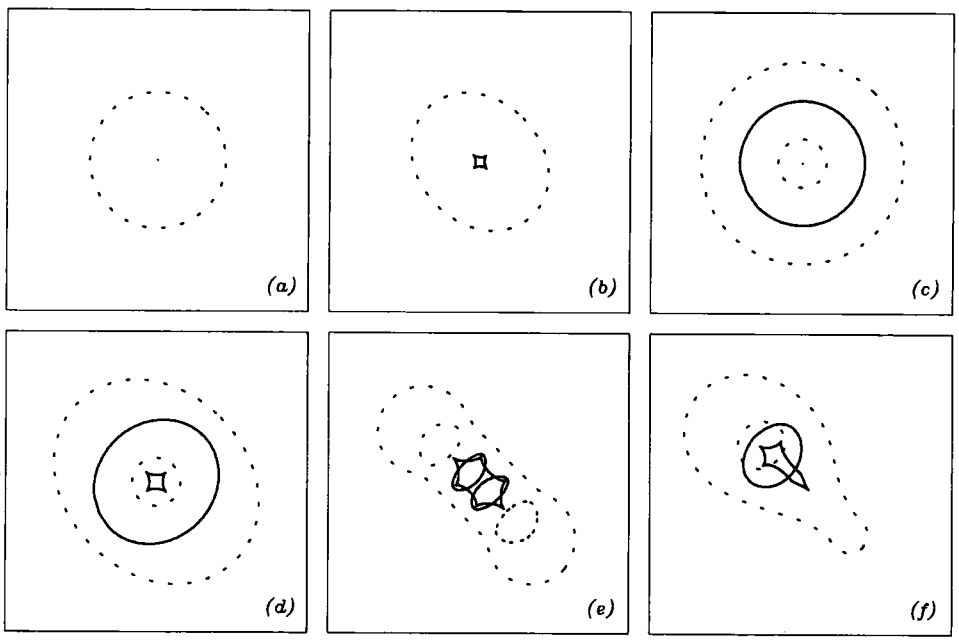

Figure 2.4: Critical lines (dotted) and caustics (solid curves) for six simple lens models: (a) Singular isothermal sphere – this model is incapable of producing radial arcs; the tangential critical line is a circle at the Einstein radius and the tangential caustic reduces to a point. (b) Singular isothermal ellipse – the tangential critical line is now an ellipse, and the broken symmetry caused the caustic to be transformed from a point to an astroid. (c) Non-singular isothermal sphere – in this case there are both radial and tangential critical lines and caustics, however the tangential caustic is reduced to a point. (d) Non-singular isothermal ellipse – the ellipticity of this model expands the tangential critical line from a point to an astroid. (e) Bimodal (equal masses) (f) Bimodal (different masses). Figure Credit: Dr. Jean-Paul Kneib, Observatoire Midi-Pyrénées, Toulouse, France.

To explore the properties of the radial and tangential critical lines and the corresponding multiple-images, we adopt a circularly symmetric lens model and write Equation 2.21 in plane polar co-ordinates in the image plane, where r is measured from the centre of the lens:

$$J = \begin{pmatrix} 1 - \frac{d^2\varphi}{dr^2} & 0 \\ 0 & 1 - \frac{1}{r}\frac{d\varphi}{dr} \end{pmatrix} \tag{2.26}$$

We form the determinant of this matrix and set it equal to zero:

$$\det J = \left(1 - \frac{d^2\varphi}{dr^2}\right)\left(1 - \frac{1}{r}\frac{d\varphi}{dr}\right) = 0 \tag{2.27}$$

from which we can see that the radial and tangential critical lines, satisfy the following equations:

$$\text{Radial critical line :} \quad \frac{d^2\varphi}{dr^2} = 1 \qquad \text{Tangential critical line :} \quad \frac{1}{r}\frac{d\varphi}{dr} = 1 \tag{2.28}$$

To relate φ to the mass of the lens, we generalise Equation 1.2 to an extended circularly symmetric lens, and substitute it into Equation 2.8 to obtain:

$$\frac{d\varphi}{dr} = \frac{4G}{c^2}\frac{D_{\rm LS}}{D_{\rm OS}}\frac{M(<r)}{r} \tag{2.29}$$

Finally, we substitute Equation 2.29 into Equation 2.28 to obtain the following equations:

$$\text{Radial critical line :} \quad 1 - \frac{4G}{c^2}\frac{D_{\rm LS}}{D_{\rm OS}}\frac{d}{dr}\left(\frac{M(<r)}{r}\right) = 0 \tag{2.30}$$

$$\text{Tangential critical line :} \quad 1 - \frac{4G}{c^2}\frac{D_{\rm LS}}{D_{\rm OS}}\frac{M(<r)}{r} = 0 \tag{2.31}$$

These two expressions reveal what information we are able to recover about the distribution of mass in the lens plane from radially and tangentially amplified multiple-images respectively. Radial images or "arcs" constrain the slope of the lens mass distribution (Equation 2.30), and tangential images or "arcs" constrain the mass enclosed within the radial position of the observed image (Equation 2.31).

We emphasise the crucial role that these results play in our lens modelling and analysis. The specific aims of this thesis include the measurement of the mass and substructure of the clusters in our sample. The properties of lens systems described in this section demonstrate the theoretical ground upon which our aims are achievable. We also note that, although we have derived these results for a

circularly symmetric lens, they are also valid in the non-symmetric case. Formally, departures from symmetry remove the singularity at the critical lines, resulting in observed images that have finite flux levels.

2.1.7 The Parity and Number of Images

The observed parity of galaxies is conserved by the lensing transformation (Schneider, Ehlers & Falco 1992). We explain the impact of this on the number and appearance of observed images of a strongly-lensed galaxy by means of a thought experiment.

Consider a galaxy with an asymmetric light profile* that is observed on a line of sight far from the super-critical region of a massive foreground cluster lens. For simplicity, we denote the parity of this single galaxy image by "+". In general multiple-images of a background galaxy are formed if that galaxy lies within one or more caustics of the foreground lens in the source plane. We therefore imagine moving our asymmetric galaxy in the source plane so as to cross a caustic of the massive foreground cluster lens. The set of multiple-images that are now observable must have the same parity ("+") as the unlensed galaxy; the caustic crossing must therefore produce two additional images, the parities of which must cancel out, leaving an overall parity of "+". This process is repeated for every caustic crossing, with the result that an odd number of images is always produced.

Regions of opposite image parity in the image-plane are bounded by the critical curves. When our imaginary galaxy crosses a caustic in the source plane, we therefore observe its single image becoming three images, two of which lie outside the corresponding critical curve and one which lies inside the critical curve. Examples of this can be seen in Fig. 2.5–2.7 which we discuss in §2.1.8. If the observed multiply-imaged galaxy is asymmetric, as in our thought experiment, then multiple-images of a single galaxy that lie adjacent to each other close to a critical line can often be recognised by the mirror symmetry of their morphologies.

*The validity of our thought experiment does not rely on the asymmetry of the "test" galaxy, however imagining this galaxy to be asymmetric helps to clarify the impact of the conservation of parity under the lensing transformation.

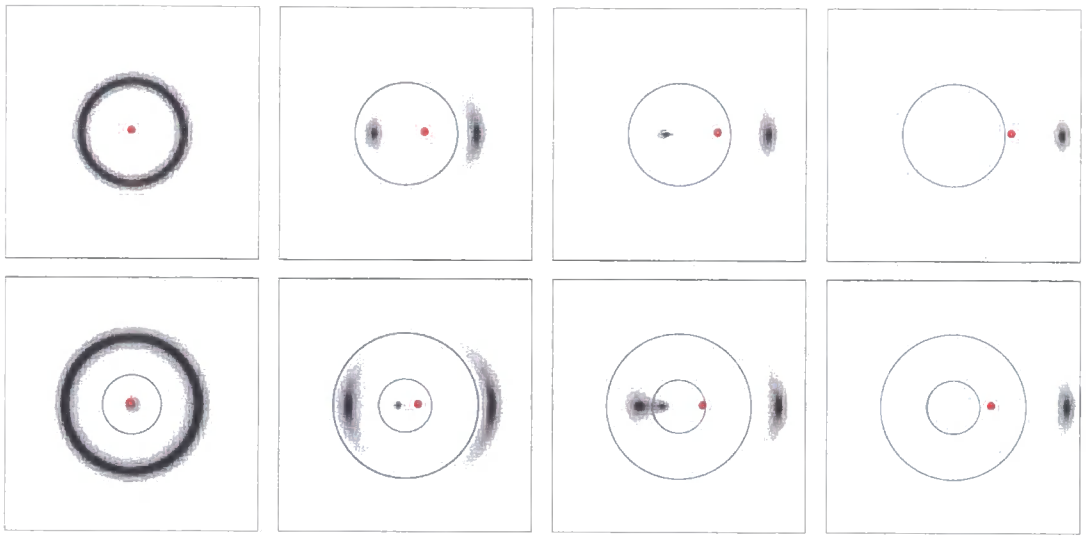

Figure 2.5: Multiple-image configurations for a singular (top) and non-singular (bottom) isothermal sphere model. The source is denoted by the red spot, and the critical lines are shown in blue. We adopt a Gaussian profile for the source, and display the resulting images as a grey-scale. TOP – In all four cases, the third image suffers infinite de-amplification and is located at the centre of the lens. When the source is perfectly aligned on the optic axis, the non-central images form an Einstein ring as described in §2.1.4. BOTTOM – The third image is now visible; as the source moves off the optic axis to the right, the third (central) image moves left and eventually fuses with another image at the radial critical line.

2.1.8 Multiple-image Configurations

We illustrate a number of multiple-image configurations in Fig. 2.5–2.7 (Kovner 1987; Blandford & Kochanek 1987; Grossman & Narajan 1989). In all figures, the red dot indicates the position of the lensed galaxy in the source-plane, and the grey scale shows the images produced in each case, assuming a Gaussian light distribution for the source. We also compute the caustic curves and critical lines in the source and image-planes respectively and mark these in red and blue respectively.

We consider first the singular isothermal sphere (Fig. 2.5) which produces an Einstein ring (§2.1.4) if the source is perfectly aligned behind the centre of the lens. As the source moves away from the centre of the lens, the symmetry of the system is broken and the ring breaks into three images. Two of these images are visible, one inside the critical line, and one outside the critical line, however the third image suffers infinite de-magnification and is undetectable at the centre of the lens. Finally, as the source moves outside the caustic, only one image of the galaxy is observed.

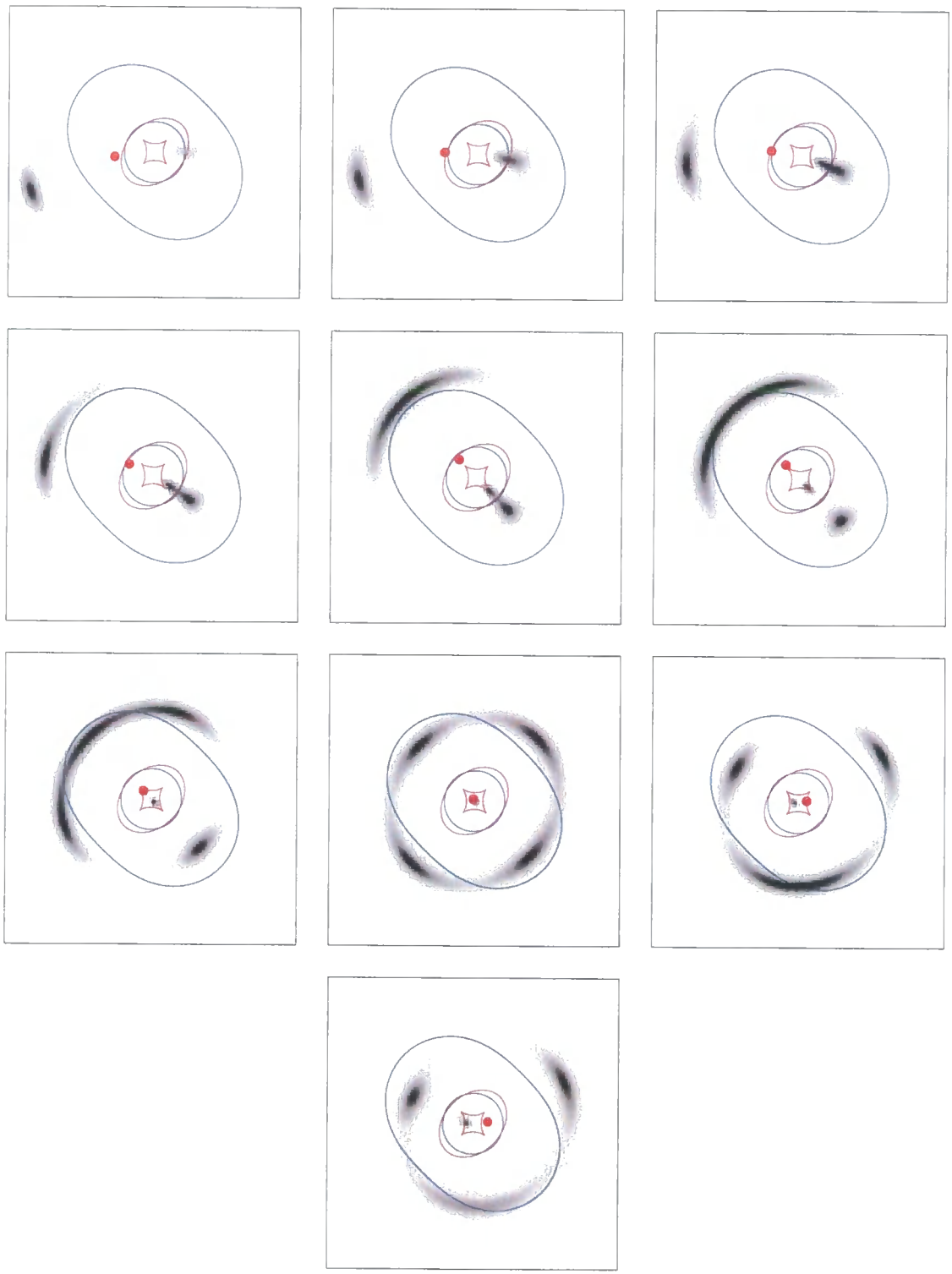

Figure 2.6: Multiple-image configurations of a non-singular elliptical potential. We adopt the same colour-scheme conventions as in Fig. 2.5, plus the caustics are shown as red curves.

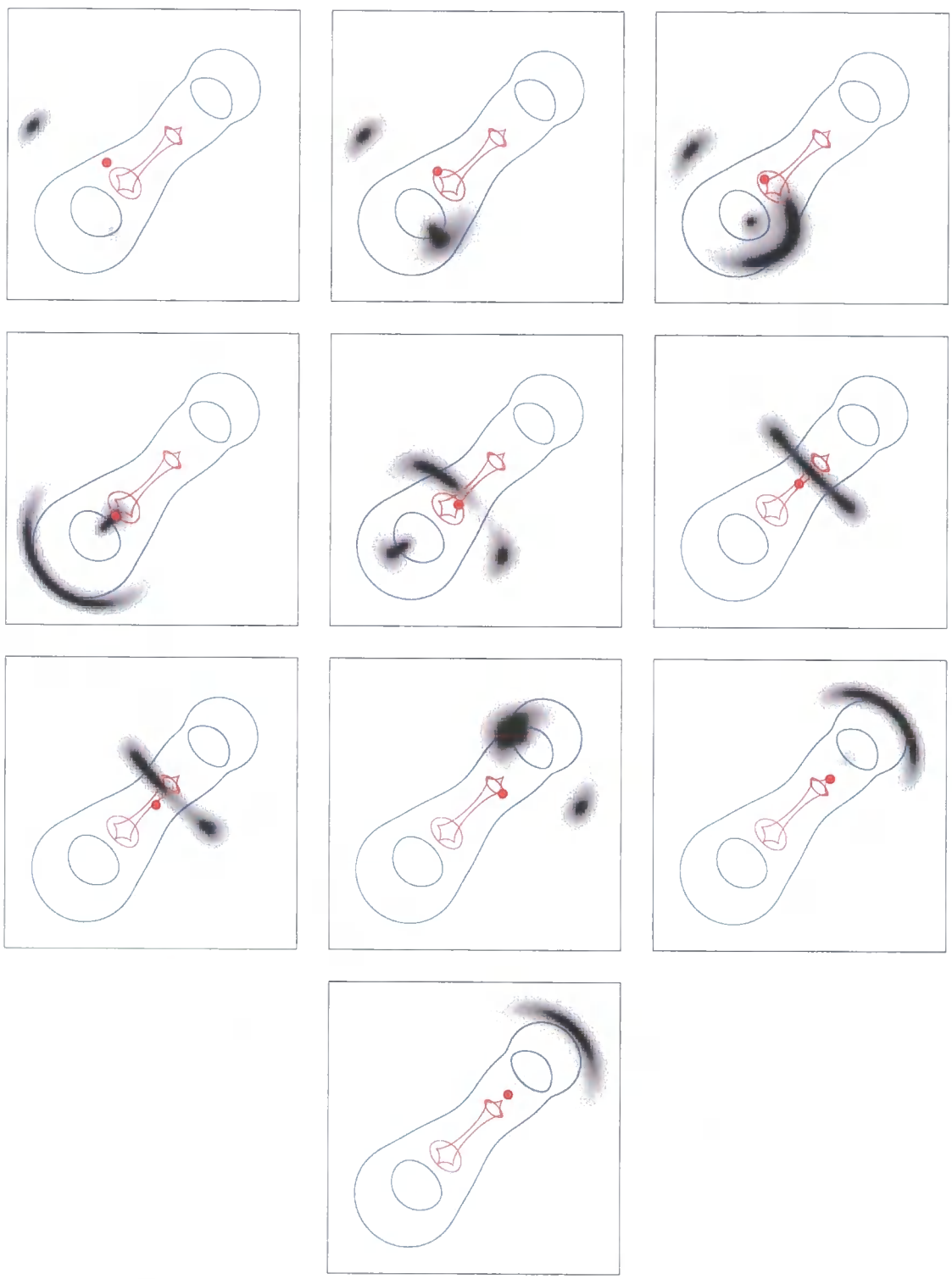

Figure 2.7: Multiple-image configurations of a bi-modal potential where the lower-left mass is greater than the upper-right mass . We adopt the same colour-scheme conventions as in Fig. 2.5, plus the caustics are shown as red curves.

We also show in Fig. 2.5 a non-singular isothermal sphere model. The behaviour of this model is qualitatively similar to the singular model, however the absence of the central singularity leads to some important modifications. Most importantly, the flat core that we have introduced to remove the singularity causes both radial and tangential caustics and critical lines to be formed, in contrast to the singular model in which only the tangential caustic and critical line are formed. As the source moves away from the centre of the lens it is therefore able to form a highly amplified radial arc that consists of two merging images.

We now turn to an elliptical model that also contains a flat core (Fig. 2.6). Key features of this model include the effect of the elliptical mass distribution which breaks the lens symmetry and means that this model is unable to produce an Einstein ring. The astroid shaped tangential caustics are also important, as they demonstrate the ability of this lens to produce "cusp" and "fold" arcs. A cusp arc occurs when the source lies at a cusp of the astroid-shaped caustic; this leads to three merging images which lie on the tangential critical curve in the image plane, and two further images at smaller radii. In contrast, a fold image consists of two merging images that straddle the relevant critical line; this configuration arises when the source lies on the smooth portion of the caustic between the cusps. In this example, there are three counter images of the merging pair, including one strongly de-amplified image near the centre of the lens.

Finally, we briefly examine the typical image-configurations of a bi-modal lens system (Fig. 2.7). In this example, both masses have a flat core and are circular, with the mass to the upper right being slightly less massive than the one to the lower left. Bimodal systems display similar cusp and fold arcs as the elliptical system discussed above. The key feature of bimodal systems is the "saddle" region that lies between the two mass components. The amplification and shear is very strong in the saddle region, and can lead to the production of straight arcs for suitably positioned sources, as illustrated in Fig. 2.7.

2.2 Gravitational Lens Modelling

We explain how we exploit the theoretical framework described in §2.1 and high-resolution imaging of galaxy clusters to constrain the distribution of mass in the cluster lenses. We begin by stating the problem in a mathematical form, then we explain how we identify multiple-image systems for use as constraints in our models, finally we describe our modelling methodology.

2.2.1 The Mathematical Problem

Consider a single source at $z_{\rm S}$ that appears to an observer under the action of a gravitational lens at $z_{\rm L}$ as N distinct images at positions $\vec{u}_i\,(1 \leq i \leq N)$. We describe the source with ν free parameters, $\Pi_j\,(1 \leq j \leq \nu)$, for example: the position of the centre of the source, the ellipticity, the orientation, the surface brightness. We write the transformation equations in the following form:

$$\Pi_j^S = f_j(\Pi_{ji}^I, \varphi(\vec{u}_i)) \qquad (1 \leq i \leq N) \;\; (1 \leq j \leq \nu) \tag{2.32}$$

where f_j are functions that depend on the parameters that describe the observed images and the gravitational potential of the lens. The source parameters , Π_j^S, and the lens potential, $\varphi(\vec{u}_i)$, are the unknowns in these equations. We use the image parameters , Π_{ji}^I (i.e. the observables), to constrain both the source parameters and the lens potential. If we are able to recover ν parameters for each image, then we have $\nu(N-1)$ constraints on our lens model. Generalising this to n sets of multiple images of sources at redshifts $z_{{\rm S}i}$, each multiple-image system being characterised by (ν_i, N_i), then the total number of constraints n_c is given by:

$$n_c = \sum_i^n [\nu_i(N_i - 1) - \epsilon_i] \tag{2.33}$$

where $\epsilon_i = 0$ if $z_{{\rm S}i}$ is known and $\epsilon_i = 1$ if $z_{{\rm S}i}$ is not known (Kneib et al. 1993). Strictly, Equation 2.33 only applies in the idealised case of all multiple-images being resolved, and none of the images being merging pairs. Clearly higher resolution imaging will increase n_c.

We describe each observed gravitational image with the following parameters: $\Pi^I = (\vec{u}^I, S^I, \vec{\tau}^I)$, where $\vec{u}^I$ is the position of the image, S^I is the observed flux and $\vec{\tau}^I = \tau^I e^{2i\theta^I}$ is the complex deformation of the image, describing its ellipticity (τ)[†] and orientation (θ). We use these quantities, their counterparts in the source-plane and the theoretical framework described in §2.1 to write down the transformation equations:

$$\begin{aligned} &\text{Position}: \quad \vec{u}^S = \vec{u}^I - \vec{\nabla}\varphi(\vec{u}^I) \\ &\text{Flux}: \quad S^S = |\det J| S^I \\ &\text{Shape}: \quad \mathrm{sgn}(\det J)\ \vec{\tau}^S = \vec{\tau}^I - \vec{\tau}_{\rm pot}\ [\delta^I - \tau^I \Re(\vec{g}^I \vec{g}^*_{\rm pot})] \end{aligned} \tag{2.34}$$

where the first equation is simply the lens equation (§2.1.2), J is the Jacobian matrix of the lensing transformation (§2.1.5), $\delta = (1+\tau^2)^{1/2}$, $\vec{g} = \vec{\gamma}/(1-\kappa)$, the subscript "pot" denotes quantities applicable to a circular source (see Kneib et al. (1996) and references therein for a detailed derivation of the shape transformation equation), $\Re$ takes the real part of dot-product between $\vec{g}^I$ and $\vec{g}^*_{\rm pot}$, and $\vec{g}^*$ is the complex conjugate of $\vec{g}$.

The gravitational potential of the lens plays a pivotal role in these transformation equations. We showed in §2.1.3 that the lensing potential, φ, is linked to the two-dimensional Newtonian potential, ϕ, through the following formula:

$$\varphi = \frac{2}{c^2} \frac{D_{\rm OL} D_{\rm LS}}{D_{\rm OS}} \phi \tag{2.35}$$

where $D_{\rm OL}, D_{\rm LS}$ and $D_{\rm OS}$ are the observer-lens, lens-source and observer-source angular diameter distances respectively. In a flat universe, the angular diameter distance between any two redshifts is given by:

$$D_{12} = \frac{c}{H_{\rm o}\,(1+z_2)} \int_{z_2}^{z_1} \frac{dz}{(1+z)[\Omega_{\rm o}\,(1+z) + \Lambda_{\rm o}\,(1+z)^{-2}]^{1/2}} \tag{2.36}$$

We therefore need to know the redshift of both the lens ($z_{\rm L}$) and the source ($z_{\rm S}$), and geometry of the Universe in order to measure the absolute value of the gravitational potential of the lens, and thus the mass of the lens. In practice, $z_{\rm L}$ is generally

[†] $\tau = (a^2 - b^2)/2ab$ where a and b are the semi-major and semi-minor axes of the image, and θ is the orientation of the image

very well known for galaxy clusters at intermediate redshifts ($z \lesssim 0.5$), and so the redshift and geometrical dependence of the lens potential reduces to a dependence on $D_{\rm LS}$ / $D_{\rm OS}$. If we assume that $\Omega_{\rm o}$= 1 and $\Lambda_{\rm o}$= 0 and use Equation 2.36 to calculate this distance ratio, we find that the geometrical terms cancel out and we are left with $D_{\rm LS}$ / $D_{\rm OS}$ depending solely on $z_{\rm L}$ (probably known quantity) and $z_{\rm S}$ (potentially unknown quantity):

$$\frac{D_{\rm LS}}{D_{\rm OS}} = \frac{(1+ z_{\rm S})^{1/2} - (1+ z_{\rm L})^{1/2}}{(1+ z_{\rm S})^{1/2}(1+ z_{\rm L})^{1/2} - (1+ z_{\rm L})^{1/2}} \tag{2.37}$$

It is therefore important to measure $z_{\rm S}$ for at least one multiple-image system per lens, in order to constrain the absolute normalisation of the lens mass distribution. The geometry of the Universe has a much smaller influence on the mass measurements (Golse et al. 2001), and consequently, we assume a cosmological model in order to define $\Omega_{\rm o}$ and $\Lambda_{\rm o}$ and concentrate our efforts on spectroscopy of candidate multiple-image systems.

2.2.2 Identification of Multiple-image Systems

We summarise the defining characteristics of multiple-image systems. We use these characteristics in §3 to search for candidate systems in our *HST* data (§3.2) and target these images in our spectroscopic survey (§3.4). The key characteristics may be summarised as: location, colour, surface brightness, redshift and morphology. We briefly explain these five criteria below:

Location – Multiple-images are only formed in (or close to) regions where the surface density of the lens is super-critical (§2.1.4). We are therefore confident that most multiple-image systems will form within a few tens of arcsec from the centre of the cluster (the Einstein radius of a singular isothermal sphere with a velocity dispersion of 1000 km s^{-1} at $z_{\rm L}$= 0.2 for a source at $z_{\rm S}$= 1 is $\theta_{\rm E}$= 14.4″). We also use our knowledge of typical image configurations (§2.1.8) to recognise likely systems.

Colour – Gravitational lensing is purely a geometrical effect, and the colour of objects is therefore not modified. The colour of multiple-images of a single background galaxy must therefore all be the same.

Surface Brightness – By the same token, gravitational lensing conserves surface brightness, and so in the absence of colour information one may examine the monochromatic surface brightness of candidate multiple-images.

Redshift – Spectroscopic identification of a candidate multiple-image is decisive evidence for or against the gravitational lensing hypothesis. Unfortunately, this evidence is often difficult to obtain, even with modern spectrographs on 10–m class telescopes, because the spectroscopic targets are generally quite faint (e.g. $R \gtrsim 23$).

Morphology – Some multiple-images suffer strong tangential or radial distortion, making them relatively easy to identify. When the shear is less strong, the intrinsic shape of the galaxy becomes more important, and may result in the image not appearing to be sheared at all. Regardless of the degree of shear suffered by the galaxy images, there must be an odd number of images and the morphology of the images must conserve parity as discussed in §2.1.7

2.2.3 Modelling Methodology

Our methodology builds on the LENSTOOL software that was first developed by Kneib (1993) and has subsequently been refined and applied to numerous clusters: A 370 (Kneib et al. 1993); MS 2137 (Mellier et al. 1993); Cl 2236 (Kneib et al. 1994); A 2218 (Kneib et al. 1995 and K96); Cl 0024+16 (Smail et al. 1996); PKS0745−191 (Allen et al. 1996); A 2390 (Kneib et al. 1999); AC 114 (Natarajan et al. 1999; RXJ1347.5−1145 (Cohen et al. 2002). In summary, we use the properties of both strongly- and weakly-lensed background galaxies to constrain a parametrised analytical representation of the total projected cluster mass. The process by which we construct these analytic models falls naturally into four steps which we illustrate in Fig. 2.8 and describe below:

Step 1: Identify Constraints

The positions, shapes, relative fluxes and redshift of each multiple-image system provide the strongest constraints, and so we search our *HST* imaging for candidate systems using the criteria listed in §2.2.2. We divide these multiple-image

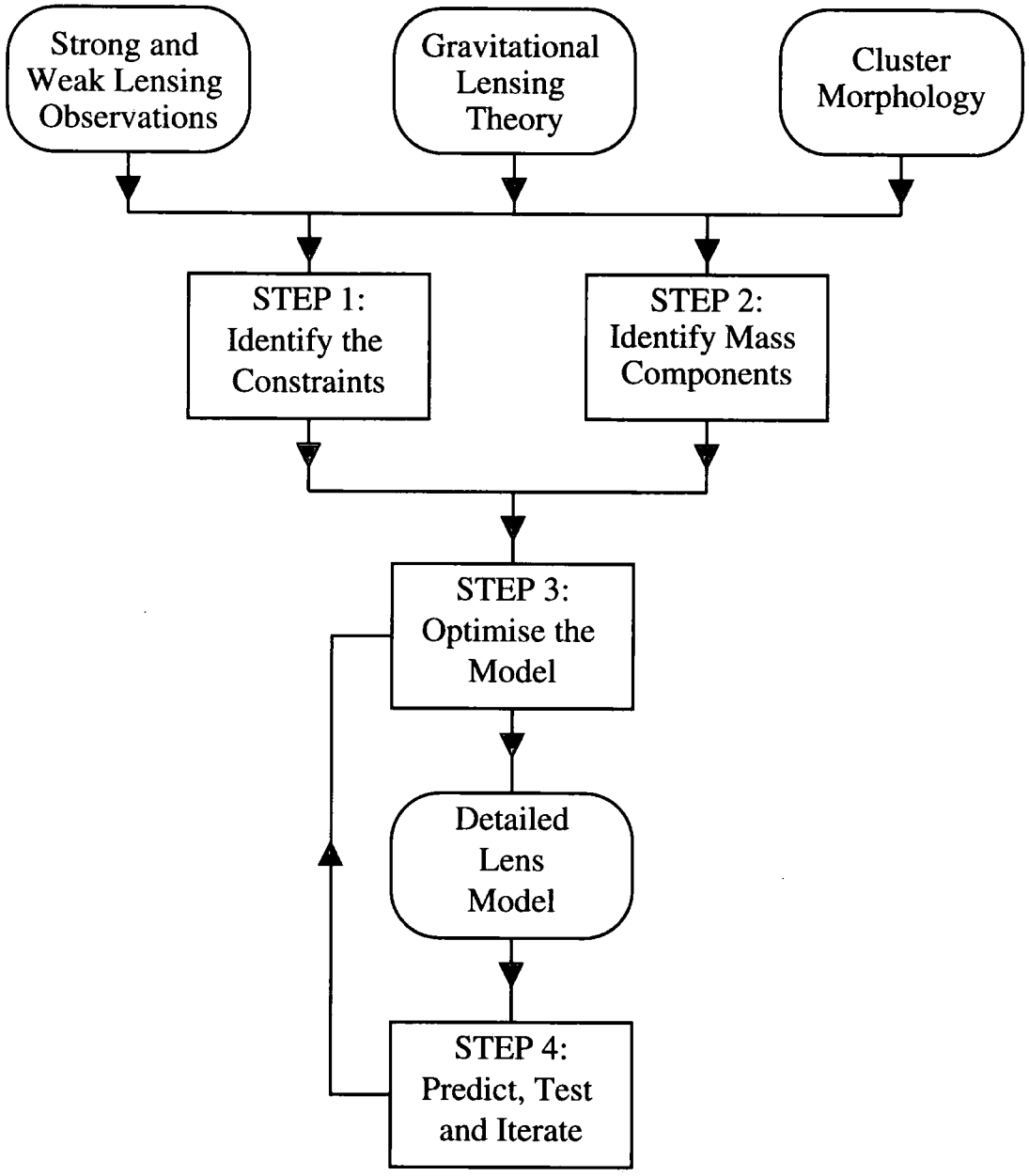

Figure 2.8: Flow diagram of our four stage lens modelling methodology.

systems into two categories: confirmed and unconfirmed. Confirmed systems are characterised by a well defined redshift ($\Delta z \leq 0.1$) and unambiguous identification of all counter-images, or clear evidence that any unidentified counter-image would be sufficiently de-amplified as to lie beneath the detection threshold of the imaging observations. By default, unconfirmed systems are those candidates that do not satisfy these criteria. We also examine our *HST* imaging to identify symmetry breaks in multiple-image systems. These breaks are a signature of the location of critical lines, and can thus be used as additional model constraints.

Multiple-image constraints probe only the central $\lesssim$ 50–100 kpc of each cluster. Therefore, to extend the lens models beyond the strong lensing regime we also use the position and shape of weakly-sheared background galaxies as model constraints. We treat the ellipticity and orientation of each faint galaxy as a measure of the tangential shear induced by the lens at that position, and constrain the model parameters by comparing these measurements with the shear induced by each trial mass distribution during the model optimisation process.

Step 2: Identify Mass Components

In order to construct the initial lens model that we aim to optimise with the constraints described above, we must decide where to put the parametrised mass components in the lens plane. We use observations of optical and X-ray morphologies of the cluster together with knowledge of the typical image configurations (§2.1.8) to identify the likely location and nature of the mass components. We use both cluster- and galaxy-scale mass components. The cluster-scale mass components account for the mass that is associated with the cluster as a whole i.e. dark matter and hot gas. The galaxy-scale mass components account for the small scale perturbations to the overall cluster potential by the cluster galaxies that we detect in our optical imaging.

We parametrise each mass component as a smoothly truncated pseudo-isothermal elliptical mass distribution (PIEMD – Kassiola & Kovner 1993; Kneib et al. 1996). This functional form is physically well motivated (it avoids the central singularity and infinite spatial extent of singular isothermal models) and can describe mass

distributions of arbitrarily large ellipticities. Each PIEMD mass component is parametrised by its position (x_c, y_c), ellipticity (ϵ), orientation (θ), core radius (r_{core}), cut-off radius (r_{cut}) and central velocity dispersion (σ_o), and the projected mass density, Σ is given by:

$$\Sigma(x,y) = \frac{{\sigma_o}^2}{2G} \frac{r_{cut}}{r_{cut} - r_{core}} \left(\frac{1}{({r_{core}}^2 + \rho^2)^{1/2}} - \frac{1}{({r_{cut}}^2 + \rho^2)^{1/2}} \right) \tag{2.38}$$

where $\rho^2 = [(x - x_c)/(1+\epsilon)]^2 + [(y - y_c)/(1-\epsilon)]^2$ and the ellipticity of the lens is defined as $\epsilon = (a-b)/(a+b)$. The geometrical parameters (x_c, y_c, ϵ, θ) of each mass component are matched to the observed light distribution of the related cluster elliptical. The dynamical parameters (r_{core}, r_{cut}, σ_o) of the "major mass components" (i.e. cluster-scale mass components and selected bright cluster ellipticals, including each central galaxy) are kept as free parameters. In order to minimise the number of model parameters, the dynamical parameters of the remaining mass components are scaled with the luminosity of their associated galaxy following Brainerd, Blandford & Smail (1996):

$$r_{core} = {r_{core}}^{\star} \, (L/L^{\star})^{1/2} \tag{2.39}$$

$$r_{cut} = {r_{cut}}^{\star} \, (L/L^{\star})^{1/2} \tag{2.40}$$

$$\sigma_o = {\sigma_o}^{\star} \, (L/L^{\star})^{1/4} \tag{2.41}$$

We also scale the mass of individual galaxies with their luminosity, using:

$$M = (\pi/G)({\sigma_o}^{\star})^2 \, {r_{cut}}^{\star} \, (L/L^{\star}) \tag{2.42}$$

These scaling laws are physically well motivated and conserve the mass-to-light ratio of the galaxies in a manner analogous to the observed Faber-Jackson and Tully-Fisher scaling relations for spiral and elliptical galaxies respectively.

In summary a typical lens model contains the following free parameters: x_c, y_c, ϵ, θ, r_{core}, σ_o, r_{cut} for each major mass component and ${r_{core}}^{\star}$, ${\sigma_o}^{\star}$, ${r_{cut}}^{\star}$ for the majority of galaxy-scale mass components.

Step 3: Optimise the Model

We first constrain each lens model with the confirmed multiple-image systems. This approach ensures that the normalisation of the cluster mass is based on the most precise constraints available. We use the unconfirmed systems to provide additional constraints on the detailed shape of the mass distribution in each cluster. We construct a χ^2-estimator to quantify how well each lens model fits the observational data:

$$\chi^2 = \chi^2_{\rm pos} + \chi^2_{\rm shape} + \chi^2_{\rm flux} + \chi^2_{\rm crit} + \chi^2_{\rm weak} \tag{2.43}$$

We explain each term in Equation 2.43 below.

The first three terms compare the source-plane properties computed for each observed image (x_i^S, y_i^S, τ_i^S, θ_i^S, S_i^S – as defined in equation 2.34). We define $\chi^2_{\rm pos}$, $\chi^2_{\rm shape}$ and $\chi^2_{\rm flux}$ as follows:

$$\chi^2_{\rm pos} = \sum_{i=1}^{N-1} \frac{(x_i^S - x_{i-1}^S)^2 + (y_i^S - y_{i-1}^S)^2}{\sigma^2_{\rm pos}} \tag{2.44}$$

$$\chi^2_{\rm shape} = \sum_{i=1}^{N-1} \frac{(\tau_i^S cos(2\theta_i^S) - \tau_{i-1}^S cos(2\theta_{i-1}^S))^2 + (\tau_i^S sin(2\theta_i^S) - \tau_{i-1}^S sin(2\theta_{i-1}^S))^2}{\sigma^2_{\rm shape}} \tag{2.45}$$

$$\chi^2_{\rm flux} = \sum_{i=1}^{N-1} \frac{(S_i^S - S_{i-1}^S)^2}{\sigma^2_{\rm flux}} \tag{2.46}$$

where $\sigma^2_{\rm pos}$, $\sigma^2_{\rm shape}$ and $\sigma^2_{\rm flux}$ are the accuracies with which we can measure the position, shape and flux of galaxies in our *HST* data.

We minimise $\chi^2_{\rm pos}$, $\chi^2_{\rm shape}$ and $\chi^2_{\rm flux}$ in the source-plane because, fundamentally, multiple-image constraints identify that a set of images will ray-trace back to the same source-plane position. This approach is also computationally simpler than the alternative of optimising in the image-plane. This simplicity arises because the lens transformation is analytical when going from the image- to the source-plane, and the same is not true in reverse.

In contrast, we minimise $\chi^2_{\rm crit}$ in the image-plane; for each trial mass distribution we compute the position of the critical line using the amplification matrix

and compare this curve with the observed symmetry break. We define $(x_{\rm ct}^{\rm obs}, y_{\rm ct}^{\rm obs})$ and $(x_{\rm ct}^{\rm mod}, y_{\rm ct}^{\rm mod})$ as the observed and model critical line positions respectively and construct $\chi^2_{\rm crit}$, where $\Delta x_{\rm crit}$ and $\Delta y_{\rm crit}$ are the uncertainties in the position of the symmetry break.

$$\chi^2_{\rm crit} = \frac{(x_{\rm ct}^{\rm obs} - x_{\rm ct}^{\rm mod})^2 + (y_{\rm ct}^{\rm obs} - y_{\rm ct}^{\rm mod})^2}{\Delta x^2_{\rm crit} + \Delta y^2_{\rm crit}} \tag{2.47}$$

Finally, we construct $\chi^2_{\rm weak}$ in a similar manner to $\chi^2_{\rm shape}$; the differences being that we sum over the F faint galaxy images detected in the cluster field, $\sigma_{\rm weak}$ is the width of the distribution of galaxy shapes from surveys of field galaxies (e.g. Ebbels 1998) and we compare the image-plane galaxy shapes with that induced by the trial mass distribution at the faint galaxy image on a circular source.

$$\chi^2_{\rm weak} = \sum_{i=1}^{F-1} \frac{(\tau_i^I cos(2\theta_i^I) - \tau_{\rm pot}^I cos(2\theta_{\rm pot}^I))^2 + (\tau_i^I sin(2\theta_i^I) - \tau_{\rm pot}^I sin(2\theta_{\rm pot}^I))^2}{\sigma^2_{\rm weak}} \tag{2.48}$$

The χ^2 estimator is minimised by varying the model parameters to obtain an acceptable ($\chi^2 \sim 1$) fit to the observational constraints. This is an iterative process, which we begin by restricting our attention to the least ambiguous model constraints (i.e. the confirmed multiple-image systems) and the relevant free parameters. For example, in a typical cluster lens there will be one spectroscopically-confirmed multiple-image system and a few other candidate multiples. The model fitting process therefore begins with using the spectroscopic multiple to constrain the dynamical parameters of the main cluster-scale mass component. We explain this process in more detail in §3.6.3.

Step 4: Predict, Test and Iterate

Once we have established the first acceptable model using the confirmed multiple-image systems, we use this model to explore the other constraints and to search for further counter-images. Specifically, we test the predictive power of the model and use this to iterate towards the final refined model. At each stage of this process we incorporate additional constraints (e.g. faint image pairs) and the corresponding free parameters (e.g. the ellipticity and orientation of key mass components, or the

velocity dispersion of cluster galaxies that lie close to faint image pairs) into the model.

2.3 Summary

We have reviewed the elements of lensing theory that are essential to the interpretation of strong lensing observations of galaxy clusters. Key aspects of our treatment are:

- the lens equation, relating image positions to the properties of the lens;
- the relationship between the deflection angle and the gravitational potential;
- the gradient transformation between the source- and image-planes;
- the existence and relevance of critical lines and caustics;
- the ability of lenses to produce both tangentially and radially distorted images;
- the parity and number of images that lenses produce;
- typical image configurations.

We have also explained our modelling methodology which consists of four steps:

- identify the constraints;
- identify the mass components;
- optimise the model;
- predict, test and iterate.

3 THE LENS MODELS AND THE STRUCTURE OF CLUSTERS

We apply our lens modelling method (§2), to the full sample of ten objectively selected clusters and construct a suite of detailed lens models. Armed with these models and a complementary analysis of archival X-ray observations with *Chandra*, we investigate the mass and structure of massive clusters at $z \sim 0.2$.

We recap on the sample selection in §3.1; present our optical data and describe the development of our custom written data reduction and analysis pipelines in §3.2 and §3.3 respectively; identify candidate multiple-image systems and describe our spectroscopic observations in §3.4; present and analyse the archival *Chandra* X-ray data in §3.5; construct the detailed lens models in §3.6 and use them to study the mass and structure of our cluster sample in §3.7; finally, we discuss our results in §3.8 and summarise our conclusions in §3.9.

We adopt the complex deformation, $\vec{\tau} = \tau_x + i\tau_y = |\vec{\tau}|e^{2i\theta}$, as our measure of galaxy shape when dealing with the weak lensing aspects of our analysis, where $\tau = (a^2 + b^2)/2ab$ and θ is the position angle of the major axis of the ellipse that describes each galaxy. For the purposes of this chapter we define the terms "ellipticity" to mean τ and "orientation" to mean θ.

3.1 Sample Selection

We explained the rationale behind our sample selection in §1.6, including our adoption of the XBACs (X-ray Brightest Abell Clusters; Ebeling et al. 1996) catalogue as the best parent sample that was available at the time of planning the observations. Here we recap on the sample selection criteria and confirm that although the parent catalogue was restricted to Abell clusters, our sample is indistinguishable from a purely X-ray selected sample.

We select ten of the most X-ray luminous clusters ($L_X \geq 8 \times 10^{44}$ erg s^{-1}, 0.1–2.4 keV) in a narrow redshift slice at $0.17 < z < 0.25$, with line-of-sight reddening

of $E(B-V) \leq 0.1$ from the XBACs sample (Ebeling et al. 1996). However because XBACs is restricted to Abell clusters (Abell, Corwin & Olowin 1989), our sample is not strictly X-ray selected. We therefore compare our sample selection with the X-ray selected *ROSAT* Brightest Cluster Sample (BCS, Ebeling et al. 1998, 2000) and find that 18 of the 19 BCS clusters that satisfy our L_X, redshift and reddening selection criteria are either Abell or Zwicky clusters. We therefore conclude that our sample is indistinguishable from an X-ray selected sample.

We also ensure that our sample spans the full range of X-ray properties (morphology, central galaxy line emission, cooling flow rate, core radius) found in larger X-ray luminous samples (e.g. Peres et al. 1998; Crawford et al. 1999). The median X-ray luminosity of our sample is 13×10^{44} erg s^{-1} and nine of the ten clusters lie within a factor of two of this luminosity. The remaining cluster, A 1835 is by far the most luminous cluster with $L_X = 38 \times 10^{44}$ erg s^{-1}. We list our cluster sample in Table 3.1 and describe the optical and X-ray morphologies of the clusters in §3.2.4 and §3.5.1 respectively.

3.2 *HST* Observations and Data Reduction

We describe our space-based optical observations and explain how we reduce these data. We develop an automated pipeline specifically for the purpose of the data processing described in this section. This pipeline accomplishes the data reduction and is based around a custom-built IRAF package called WFPC2_DRIZ that we have developed for the purpose of reducing the data presented in this thesis.

3.2.1 The Observations

All ten clusters were observed through the F702W filter using the WFPC2 camera on board *HST*: A 2218 was observed in Cycle 4, A 2219 in Cycle 6 and the remaining eight clusters were observed specifically for the purpose of this experiment in Cycle 8 (GO-8249 – PI Kneib). With the exception of A 2219 (six single-orbit exposures), all clusters were observed for three single-orbit exposures. Each exposure lasted for $\sim$ 2.1–2.5 ks, and we list the total exposure time T_{exp}, for each cluster in Table 3.1.

Table 3.1: Summary of *HST* Observations

Cluster	Redshift	Scale (kpc/″)	L_X[c] [0.1–2.4 keV] (10^{44} erg s^{-1})	T_{exp} (ks)	R_{702}*	N_{fgal} [a]	K*	N_{cgal} [b]	Confirmed[d] Strong Lens?	Optical Morphology
A 68	0.255	4.97	8.4 ± 2.3	7.5	18.75	452	15.16	50	Yes	Clumpy
A 209	0.209	4.35	13.8 ± 2.3	7.8	18.33	439	14.85	27	No	Compact
A 267	0.230	4.65	13.3 ± 2.8	7.5	18.54	466	15.00	35	No	Compact
A 383	0.187	4.02	8.0 ± 2.4	7.5	18.10	502	14.66	24	Yes	Compact
A 773	0.217	4.47	12.5 ± 2.1	7.2	18.41	434	14.91	79	No	Clumpy
A 963	0.206	4.31	10.2 ± 1.9	7.8	18.30	539	14.82	31	Yes	Compact
A 1763	0.228	4.62	14.2 ± 2.1	7.8	18.52	478	14.99	49	No	Compact
A 1835	0.253	4.94	38.3 ± 5.4	7.5	18.73	441	15.15	62	No	Compact
A 2218	0.171	3.77	9.0 ± 0.8	6.5	17.90	434	14.51	54	Yes	Clumpy
A 2219	0.228	4.62	19.8 ± 2.2	14.4	18.52	413	14.99	57	Yes	Clumpy

[a] N_{fgal} is the number of weakly sheared faint galaxies used to constrain the gravitational lens model of each cluster (§3.6); the selection criteria for these galaxies are $R_{702} \geq R_{702}^* + 3.5$ and $N_{pixels} \geq 30$ (§3.3.3);
[b] N_{cgal} is the number of cluster galaxies included in the cluster lens models as galaxy-scale mass components (§3.6.2); the selection criterion for these galaxies is $K < K^* + 2.5$ (§3.3.2).
[c] Ebeling et al. (1996).
[d] Confirmed strong lensing is defined as unambiguous identification of counter-images and a redshift constraint to a precision of $\Delta z \leq 0.1$ (§3.4).

We adopted a three-point dither pattern for the eight clusters observed in Cycle 8: each exposure was shifted relative to the previous one by ten WFC pixels ($\sim 1.0''$) in x and y. The archival observations of A 2218 follow the same dither pattern, except the offsets were three WFC pixels in x and y. A 2219 was observed with a six-point dither pattern that comprised two three-point dithers each of which were identical to that used for the Cycle 8 observations. These two dither patterns were offset from each other by 10 pixels in x and y.

3.2.2 Data Reduction Strategy

Dithered *HST* observations have the following benefits for the quality of the final reduced frames:

- reduced impact of pixel-to-pixel errors in the flat-field or spatially varying detector sensitivity;
- small scale detector defects such as hot pixels, bad columns and charge traps can be removed;
- the gap between the three wide field camera (WFC) chips is filled in.

Unfortunately, the WFC detectors are unable to take full advantage of the superb resolving power of the *HST* optics because the angular size of each WFC pixel ($\sim 0.1''$) is comparable with the full-width at half-maximum (FWHM) of the point spread function (PSF). The WFC chips therefore under-sample the PSF. For this reason, dither patterns incorporating sub-integer pixel offsets have been employed (e.g. Williams et al. 1996; van Dokkum et al. 2000) in an attempt to recover some of the spatial information lost through the under-sampling of the PSF. In principle this approach should allow images offset by sub-pixel amounts to be interlaced onto a finer grid, thus improving the spatial resolution of the final image. In practice, this approach is generally not feasible because small telescope pointing errors and variation of plate scale across the detector (often caused by geometric distortion) undermine it. A much simpler approach is "shift-and-add" which involves block-replicating each input pixel onto a finer grid, shifting into place and adding to the

final image. The disadvantage of this is that it convolves the image once again with the original pixel, thus adding to the blurring of the image and correlation of the noise. It is also difficult to use this method when data is missing (e.g. from cosmic rays) and when the optics suffer geometric distortion.

Fruchter & Hook (1997; 2002) developed the "drizzle" technique to combat these problems. The crux of drizzling is the parameter PIXFRAC, which can take values between zero and unity, and controls how much the input pixels are shrunk before mapping them to the output image. Setting PIXFRAC $= 0$ is equivalent to interlacing, i.e. reducing each pixel to a delta-function; if PIXFRAC > 0, then the output PSF is broadened due to convolution of the original PSF with a non-zero pixel; PIXFRAC $= 1$ is equivalent to shift-and-add.

Another issue that affects the final *HST* image quality is geometrical distortion. This effect arises because the focal plane of each WFC chip is not flat; the distortion increases with distance from the chip centres. At the edge of the field of view, the deviation of the x–y chip axes from a Cartesian grid on the sky is a few per cent. Several authors have measured this distortion (Gilmozzi et al. 1995; Holtzmann et al. 1995; Trauger et al. 1995; Casertano & Wiggs 2001) and we note that the DITHER package in IRAF that implements Fruchter & Hook's drizzle algorithm incorporates corrections for geometrical distortion, based on the polynomial solution of Trauger et al. (1995).

The dither patterns employed by our observations are based on integer pixel offsets. Therefore in principal, it is not possible for us to recover any spatial information using the drizzle algorithm because our observations do not sub-sample the nominal pixel-scale of the WFC detectors. We investigate whether this is true in practice by measuring the accuracy of the telescope pointing. We use the PRECOR, OFFSETS, SHIFTFIND and AVSHIFT tasks from the DITHER package to cosmic-ray clean and cross-correlate the images and then measure the actual shifts between the different observations of each cluster. We find that the median difference between the commanded and actual offsets is ~ 0.2 pixels, and generally lies in the range $\sim 0.0 - 0.4$ pixels. The geometrical distortion at the edge of each chip ($\sim 2\%$ – Koekemoer et al. 2002) translates to an additional ~ 0.2 pixel shift at the edge

of each detector, falling to zero at the chip centres. Our observations therefore sub-sample the 0.1″ WFC pixels at a level that varies in the range $\sim 0-0.5$ pixels depending on the (x, y) position on each chip and the difference between the commanded and actual telescope pointing for each cluster. We therefore incorporate drizzling techniques into our data reduction pipeline for two reasons. First, the inaccuracies in the telescope pointing and the variation of pixel scale across the WFC chips mean that there is an opportunity to recover a limited amount of spatial information by adopting the drizzle techniques. Second, we wish to eliminate the geometrical distortion of the *HST*/WFPC2 optics from our data (§3.3.3).

3.2.3 Data Reduction Pipeline

We purpose build an IRAF package called WFPC2_DRIZ that uses the tasks available in the DITHER package, and exploit this to construct a data reduction pipeline to reduce the *HST* data for this thesis. The pipeline takes the data-products from the Space Telescope Science Institute (STScI) data calibration pipeline and produces a final reduced frame without manual intervention. We describe the key steps of our data reduction pipeline. After unpacking the data products from the STScI pipeline, we measure the actual offsets between the observations as described above. We then construct a bad pixel mask file that flags static pixels (based on the data quality files) and cosmic ray events (using the DRIZZLE, IMCOMBINE, BLOT, DERIV and DRIZ_CR tasks). Each input image is then drizzled (PIXFRAC = 0.5), applying the shifts calculated above, and the bad pixel mask files to create one drizzled frame per chip (there are four individual frames per cluster, one each for the four chips: PC, WF2, WF3, WF4). We combine the four frames into a single mosaic per cluster using the astrometric solution contained in our panoramic CFH12k frames (Czoske 2002) which matches the Digitized Sky Survey to an rms accuracy of 0.15″. Each mosaic contains a small number of residual cosmic rays at the edge of each WFC chip (within 1″ of the edge) that our automated pipeline was unable to remove because the dither pattern resulted in these regions being covered by just one or two exposures. We manually remove these events using the IMEDIT task in IRAF, however this is largely a cosmetic exercise as we discard any sources detected with

a centroid within 3″ of the edge of each chip from our analysis (§3.3.3).

3.2.4 The Reduced Frames

We present the final *HST* mosaics in Figs. 3.1–3.10. They have a pixel scale of 0.0498″ and an effective resolution of 0.15″. These data are an unprecedented high-resolution view of X-ray luminous clusters at $z \sim 0.2$, revealing (e.g. A 68 and A 383) for the first time numerous faint lensed features in the crowded central regions of our unique cluster sample. We exploit the exquisite spatial resolution of these mosaics to construct a high precision lens model of each cluster in §3.6. As the crucial next step towards these models, we also describe the candidate multiple-image systems that we detect in these frames in §3.4.

The *HST* data also reveal the optical morphology of each cluster, as traced by the distribution of cluster galaxies. We classify qualitatively the clusters based on whether there is obvious bi/multi-modal structure in the spatial distribution of cluster galaxies in our *HST* frames (4.9 arcmin^2; Figs. 3.1–3.10). We classify six clusters (A 209, A 267, A 383, A 963, A 1763, A 1835) as compact*, and the remaining four clusters (A 68, A 773, A 2218, A 2219) as clumpy. Whilst the galaxies only trace directly the distribution of stellar mass in the clusters, these crude visual morphologies are a useful indicator of the likely dynamical maturity of each cluster. We list these morphologies in Table 3.1.

*We employ a number of complementary techniques to investigate the prevalence of substructure in our sample (e.g. detailed lens models in §3.6 and analysis of X-ray data in §3.5.1). These diagnostics are sometimes contradictory as to the dynamical state of each cluster. For clarity, we adopt a simple classification scheme: a cluster is labelled "compact" if a given diagnostic indicates that it contains a single, central, dominant mass component and a cluster is labelled "clumpy" if that diagnostic reveals that it is not dominated by a single, central mass component.

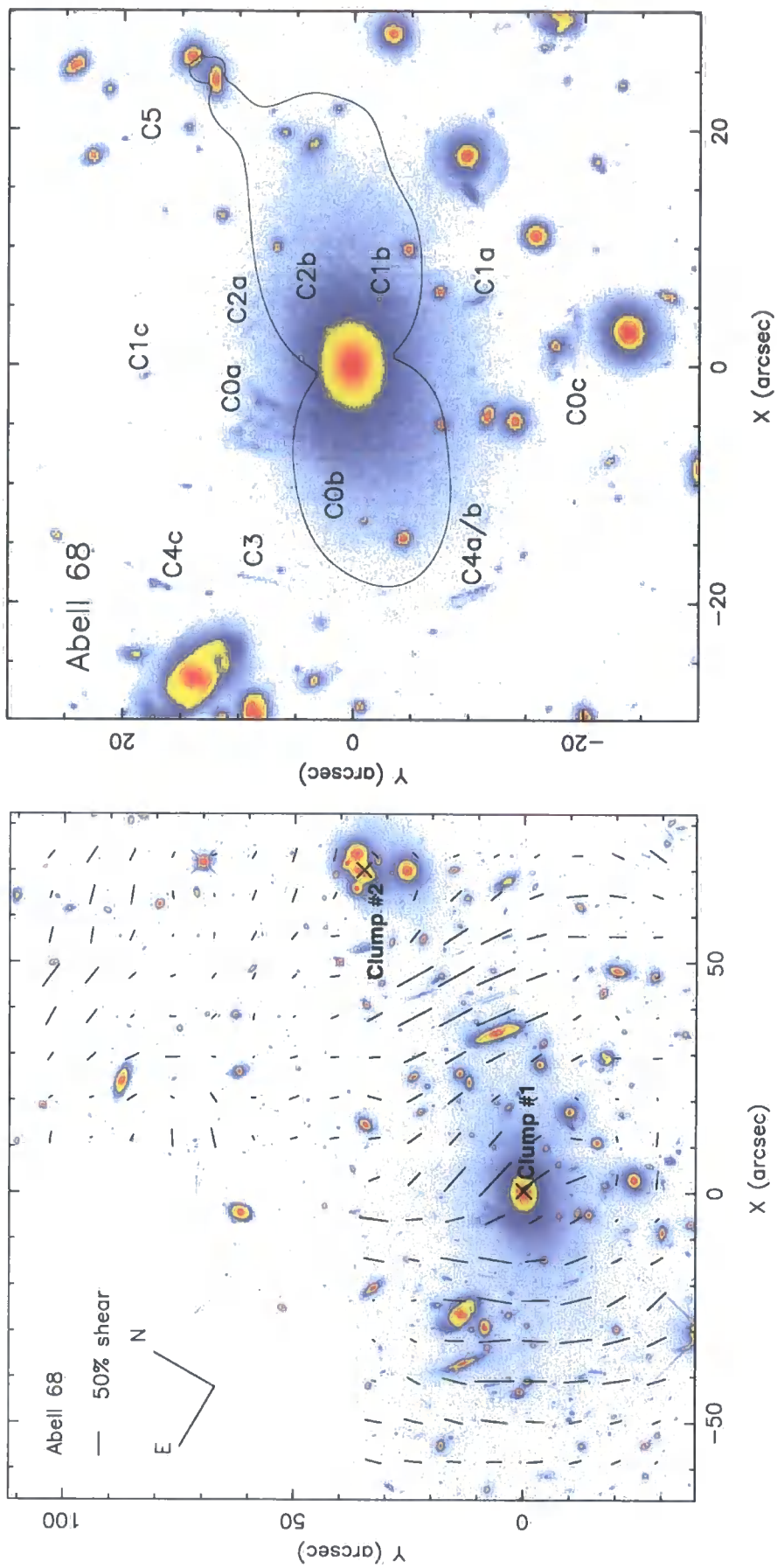

Figure 3.1: We present the *HST*/WFPC2 images of A 68, displayed on a logarithmic scale with a false colour table. LEFT – The full field of view of our *HST*/WFPC2 observations. We overplot the weak shear field; these vectors show the mean ellipticity and orientation of faint background field galaxies on a grid that has been smoothed with a Gaussian of $\sigma = 10''$. The positions of the two cluster-scale mass components included in the lens model of this cluster (Table 3.5) are marked with an "X". RIGHT – We show a zoom into the cluster core and mark the confirmed and candidate multiple-image systems. The thin curve shows the $z = 1.6$ critical line (Table 3.2).

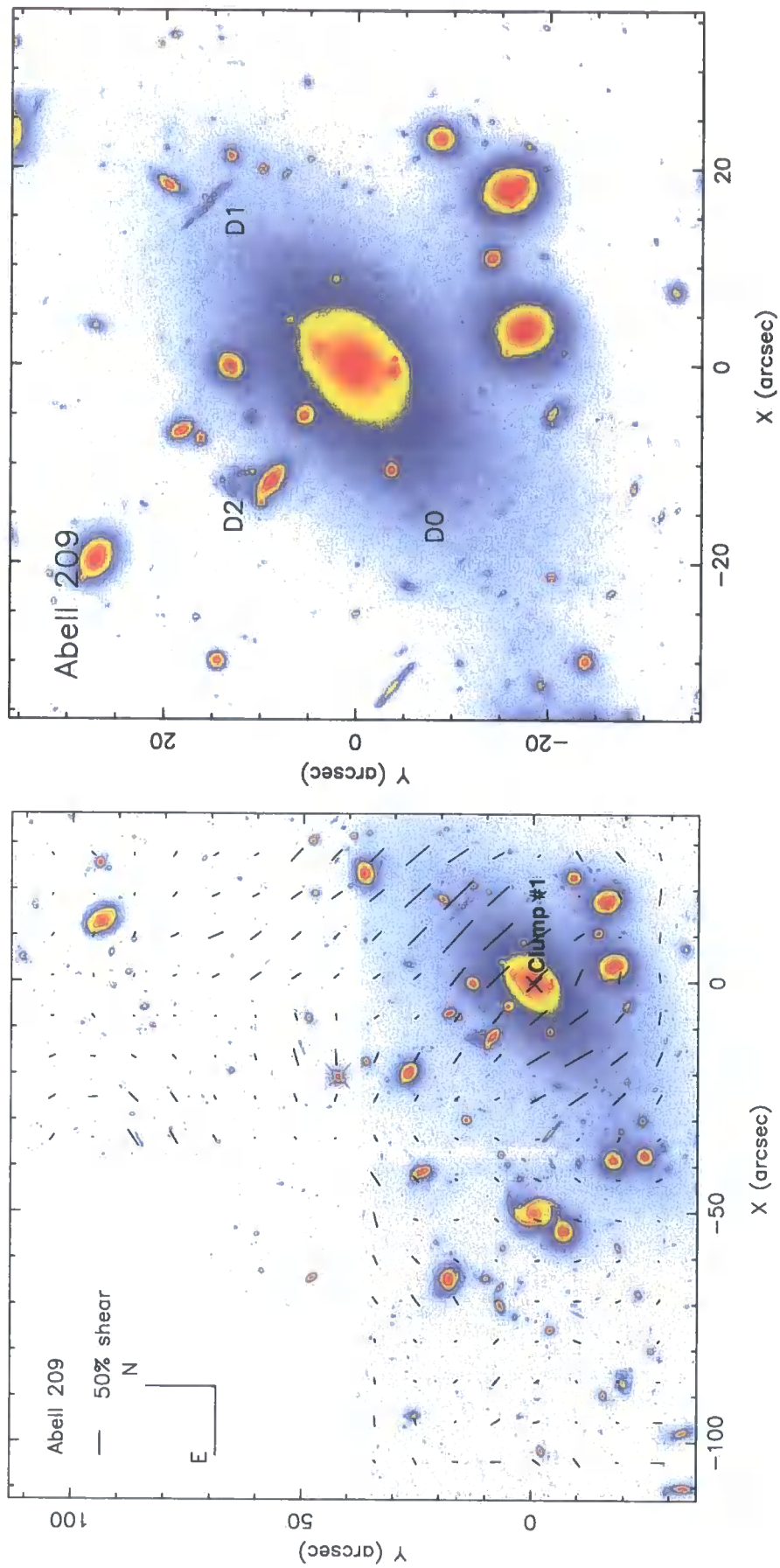

Figure 3.2: We present the *HST*/WFPC2 images of A 209, displayed on a logarithmic scale with a false colour table. LEFT – The full field of view of our *HST*/WFPC2 observations. We overplot the weak shear field; these vectors show the mean ellipticity and orientation of faint background field galaxies on a grid that has been smoothed with a Gaussian of $\sigma = 10''$. The position of the cluster-scale mass component included in the lens model of this cluster (Table 3.5) is marked with an "X". RIGHT – We show a zoom into the cluster core and mark the candidate lensed features.

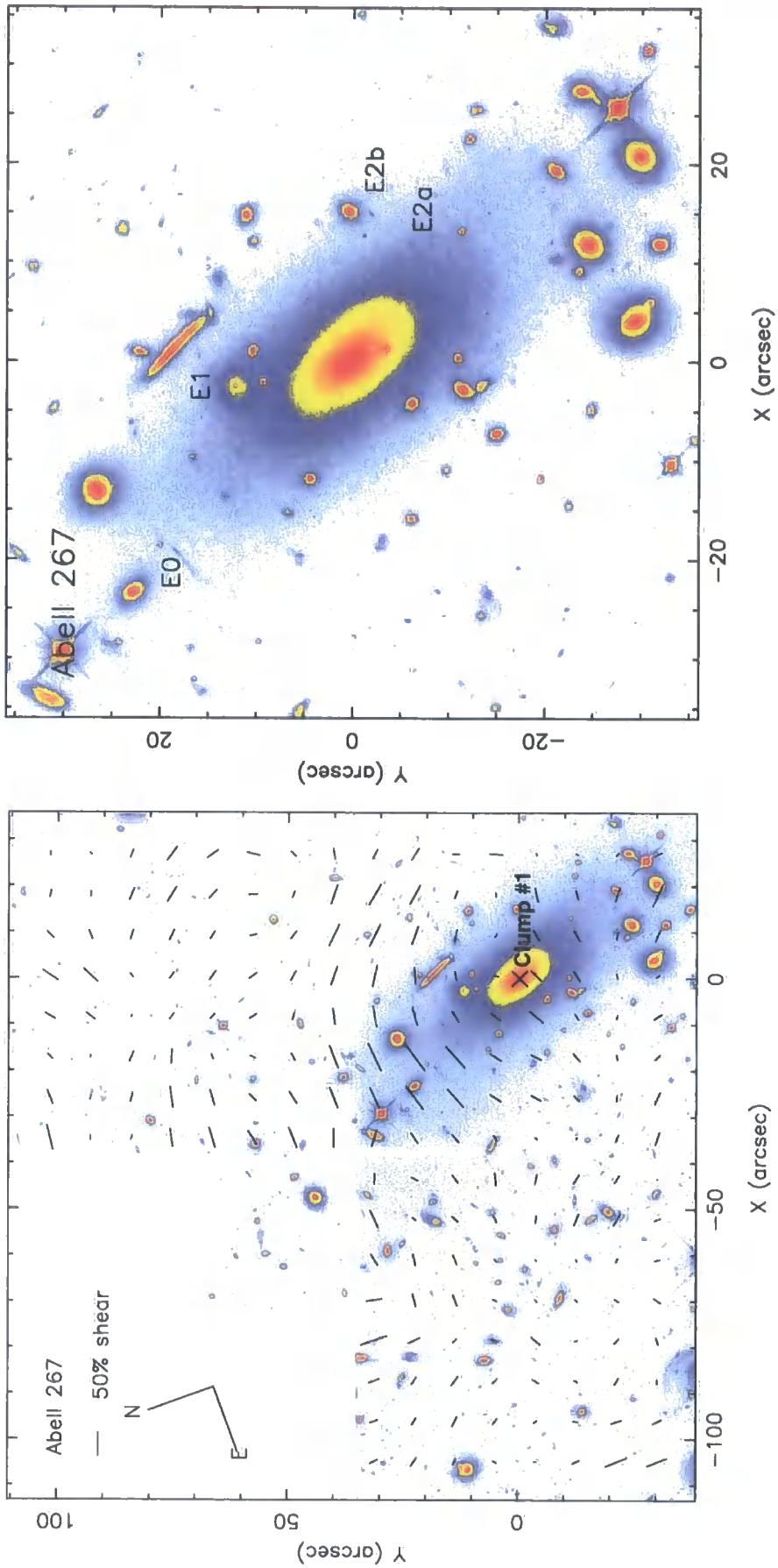

Figure 3.3: We present the *HST*/WFPC2 images of A 267, displayed on a logarithmic scale with a false colour table. LEFT – The full field of view of our *HST*/WFPC2 observations. We overplot the weak shear field; these vectors show the mean ellipticity and orientation of faint background field galaxies on a grid that has been smoothed with a Gaussian of $\sigma = 10''$. The position of the cluster-scale mass component included in the lens model of this cluster (Table 3.5) is marked with an "X". RIGHT – We show a zoom into the cluster core and mark the candidate lensed features.

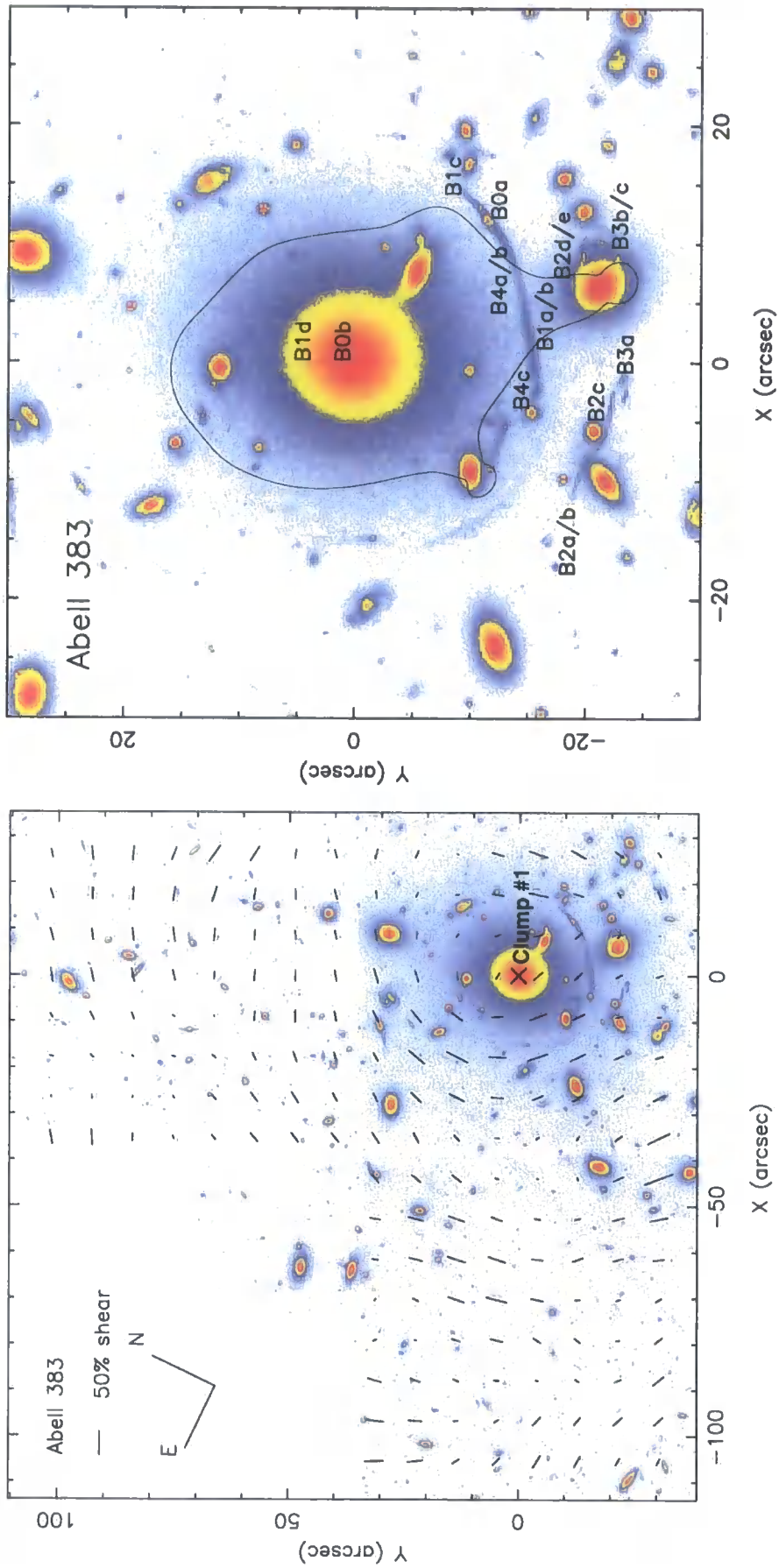

Figure 3.4: We present the *HST*/WFPC2 images of A 383, displayed on a logarithmic scale with a false colour table. LEFT – The full field of view of our *HST*/WFPC2 observations. We overplot the weak shear field; these vectors show the mean ellipticity and orientation of faint background field galaxies on a grid that has been smoothed with a Gaussian of $\sigma = 10''$. The position of the cluster-scale mass component included in the lens model of this cluster (Table 3.5) is marked with an "X". RIGHT – We show a zoom into the cluster core and mark the confirmed and candidate multiple-image systems. The thin curve shows the $z = 1.01$ critical line (Table 3.2).

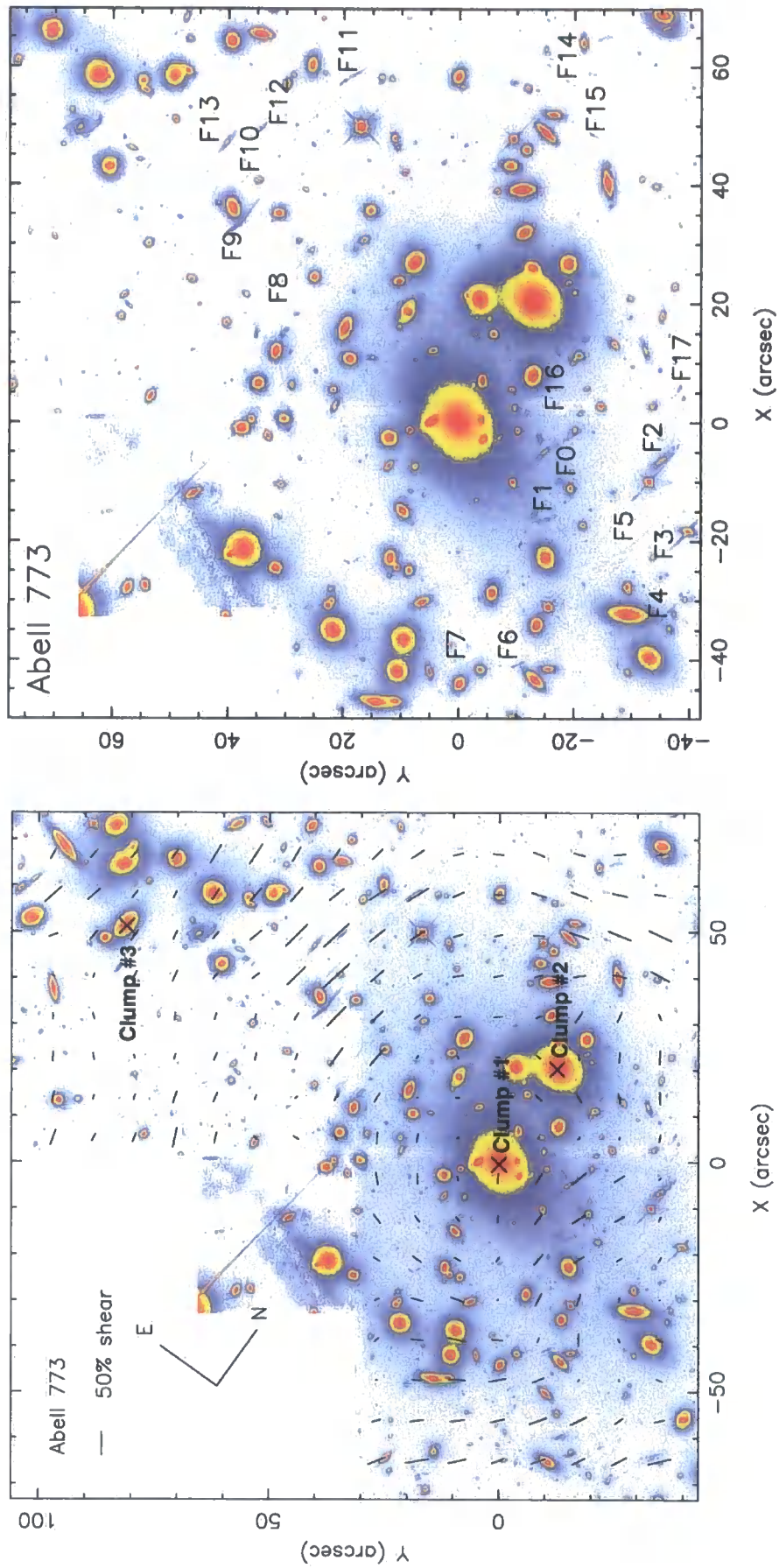

Figure 3.5: We present the *HST*/WFPC2 images of A 773, displayed on a logarithmic scale with a false colour table. LEFT – The full field of view of our *HST*/WFPC2 observations. We overplot the weak shear field; these vectors show the mean ellipticity and orientation of faint background field galaxies on a grid that has been smoothed with a Gaussian of $\sigma = 10''$. The positions of the three cluster-scale mass components included in the lens model of this cluster (Table 3.5) are marked with an "X". RIGHT – We show a zoom into the cluster core and mark the candidate lensed features.

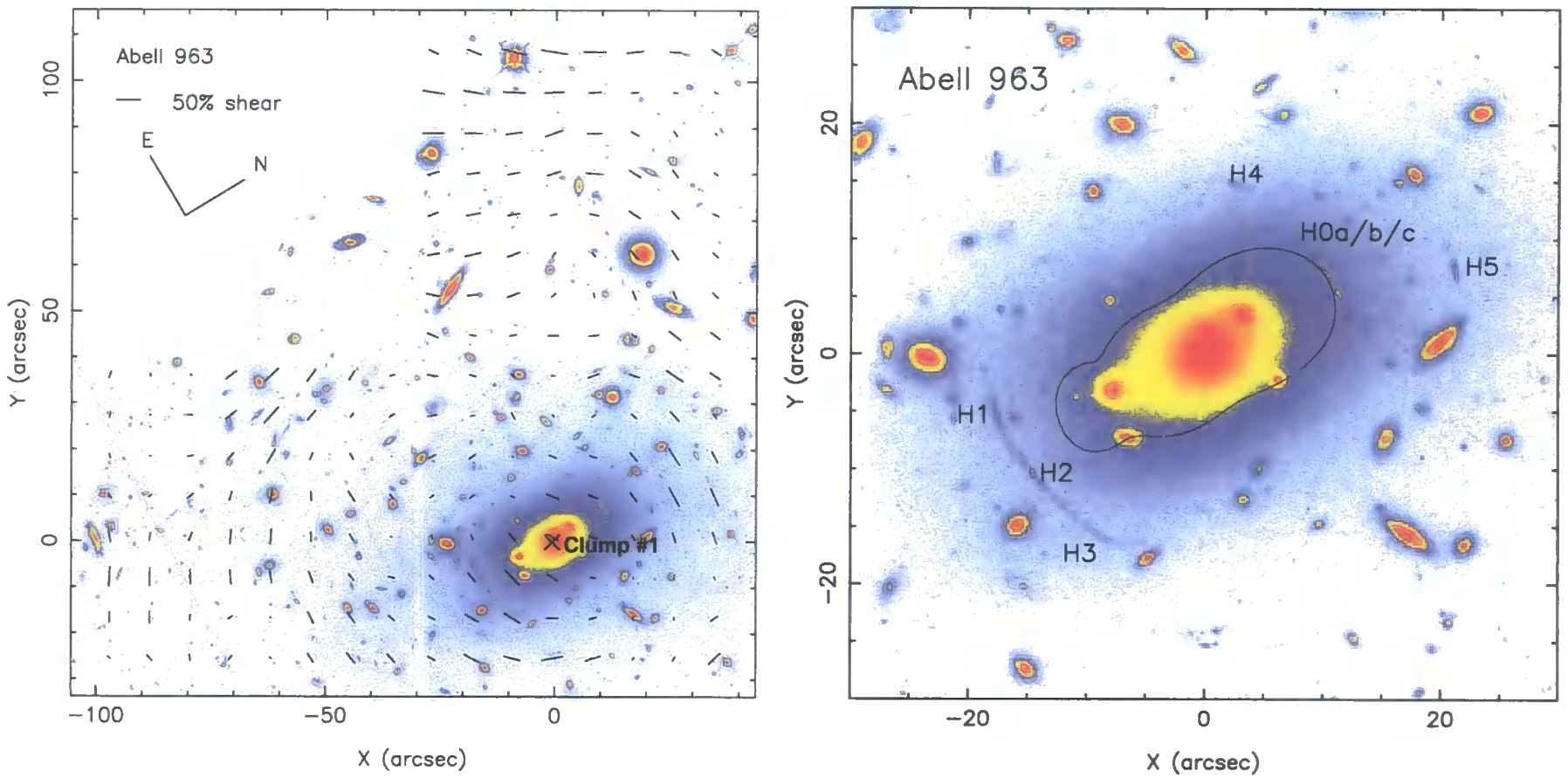

Figure 3.6: We present the *HST*/WFPC2 images of A 963, displayed on a logarithmic scale with a false colour table. LEFT – The full field of view of our *HST*/WFPC2 observations. We overplot the weak shear field; these vectors show the mean ellipticity and orientation of faint background field galaxies on a grid that has been smoothed with a Gaussian of $\sigma = 10''$. The position of the cluster-scale mass component included in the lens model of this cluster (Table 3.5) is marked with an "X". RIGHT – We show a zoom into the cluster core and mark the confirmed and candidate multiple-image systems. The thin curve shows the $z = 0.771$ critical line (Table 3.2).

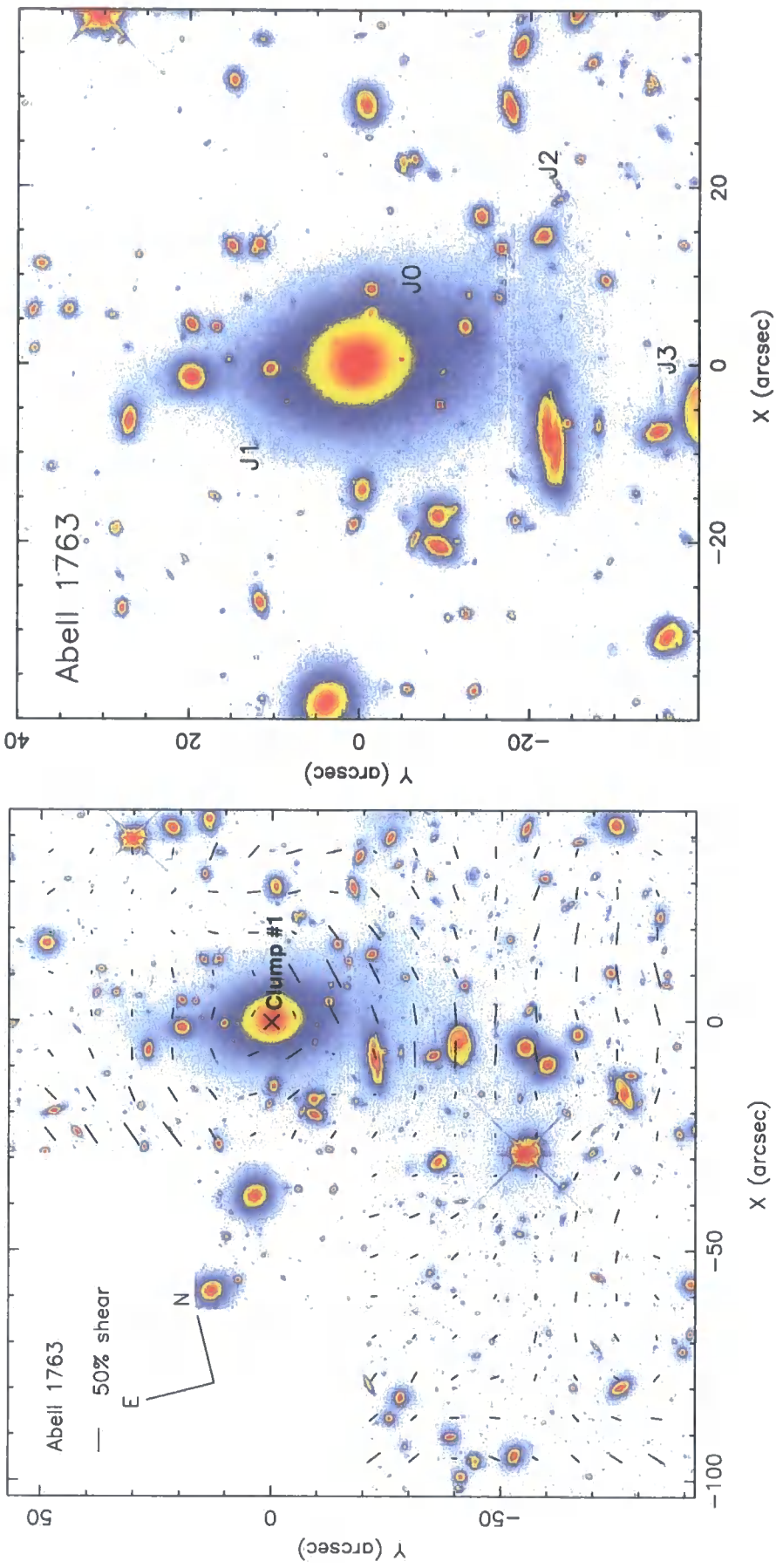

Figure 3.7: We present the *HST*/WFPC2 images of A 1763, displayed on a logarithmic scale with a false colour table. LEFT – The full field of view of our *HST*/WFPC2 observations. We overplot the weak shear field; these vectors show the mean ellipticity and orientation of faint background field galaxies on a grid that has been smoothed with a Gaussian of $\sigma = 10''$. The position of the cluster-scale mass component included in the lens model of this cluster (Table 3.5) is marked with an "X". RIGHT – We show a zoom into the cluster core and mark the candidate lensed features.

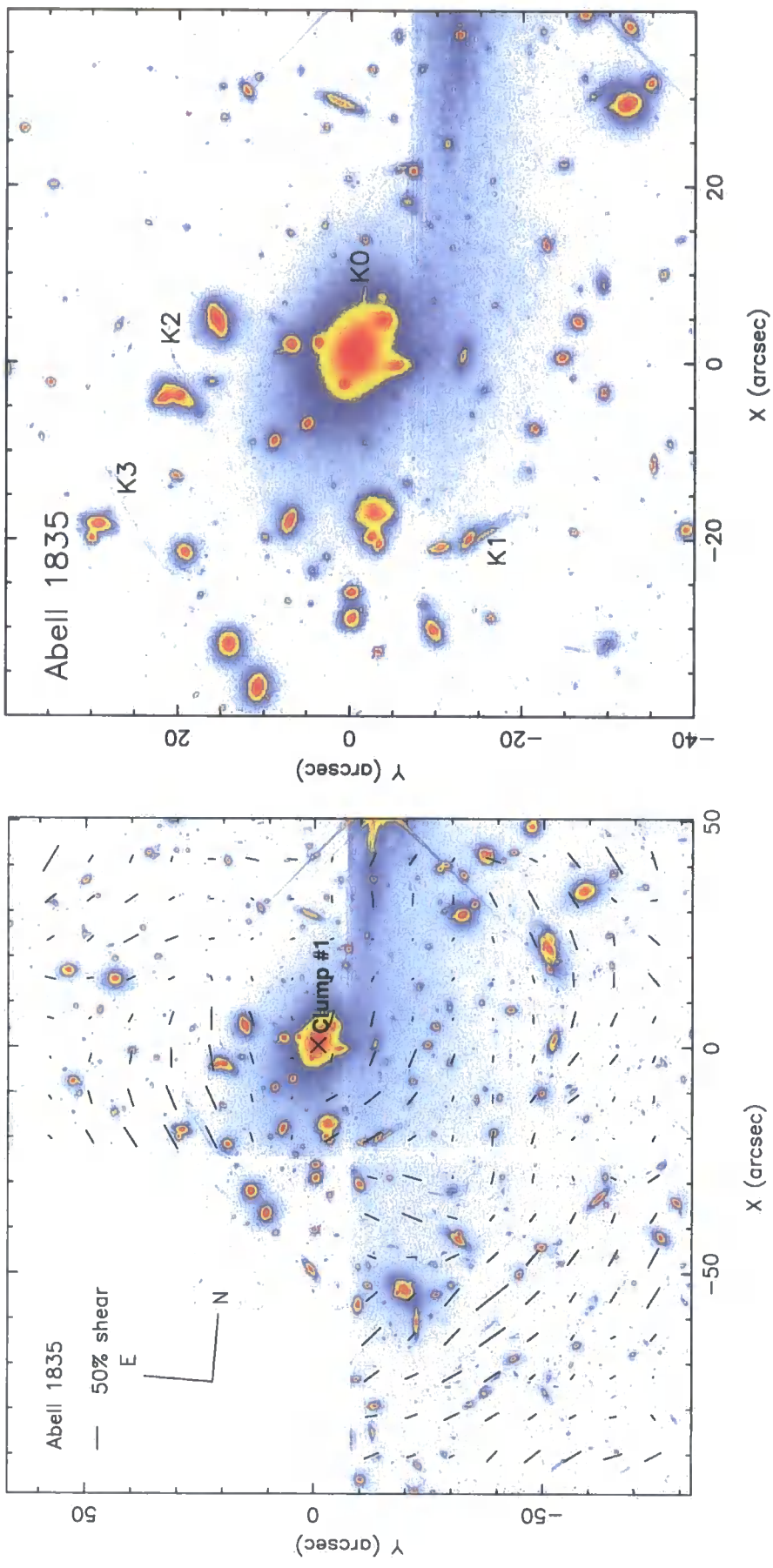

Figure 3.8: We present the *HST*/WFPC2 images of A 1835, displayed on a logarithmic scale with a false colour table. LEFT – The full field of view of our *HST*/WFPC2 observations. We overplot the weak shear field; these vectors show the mean ellipticity and orientation of faint background field galaxies on a grid that has been smoothed with a Gaussian of $\sigma = 10''$. The position of the cluster-scale mass component included in the lens model of this cluster (Table 3.5) is marked with an "X". RIGHT – We show a zoom into the cluster core and mark the candidate lensed features.

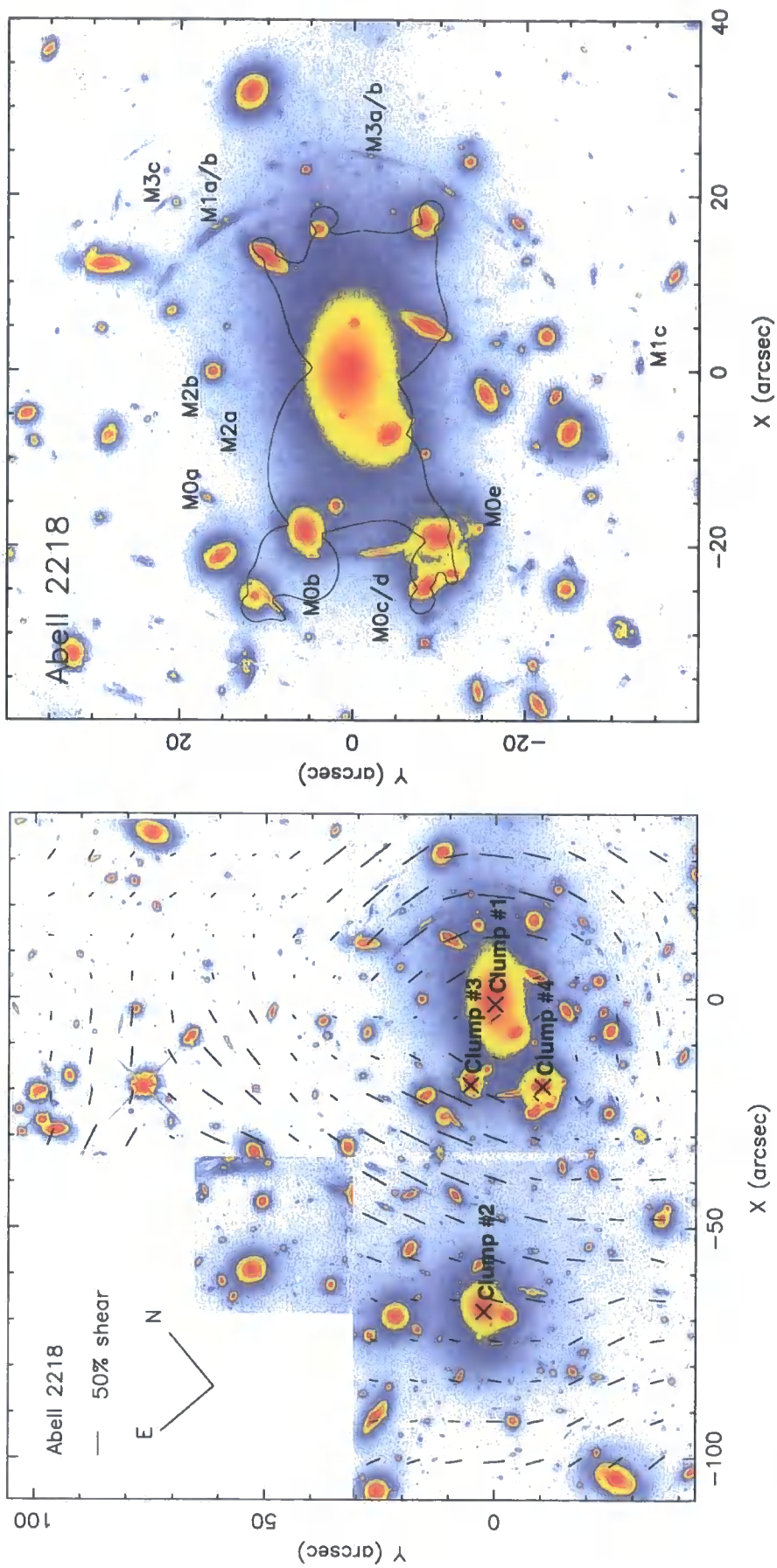

Figure 3.9: We present the *HST*/WFPC2 images of A 2218, displayed on a logarithmic scale with a false colour table. LEFT – The full field of view of our *HST*/WFPC2 observations. We overplot the weak shear field; these vectors show the mean ellipticity and orientation of faint background field galaxies on a grid that has been smoothed with a Gaussian of $\sigma = 10''$. The positions of the four cluster-scale mass components included in the lens model of this cluster (Table 3.5) are marked with an "X". RIGHT – We show a zoom into the cluster core and mark the confirmed and candidate multiple-image systems. The thin curve shows the $z = 0.702$ critical line (Table 3.2).

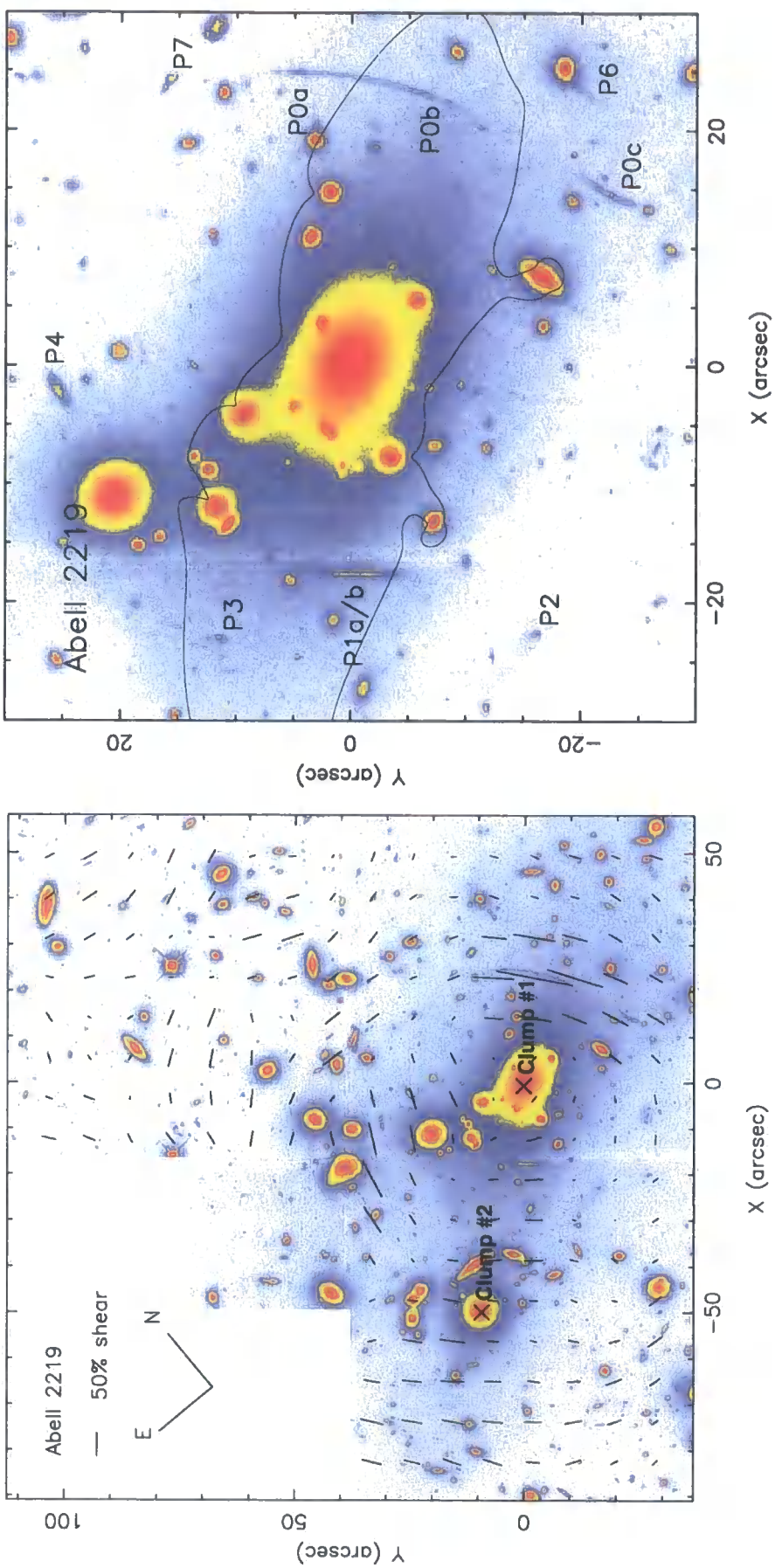

Figure 3.10: We present the *HST*/WFPC2 images of A 2219, displayed on a logarithmic scale with a false colour table. LEFT – The full field of view of our *HST*/WFPC2 observations. We overplot the weak shear field; these vectors show the mean ellipticity and orientation of faint background field galaxies on a grid that has been smoothed with a Gaussian of $\sigma = 10''$. The positions of the two cluster-scale mass components included in the lens model of this cluster (Table 3.5) are marked with an "X". RIGHT – We show a zoom into the cluster core and mark the confirmed and candidate multiple-image systems. The thin curve shows the $z = 1.768$ critical line (Table 3.2).

3.3 Analysis of *HST*/WFPC2 Data

3.3.1 Source Extraction

We analyse each *HST* frame using the SExtractor package (Bertin & Arnouts 1996), selecting all objects with isophotal areas in excess of 7 pixels (0.017 arcsec^2) at the $\mu_{702} = 25.2\,\mathrm{mag\,arcsec^{-2}}$ isophote (1.5–σ/pixel). From these catalogues we discard all detections whose centroid lies within 3″ of the edge of the field of view, and within regions affected by diffraction spikes near bright stars; this leaves a total of 8,730 "good" detections. We classify 193 of these as stars on the basis of their profile shapes leaving a total of 8,537 galaxies in a combined 49 arcmin^2 observed field of view. For our current purposes, we adopt MAG_BEST as the total R_{702} magnitude of each galaxy[†] and plot the differential number counts of these galaxies in Fig. 3.11. The number counts reveal an excess of galaxies with magnitudes in the range $18 \lesssim R_{702} \lesssim 22$ which we attribute to the galaxies in the ten foreground clusters. At $22 \lesssim R_{702} \lesssim 26$, the number counts follow a power law slope of 0.24 ± 0.01. Finally, at $R_{702} \gtrsim 26$, the number counts decline rapidly with magnitude as the sensitivity limit of the observations is reached. We adopt $R_{702} = 26$ as the 80% completeness limit of our galaxy catalogues.

Separation of source catalogues into cluster galaxies and background galaxies is fundamental to the construction of robust lens models. We therefore investigate the relative fraction of cluster and background galaxies as a function of R_{702} magnitude. We construct a simple model which comprises a composite luminosity function for the clusters plus a power law to account for the blank-field number counts. We parametrise the cluster luminosity functions as Schechter (1976) functions. The fraction of cluster galaxies in our catalogues as a function of R_{702} magnitude is sensitive to the choice of faint-end slope (α) of the cluster luminosity function. Measurements of the rest-frame V–band slope generally lie in the range $-1.6 \lesssim \alpha \lesssim -0.8$ (e.g. Driver et al. 1994; Bernstein et al. 1995; Wilson et al. 1997; Trentham 1998;

[†]We apply two corrections to MAG_BEST in §3.3.2 to convert the cluster galaxy R_{702} magnitudes into total K–band magnitudes. However, the raw MAG_BEST values from SExtractor are adequate, in §3.3.1, for the purpose of estimating the completeness limit of the *HST* data and the fraction of cluster galaxies as a function of magnitude.

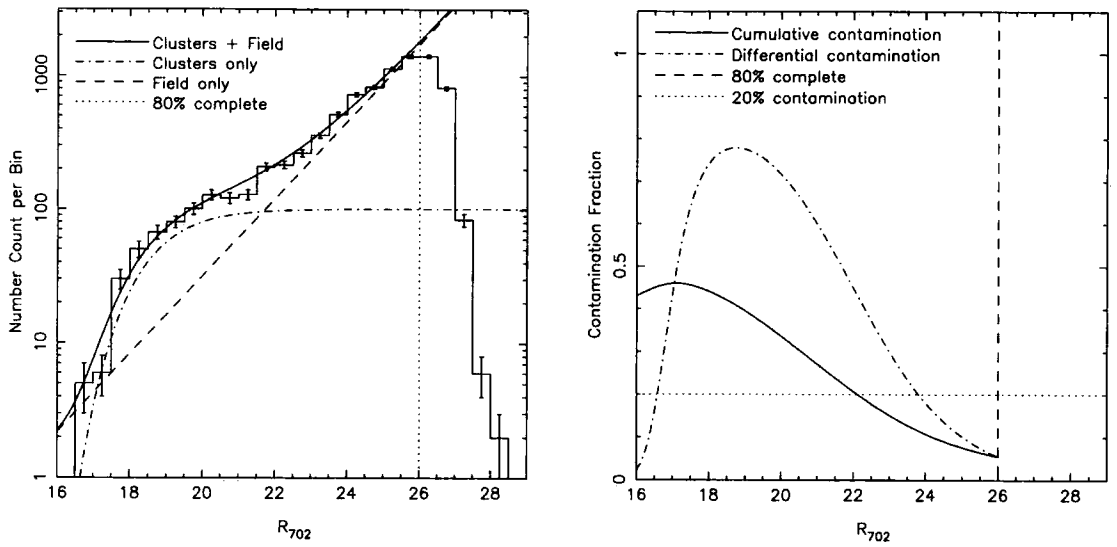

Figure 3.11: We use the combined differential source counts from the ten *HST* observations, together with a simple model of the cluster and faint field luminosity functions to estimate the fraction of cluster galaxies as a function of magnitude. This fraction is very sensitive to the faint-end slope of the cluster luminosity function. We adopt $\alpha = -1$ in line with recent spectroscopic and photometric redshift studies (Adami et al. 2000; Goto et al. 2002). Based on this value, we estimate that the cumulative cluster galaxy fraction reaches $\sim$ 20% at R_{702}= 22, which is equivalent to $R_{702}{}^{*}$ +3.5 at the median cluster redshift. We adopt this as the bright limit on our background galaxy catalogues and investigate how the residual level of contamination affects the lens models in §3.6.4. LEFT — Differential number counts of sources detected in all ten cluster fields. The error bar plotted on each bin is the Poissonian uncertainty in the number count. RIGHT — Differential and cumulative ($n(\geq R_{702})$) fraction of galaxies that belong to the clusters as a function of R_{702}.

Trentham & Hodgkin 2002; Dye et al. 2002). However, these surveys generally use solely imaging data, and contain very little information on the redshift of the cluster and field galaxies. In contrast, a small number of studies that include photometric or spectroscopic redshift information appear to favour the lower end of the range allowed by the imaging-only studies i.e. $-1.2 \lesssim \alpha \lesssim -0.8$ (e.g. Adami et al. 2000; Goto et al. 2002). A detailed discussion and analysis of uncertainties in the determination of cluster luminosity functions is beyond the scope of this thesis. We therefore adopt $\alpha = -1$ as being broadly representative of the studies that include redshift information. We also note that the design of our survey, specifically the selection of ten clusters in a narrow redshift slice, allows us to calibrate independently the uncertainties caused by contamination of our faint galaxy catalogues by cluster members. We describe these tests in §3.6.4 when we exploit the five clusters for which both multiple-image and weak-shear constraints are available to calibrate the weak-shear signal.

For the remainder of this section, we assume that $\alpha = -1$, and incorporate this into our model to estimate the contamination of the background galaxy catalogues. Given the large uncertainties in α, and our ability to empirically calibrate the uncertainties (§3.6.4), we stress that this exercise serves is more of an illustration than a definitive measurement of the contamination level.

We model the background galaxy population using the blank-field R–band number counts of Smail et al. (1995) and Hogg et al. (1997), from which we obtain a power-law slope of 0.31 ± 0.02. The model therefore contains two free parameters, the normalisation of the cluster and background galaxy counts. We fit this model to the data and present the results in Fig. 3.11. We use the model to estimate the fraction of galaxies as a function of magnitude that belong to the clusters. We show the differential contamination fraction in Fig. 3.11; as expected, the fraction of galaxies at a fixed magnitude that belong to the clusters peaks at R_{702}= 18.5, the median value of $R_{702}{}^{*}$ for the cluster sample. We integrate this function, to construct the cumulative contamination fraction, i.e. the fraction of galaxies with magnitudes between a given value of R_{702} and the 80% completeness limit of R_{702}= 26 that are cluster galaxies. We show this cumulative contamination function in Fig. 3.11. We use this function to estimate that, if $\alpha = -1$, then the cumulative cluster galaxy contamination fraction is $\lesssim$ 20% for sub-samples of galaxies with bright limits of $R_{702} \gtrsim 22 \simeq R_{702}{}^{*}+3.5$. We adopt this magnitude limit as the dividing line between our faint ($R_{702} > R_{702}{}^{*}+3.5$) and bright ($R_{702} \leq R_{702}{}^{*}+3.5$) sub-samples; we will select weakly sheared background galaxies and cluster-scale mass components from these two sub-samples in §3.6.1 and §3.6.2 respectively. As stated above, we will also test the calibration of our weak-shear constraints in §3.6.4.

3.3.2 Photometry of Cluster Galaxies

The parameterised strong lens models that we construct in §3.6 include both cluster- and galaxy-scale mass components. As we explain in §2.2, we minimise the number of free parameters in our models by scaling the mass of most of the galaxy-scale mass components with the luminosity of the associated cluster galaxy. On most scales the clusters are dominated by the cluster-scale mass components (i.e. dark matter

and hot gas) and the galaxy-scale mass components (i.e. some dark matter and gas, plus the stars) make a negligible contribution. However, the mass of cluster galaxies makes an important contribution on small scales, and can be crucial to the accurate modelling of some multiple-image systems (e.g. §4.2). Luminosity measurements that reflect accurately the total stellar mass of each galaxy are therefore crucial to the assumption of a fiducial mass-to-light ratio for galaxy halos (§2.2.3), and thus to the construction of robust lens models. To obtain robust galaxy luminosity measurements, we therefore apply two corrections to the R_{702} MAG_BEST magnitude measurements. Firstly, we adopt a better measure of the total R_{702} magnitude of these bright galaxies, and secondly, we convert these magnitudes to the observed K–band. We describe both of these two corrections below.

Balogh et al. (2002a) used GIM2D (Simard 1998) to fit parametrised bulge and disk surface brightness profiles to the cluster galaxies in our cluster sample. Balogh et al. found that their surface photometry deliver a more accurate measure of the total flux from cluster galaxies than their SExtractor analysis. We therefore compare the SExtractor MAG_BEST values in our bright galaxy catalogues (§3.3) with Balogh et al.'s surface photometry of the same galaxies. We find that our MAG_BEST magnitudes are systematically fainter than the GIM2D magnitudes. The difference is typically $\Delta\, R_{702}\sim$ 0.1–0.2, increasing to $\Delta\, R_{702}\sim$ 0.5–1.5 for the brightest cluster members including the cluster central galaxies. These differences are consistent with those found by Balogh et al. and arise for two reasons. First, SExtractor's local sky estimation algorithm over-estimates the sky background for the brighter and thus larger cluster galaxies, because as the size of these galaxies approaches the mesh size used for constructing the background map, source flux is absorbed into the background estimation. A second problem occurs in crowded cluster cores when a smaller galaxy is de-blended from the flux profile of a brighter galaxy. When this occurs SExtractor often identifies the correct centroids, but incorrectly associates a large number of pixels from the bright galaxy with the fainter, thus the flux from fainter cluster galaxies is systematically over-estimated, and the flux from brighter cluster galaxies is under-estimated. We therefore adopt Balogh et al.'s surface photometry as the total R_{702} magnitudes of the cluster galaxies. Unfortunately, some

cluster galaxies are absent from Balogh et al.'s sample due to their proximity to the edge of the individual WFC chips. We therefore use the majority of galaxies that are common to both catalogues to derive the mean correction as a function of magnitude and apply this mean correction to the $\sim$ 5–10% of cluster galaxies that are excluded from Balogh et al.'s analysis. We estimate that this typically introduces an uncertainty of $\lesssim 0.05$ magnitudes.

Our total R_{702} magnitudes are an important improvement on the original SExtractor measurements, however optical photometry has the disadvantage that it is sensitive to any ongoing star formation in the cluster population. In contrast, near-infrared emission is a more reliable tracer of a galaxy's stellar mass, as it is dominated by evolved, low mass stars and is less affected by luminous, young, blue stars. We therefore exploit the K–band imaging of our cluster fields, obtained as part of our search for gravitationally-lensed EROs (§5), to convert our total R_{702} magnitudes to total K–band magnitudes. Specifically, we subtract the 2″ aperture $(R_{702} - K)$ colours of the cluster galaxies measured in §5 from our total R_{702} magnitudes to obtain total K–band magnitudes.

3.3.3 Selection and Measurement of Faint Galaxies

We use both strong and weak lensing information to constrain the distribution of mass in each cluster (§3.6). We therefore need to measure accurate ellipticities and orientations for a well-defined sample of faint background galaxies in each cluster field. Reliable shape measurements demand that any artificial enhancement or suppression of image ellipticities is fully characterised and eliminated. Such effects may arise from the topology of the focal plane, isotropic and anisotropic components of the PSF and pixelisation of faint galaxy images due to the finite sampling capabilities of CCD detectors. We deal with each of these issues in turn below.

Topology of the *HST*/WFPC2 Focal Plane

The focal plane of *HST*/WFPC2 is not flat, the distortion increasing with distance from the centre of each WFC chip. A correction for this "geometrical distortion"

was applied in our data reduction pipeline using Trauger et al. (1995) polynomial solution (§3.2).

PSF Anisotropy

Hoekstra et al. (1998) found that the *HST*/WFPC2 PSF is not isotropic and that the anisotropy varies both across the field of view and with time. In contrast, Ebbels (1998) found no such variation in the Medium Deep Survey WFPC2 data. We examine the spatial variation of the PSF in our ten cluster observations, however each field contains just $\sim$ 20 stars, including a fraction of saturated, blended or very faint sources. We therefore exploit *HST*/WFPC2 observations of a further eight low X-ray luminosity clusters ($L_{\rm X} \leq 10^{44}$(0.1–2.4 keV) erg s^{-1}) at $z \sim 0.25$ (Cl 0818+56, Cl 0819+70, Cl 0841+70, Cl 0849+37, Cl 1309+32, Cl 1444+63, Cl 1701+64 and Cl 1702+64) to enlarge our sample of stars. These clusters were observed in an identical manner to our Cycle 8 observations, i.e. three integer-pixel dithered single-orbit exposures through the F702W filter (Balogh et al. 2002a). We processed these data using our data reduction (§3.2) and source detection (§3.3.1) pipelines and applied stringent selection criteria to construct a sample of 103 isolated, high signal-to-noise, unsaturated stars from both sets of cluster observations. We plot R_{702}–magnitude versus area for the combined source catalogue of all 18 clusters in Fig. 3.12. The sample of 103 stars occupies a well-defined locus in this plane.

We find that the PSFs of these stars are tangentially distorted with respect to the centre of each WFC chip with the magnitude of the distortion increasing with distance from each chip centre. The typical tangential shear at the edge of each chip is $\sim$ 5–10%, falling to $\lesssim$ 1–2% at each chip centre, in broad agreement with Hoekstra et al. (1998). However, even with the addition of the Balogh et al. data, this sample of stars is too small to quantify robustly the distortion pattern for each WFC chip individually. We therefore stack the three chips and derive a global solution by fitting a second order polynomial function to the tangential shear as a function of distance from the chip centre (Fig. 3.12). We then use this function to correct the entire star sample from all 18 cluster fields and measure the median tangential shear of the stars before and after the correction is applied.

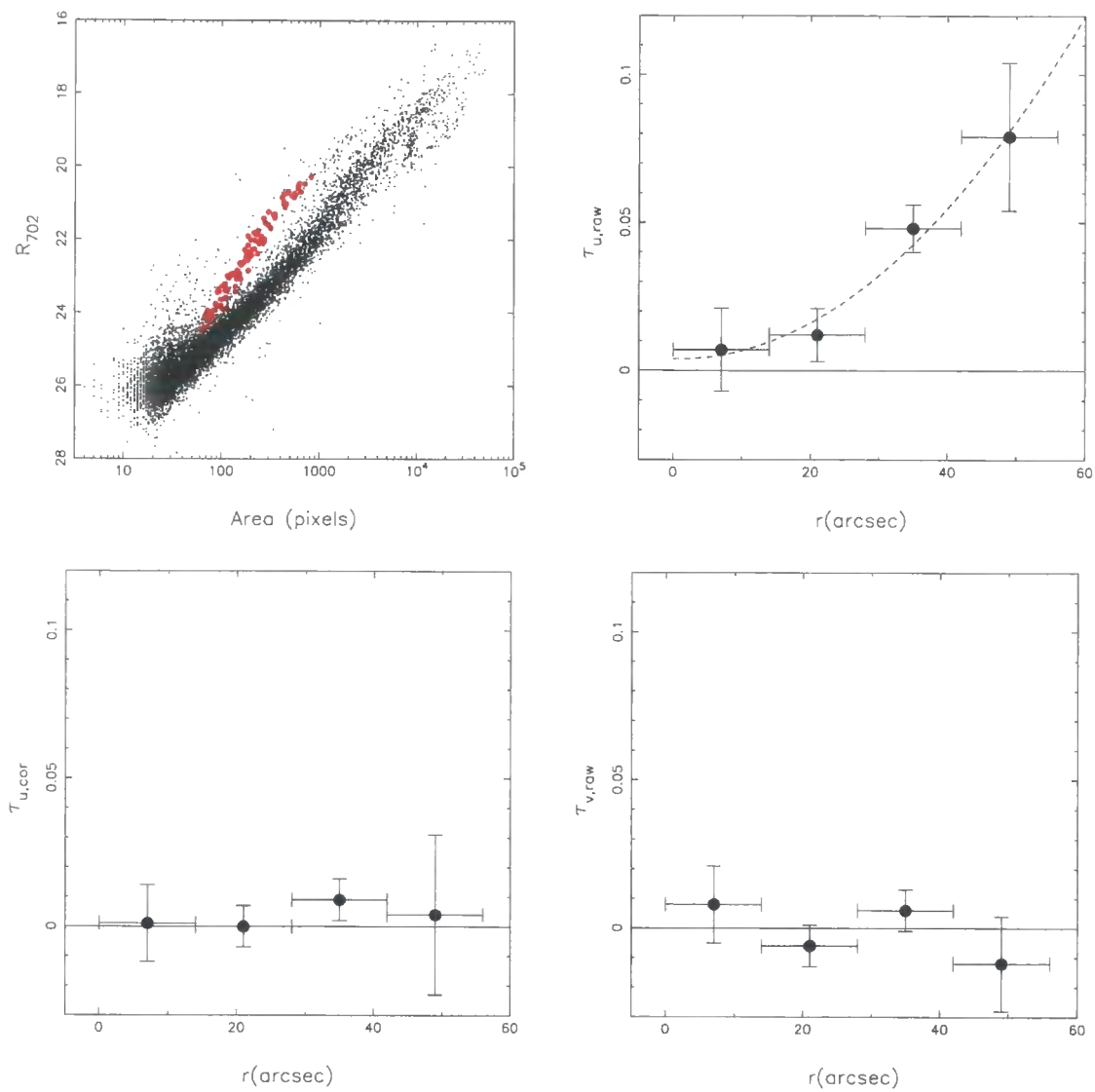

Figure 3.12: TOP LEFT — R_{702} versus area for the combined source catalogue for the 18 cluster observations used in the PSF anisotropy correction. The 103 stars used to derive the tangential shear correction occupy a well defined locus and are marked in red. TOP RIGHT — Mean tangential shear, $\tau_{u,raw}$, of the high-signal-to-noise star sample as a function of radial distance from the stacked chip centre. The dashed line shows the polynomial fit to these data that we used to remove the PSF anisotropy. BOTTOM LEFT — Mean tangential shear, $\tau_{u,cor}$, of the entire star sample after removal of the PSF anisotropy using the polynomial correction function. BOTTOM RIGHT — Mean radial shear, $\tau_{v,raw}$, of the high-signal-to-noise star sample.

The net result is that our correction reduces the tangential shear of stellar images to the same level as the radial stellar shear i.e. $\lesssim$ 1–2% (Fig. 3.12). We interpret the residuals as random noise in our shape measurements, and test this hypothesis using Monte Carlo simulations. We insert 10^4 stellar profiles that are sheared in small increments between zero and 10% into random blank-sky positions in our science frames. We then run the same SExtractor detection algorithm as described in §3.3.1 on these frames. Our simulations reveal that the position angle of a nearly circular stellar source can only be measured to $\lesssim$ 10% accuracy if the ellipticity of the source is $\gtrsim$ 2.5%, thus confirming our interpretation of the residuals. We therefore use our polynomial correction function to remove the PSF anisotropy from the shape measurements in our faint galaxy catalogues.

Image Circularisation

Finally, we address the impact of both the isotropic component of the PSF and pixelisation on our faint galaxy shape measurements. We use Monte Carlo simulations to estimate the minimum number of contiguous pixels required for a reliable shape measurement ($\lesssim$ 10% uncertainty) and to quantify the efficiency with which SExtractor can recover the input shape as a function of galaxy size. We first select a sample of relatively bright ($R_{702} \sim$ 19–21) background galaxies to use as test objects, ensuring that these galaxies cover the observed range of ellipticities in deep field galaxy surveys (Ebbels 1998). We scale and insert these test objects into random blank-sky positions in the science frames and attempt to detect them by running SExtractor in the same configuration as used in §3.3. We perform $\sim 10^6$ realisations spanning the full range of expected apparent magnitudes and scale sizes of faint galaxies (e.g. Smail et al. 1995a). We present the result of this experiment in Fig. 3.13; the measured ellipticity declines markedly as a fraction of the input ellipticity for sources with areas smaller than $\sim$ 1,000 pixels. Also, the smallest galaxy area for which the uncertainty in its shape measurement is $\lesssim$ 10% is $\sim$ 30 pixels. This limit represents, for the expected ellipticity distribution ($0 \leq \tau \lesssim 1.5$ – Ebbels 1998), the minimum galaxy size for which both the minor and major axes are resolved by *HST*/WFPC2. We therefore adopt 30 contiguous pixels as the "faint"

limit of our background galaxy catalogues. We list the number of sources in our final faint galaxy catalogues in Table 3.1. We also fit a second order polynomial to our simulation results in the range $30 \leq$ area $\leq 1,000$ pixels (Fig. 3.13), and use this recovery function to correct the measured ellipticity of each source in our faint galaxy catalogues.

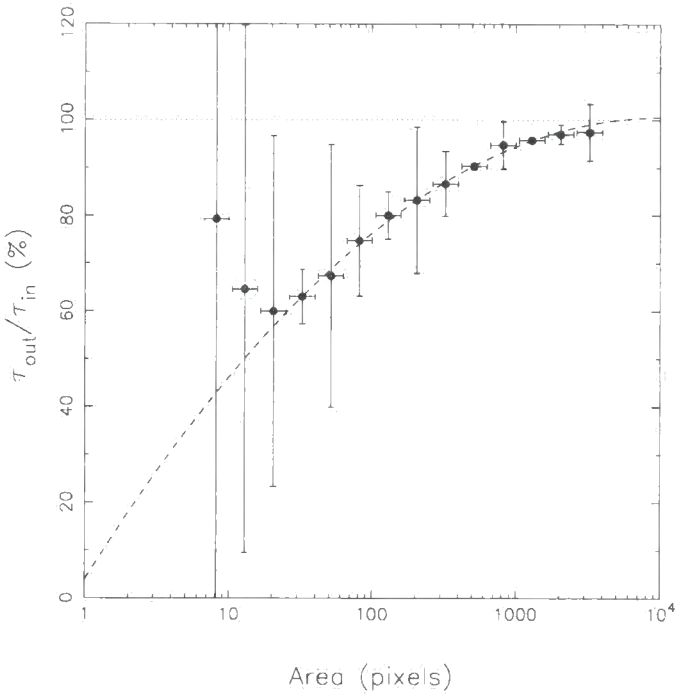

Figure 3.13: The results of Monte Carlo simulations to test how accurately we can measure the ellipticity of faint galaxies. The measured ellipticity as a fraction of the true ellipticity is well-fitted by a second-order polynomial function (dashed curve). When the galaxy image is smaller than $\sim$ 30 pixels, the shape measurements are overwhelmed by the PSF and the effects of pixelisation. We therefore cut our faint galaxy catalogues at a "faint" limit of area$\geq$ 30 pixels. We also use the polynomial function plotted in this figure to correct the observed ellipticities to intrinsic ellipticities.

3.4 Multiple-image Identification and Spectroscopy

The strongest constraints on gravitational lens models come from spectroscopically confirmed multiple-images of background galaxies (e.g. Kneib et al. 1996; §2). We therefore search our *HST* frames for candidate multiple-images to target with optical and near-infrared spectrographs on a range of ground-based 4– and 10–m class telescopes. We summarise the successes of our spectroscopic campaign and the spectroscopic redshifts that we draw from the literature. We also list the confirmed

multiple-image systems for which the redshift is known to $\Delta z \leq 0.1$ in Table 3.2 and present a zoom into the central region of each cluster that contains the multiple-image systems in Figs. 3.1–3.10. In the rest of this Chapter we adopt the notation that, for example, B0 is the background galaxy in the source-plane that gives rise to the multiple images B0a and B0b that are observed in the image-plane.

Table 3.2: Confirmed Multiple-image Systems ($\Delta z \leq 0.1$)

Cluster	Multiple-image	Redshift [a] [b]	Reference
A 68	C0a/b/c/d	1.60 ± 0.03	§5, §6.3
	C1a/b/c	1.9 ± 0.1	
A 383	B0a/b	1.0103 ± 0.0001	§4.2
	B1a/b/c/d	1.1 ± 0.1	
	B4a/b/c	1.2 ± 0.1	
A 963	H0a/b/c	0.771	Ellis et al. (1991)
A 2218	M0a/b/c/d/e	0.702	Pelló et al. (1992)
	M1a/b/c	2.515	Ebbels et al. (1998)
	M2a/b	5.576	Ellis et al. (2001)
	M3a/b/c	1.1 ± 0.1	Kneib et al. (1996)
A 2219	P0a/b	1.07	Kneib et al. (2002, in prep.)
	P1a/b/c	1.768	

[a] Redshift uncertainties are not available for all multiple-image systems listed in this table. The missing uncertainties all relate to spectroscopic redshifts drawn from the literature.
[b] Redshift uncertainties that are quoted to at least two decimal places have determined spectroscopically. The four redshifts that are quoted to a single decimal place have been obtained geometrically from lens models which are calibrated by at least one spectroscopically confirmed multiple-image system.

A 68

This cluster contains numerous candidate multiple-image systems close to the central galaxy and in the saddle region between the central galaxy and the group of cluster members to the North-West. The most striking of these is C0a/b/c, which

we identify as a multiply-imaged extremely red galaxy (ERO J003707; §5). Using UKIRT/CGS4 (Mountain et al. 1990) and Keck-II/NIRSPEC (McLean et al. 1998), we measure the redshift of this system to be $z = 1.60 \pm 0.03$ (§6.3). The South-West corner of this galaxy also appears to straddle the $z = 1.6$ radial caustic, causing an additional, radially amplified image of this portion of the galaxy. We search the *HST* frame in the vicinity of the predicted fourth image, and find a faint radial feature (C0d) $\sim 4''$ North-West of the central galaxy which is consistent with this interpretation. Despite a number of promising candidates (e.g. C1a/b/c and C2a/b), no other spectroscopically confirmed multiple-image systems are identified in this cluster. However, given the tight constraint from C0a/b/c/d, we conclude that C1a/b/c lies at $z = 1.9 \pm 0.1$.

A 209

In contrast to A 68, this cluster contains very few candidate multiple images. For example, although D1 is highly elongated, its morphology and the lack of candidate counter images strongly suggest that this is the only image of this galaxy. We conclude that there are no visible multiple-image systems with which to constrain the mass of this cluster.

A 267

Dahle et al. (2002a) speculate that the elongated galaxy $\sim 18''$ North-West of the central galaxy is a gravitationally lensed background galaxy. Kneib et al. (2002, in prep.) have observed this galaxy with the LDSS2 spectrograph on the William Herschel Telescope and confirm that it lies at the cluster redshift and is therefore not gravitationally-lensed. The superlative resolution of our *HST* data reveal E2a/b, a pair faint images that appear to be two images of the same high-redshift galaxy. A counter-image of this pair would be very much fainter than these two and therefore probably lies below the detection threshold of our observations.

A 383

This spectacular cluster contains numerous multiply-imaged features including a "giant" arc and two radial arcs that appear to comprise images of three distinct galaxies. We study these features in detail in §4.2 and report Keck/LRIS (Oke et al. 1995) spectroscopy of B0a, the brightest component of the giant arc, placing it at $z = 1.0103 \pm 0.0001$. We also conclude that B1a/b/c/d and B4a/b/c lie at $z = 1.1 \pm 0.1$ and $z = 1.2 \pm 0.1$ respectively.

A 773

This cluster contains many faint, elongated galaxy images, however their differing morphologies and surface brightness argue against any of them comprising a bona fide multiple-image system.

A 963

H0a/b/c and H1/H2/H3[‡] were first detected in ground-based imaging by Lavery & Henry (1988). Subsequent spectroscopy revealed that H0a/b/c lies at $z = 0.771$ (Ellis et al. 1991). Our *HST* imaging reveals the morphology of H0a/b/c and H1/H2/H3 in much greater detail than these ground-based studies. The featureless appearance of H0a/b/c confirms that these are three merging images of a single galaxy that appear to form a naked cusp arc. In contrast, the differing morphologies and centres of curvature of H1/H2/H3 argue against them being images of the same galaxy. We therefore interpret H1/H2/H3 as three singly-imaged galaxies, probably lying at similar redshifts of $z \sim 1$–2.

A 1763

This cluster is qualitatively similar to A 209 in that it contains a small number of faint, apparently sheared galaxy images, but no obvious multiple-image systems.

[‡]H0a/b/c and H1/H2/H3 are known as the "Northern" and "Southern" arc respectively in Lavery & Henry (1988) and Ellis et al. (1991).

A 1835

A blue elongated structure (K3)[§], situated $\sim 30''$ South West of the central galaxy has been reported by Schmidt et al. (2001) and Dahle et al. (2002a). The very low surface brightness of this feature (K3) in our *HST* data prevent us from identifying robustly any multiply-imaged features in this arc. We also detect the radial (K0)[§]and tangential (K1)[§]arclets that Schmidt et al. (2001) suggest may be images of a single galaxy at $z \sim 2.25$. The superlative resolution of the *HST* data appears to rule out this identification as the surface brightness of these two (resolved) images differ by several sigma. We therefore conclude that, whilst there are several promising candidates, there are currently no secure multiple-image systems in this cluster.

A 2218

This is arguably the most spectacular and extensively studied of all cluster lenses (e.g. Kneib et al. 1995, 1996), containing three spectroscopically confirmed multiple-image systems: M0a/b/c/d/e[¶] ($z = 0.702$ – Pelló et al. 1992); M1a/b/c[‖] ($z = 2.515$ – Ebbels et al. 1998); and M2a/b ($z = 5.576$ – Ellis et al. 2001). There also several other multiple-image systems for which spectroscopic redshifts are not available, including M3a/b/c[**] at $z = 1.1 \pm 0.1$ (Kneib et al. 1996).

A 2219

P0a/b/c[††] and P1a/b[††]were discovered in ground-based imaging of this cluster by Smail et al. (1995b). Previous attempts to constrain the redshifts of P0a/b/c and P1a/b have met with limited success: Smail et al. (1995) tentatively detected the 4000Å break in P1a/b at $\lambda_{obs} \sim 7500$Å placing this system at $z \sim 0.9$–1; Bézecourt et al. (1999) used HYPER-Z (Bolzonella et al. 2000) to place photometric constraints on the redshift of P0a/b/c, obtaining $z \leq 2.6$. In contrast, Kneib et al. (2002, in

[§]K0, K1 and K3 are labeled B′, B and A respectively by Schmidt et al. (2001).

[¶]These images are labeled 359/328/337/389 in the catalogue of Kneib et al. (1996).

[‖]These images are labeled 384/468 in the catalogue of Kneib et al. (1996).

[**]These images are labeled 444/H6 in the catalogue of Kneib et al. (1996).

[††]P0a/b/c and P1a/b are labeled $L_1/L_2/L_3$ and N_{12} respectively by Smail et al. (1995b).

prep.) report successful Subaru spectroscopy of P0a/b/c and P1a/b, placing these two systems at $z = 1.07$ and $z = 1.768$ respectively.

3.5 X-ray Observations and Data Analysis

Observations of the X-ray emission from galaxy clusters provides a complementary view of the mass and structure of these massive systems as traced by the hot gas trapped within the cluster potential well. Indeed, in the absence of large-scale weak-lensing surveys, this study is based on a sample of X-ray selected clusters (§1.6 & §3.1). Our lens models will deliver a high-precision mass-map of each cluster and enable us to measure the mass and structure of each cluster ($r \lesssim 500$ kpc). The X-ray morphology of the clusters, together with spatially resolved measurements of the temperature of the hot intra-cluster gas are powerful probes of the physical state of this gas. In conjunction with our lensing analysis, such X-ray measurements will help us to build a coherent picture of the dynamical maturity of our cluster sample.

3.5.1 Archival *Chandra* Observations

We exploit archival *Chandra* data for the eight clusters in our sample (A 209, A 267, A 383, A 773, A 963, A 1835, A 2218 and A 2219) that have been observed to date with this satellite. The clusters were observed with *Chandra* either in ACIS-I or ACIS-S detector configuration. Some observations where made during the so called period "B" (when the detector temperature was -110 °C), and others during the period "C" (when the detector temperature was -120 °C). We summarise the details of these observations in Table 3.3. Dr. Pasquale Mazzotta kindly reduced these data and performed the spectral fitting required to measure the temperature of each cluster.

In his spectral and imaging analysis Dr. Mazzotta used only chips I0-I1-I2-I3 and chip S3 for observations in ACIS-I and ACIS-S detector configurations respectively. To clean the data he used the data analysis procedures described by Markevitch et al. (2000), Vikhlinin et al. (2001a), Markevitch & Vikhlinin (2001), and Mazzotta et

al. (2001). It is important to note however that the three observations of A 383 were not performed in the same configuration. The spectral response and background for each observation was therefore generated individually before combining the data. The data were also cleaned for the presence of strong background flares following the prescription of Markevitch et al. (2000a). The net exposure time for each observation is listed in Table 3.3.

We adaptively smooth the final reduced *Chandra* frames and overlay these flux contours on the optical emission from each cluster in Fig. 3.14. We check the pointing accuracy of the *Chandra* observations using our $28'' \times 42''$ panoramic CFH12k imaging of these cluster fields (Czoske 2002). These optical data have been aligned with the Digital Sky Survey (DSS) frames of the same fields to an absolute rms accuracy of $0.15''$ (Czoske 2002). We compare the positions of the ten brightest point sources in each *Chandra* frame with their optical counterparts. We estimate that the X-ray frames are aligned with the DSS frames to an rms accuracy of $\lesssim 0.5''$, i.e. with sufficient accuracy to allow a robust comparison of the X-ray and optical morphology of each cluster (§3.5.3)

Dr. Mazzotta also performed spectral analysis in the 0.8–9 keV energy band in PI channels. This band avoids problems connected with the poor calibration of the detector at energies below 0.8 keV. Spectra were extracted using circular regions centred in the X-ray centroid of each cluster with a radius of 2 Mpc at the cluster redshift, being careful to mask out all the strong point sources. We note that, in the case of all the ACIS-S observations, the 2 Mpc radius is slightly larger than the physical size of the S3 chip. However, as the cluster temperature is mainly affected by the bright, central cluster region, this should not significantly affect our temperature measurements. The spectral fitting was performed using an absorbed MEKAL model with the equivalent hydrogen column density fixed to the relative Galactic value (Dickey & Lockman 1990). The temperature, the plasma metallicity, and the normalisation, were left as free parameters. Because of the hard energy band used in this analysis, the derived plasma temperatures are not very sensitive to the precise value of $N_{\rm H}$. We present the temperature of each cluster derived from the total field of view (i.e. $T_{\rm X,tot}$=$T_{\rm X}$ ($r \leq 2$ Mpc)) in Table 3.3.

Table 3.3: Summary of X-ray Observations

Cluster	Observation ID No.	Detector Configuration	Detector Temp. (°C)	Net Exposure Time (ks)	X-ray Morphology	$\Delta r_{\rm peak}$ (")	$T_{\rm X,tot}$(keV) ($r < 2$ Mpc)	$T_{\rm X,ann}$(keV) ($0.1 < r < 2$ Mpc)
Chandra Observations								
A 209	522	ACIS-I	−120	10.0	Clumpy	4 ± 1	$8.4^{+1.0}_{-0.9}$	$8.7^{+1.2}_{-1.0}$
A 267	1448	ACIS-I	−110	6.4	Clumpy	22 ± 1	$5.9^{+1.0}_{-0.7}$	$6.0^{+1.3}_{-0.9}$
A 383	524	ACIS-I	−120	7.4	Compact	< 1	$4.3^{+0.3}_{-0.1}$	$5.2^{+0.3}_{-0.4}$
	2320	ACIS-I	−120	17.9				
	2321	ACIS-S	−120	14.3				
A 773	533	ACIS-I	−120	11.3	Clumpy	10 ± 2	$8.0^{+0.9}_{-0.7}$	$8.2^{+1.0}_{-0.9}$
A 963	903	ACIS-S	−120	3.6	Compact	< 1	$7.3^{+0.5}_{-0.5}$	$7.2^{+0.6}_{-0.6}$
A 1835	496	ACIS-S	−120	10.5	Compact	< 1	$7.7^{+0.5}_{-0.4}$	$9.3^{+1.2}_{-0.8}$
A 2218	1454	ACIS-I	−110	9.7	Clumpy	10 ± 2	$6.9^{+0.9}_{-0.9}$	$6.8^{+1.0}_{-1.0}$
	553	ACIS-I	−110	5.4				
A 2219	896	ACIS-I	−120	42.3	Clumpy	3 ± 1	$14.0^{+1.5}_{-1.2}$	$13.8^{+1.5}_{-1.3}$
ROSAT Observations								
A 68	801046	HRI	...	17.1	Clumpy	...	...	...
A 1763	801049	HRI	...	18.0	Clumpy	...	$8.9^{+1.0}_{-0.8}$ [a]	...

[a] The temperature of A 1763 is taken from Mushotzky & Scharf (1997) and is based on their analysis of *ASCA* observations of this cluster.

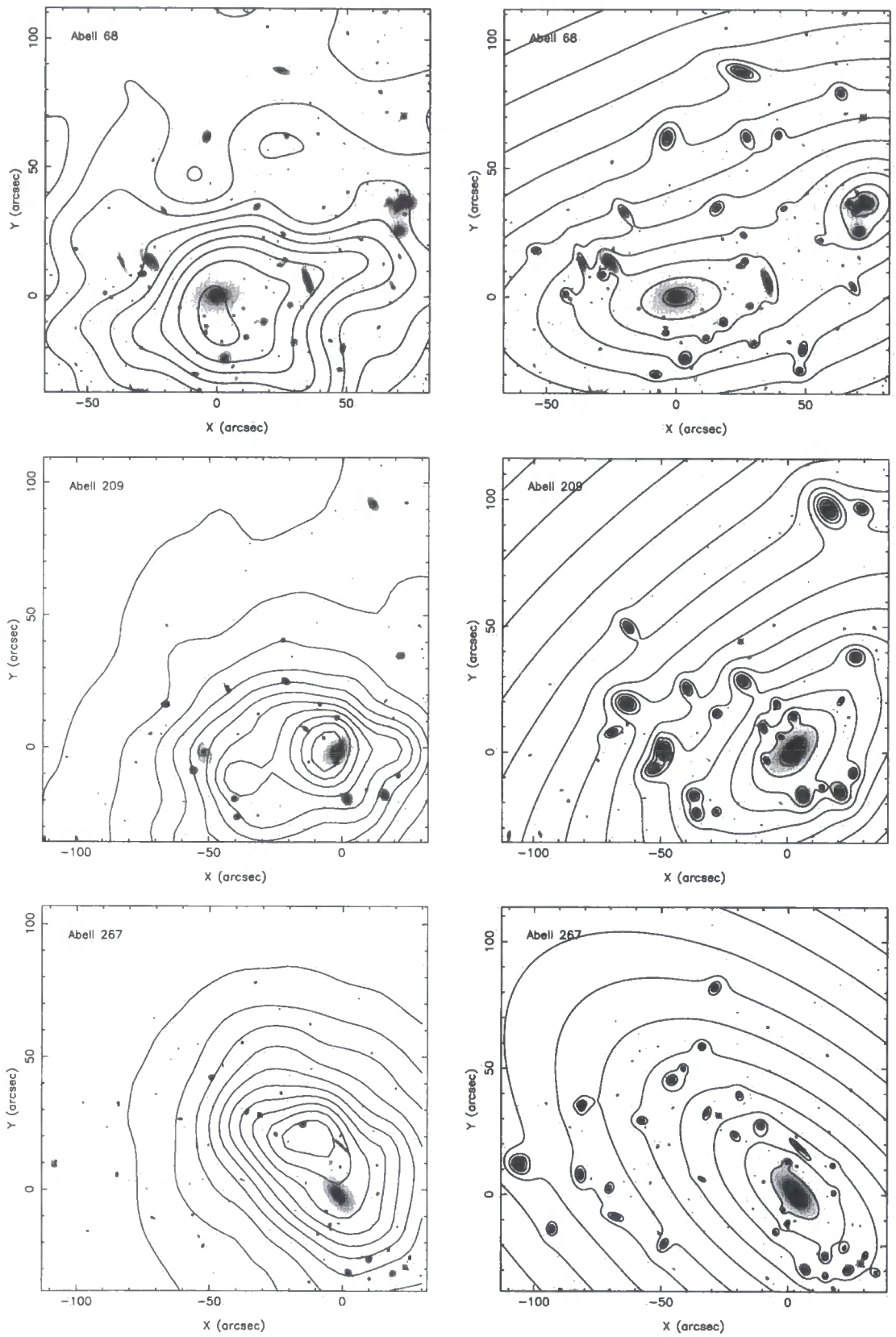

Figure 3.14: LEFT – X-ray flux contours of the adaptively smoothed emission from our cluster sample. All panels show data acquired with *Chandra* /ACIS except A 68 and A 1763 for which only *ROSAT* /HRI datasets are available. The contours divide the X-ray data into equally spaced intervals. RIGHT – Projected iso-density contours extracted from our suite of detailed lens models. The contours are equally spaced in the log. The grayscales in both left and right panels are low-resolution renderings of the relevant *HST* /WFPC2 frame.

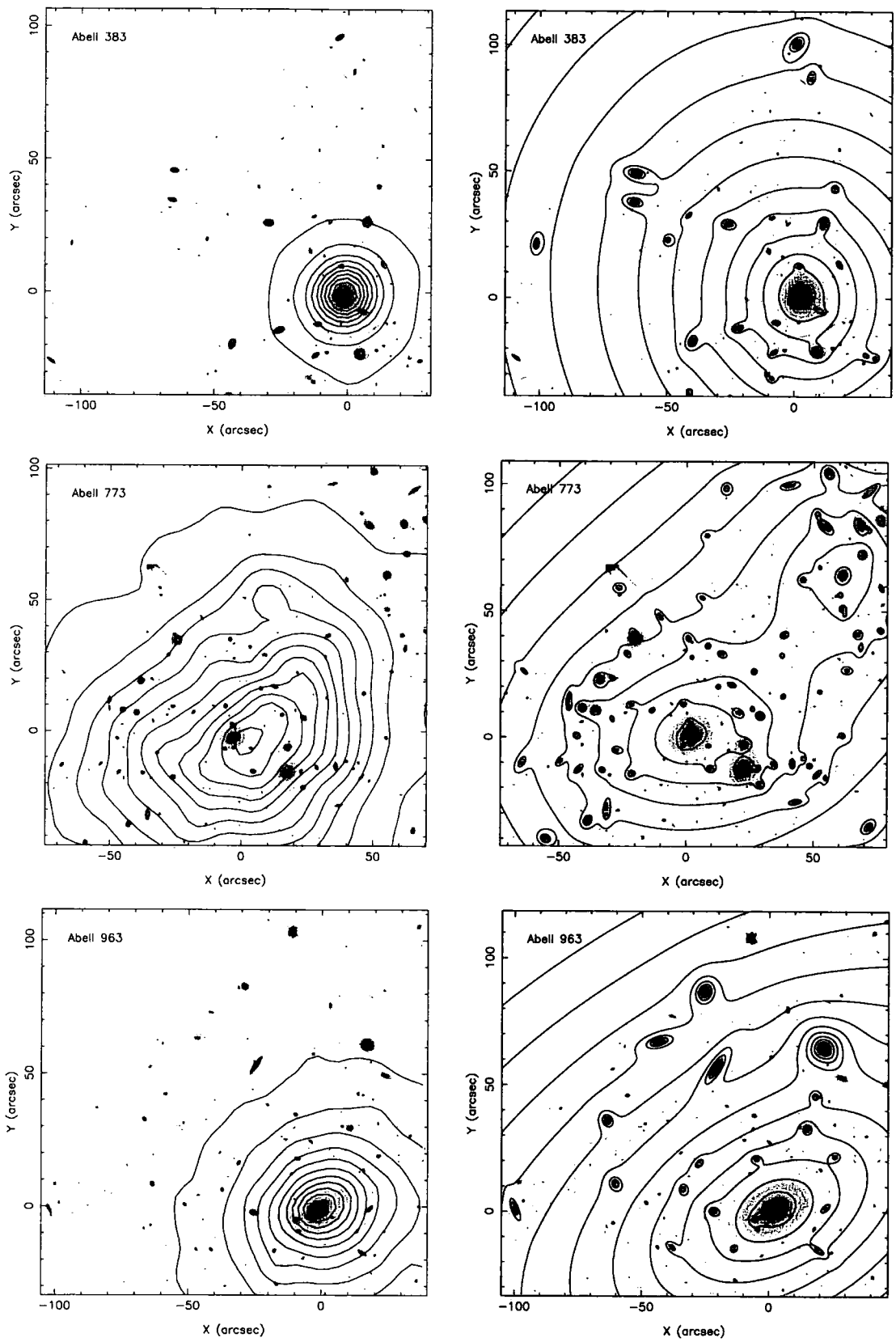

Figure 3.14: [continued] LEFT – X-ray flux contours of the adaptively smoothed emission from our cluster sample. All panels show data acquired with *Chandra* /ACIS except A 68 and A 1763 for which only *ROSAT* /HRI datasets are available. The contours divide the X-ray data into equally spaced intervals. RIGHT – Projected iso-density contours extracted from our suite of detailed lens models. The contours are equally spaced in the log. The grayscales in both left and right panels are low-resolution renderings of the relevant *HST*/WFPC2 frame.

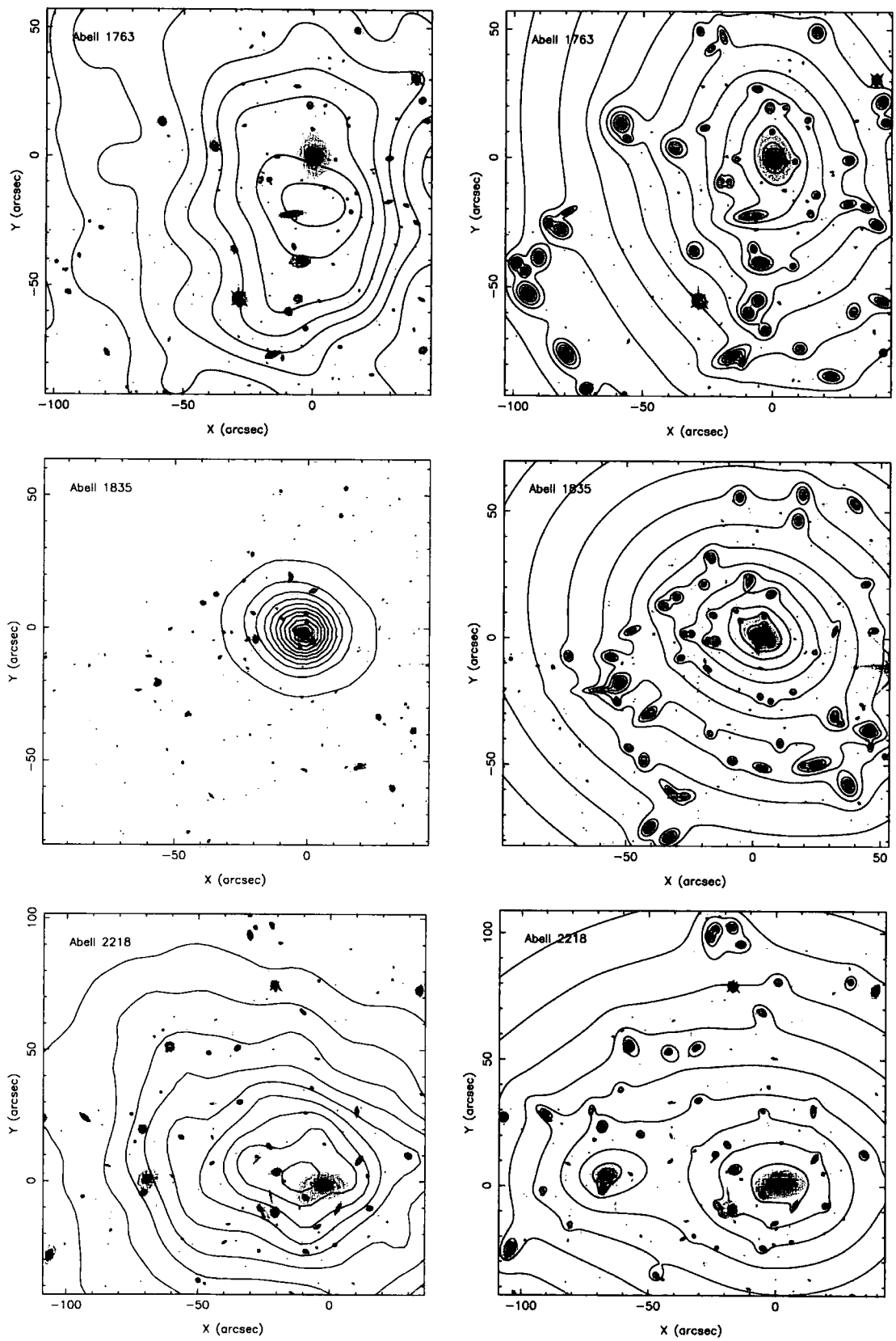

Figure 3.14: [continued] LEFT – X-ray flux contours of the adaptively smoothed emission from our cluster sample. All panels show data acquired with *Chandra* /ACIS except A 68 and A 1763 for which only *ROSAT* /HRI datasets are available. The contours divide the X-ray data into equally spaced intervals. RIGHT – Projected iso-density contours extracted from our suite of detailed lens models. The contours are equally spaced in the log. The grayscales in both left and right panels are low-resolution renderings of the relevant *HST* /WFPC2 frame.

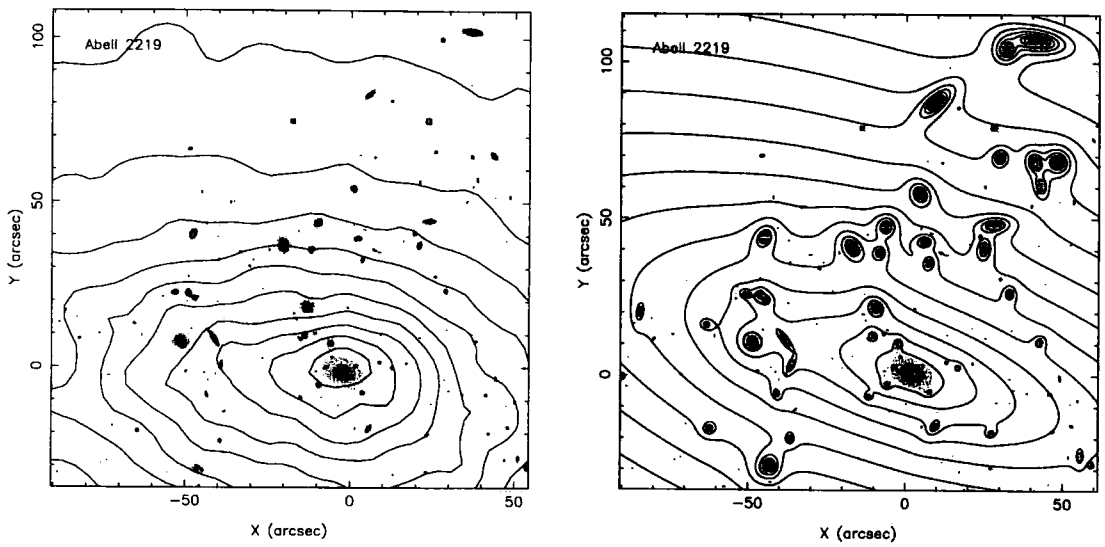

Figure 3.14: [continued] LEFT – X-ray flux contours of the adaptively smoothed emission from our cluster sample. All panels show data acquired with *Chandra* /ACIS except A 68 and A 1763 for which only *ROSAT* /HRI datasets are available. The contours divide the X-ray data into equally spaced intervals. RIGHT – Projected iso-density contours extracted from our suite of detailed lens models. The contours are equally spaced in the log. The grayscales in both left and right panels are low-resolution renderings of the relevant *HST*/WFPC2 frame.

The X-ray surface brightness of some clusters is observed to be very peaked in the cluster central regions. This phenomenon is associated with cooling timescales of $t_{\rm cool} \sim 10^9$–10^{10}years in the centre of such clusters (e.g. White et al. 1998), optical line emission from the cluster central galaxy (e.g. Crawford et al. 1999), the presence of significant quantities of cold ($T \sim$ 10K) gas inferred from detection of CO (Edge et al. 2001), a disturbed central galaxy morphology and an otherwise very relaxed and centrally condensed optical and X-ray morphology. These data have been interpreted as evidence for a fraction of the intra-cluster medium cooling as it flows in towards the centre of the cluster potential well i.e. a "cooling flow" (e.g. Fabian 1994).

Sensitive, high resolution observations with *Chandra* and *XMM-Newton* have confirmed that there is a steep temperature gradient in the centre of cooling flow clusters [‡‡] in the sense that the central region is colder than the outer regions, and

[‡‡]Given the current debate regarding the cooling flow interpretation of X-ray observations of clusters (which is outside the scope of this thesis), we define the term "cooling-flow cluster" to mean the most extreme examples of the genre. We identify these systems by the detection of line emission from the central galaxy which is arguably the cleanest test available (Edge et al. 1991). We also note that the cooling time for these extreme clusters is $\sim 10^9$ years, in contrast to the

there is possibly a universal temperature profile for these systems (Allen, Schmidt & Fabian 2001 – ASF). The presence of this central cold region could therefore bias low the cluster temperature measurements. As our aim is to obtain a reliable global measurement of the cluster temperatures, Dr. Mazzotta therefore re-measured the cluster temperatures following Markevitch (1998). The innermost cluster region was masked out from the spectral fit and the temperature was re-measured in an annulus ($0.1 \leq r \leq 2$ Mpc) centred on the X-ray centroid of each cluster. We list these measurements ($T_{\rm X,ann}$=$T_{\rm X}$ ($0.1 \leq r \leq 2$ Mpc)) in Table 3.3. We find a significant difference between $T_{\rm X,tot}$ and $T_{\rm X,ann}$ in just two clusters: A 383 and A 1835. Both of these clusters also satisfy our definition of cooling flow clusters (Smith et al. 2001; Allen et al. 1996). We also note that the six clusters whose values of $T_{\rm X,tot}$ and $T_{\rm X,ann}$ are formally consistent within the errors do not satisfy our definition of cooling flow clusters; none of these clusters have previously been identified as extreme cooling flow clusters (e.g. White et al. 1998).

3.5.2 Archival *ROSAT* Observations

A 68 and A 1763 have not been observed with *Chandra* . We therefore exploit archival *ROSAT*/HRI imaging observations of these two clusters. We simply wish to compare the gross features of the X-ray morphology of these two clusters with our lens models and the eight clusters observed with *Chandra*. We therefore just project the event file from these observations onto the (x, y) plane and adaptively smooth the resulting frame in the same manner as in §3.5.1. We overplot the smoothed flux contours on the optical frames in Fig. 3.14. We note that the astrometric solution of these data is only good to $\sim 10''$ because of the guiding and tracking errors and the large PSF ($\sim 4''$) of these observations. We attempted to check the relative astrometry of the *ROSAT* and *HST* frames by searching for point sources in the *ROSAT* frames. Unfortunately, the small number of bright point sources and the large positional error box undermined our ability to quantify the relative astrometry. Nevertheless, the *ROSAT* data do allow us to view the shape of the X-ray emission

less extreme systems which exhibit cooling times that are more comparable with the age of the Universe (i.e. 10^{10} years).

contours from these two clusters and crudely classify their morphologies.

3.5.3 X-ray Morphology

Fig. 3.14 reveals the diverse X-ray morphology of the clusters in our sample. We classify the clusters based on their X-ray morphology. "Compact" clusters have a regular circular or mildly elliptical morphology with strong alignment between their X-ray peak and the optical position of the central galaxy. "Clumpy" clusters are those that are not compact clusters because they have strongly elliptical or irregular X-ray contours. We classify three clusters as compact systems (A 383, A 963 and A 1835), and seven as clumpy systems (A 68, A 209, A 267, A 773, A 1763, A 2218, A 2219). To study the presence of substructure in the very centre of each cluster, we also measured the position of the X-ray peak in each *Chandra* frame and list $\Delta r_{\rm peak}$, the offset between this position and the central peak of our lensing mass-maps, in Table 3.3. All of the compact clusters have values of $\Delta r_{\rm peak}$ consistent with zero, and all the clumpy clusters have at least a 3–σ significant detection of an offset between the X-ray and mass peaks. We return to the X-ray morphology of the clusters in §3.7.

3.6 Gravitational Lens Modelling

We reviewed the relevant lensing theory and explained our modelling methodology in §2. Here, we define the model constraints in §3.6.1 and identify the mass components to be included in each model in §3.6.2. We then describe the model fitting process, present the best-fit models and test the robustness of the models in §3.6.3.

3.6.1 Model Constraints

The model constraints fall into three categories: confirmed multiple-images, candidate multiple-images and weak-shear constraints. Confirmed multiples have a well-defined redshift ($\Delta z \leq 0.1$) and all the counter-images are either identified or lie fainter than the detection threshold of our observations. The morphology of candidate multiples strongly suggests that they are multiply-imaged, but the redshift

of these systems is less well defined ($\Delta z > 0.1$) and not all counter-images may be identified. Regardless of the precision of the redshift measurement, multiple-image systems are generally found within $\lesssim 1$ arcmin of the centre of clusters, and therefore place tight constraints on the very centre of the cluster mass distribution. In contrast, the weak-shear constraints exploit the shape and orientation of individual weakly-sheared galaxies to constrain the cluster mass distribution on scales of $\gtrsim 1$ arcmin.

One of the most important aspects of constructing an accurate lens model is the normalisation, i.e. relating the observed lensing signal to an absolute measurement of the cluster mass. In a given cosmology, the lensing signal depends on the redshift of both the cluster lens ($z_{\rm L}$) and the lensed galaxy ($z_{\rm S}$). Since we know $z_{\rm L}$ for all of our clusters, knowledge of the $z_{\rm S}$ is critical to achieving a precise model calibration. Five of the clusters (A 68, A 383, A 963, A 2218 and A 2219) contain spectroscopically confirmed multiple-image systems (§3.4 & Table 3.2). These multiple-images therefore place tight constraints on these lens models on small scales, and also provide an accurate overall model normalisation. We supplement these constraints with the candidate multiples and the weak-shear to further constrain the structure of the cluster potential and to extend the lens models to larger scales in these five clusters.

The other five clusters (A 209, A 267, A 773, A 1763, A 1835) do not contain any confirmed multiple-image systems. We therefore rely on the candidate multiples and the weakly-sheared background galaxies to constrain our models of these clusters. In general we do not know the redshift of the candidate multiples and the weakly-sheared galaxies. We could estimate the redshift of the candidate multiples and use this to calibrate the relevant models, however this would leave us open to potentially large systematic uncertainties that would difficult to quantify. Alternatively, if the weakly-sheared galaxies follow a well-defined redshift distribution, then we could estimate the median redshift of this population and use this to calibrate the models of the clusters that do not contain confirmed multiple-images. This approach avoids reliance on any individual (possibly multiply-imaged) galaxy, and makes it easier to quantify the uncertainties in the resulting lens models.

We use the Hubble Deep Field North (HDF-N) photometric redshift catalogue of Fernández-Soto et al. (1999) to estimate the median redshift of our faint galaxy catalogues. Fig. 3.12 indicates that the $N_{\rm pixels} \geq 30$ limit our catalogues is broadly equivalent to a magnitude limit of $R_{702} \lesssim 26$. Using a simple no-evolution model (King & Ellis 1985) we estimate that a typical galaxy at $z \sim 0.5$–1.5 has a colour of $(R_{702} - I_{814}) \sim 0.7$ in the Vega system; converting to AB magnitudes, this translates into a faint limit of $I_{814,AB} \leq 25.8$ for selection of galaxies from the HDF-N catalogue. We show the redshift distribution of these sources (excluding foreground sources, i.e. $z \leq 0.25$) in Fig. 3.15, and measure the median redshift of this sub-sample to be $z_{\rm median} = 0.9$. We estimate that the uncertainty in $z_{\rm median}$ is ~ 0.2; this stems from the dispersion in galaxy colours at $z \sim 0.5$–1.5 and the uncertainty in our conversion between the $N_{\rm pixels} \geq 30$ and $R_{702} \leq 26$ selection functions. We adopt $z = 0.9 \pm 0.2$ as the fiducial redshift of our faint galaxy catalogues when using them to constrain the lens models. We note however that the dominant source of error in the final lens models that are constrained by just the weak-shear signal is the statistical uncertainty in the shear measurments and the ± 0.2 uncertainty in the median redshift of the faint galaxy catalogues contributes just $\sim$ 10–20% of the total error budget.

Using the shape of weakly-sheared galaxies as model constraints introduces two further uncertainties. First, the background galaxies are not circular, and so the measured shape and orientation of each faint galaxy combines its intrinsic shape and the weak lensing distortion. We assume that the orientation of background galaxies is random, and so we include the intrinsic shape distribution as a noise component when computing the χ^2 value for each model (§2.2.3). Second, there is a systematic uncertainty in the model shear values computed at the position of each faint galaxy as we do not know the redshift of each individual faint galaxy. This effect is a slowly varying function of redshift provided that we restrict our analysis to faint galaxies that lie outside of the strong-lensing regime. In principle we therefore need to choose a projected radius (say 100 kpc) outside of which we may safely assume that the background galaxies follow the redshift distribution determined above. However, adopting a single radius has two disadvantages: first,

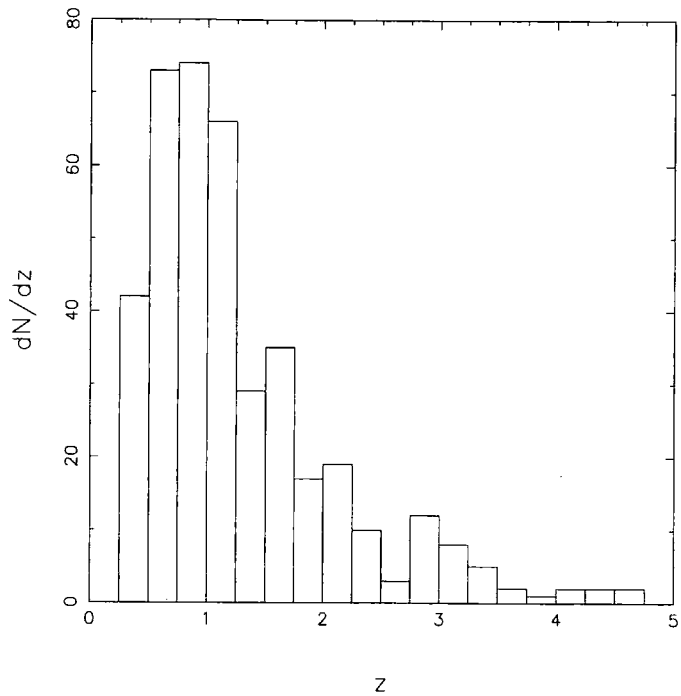

Figure 3.15: The redshift distribution of galaxies from the HDF-N photometric redshift catalogue (Fernández-Soto et al. 1999) that match the selection criteria used to construct our faint galaxy catalogues. We estimate that the median redshift of this sub-sample of HDF-N galaxies is $z = 0.9 \pm 0.2$, where the uncertainties are estimated based on the corrections applied between different filters and photometric systems (see text for details).

for a low-mass lens, the strong-lensing regime may be much smaller than the chosen radius, and thus the signal-to-noise ratio of the observational constraints is diluted; second, for a high-mass lens, the strong-lensing regime may have a much larger radius than that chosen, and thus the weak-lensing assumption may not be valid. We therefore investigate the redshift dependence of the weak shear constraints on a cluster-by-cluster basis. Specifically, we experiment with a number of different inner radii (25, 50, 75, 100, 125, 150 kpc) and study the behaviour of the mean tangential shear with inner radius. We find that the mean tangential shear of each cluster asymptotes to a fixed value as the size of the inner radius increases. We therefore select for each cluster an inner radius that maximises the signal-to-noise ratio of the weak-shear constraints, whilst at the same time producing results that are consistent with the asymptotic mean tangential shear.

We summarise the multiple-image and weak-shear information used to constrain each cluster lens model in Table 3.4.

Table 3.4: Summary of Model Constraints

Cluster	Multiple-image Systems		Weak-shear Measurements		
	Confirmed[a]	Candidate[b]	$r_{\rm min}$ (kpc)	$N_{\rm fgal}$	$\langle\tau_{\rm u}\rangle^{c}$
A 68	C0, C1	C2, C4	200	343	0.18 ± 0.03
A 209	...	...	100	431	0.10 ± 0.02
A 267	...	E2	200	323	0.06 ± 0.02
A 383	B0, B1, B4	B2, B3	160	357	0.12 ± 0.02
A 773	...	...	200	297	0.19 ± 0.03
A 963	H0	...	120	455	0.13 ± 0.02
A 1763	...	...	150	399	0.09 ± 0.02
A 1835	...	...	300	190	0.20 ± 0.03
A 2218	M0, M1, M2, M3	730, H1-3, H4-5[d]	250	187	0.16 ± 0.03
A 2219	P0, P1	...	200	246	0.15 ± 0.03

[a] Confirmed multiple-image systems have well-defined redshifts ($\Delta z \leq 0.1$) and all counter-images are either identified or are too faint to be detected in our *HST* data. We use these systems to both calibrate the lens models and constrain the structure of the cluster potential.

[b] Candidate multiple-image systems have $\Delta z > 0.1$ and/or unidentified counter-images. We use these systems to place additional constraints on the structure of the cluster potential.

[c] $\langle\tau_{\rm u}\rangle$ is the mean tangential shear of the faint background galaxies selected for inclusion in the weak-shear constraints. We use the shape and orientation of each galaxy as an individual constraint on the lens model, and here summarise the strength of these constraints by listing $\langle\tau_{\rm u}\rangle$ for each cluster.

[d] 730, H1–3 and H4–5 were studied in detail by Kneib et al. (1996), and are not discussed in this chapter. We include them in this table for completeness, as they help to constrain the structure of A 2218.

3.6.2 Mass Components

Each lens model consists of a single lens plane at the cluster redshift (Table 3.1), populated with mass components that are based on the observed properties of each cluster. The sum of these mass components should equal the total projected mass of the cluster i.e. matter associated with the cluster as a whole (i.e. most of the dark matter and X-ray emitting gas) and matter associated with individual galaxies (i.e. stars, cold gas and some dark matter). We therefore investigate the gravitational potential of each cluster and the galaxy populations of each cluster as a basis for identifying the relevant mass components for each model. We stress that the mass components identified by the methods described in this section simply provide the "first cut" lens model, and that the subsequent model fitting process optimises the parameters of these mass components. We also stress that we ignore the X-ray morphology of each cluster when identifying the mass components in this section. We adopt this somewhat conservative approach because any initial design of the lens model based on the X-ray emission would leave us open to biases from the effects of non-gravitational processes (e.g. shock-heating during merger events) on the X-ray morphologies.

Cluster-scale Mass Components

First we identify the likely cluster-scale mass components, and classify the mass structure of the clusters. We compute the mean ellipticity of the weakly-sheared background galaxies behind each cluster on a grid with 10″ spacing using our faint galaxy catalogues (§3.3.3). We smooth this grid with a Gaussian of $\sigma = 10''$ and overplot the resulting weak shear maps on the optical data in Figs. 3.1–3.10. These maps provide a direct view of the gravitational potential of each cluster. The tangential alignment of the shear vectors around the central galaxy in each cluster reveal that the main mass component of each cluster is approximately coincident with the central galaxy. In some clusters, the shear vectors depart from the general trend of tangential alignment around the central galaxy, revealing the likely presence of additional cluster-scale mass components. This substructure occurs in the vicinity of groups of bright cluster members. We briefly list the shear-map-based

evidence for including two or more cluster-scale mass components in four of the clusters:

A 68 — The shear vectors are perturbed from a concentric pattern around the central galaxy in the vicinity of the group of galaxies to the North-West of the central galaxy in A 68. There is also a strong shear signal in the saddle region between the central galaxy and this group of galaxies.

A 773 — This cluster also displays a strong shear signal in the saddle region between the central galaxy and a group of cluster galaxies, this time lying to the East of the central galaxy. The orientation of the shear vectors around the central galaxy and its bright neighbour also suggest that individual cluster-scale mass components are associated with these two galaxies. A 773 therefore appears to be tri-modal on the basis of its shear-map.

A 2218 — The substructure of this cluster has been investigated my numerous authors (e.g. Kneib et al. 1995, 1996; see also references listed in §3.8). Here, we simply note that our shear map is based on a fresh source extraction and shape analysis of the weakly sheared background galaxies in the Kneib et al. (1996) data, and thus *independently* confirms the bimodal nature of the mass distribution of this cluster. Specifically, the shear vectors are perturbed by the mass associated with the second brightest cluster galaxy that lies South-East of the central galaxy.

A 2219 — The shear vectors are not very strongly perturbed by the mass associated with the group of galaxies that lie to the South-East of the central galaxy. Nevertheless, we identify this group as the likely location of a cluster-scale mass component because such a bi-modal mass distribution is the most natural explanation for the very straight morphology of the P1a/b multiple-image system.

Many of the other clusters exhibit spatial variations in the strength of the weak shear signal, however none of them contain systematic perturbations of the shear vectors away from a concentric pattern around their respective central galaxy. On the basis of the weak-shear maps, the lens models of the remaining six clusters (A 209, A 267, A 383, A 963, A 1763, A 1835) should all contain just one cluster-scale mass component.

To put this morphological analysis onto a quantitative footing, we also measure the dipole moments of the cluster mass distributions using the shapes of faint background galaxies. We apply a discretised version of the aperture moment method (Schneider & Bartelmann 1997) to those background galaxies that we also select for inclusion in the weak-shear constraints in §3.6.1. Specifically, we compute the dipoles ($n = 1$) using the following formula:

$$Q_n = \frac{1}{\nu} \sum_j (r_j \, e^{i\alpha_j})^n \, \tau_j \, e^{2i(\alpha_j - \theta_j)} \tag{3.1}$$

where ν is the number density of galaxies used to measure the moments, (r_j, α_j) are the co-ordinates of each faint galaxy in plane polar co-ordinates and (τ_j, θ_j) describe the ellipticity and orientation of each faint galaxy image. We also use the following formula to estimate the signal-to-noise ratio of our measurements:

$$\sigma_n^2 = \frac{2\pi\sigma_\tau^2}{\nu^{3/2}} \sum_j r_j^{2n+1} \tag{3.2}$$

where σ_τ is the width of the ellipticity distribution of faint field galaxies from Ebbels (1998).

We plot Q_1 in arbitrary units versus L_X (0.1–2.4 keV) in Fig. 3.16. Despite the superlative resolution of our *HST* data, the individual dipole measurements typically have a signal-to-noise ratio of $\sim$ 2–4. Nevertheless, as expected, the clusters that were classified as requiring two or more cluster-scale mass components on the basis of their weak-shear map generally have higher dipole moments than those that were classified as requiring one cluster-scale mass. We note however that among the apparently relaxed clusters, A 1763 appears to display a relatively large dipole, and among the bi/multi-modal clusters, A 2219 has a relatively small dipole.

In summary, the "first-cut" lens models of A 209, A 267, A 373, A 963, A 1763 and A 1835 contain one cluster-scale mass component centred on the central galaxy of each cluster; the "first-cut" models of A 68, A 2218 and A 2219 contain two and of A 773 contains three cluster-scale mass components.

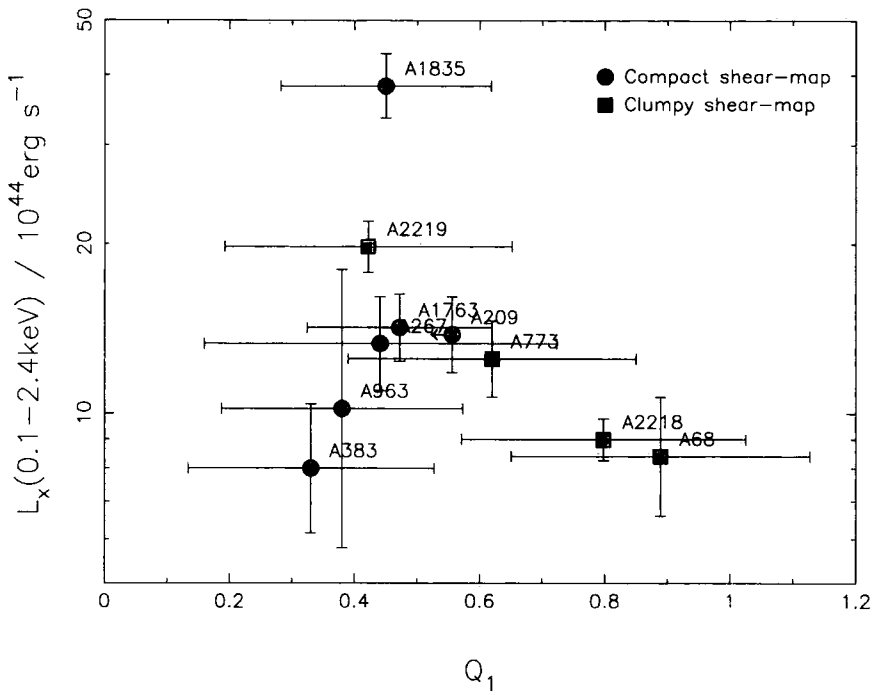

Figure 3.16: Mass dipole (arbitrary units) versus X-ray luminosity. The dipoles are computed directly from the ellipticity and orientation of individual faint background galaxies, using a discretised adaptation of the aperture moment method proposed by Schneider & Bartelmann (1997).

Galaxy-scale Mass Components

We include galaxy-scale mass components in our lens models down to the limit where the mass of additional components would be comparable with the uncertainties in the overall cluster mass. The mass typically enclosed by a multiple-image system in the central $\sim$ 50–100kpc of an X-ray luminous (i.e. $L_{\rm X}\sim 10^{45}$ erg s^{-1}) galaxy cluster at $z \sim 0.2$ is $\sim 10^{13}$ M$_\odot$, with a typical uncertainty (if constrained by a spectroscopic redshift) of a few per cent. We therefore only include cluster galaxies in our lens models if they have a mass $\gtrsim 10^{11}$ M$_\odot$, which assuming a K–band mass-to-light ratio of order unity (Bell & de Jong 2001) and $M_K^\star = -25.1$ (Cole et al. 2001) equates to a magnitude limit of $K \leq K^\star + 2.5$. Each lens model therefore contains galaxy-scale mass components from our cluster galaxy catalogues down to this limit. We list the number of galaxies in each cluster which satisfy this selection criterion in Table 3.1.

Summary

In this section we have used simple tools to design the "first-cut" lens models. Despite the simplicity of this approach and the relative sophistication of the detailed model fitting process, the analysis presented in this section is the first time that a homogeneous sample of X-ray luminous clusters have been classified on the basis of their mass morphology. Previous attempts at such classification have relied on the cluster X-ray morphology using relatively poor resolution data from satellites such as *ROSAT*. In contrast, our analysis exploits high spatial resolution *HST* data and employs gravitational lensing to probe directly the underlying mass distributions. The construction and optimisation of our lens models will quantify the structure of these clusters in significantly more detail, however it is striking that a large fraction (40%) of the clusters appear, from our analysis to date, to contain significant substructure, suggesting that dynamical activity may be common in massive clusters at $z \sim 0.2$. The detailed *HST* lens models and complementary analysis of *Chandra* data will enable us to test and quantify this preliminary assessment.

3.6.3 The Models

We use the strong- and weak-lensing information presented in Table 3.4 to constrain the lens models. We list the best-fit parameters of the lens models in Table 3.5, together with the χ^2 value and number of degrees of freedom (ν) for each best-fit model. We also estimate the 1–σ uncertainties in the model parameters using the standard $\Delta\chi^2$ technique. For each model, this involves varying each free-parameter in turn while allowing the other parameters to find their optimum values, and then re-computing the χ^2 value for each parameter set. The resulting regions of parameter space (i.e. for which $\Delta\chi^2 \leq 1$) are roughly equivalent to an uncertainty in image positions of $\sim 0.1''/\nu$ for the models constrained by multiple images and an uncertainty in mean tangential shear of $\langle\tau_{\rm u}\rangle/\nu$ for the models constrained by just weak shear information. We list these uncertainties in Table 3.5; those parameters for which we do not quote an uncertainty were not included as free-parameters in the model fits. We describe the construction of each cluster lens model below.

Table 3.5: Best-fit Parameters of the Lens Models

Cluster	Mass Component	ΔR.A.[a] (″)	ΔDec.[a] (″)	a/b	θ (deg)	$r_{\rm core}$ (kpc)	$r_{\rm cut}$ (kpc)	$\sigma_{\rm o}$ (km s^{-1})	χ^2/ν
				Individually Optimised Mass Components					
A 68	Clump #1	$-0.7^{+0.2}_{-0.2}$	$-1.1^{+0.2}_{-0.2}$	$2.1^{+0.2}_{-0.2}$	39^{+2}_{-2}	100^{+2}_{-2}	> 750	950^{+5}_{-5}	11.6/11
	Clump #2	−45.8	68.4	$1.2^{+0.3}_{-0.1}$	50^{+40}_{-20}	< 80	> 800	660^{+15}_{-15}	
	cD Galaxy	0.0	0.0	$1.7^{+0.5}_{-0.5}$	33^{+17}_{-23}	< 3	83^{+27}_{-13}	300^{+10}_{-10}	
A 209	Clump #1	0.0	0.0	1.9	43	50	1000	630^{+120}_{-100}	0.6/1
A 267	Clump #1	0.0	0.0	$2.0^{+0.4}_{-0.3}$	−60	115^{+15}_{-15}	1000	1060^{+40}_{-40}	3.6/3
A 383	Clump #1	$-0.3^{+0.1}_{-0.1}$	$0.5^{+0.1}_{-0.1}$	$1.13^{+0.05}_{-0.05}$	129^{+5}_{-5}	53^{+2}_{-2}	> 750	920^{+5}_{-5}	12.8/16
	cD galaxy	$-0.1^{+0.1}_{-0.1}$	$-0.3^{+0.1}_{-0.1}$	$1.07^{+0.09}_{-0.03}$	98^{+15}_{-10}	$0.5^{+1.5}_{-0.4}$	> 10	250^{+30}_{-20}	
A 773	Clump #1	0.0	0.0	1.9	−38	75	1000	750^{+60}_{-70}	3.6/3
	Clump #2	1.0	24.0	1.8	−10	75	1000	700^{+70}_{-100}	
	Clump #3	84.4	12.0	1.0	0	75	1000	550^{+75}_{-150}	
A 963	Clump #1	0.0	0.0	$1.7^{+0.1}_{-0.1}$	90^{+3}_{-3}	95^{+5}_{-5}	> 550	980^{+15}_{-15}	1.4/2
	cD galaxy	0.0	0.0	$1.1^{+0.1}_{-0.1}$	85^{+45}_{-35}	< 2	96^{+9}_{-6}	320^{+15}_{-15}	
A 1763	Clump #1	0.0	0.0	1.9	180	70	1000	700^{+120}_{-150}	5.1/3
A 1835	Clump #1	0.0	0.0	1.5	70	70	> 350	1210^{+80}_{-100}	0.7/1
A 2218	Clump #1	$0.2^{+0.1}_{-0.1}$	$0.5^{+0.1}_{-0.1}$	$1.2^{+0.1}_{-0.1}$	32^{+2}_{-2}	83^{+2}_{-2}	> 650	1070^{+5}_{-5}	17.8/19
	Clump #2	47.0	−49.4	$1.4^{+0.2}_{-0.1}$	53^{+15}_{-15}	57^{+10}_{-10}	> 400	580^{+15}_{-15}	
	Clump #3	16.1	−10.4	1.1	70	< 2	65^{+7}_{-7}	195^{+10}_{-10}	
	Clump #4	4.8	−20.9	1.4	−23	< 2	77^{+6}_{-8}	145^{+10}_{-10}	
	cD galaxy	$0.3^{+0.2}_{-0.2}$	$0.1^{+0.1}_{-0.1}$	$1.8^{+0.2}_{-0.1}$	53^{+14}_{-12}	< 3	136^{+20}_{-16}	270^{+7}_{-7}	
A 2219	Clump #1	$0.0^{+0.1}_{-0.1}$	$0.0^{+0.1}_{-0.1}$	$2.9^{+0.3}_{-1.1}$	32^{+2}_{-2}	86^{+3}_{-3}	> 600	1000^{+10}_{-10}	3.7/3
	Clump #2	39.2	−32.0	1.1	8	100^{+30}_{-20}	> 500	275^{+15}_{-15}	
	cD Galaxy	0.0	0.0	$1.6^{+0.6}_{-0.5}$	29^{+5}_{-5}	< 3	85^{+20}_{-5}	335^{+10}_{-10}	
				Luminosity Scaled Mass Components					
L_K^* galaxy		...	...	...	...	$0.2^{+0.1}_{-0.1}$	30^{+10}_{-5}	180^{+20}_{-20}	

[a] The position of each mass component is given relative to the optical centroid of the central galaxy in each cluster (Table 3.1). We also mark the positions of the cluster-scale mass components in Figs. 3.1–3.10.

A 68

We first attempted to fit a model containing just one cluster-scale mass component (#1); unsurprisingly, given the evidence for substructure in this system (§3.6.2), we were unable to obtain a satisfactory fit ($\chi^2/\nu \simeq 5$). We therefore added a second cluster-scale mass component (#2) to the North-West of the central galaxy. Despite the strong evidence for the presence of this mass component, no single bright cluster elliptical dominates the group of galaxies found in this region (Fig. 3.1). We also check Czoske's (2002) panoramic CFH12k imaging of this cluster to confirm that there is no dominant bright cluster galaxy lying just off the edge of the WFPC2 field of view. We therefore adopt the brightest of the available galaxies as the centre of clump #2.

The multiple-image systems detected close to the central galaxy place strong constraints on the absolute mass required in this second clump because the spatial configuration of the images is sensitive to the details of the bimodal mass structure of the cluster. In addition to tight constraints on the parameters of clump #1, we therefore also obtain a reasonably tight constraint on the velocity dispersion of clump #2. For the other parameters that describe clump #2, we must rely on the weak-shear which by definition does not probe the small scales required to place a tight constraint on $r_{\rm core}$. The proximity of clump #2 to the edge of the field of view of our *HST* observations also limits our ability to constrain its shape, resulting in quite weak constraints on a/b and θ. We also find that, in common with clump #1 and all of the other cluster-scale mass components in our models, we are only able to place a lower limit on $r_{\rm cut}$.

In contrast to the cluster-scale mass components, the smaller spatial scale of the central galaxy means that we can constrain $r_{\rm cut}$ for this mass component. We also experiment with a model that does not include a central galaxy, and in common with previous strong lensing studies (e.g. Kneib et al. 1996; Smith et al. 2001) we find that we cannot obtain a satisfactory fit without the inclusion of the central galaxy.

A 209

This is one of the least well constrained models because there are no confirmed multiples with which to calibrate the mass and no candidate systems with which to constrain the shape of the potential, and a relatively low signal-to-noise weak-shear signal. Nevertheless, we are able to use the weak-shear to constrain σ_o for the central (and only) cluster-scale mass component.

A 267

The important difference between this cluster and A 209 is that it contains a candidate multiple-image pair (E2a/b). In addition to constraining σ_o and r_{core} for the central cluster-scale mass component we therefore use this image pair to constrain the shape of the potential.

A 383

We use the many constraints available for this cluster to determine precisely the full range of geometrical and dynamical parameters for the cluster-scale and central galaxy mass components. Despite the overall relaxed appearance of this cluster, substructure plays a crucial role in producing the observed multiple-images. The bright cluster elliptical South-West of the central galaxy actually renders this a bi-modal cluster (albeit with very unequal masses) on small scales. This structure is crucial to the geometrical properties of the B1a/b/c and B4a/b/c systems. The cluster-scale mass component is also not circular in projection; without this departure from circular symmetry in the projected mass distribution, the radial and tangential arcs would lie directly opposite each other and not offset in the manner observed (see typical multiple-image configurations in Fig. 2.6). As explained above in connection with A 68, we also tested the need for a central galaxy mass component in this model by trying to fit a model without a central galaxy. We found that this was not possible because such a model could not simultaneously satisfy the constraint on the slope of the mass profile provided by the radial arcs and the need for a sufficiently large core radius in the cluster-scale mass component required to produce the radial arcs (e.g. Mellier et al. 1993).

A 773

Although we have not identified any multiple-image systems in this cluster, the large number of elliptical galaxies and the strength of the weak-shear signal suggest that this cluster is probably quite massive. First we use the mean tangential shear (Table 3.4) to constrain a model that contains a single cluster-scale mass component centred on the brightest cluster elliptical (clump #1). The best-fit velocity dispersion of clump #1 in this model is $\sim$ 1000 $\mathrm{km\,s^{-1}}$. Although this model is an acceptable fit, it does not reproduce the spatial variation of the shear signal. Specifically, it cannot reproduce the strong shear signal observed to the North of the second brightest cluster galaxy and to the East of clump #1, i.e. in the saddle region between clump #1 and the group of cluster ellipticals at the Eastern extreme of the field of view. We interpret these residuals as evidence for substructure in the cluster potential and introduce two more cluster-scale mass components into the model: clump #2 is coincident with the second brightest cluster elliptical and clump #3 coincides with the brightest member of the Eastern group of galaxies. We constrain this model using both the overall mean tangential shear and the mean shear computed in two $30'' \times 30''$ sub-fields, each co-located with the residuals described above. This model faithfully reproduces the mean observed shear, however it also reproduces the spatial variation of the shear and thus provides a superior description of the cluster potential than the initial simple model.

A 963

The H0 multiple-image system provides a straightforward yet powerful constraint on the potential of this compact cluster. However in contrast to the situation in A 383, this constraint is insufficient to obtain detailed constraints on the position of the central galaxy and cluster-scale mass components. We therefore adopt the optical centroid of the central galaxy as the position of these two mass components. We note that the offset of such mass components from the position of the optical centroid in clusters such as A 383 and A 2218 are $\lesssim 1''$; we therefore expect that our adoption of the optical centroid as the centre of mass to be a valid assumption.

A 1763

This cluster is similar to A 209 in that there are no confirmed or candidate multiple-image systems and the weak-shear signal is relatively low (Table 3.4). We therefore fit a model that contains the velocity dispersion of the (single) cluster-scale mass component as the only free-parameter. Overall, this simple model is an acceptable fit to the weak shear data, however it fails to reproduce the large observed shear signal to the West of the central galaxy (Fig. 3.7). We interpret these residuals as a signature of substructure in this cluster. Unfortunately the weak-shear signal is not strong enough to place any further constraints on this cluster.

A 1835

The large observed shear signal (Table 3.4) in A 1835 indicates that this is a very massive cluster. However, the absence of any confirmed multiple-image constraints means that the model is no more sophisticated than those of A 209 and A 1763. We therefore include just one free parameter in the model of this cluster, the velocity dispersion of the central cluster-scale mass component.

A 2218

Dr. Jean-Paul Kneib constructed the model of this cluster. It builds on the models published by Kneib et al. (1995; 1996) and incorporates for the first time the spectroscopic redshifts of the M2 and M3 multiple-image systems. The numerous constraints available for this cluster (Table 3.4) enable a more extensive list of free-parameters to be included in this model. In addition to the central cluster-scale mass component (clump #1), this model contains a cluster-scale mass component (clump #2) centred on the second brightest cluster galaxy which lies South-East of the optical centre of the cluster. The velocity dispersion and cut-off radius of the two bright cluster ellipticals (clumps #3 & #4) that lie adjacent to the M0 multiple-image system are also included as free-parameters.

A 2219

We approach this cluster in much the same manner as A 68. We first attempt to find an acceptable solution that is based on a single cluster-scale mass component centred on the central cluster galaxy. The main problem with this model is that it cannot reproduce the very straight morphology of P1a/b (Fig. 3.10). We therefore add a second cluster-scale mass component (clump #2) at the position of the second brightest cluster elliptical (South-East of the central galaxy). In contrast to A 68, the constraints on clump #2 are weaker and we therefore are forced to adopt the shape and orientation of the co-located cluster galaxy for this mass component. Nevertheless, the model faithfully reproduces the observables and we are able to constrain the mass of both cluster-scale clumps and the central galaxy.

The objective of this modelling exercise is to measure the mass and substructure of the clusters in our sample using gravitational lensing. Inevitably, the goodness of fit of the lens models depends on the quality of the constraints available for each cluster. Nevertheless, our models place statistically acceptable constraints on the mass of each cluster, and in all but one cluster (A 1763), we have sufficient data to both identify the need for (or not) and constrain the parameters of additional cluster-scale mass components. In §3.6.4 we apply three independent tests, including a comparison with previous studies, to further validate the robustness of our models.

3.6.4 Model Tests

First we test the ability of the models to reproduce the observed multiple-image statistics; second we search for systematic uncertainties in the models that have been constrained using just weak-shear information; finally we compare our results with independent analyses of the clusters in the literature.

Multiple-image Statistics

We quantify the frequency of multiple-imaging in our cluster sample. First, we define a simple selection criterion for our observational measurement: we count the

number of multiple-image systems for which at least one image has $R_{702} \leq 23$. This translates into a requirement that the multiple-image system must be accessible to targeted spectroscopic observations with a 10–m class telescope. Another, more immediate benefit of this selection criterion is that these brighter multiple-images are easier to identify than those that lie closer to the detection threshold of the data, and thus our multiple-image catalogue is less likely to suffer from significant incompleteness. The number of multiple-image systems that fulfil this criterion comprises those listed in Table 3.2, excluding M2a/b, plus several images for which successful spectroscopic observations have yet to be achieved. For example, these additional multiple-image systems include the B2 and B3 systems in A 383 (§4.2), but exclude all of K0, K1, K2 and K4 in A 1835 as they are either too faint, or they appear to be singly-imaged (§3.4; Fig. 3.8). In total, 13 multiple-image systems fulfill our selection criterion. Attaching a simple Poisson uncertainty, and dividing by the number of clusters, gives us a crude probability of detecting a spectroscopically accessible multiple-image system of 1.3 ± 0.4 per cluster. This statistic masks significant cluster-to-cluster variations: 50% of our cluster sample contain no spectroscopically accessible multiple-images; the 50% of our sample that do contain multiple images are split roughly equally between those containing one multiple-image system, and those that contain more than one such system.

We test whether our suite of detailed lens models can reproduce the observed frequency of multiple-imaging using Monte Carlo simulations. We construct a number of artificial galaxy catalogues and ray trace the galaxies that they contain through our suite of best-fit lens models. These catalogues match the HDF-N redshift and magnitude distributions (Fernández-Soto et al. 1999). In total we ray-trace 10^7 artificial background galaxies through the lens models. These simulations produce 14.3 ± 0.3 multiple-image systems that satisfy our selection criterion, which translates to 1.43 ± 0.03 per cluster, in good agreement with the observations. We therefore conclude that, as an ensemble, the lens models describe accurately the distribution of mass in the central regions of the clusters.

Calibration of Weak-shear Constrained Models

We investigate the systematic uncertainties that may arise as a result of calibrating some cluster lens models using just the weak-shear signal.

First, we focus on the five clusters for which both multiple-image and weak-shear constraints are available (A 68, A 383, A 963, A 2218, A 2219). We ignore the multiple-image constraints and construct a model of each of these clusters using just the weak-shear information. In common with the five lens models that are based solely on weak-shear constraints (A 209, A 267, A 773, A 1763, A 1835) we find that the weak-shear signal can only constrain one free-parameter (σ_o) per cluster-scale mass component. Individually, the velocity dispersions of the cluster-scale mass components in the weak-shear constrained models agree within the uncertainties with the velocity dispersions obtained in the multiple-image constrained models. However, when treated as a sample, there appears to be a small systematic offset; the mean ratio of weak-shear constrained velocity dispersion to multiple-image constrained velocity dispersion is 0.94 ± 0.04. Based on just five clusters, it therefore appears that σ_o for the cluster-scale mass components in the models of weak-shear only clusters may be under-estimated, on average, by $\sim 6\%$. Cluster mass scales as the square of σ_o; this possible systematic error in σ_o therefore translates into a possible $\sim 12\%$ under-estimate in cluster mass. We choose not to correct the parameters of weak-shear constrained models for this effect because the uncertainties in these models are dominated by the statistical uncertainty which is typically $\Delta\,\sigma_o \sim$ 10–20%. However, we assess critically the impact of this possible systematic effect on the results that we obtain in §3.7.

We also note that, when the multiple-image-constrained clusters are incorporated in our analysis, the average systematic offset in mass for the whole sample is just $\sim 6\%$. We compare this offset with that expected if the background galaxy catalogues are contaminated by cluster galaxies at the $\sim 20\%$ level (§3.3.1). In summary, because the contaminant galaxies would have random orientations on the sky, they would reduce the measured mean shear of each cluster by $\sim 20\%$, and thus reduce the mass estimates based on the weakly-sheared galaxies by the same fraction. Again, this fraction falls to $\sim 10\%$ for the whole sample when the

multiple-image-constrained clusters are taken into account. It is therefore appears that we may have slightly overestimated the contamination rate in §3.3.1.

Comparison with the Previous Studies

Finally, we compare the best-fit values of σ_o with the parametrised weak-lensing models of Dahle et al. (2002a). Dahle et al. used ground-based wide-field imaging of 38 X-ray luminous clusters including eight of our sample (A 68, A 209, A 267, A 773, A 963, A 1763, A 1835, A 2219) to study the weak-shear signal on scales of $\sim 20'$ (i.e. linear scales $10\times$ larger than our *HST* data). They fit a singular isothermal shear profile to the radially binned weak shear measurements for their cluster sample, and they list the best-fit velocity dispersion for each cluster. The median velocity dispersion on Dahle et al.'s models is (1005 ± 100) $\mathrm{km\,s^{-1}}$ where the error bar is estimated by bootstrap resampling. We calculate the same statistic for our lens models, adding the velocity dispersion of the multiple cluster-scale mass components in the clumpy clusters in quadrature. We obtain a median velocity dispersion for these eight clusters from our models of (1050 ± 75) $\mathrm{km\,s^{-1}}$, in good agreement with Dahle et al.'s models. This brief comparison of our model parameters with a completely independent analysis adds to the body of evidence that our models are an accurate representation of the mass and structure of the clusters in our sample.

3.7 Results

3.7.1 Mass and Substructure Measurements

We begin by measuring the mass and structure of each cluster using the suite of detailed lens models constructed in §3.6.3. Each best-fit model specifies the parameters of an analytic mass distribution; we therefore use these parameters to compute a map of the projected mass in each cluster within the *HST* field of view. We extract the mass and substructure measurements described in this section directly from these maps. We present the projected mass enclosed by each multiple-image constraint in Table 3.6, together with the projected mass within a fixed projected radius of $r = 500$ kpc. We also compare the total projected mass

of each cluster, $M_{\rm tot}$ =$M(r \leq 500$ kpc), with the projected mass within this radius that is not associated with the main cluster mass component, i.e. the amount of substructure, $M_{\rm sub}$. We present these measurements in Table 3.6.

The most striking aspect of these measurements is the large number of clusters that contain significant substructure; six of the ten clusters contain at least 10% substructure. This is the first time that such detailed and precise measurements of the *mass* structure of galaxy clusters have been made. This result confirms and indeed strengthens our conclusions from the weak-shear maps and dipole mass measurements in §3.6.2 that a large fraction of X-ray luminous clusters are dynamically active at $z \sim 0.2$. We classify the clusters into compact clusters with $M_{\rm sub}$ / $M_{\rm tot}$< 0.1 (A 267, A 383, A 963, A 1835) and clumpy clusters with $M_{\rm sub}$ / $M_{\rm tot}\geq$ 0.1 (A 68, A 209, A 773, A 1763, A 2218, A 2219). We note that two clusters (A 209, A 1763) that were formerly classified as compact based on their weak-shear map and mass dipole measurements are now classified as clumpy, although they lie very close to the (somewhat arbitrary) dividing line between the two sub-samples. This clumpy classification therefore suggests that these two clusters may be dynamically active in ways that are not apparent from the optical data alone. We return to these two clusters in §3.8.

3.7.2 Mass and Substructure versus X-ray Luminosity

We use our measurements of cluster mass and substructure to investigate the scatter in the cluster mass-luminosity relation. We plot our cluster mass and substructure measurements against the *ROSAT* X-ray luminosities that were used to select our cluster sample in Fig. 3.17. We noted in §1.6 and it is clear from Fig. 3.17 that A 1835 is an outlier within our sample, due to its extremely high X-ray luminosity*. We therefore conservatively exclude this cluster from the following calculations to avoid our results being dominated a single cluster with extreme properties.

First, we calculate the mean X-ray luminosity: $\langle L_{\rm X} \rangle = (12.1 \pm 3.7) \times 10^{44}$(0.1–2.4 keV) erg s^{-1}†, where the quoted uncertainty is the rms dispersion. We also

*The high X-ray luminosity of A 1835 is boosted by the cooling flow that dominates the X-ray emission from the central regions of this compact cluster.

†These calculations use the X-ray luminosities from the parent XBACs catalogue (Ebeling et

Table 3.6: Cluster Mass and Substructure Measurements

Cluster	Multiple-Image Constraint		Fixed Aperture($r \leq 500$ kpc)		Scaled Aperture	
	$r_{\rm mult}$	$M(r \leq r_{\rm mult})$	$M_{\rm tot}$	$M_{\rm sub}$ / $M_{\rm tot}$ [a]	$r^{b}_{\rm scaled}$	$M(r \leq r_{\rm scaled})$
	(kpc)	(10^{13} $M_\odot$)	(10^{14} $M_\odot$)		(Mpc)	(10^{14} $M_\odot$)
A 68	40	1.13 ± 0.04	4.4 ± 0.1	0.32 ± 0.01	0.50 ± 0.02	4.5 ± 0.3
A 209	...	...	1.6 ± 0.5	0.13 ± 0.06	0.21 ± 0.04	0.8 ± 0.3
A 267	...	...	2.6 ± 0.4	0.04 ± 0.01	0.31 ± 0.04	1.7 ± 0.3
A 383	65	3.47 ± 0.08	3.6 ± 0.1	0.03 ± 0.001	0.37 ± 0.04	2.8 ± 0.3
A 773	...	...	5.1 ± 1.2	0.59 ± 0.20	0.52 ± 0.11	5.3 ± 1.2
A 963	52	2.06 ± 0.05	3.3 ± 0.2	0.03 ± 0.003	0.36 ± 0.04	2.5 ± 0.2
A 1763	...	...	2.1 ± 0.8	0.10 ± 0.05	0.25 ± 0.03	1.1 ± 0.2
A 1835	...	...	5.8 ± 1.1	0.03 ± 0.01	0.51 ± 0.03	5.9 ± 1.1
A 2218	82	7.73 ± 0.15	5.6 ± 0.1	0.23 ± 0.01	0.49 ± 0.03	5.5 ± 0.1
A 2219	83	4.21 ± 0.06	3.4 ± 0.1	0.15 ± 0.01	0.36 ± 0.04	2.6 ± 0.2

[a] $M_{\rm sub}$ is the mass that resides in mass components other than the central mass component (§3.7.1).

[b] $r_{\rm scaled}$ is the projected radius within which the projected total mass density exceeds 2.9×10^8 $M_\odot$ (§3.7.3).

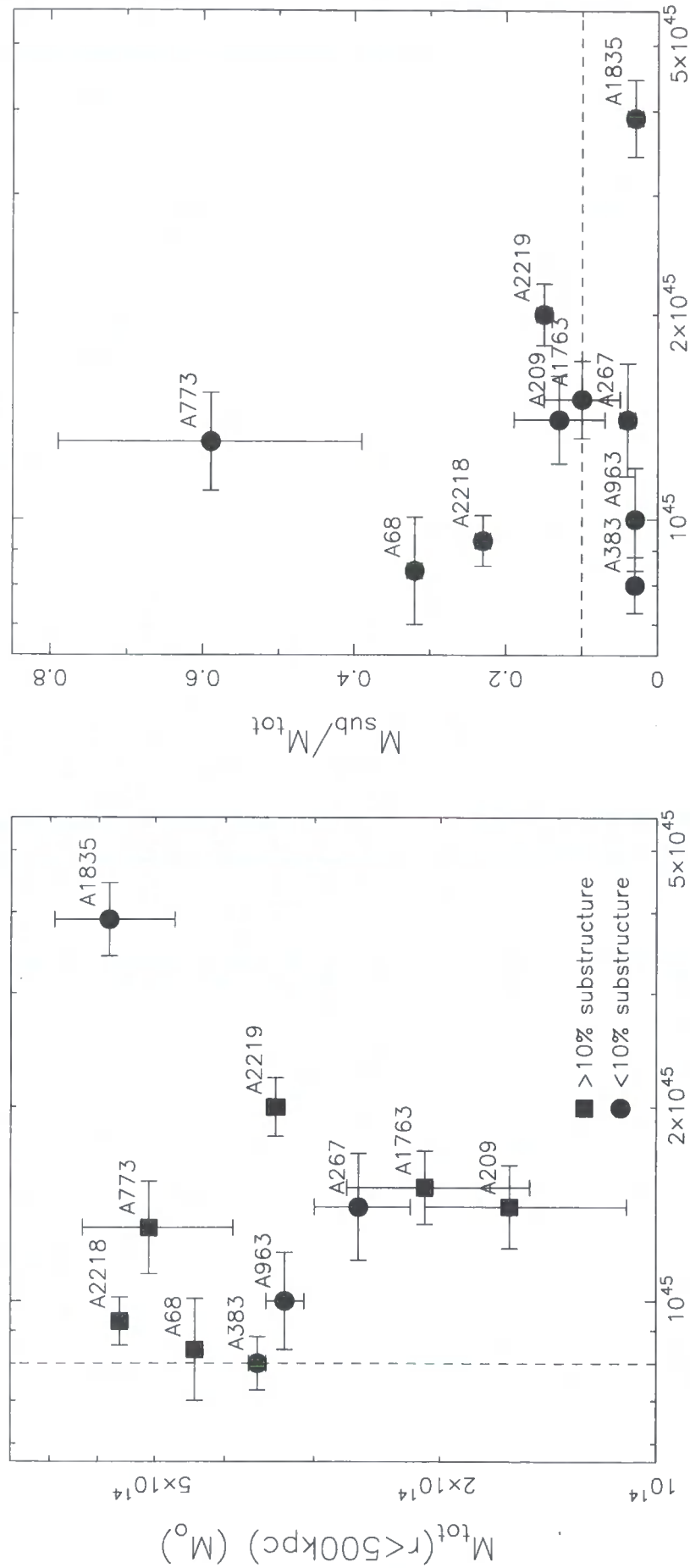

Figure 3.17: Cluster mass and substructure versus X-ray luminosity of our cluster sample. LEFT: We plot the projected mass within a fixed projected radius of $r \leq 500$ kpc. The dashed line marks the $L_X \geq 8 \times 10^{44}$(0.1–2.4 keV) erg s^{-1} selection criteria used to construct our sample from the XBACs sample (Ebeling et al. 1996). RIGHT: We plot the cluster substructure versus X-ray luminosity. The substructure fraction (M_{sub} / M_{tot}) measures the amount of mass that is not associated with the dominant central mass component as a fraction of the total projected mass within the $r \leq 500$ kpc aperture. The dashed line marks M_{sub} / M_{tot} = 0.1 which we use to split our sample into two groups: compact and clumpy systems.

express the dispersion as a fraction of the mean luminosity: $\sigma_{L_X}/\langle L_X \rangle = 0.31$. Observational analyses that assume hydrostatic equilibrium between the X-ray gas and the cluster potential well (e.g. Edge & Stewart 1991; Mushotzky & Scharf 1997; Nevalainen, Markevitch & Forman 2000; Finoguenov, Reiprich & Böhringer 2001; Reiprich & Böhringer 2002) find that $L_X \propto {M_{tot}}^2$. If this relationship holds in cluster cores, then we should find $\sigma_{L_X}/\langle L_X \rangle = 2\sigma_{M_{tot}}/\langle M_{tot} \rangle$, and we would therefore expect that the mass dispersion should be half the X-ray luminosity dispersion, i.e. $\sigma_{M_{tot}}/\langle M_{tot} \rangle = 0.15$. In contrast we find that the mean cluster mass and dispersion around this mean are: $\langle M_{tot} \rangle = (3.5 \pm 1.3) \times 10^{14}$ $M_\odot$ and $\sigma_{M_{tot}}/\langle M_{tot} \rangle = 0.37$. The mass dispersion is therefore 2.5× larger than would be expected if the cluster cores were in hydrostatic equilibrium.

To investigate this further, we split our sample into compact (M_{sub} / M_{tot}< 0.1) and clumpy (M_{sub} / M_{tot}≥ 0.1) systems. We find that $\langle M_{tot} \rangle_{<0.1} = (3.2 \pm 0.5) \times 10^{14}$ $M_\odot$, $\sigma_{M_{tot}}/\langle M_{tot} \rangle_{<0.1} = 0.15$ and $\langle M_{tot} \rangle_{>0.1} = (3.7 \pm 1.6) \times 10^{14}$ $M_\odot$, $\sigma_{M_{tot}}/\langle M_{tot} \rangle_{>0.1} = 0.43$. The compact clusters therefore have a mass dispersion that is consistent with the assumption of hydrostatic equilibrium, and the mass dispersion of the clumpy clusters is ∼ 3× times that of the compact clusters. This result is consistent with those of Allen (1998) who concluded that the breakdown of hydrostatic equilibrium in cluster cores due to dynamical activity was at least partly responsible for the discrepancy between lensing and X-ray based cluster mass estimates. However, in contrast to Allen's analysis of lensing clusters for which X-ray data were available, we have studied an objectively selected sample of X-ray luminous systems at a well-defined epoch. Our lens models are also significantly more sophisticated than Allen's simple lensing analysis and reliance on X-ray morphology as a qualitative indicator of cluster structure. This is therefore the first time that the scatter in the cluster mass-luminosity relation has been measured reliably.

al. 1996). Dr. Pasquale Mazzotta also measured the X-ray luminosity of the clusters using the *Chandra* data listed in Table 3.5.1. The scatter in these measurements is comparable with those based on the *ROSAT* data. We therefore use the *ROSAT* data to maintain consistency with the parent catalogue.

3.7.3 Mass Versus X-ray Temperature

Simple models of structure formation that incorporate solely gravitational physics predict that galaxy clusters are a self-similar family of objects and that their global properties such as temperature and X-ray luminosity are related to the cluster mass through simple scaling relations (Kaiser 1986; Navarro, Frenk & White 1997; Teyssier et al. 1997; Eke et al. 1998; Bryan & Norman 1998). In these models, self-similarity applies to both the dark matter and hot X-ray gas components, thus application of the virial theorem yields the following cluster scaling relations:

$$\begin{aligned} M_\delta &\propto T^{3/2}(1+z)^{-3/2} \\ R_\delta &\propto T^{1/2}(1+z)^{-3/2} \end{aligned} \tag{3.3}$$

where M_δ is the total mass within the sphere of radius R_δ corresponding to a mean over-density (relative to the critical density $\rho_c(z)$ at that redshift z) of δ and T is the cluster temperature. Comparison of these predictions, specifically in this context the mass-temperature relation, with observations can provide important insights into the role that non-gravitational physics plays in cluster formation and evolution.

The mass-temperature relation is a crucial step in many cosmological studies of galaxy clusters (e.g. Eke, Cole & Frenk 1996; Viana & Liddle 1996; Bahcall, Fan & Cen 1997; Kay & Bower 1999), as it provides the link between the cluster temperature and mass functions. Observationally, this relation has been constrained primarily using X-ray observations of galaxy clusters (e.g. Markevitch 1998; Nevalainen, Markevitch & Forman 2000; Finoguenov, Reiprich & Böhringer 2001; ASF; Reiprich & Böhringer 2002), and assuming spherical symmetry and hydrostatic equilibrium. Numerical simulations (e.g. Evrard, Metzler & Navarro 1996) have also been used to calibrate the normalisation and scatter around this relation.

X-ray observations and the theoretical predictions generally agree on two things: the existence of a power-law relationship between cluster mass and temperature and the slope of the relationship for massive systems, $\alpha = 1.5$ where $M \propto T^\alpha$. However important differences between theory and observation remain unresolved and crucial aspects of the theory remain untested. Principal among these outstanding points

are the normalisation of and scatter around the mass-temperature relation, which probe directly the depth of the potential well in a cluster of a given mass and the amplitude of any non-gravitational effects. In striving to address these issues, the fundamental limitation of the all the theoretical and observational analyses to date is that both assume that the ICM is in hydrostatic equilibrium with the gravitational potential of the cluster (e.g. Voit et al. 2002). There is therefore an urgent need to study the mass-temperature relation in a manner that is free from assumption about the physical nature and thermodynamic history of the cluster matter. Our lensing survey of X-ray luminous clusters is an ideal opportunity to do this.

We re-measure the projected mass of each cluster, this time measuring the mass of each cluster down to a fixed iso-density contour; this has the effect of scaling the aperture used for each cluster with its mass, in a manner analogous to measuring three-dimensional cluster masses (M_{δ}) down to a fixed density contrast over the critical density of the Universe. For this purpose we select the iso-density contour at $\Sigma = 2.9 \times 10^{8}$ $\mathrm{M_{\odot}kpc^{-2}}$, as this ensures that none of the mass measurements involve very much extrapolation beyond the field of view of our *HST* observations. We use the lens model of each cluster to measure $r_{\mathrm{scaled}} = r(\Sigma = 2.9{\times}10^{8}\ \mathrm{M_{\odot}kpc^{-2}})$, and then measure $M(r \leq r_{\mathrm{scaled}})$. We present these mass measurements in Table 3.6 and plot them against $T_{\mathrm{X,tot}}$ from §3.5.1 in Fig. 3.18. We note that the temperatures of only A 383 and A 1835 differ significantly depending on whether the central $r <$ 100 kpc region is excised from the spectral fit (see §3.5.1 for more details).

The most striking feature of Fig. 3.18 is the degree of scatter between the various clusters. To investigate this scatter, we divide the clusters into the compact and clumpy sub-samples based on the substructure fractions measured in §3.7.1. The mean temperature of the compact and clumpy clusters are $\langle T_{\mathrm{X,tot}} \rangle = 6.3 \pm 0.8$ keV and $\langle T_{\mathrm{X,tot}} \rangle = 9.2 \pm 1.3$ keV respectively. The clumpy clusters therefore appear to be systematically hotter than the compact clusters. However, if we take account of the negative temperature gradient in the centre of the two compact clusters that contain a cooling flow (A 383 and A 1835; §3.5.1), and recompute the mean temperature of the compact clusters, we obtain $\langle T_{\mathrm{X,ann}} \rangle = 6.9 \pm 0.9$ keV. Whilst this correction reduces the statistical significance of the difference between the two clus-

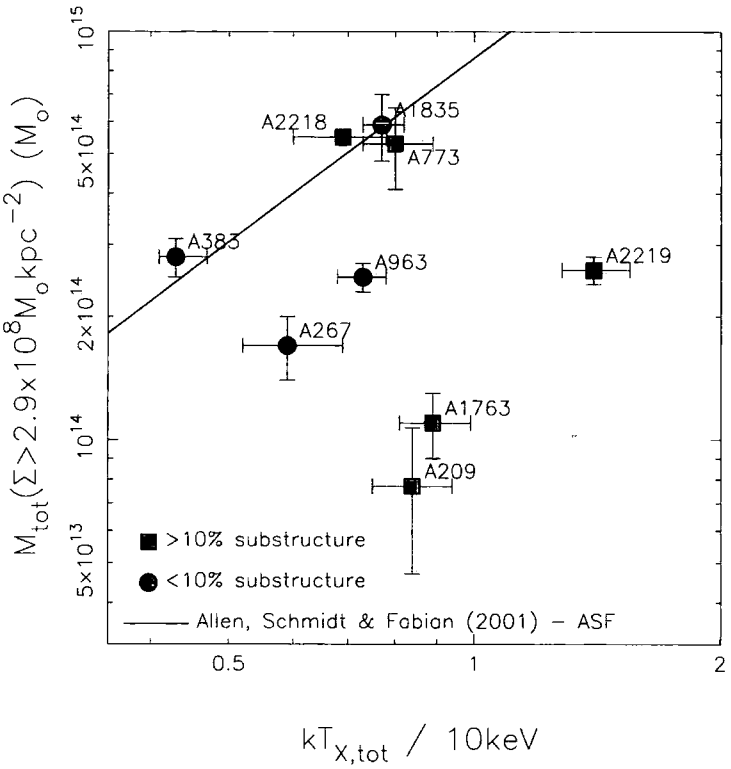

Figure 3.18: Projected mass within the $\Sigma = 2.9 \times 10^8$ $M_\odot kpc^{-2}$ iso-density contour versus X-ray temperature measured within a projected annulus of $0.1 \leq r \leq 2$ Mpc. The line shows the empirical mass-temperature relation recently derived by Allen, Schmidt & Fabian (2001) for a sample of relaxed cooling flow clusters. The two cooling flow clusters in our sample agree with this relation, and most of the non-cooling flow clusters do not. We interpret this is as evidence that dynamical activity in these clusters boosts the temperature of the ICM.

ter populations, we conclude that the clumpy clusters are hotter than the compact clusters by $\sim 25\%$. We also calculate the mean cluster mass of each sub-sample: $\langle M_{\rm tot} \rangle = (3.2 \pm 0.9) \times 10^{14}$ $M_\odot$ and $\langle M_{\rm tot} \rangle = (3.1 \pm 1.0) \times 10^{14}$ $M_\odot$ for the compact and clumpy clusters respectively. We also re-calculate these quantities assuming that the mass measurements of the cluster lens models that are constrained by just the weak-shear signal are under-stated by $\sim 12\%$ on average. We obtain $\langle M_{\rm tot} \rangle = (3.5 \pm 1.1) \times 10^{14}$ $M_\odot$ and $\langle M_{\rm tot} \rangle = (3.2 \pm 1.1) \times 10^{14}$ $M_\odot$ for the compact and clumpy clusters respectively. We therefore conclude that the mean mass of the clumpy and compact clusters are consistent within the errors and that any possible slight under-estimation of the mass of the less well constrained clusters does not affect this result.

We also plot a projected version of the mass-temperature relation recently obtained by ASF from a sample of relaxed cooling flow clusters observed with *Chandra*

This relation is based on measurements of M_{2500}, which is the mass enclosed within an iso-density contrast of $2500\rho_c$, where ρ_c is the critical density required to close the Universe. We check the cluster radii corresponding to $\rho = 2500\rho_c$ within which ASF made their mass measurements and confirm that they are broadly consistent with our measurements of $r_{\rm scaled}$. Four of the clusters agree with the ASF relation within the errors: two compact clusters that are also cooling flow systems (A 383 and A 1835) and the two most massive clumpy clusters (A 773 and A 2218). The agreement of the two cooling flow clusters with the ASF relation is a useful cross-check of our analysis and confirms that the locus of the most relaxed clusters in Fig. 3.18 is at the cold and massive extreme. Most of the non-cooling flow clusters lie to the right of this locus; intriguingly, A 773 and A 2218 do not. Both of these clusters are extreme systems within the sample: A 2218 contains the most spectacular multiple-image systems, and A 773 is dominated by a very large fraction of early-type galaxies (Balogh et al. 2002a). We discuss possible explanations for the position of A 773 and A 2218 in mass-temperature space in §3.8.

In summary, clumpy clusters are on average 25% hotter than compact clusters at a fixed mass. Whilst comparison of this result with detailed theoretical modelling is beyond the scope of the current work, we illustrate the potential power of this and future gravitational lensing studies of larger cluster samples to constrain the normalisation of the matter power spectrum in §4.4.

3.8 Discussion

In this chapter we have used gravitational lensing to study the distribution of mass in X-ray luminous galaxy clusters. The structure of galaxy clusters is expected to be dominated on most scales by dark matter, and so to first order our lens models probe the projected distribution of dark matter in these systems. We complement our gravitational lensing study with analysis of the X-ray and optical morphologies of the clusters (§3.5.3; §3.2). These analyses probe the distribution of baryons in the clusters in the form of hot intra-cluster gas and stars respectively. Our dataset therefore comprises key information about the three principle components

of galaxy clusters: dark matter, gas and stars. We summarise in Table 3.7 a number of indicators of cluster substructure from earlier sections of this chapter.

We use the substructure fractions measured in §3.7.1 to divide the clusters into compact ($M_{\rm sub}$ / $M_{\rm tot}$< 0.1) and clumpy ($M_{\rm sub}$ / $M_{\rm tot}\geq$ 0.1) systems. We discuss properties of the clusters in these two populations and assess the diversity of each population.

3.8.1 Compact Clusters

We first discuss the four compact clusters: A 267, A 383, A 963 and A 1835.

A 267

Our lens model of this cluster contains a single cluster-scale mass component (Table 3.5) and has a very low substructure fraction (Table 3.7). However, A 267 differs from the other compact systems in that its X-ray peak is offset from the central galaxy and the centre of mass of the total matter distribution (Table 3.7; Fig. 3.14) by $(22 \pm 1)''$. A 267 also contains an extremely elliptical central galaxy and central cluster-scale mass component (Table 3.5 and Figs. 3.3). The major axes of both the central galaxy and the central mass component in the lens model point towards the X-ray peak, suggesting that there is a connection between the central galaxy morphology and the origin of the offset X-ray peak. This connection could be a merger event, in which case the X-ray peak could be caused by shock-heating of or bulk-motions within the ICM, rather than excess mass at this position. This is supported by the mass-temperature relation presented in Table 3.18, which reveals that A 267 is hotter than would be expected purely from its mass and self-similar scaling relations. The shear-field of this cluster (Figs. 3.3) is also consistent with the merger hypothesis, because the shear vectors are not perturbed from tangential alignment around the mass centre of the cluster in the vicinity of the X-ray peak.

Dahle et al. (2002a) constructed a weak-lensing mass map of this cluster and concluded that it is a relaxed cluster. However, their mass map reveals an elongated mass morphology that is consistent with our lens model. There also appears to be a mass over-density $\sim 3'$ North-North-East of the cluster centre (i.e. in the same

Table 3.7: Summary of Cluster Substructure Indicators

Cluster	Optical (§3.2)	X-ray (§3.5.3)			Gravitational Lensing (§3.7)		
	Morphology	Morphology	$\Delta r_{\rm peak}$ ($''$)[a]	$T_{\rm X,tot}$ / $T_{\rm X,ann}$	Morphology	$N_{\rm clus}$[b]	$M_{\rm sub}$ / $M_{\rm tot}$
A 68	Clumpy	Clumpy	...	...	Clumpy	2	0.32 ± 0.01
A 209	Compact	Clumpy	4 ± 1	0.97 ± 0.16	Clumpy	1	0.13 ± 0.06
A 267	Compact	Clumpy	22 ± 1	0.98 ± 0.23	Compact	1	0.04 ± 0.01
A 383	Compact	Compact	< 1	0.83 ± 0.07	Compact	1	0.03 ± 0.001
A 773	Clumpy	Clumpy	10 ± 2	0.98 ± 0.15	Clumpy	3	0.59 ± 0.20
A 963	Compact	Compact	< 1	1.01 ± 0.11	Compact	1	0.03 ± 0.003
A 1763	Compact	Clumpy	...	...	Clumpy	1	0.10 ± 0.05
A 1835	Compact	Compact	< 1	0.83 ± 0.10	Compact	1	0.03 ± 0.01
A 2218	Clumpy	Clumpy	10 ± 2	1.01 ± 0.20	Clumpy	2	0.23 ± 0.01
A 2219	Clumpy	Clumpy	3 ± 1	1.01 ± 0.14	Clumpy	2	0.15 ± 0.01

[a] $\Delta r_{\rm peak}$ is the offset between the peak of the X-ray emission and the peak of the mass map derived from our detailed lens models. The 2–σ upper limits are based conservatively on the alignment of the X-ray and optical frames to a 1–σ rms accuracy of $\sim 0.5''$ (§3.5.1). The error bars are 1–σ.

[b] $N_{\rm clus}$ is the number of cluster-scale mass components contained in each lens model.

direction as the major axis of the central galaxy and the X-ray-optical peak offset) which may be associated with merger activity in this cluster. Whilst we treat the weak-lensing mass maps with caution, they do appear to support the idea that A 267 is a dynamically active cluster.

A 383

This cluster satisfies our definition of a cooling flow cluster (§3.5.1; Smith et al. 2001) and we confirm that there is a steep temperature gradient in the core of this very relaxed system ($T_{\rm X,tot}$ / $T_{\rm X,ann}$= 0.8 ± 0.1). The radial arcs that we detect in the centre of A 383 also enable us to place tight constraints on the radial distribution and geometrical shape (projected on the sky) of the central dominant dark matter halo in this cluster. We explore and quantify these constraints and assess their impact on currently popular cosmological models in §4.

A 963

In common with A 267 and in contrast to both A 383 and A 1835, this cluster has a temperature ratio that is consistent with unity and therefore appears to be the less dynamically mature than the two cooling flow systems. This is consistent with *ROSAT* analysis which classified A 963 as being intermediate between the extreme cooling flow systems and the extremely irregular systems (e.g. Allen 1998; Rizza et al. 1998). The small substructure fraction in this cluster together with the relatively smooth X-ray contours and alignment of the X-ray and mass peaks imply that A 963 (Fig. 3.14) is at a relatively advanced stage of relaxation, possibly following previous merger activity.

A 1835

This is one of the most intensively studied cooling flow clusters (e.g. Peterson et al. 2001; Fabian et al. 2001; Schmidt et al. 2001; Majerowicz et al. 2002; Voigt et al. 2002; Markevitch 2002). We confirm the relaxed nature of this cluster and the presence of cooler material on projected scales of $r \leq 100$ kpc ($T_{\rm X,tot}$ / $T_{\rm X,ann}$= 0.8 ± 0.1). Of most relevance to the current work is the study of Schmidt et al.

(2001). Schmidt et al. use both X-ray and lensing data to measure the mass of this cluster, and claim that these two independent analyses yield consistent results, although they do not publish a mass measurement for each method. Nevertheless, A 1835 appears to be a very relaxed system, and Allen (1998) showed that X-ray and lensing mass estimates should agree providing the cooling flow is properly taken into account in the X-ray modelling.

As Schmidt et al. concede, their lensing analysis is quite simple and is based on a single circular NFW (Navarro, Frenk & White 1997) dark matter halo centred on the central galaxy. Their preferred model is based on the identification of K0 and K1 (Fig. 3.8) as two images of the same background galaxy at $z \sim 2.25$. In contrast, we conclude that K0 and K1 are more likely to be individual images of two different galaxies because they have significantly different surface-brightnesses (§3.4). It is also not clear on geometrical grounds how their circular model is capable of reproducing the observed image positions. Inspection of Fig. 2.5 & 2.6 reveal that an offset in the position angle of radial and tangential multiple-images relative to the centre of the lensing mass distribution requires the broken radial symmetry of an elliptical mass distribution.

In summary the compact clusters include two cooling flow systems: A 383 and A 1835. In contrast, A 963 appears to be in an advanced stage of relaxation following previous merger activity, although it does not contain a cooling flow. Finally, A 267 is probably a merging system; the wide-field weak-lensing analysis of Kneib et al. (in prep.) should supplement previous weak-lensing studies of this cluster and help to identify the origin of the extremely elliptical mass morphology and the large offset between the X-ray and mass peaks.

3.8.2 Clumpy Clusters

We turn to the clumpy clusters. Four of these clusters (A 68, A 773, A 2218 A 2219) require a bi/multi-modal lens model to explain the observed lensing signal. On the other hand, the models of A 209 and A 1763 require just one cluster-scale mass component and the origin of the internal structure of these two clusters is less clear. We discuss each cluster in turn.

A 68

The structure of this cluster is well-constrained by the observed multiple-image systems (§3.2). Dahle et al. (2002a) also noted the presence of numerous candidate multiple-image systems in their ground-based imaging of this cluster, however they concentrated on a weak-lensing analysis of the cluster mass distribution, obtaining a best-fit singular isothermal model with a velocity dispersion of $\sigma = 1650 \pm 220\,\mathrm{km\,s^{-1}}$ and a formal χ^2 of 1.85 per degree of freedom. Their weak-lensing mass-map reveals a mass distribution that is elongated in the direction of the North-West group of galaxies (clump #2 in our lens model). We also note that the X-ray flux contours of this cluster are highly irregular including a significant extension to the North-West. We interpret the substructure in this cluster as a signature of merger activity that is probably associated with the North-West group of galaxies. This is also provides a natural explanation for the discrepancy between the high velocity dispersion of Dahle et al.'s isothermal single-component model and the lower values contained in our detailed strong lensing model (see Table 3.5).

A 209

This is the least massive cluster in our sample and its lens model contains just one cluster-scale mass component. Before considering the structure of this cluster, we briefly revisit the mass of this cluster. Together with A 1763, the significant offset of this cluster from ASF's cooling-flow mass-temperature relation plays an important role in our merger-boosted interpretation of the temperatures in Fig. 3.7.3 in §3.6. We consider to what extent the offset of A 209 from the cooling flow relation could be caused by under-estimating the cluster mass, as opposed to an increase in its temperature. Specifically, we explore the assumption that is built-in to our lens models that the mass components all follow the same analytic mass profile. If the cluster-scale mass component in A 209 actually has a much shallower profile than the other clusters, then its virial mass would be much larger than our small field of view mass measurement suggests. Therefore the large offset would be reduced when wide-field mass measurements are available. We test whether this is a feasible explanation by comparing our lens model with Dahle et al.'s (2002a) parametrised

singular isothermal weak-lensing model of this cluster. We find that the best-fit velocity dispersion of Dahle et al.'s model agrees very well with our model. This comparison therefore appears to rule out the flat density profile hypothesis because if the profile is much shallower than isothermal on large scales, then Dahle et al. would probably not be able to fit an isothermal profile to their wide-field weak-lensing data.

We now turn to the structure of A 209. The two pieces of evidence for substructure in this cluster are its substructure fraction ($M_{\rm sub}$ / $M_{\rm tot}$= 0.13 ± 0.06) and the complex X-ray emission from its core (Fig. 3.14, Table 3.7). Given the low mass of this cluster, and the proximity of it to our somewhat arbitrary compact/clumpy dividing line of $M_{\rm sub}$ / $M_{\rm tot}$= 0.1, the substructure fraction is not compelling evidence that this cluster contains significant substructure. However the X-ray flux contours in the very centre of the cluster are offset from both the central galaxy and the centre of mass of the lens model by $(4 \pm 1)''$ which suggests that the core of this cluster is dynamically active. The "shoulder" of X-ray emission that extends $\sim 40''$ East from the cluster centre also strongly suggests a dynamically immature core (see also Rizza et al. 1998). In contrast to other clumpy clusters, there is no evidence from our detailed lens model for a merger event in this cluster. Neither does our panoramic CFH12k imaging of this cluster (Czoske 2002) reveal any nearby galaxy groups or filaments that may be associated with ongoing merger activity. We therefore conclude that the core of A 209 is probably dynamically active, however the cause of this activity is not apparent from our current dataset.

A 773

The structural details of A 773 are not as precisely determined as for the other clumpy clusters because there are no confirmed multiple-image systems in this cluster. Nevertheless, the superlative resolution of our *HST* data and our carefully constructed and calibrated catalogue of weakly-sheared background galaxies enable us to constrain the parameters of three cluster-scale mass components in the lens model. The X-ray emission peaks between the two brightest cluster galaxies and is elongated East-West, i.e. in the direction of the group of galaxies that we associate

with clump #3 in the lens model of this cluster. This suggests that the present optical and X-ray morphology of A 773 may be due to an ongoing merger between three systems, two of which (clumps #1 and #2) are associated with the two brightest cluster galaxies. Dahle et al.'s (2002a) weak lensing mass map appears to support this interpretation because it contains a highly significant mass peak that coincides with our clumps #1 and #2, plus a less massive extension to the East that appears to coincide with our clump #3.

However, it is surprising that such a complex merging cluster lies on the cooling flow mass-temperature relation of ASF (Fig. 3.18). One explanation is that the three-dimensional separation of clumps #1 and #2 is much larger than suggested by their two-dimensional separation on the sky and we may be observing A 773 at the early stages of the merger between these two clumps, i.e. prior to significant merger-induced heating of or bulk motion within the ICM has taken place. Alternatively, our view of A 773 could be contaminated by projection of an unrelated structure, leading to an overestimate of the cluster mass. Spectroscopic analysis of the cluster galaxies should shed light on these questions (Kneib et al. in prep.; see also Czoske et al. 2001).

A 1763

This cluster lens model contains a single cluster-scale mass component (Table 3.5), and we measure a sub-structure fraction of 0.10 ± 0.05. A 1763 has not yet been observed with *Chandra*, however we overplot the *ROSAT*/HRI contours of this cluster on our optical *HST* data in Fig. 3.14. These contours reveal a highly elongated X-ray morphology with the peak offset from the peak of the mass model (Table 3.7). Both the elongation and offset are in a Westerly direction which coincides with an apparent excess of cluster galaxies and a strong shear signal (Fig. 3.7) in our *HST* frame. We also examine our CFH12k frames of this cluster (Czoske 2002) and identify a possible filament of galaxies with colours consistent with cluster ellipticals extending $\sim$ 1 Mpc West from the central galaxy. The shear vectors near to the X-ray peak in Fig. 3.7 are aligned with the centre of the lens model, and do not appear to be perturbed by any mass that might be associated with the X-ray

peak emission. A 1763 therefore appears to be similar to A 267 in that the offset of the X-ray peak may be due to dynamical activity that is probably associated with the Westerly filament of cluster galaxies. We also note that the central galaxy is a wide-angle radio source, the morphology of which is consistent with our merger interpretation of this cluster (Vallée & Bridle 1982).

A 2218

The lens model of this cluster is the most precisely constrained of the whole sample, with a substructure fraction of $M_{\rm sub}$ / $M_{\rm tot}$= 0.23 ± 0.01. The X-ray peak is also off-set from the mass peak by $10 \pm 2''$ (Table 3.7). The most intriguing aspect of our analysis of this cluster is that it lies on the cooling flow mass-temperature relation recently derived by ASF (Fig. 3.18). Taken as a whole our analysis implies that this cluster is not in hydrostatic in its central region ($r \lesssim 500$ kpc), and we suggest that its cool temperature relative to the other merging clusters in our sample may arise from cold gas deposited into the cluster potential by the infalling clump (#2).

Previous structural analyses of this cluster (e.g. Kneib et al. 1995, 1996; Squires et al. 1996; Markevitch 1997; Wang & Ulmer 1997; Abdelsalam, Saha & Williams 1998; Neumann & Böhringer 1999; Cannon, Ponman & Hobbs 1999; Machacek et al. 2002) have all concluded, in agreement with our analysis, that this cluster is undergoing a merger and that the core ($r \lesssim 500$ kpc) is not in hydrostatic equilibrium. Machacek et al. (2002) have performed the most detailed X-ray analysis of this cluster to date, and conclude that their data are consistent with a slightly off-axis merger that is viewed $\sim$ 1–2 Gyr after the initial interaction. They find no evidence for strong shocks in the ICM, although they cannot rule out weak shocks, and they find some evidence for cold gas in the cluster core. Although it does not provide a definitive answer, Machacek's results appear to be consistent with our interpretation of the location of A 2218 in the mass-temperature plane.

We also explore an alternative explanation, which is that our lens model overestimates the true mass of the cluster due to projection effects along the line of sight. Such projection effects would boost the ability of a cluster to produce multiple-images; indeed, A 2218 is the most spectacular strong-lensing system in the entire

sample. Machacek et al. (2002) estimate that projection of an in-falling galaxy group along the line of sight to A 2218 could lead to a $\sim$ 30–70% over-estimate in the cluster mass. If true, this could shift the mass of A 2218 down by $\sim$ 20–40% and thus move it off the cooling flow mass-temperature relation, in line with its status as a merging cluster. However, there are severe problems with this interpretation, most notably the absence in the optical data of a candidate infalling galaxy group that could be responsible for such a gross effect. We also note that the X-ray-lensing mass discrepancy for this cluster is strongest on projected scales of $r \lesssim 80$ kpc, i.e. in the region where the cluster physics is expected to be most complex. We therefore suggest that the X-ray mass estimates are unlikely to be very reliable on these scales, and that our lensing analysis, which is insensitive to the details of the cluster physics, will provide a more robust estimate of the cluster mass.

A 2219

The lens model of this cluster contains two cluster-scale mass components, however its substructure fraction ($M_{\rm sub}\,/\,M_{\rm tot}= 0.23 \pm 0.01$) is the lowest of the clusters that contain more than one cluster-scale clump. This is consistent with the relatively low mass dipole that we measured in our weak lensing analysis in §3.6.2. Despite not being the most massive cluster in the sample, A 2219 is the hottest cluster. Randall et al. (2002) recently used semi-analytic models to study the impact of merger activity on cluster temperatures. They showed that the factor of $\sim$ 3 difference between the temperature of A 2219 and the cooling flow mass-temperature relation (Table 3.7) appears to be a natural outcome from such merger activity, although such extremely high temperatures may not be very long lived. The bi-modal and highly elongated mass morphology of this cluster and the highly elongated X-ray emission both support the proposal that this cluster is undergoing a major merger (see also Smail et al. 1995b). We therefore conclude that the high temperature of this cluster is caused by dynamical activity in the central regions.

Other Indicators of Merger Activity

We close this section by briefly comparing observations of diffuse radio emission from the clusters with our lensing/X-ray analysis. The origin of diffuse radio emission from clusters remains controversial, however recent joint radio/X-ray analyses (Colafrancesco 1999; Liang et al. 2000; Feretti 2001; Buote 2001; Govoni et al. 2001) have established a correlation between the diffuse X-ray and radio emission from clusters and identified that the rest-frame 1.4 GHz radio power correlates with the X-ray luminosity. Buote (2001) also measured a correlation between the multipole moments of clusters that exhibit radio halos with their radio power in the sense that clusters with more substructure have more radio power. Indeed, Buote proposed that the extremely large kinetic energies required to accelerate thermal electrons to relativistic speeds means that the most extreme examples of diffuse radio emission should arise in X-ray luminous ($L_X \gtrsim 5 \times 10^{44}$ erg s^{-1}) clusters that are experiencing "violent" mergers that have a "seriously disrupted core". Our cluster sample clearly satisfies Buote's X-ray luminosity criterion, and so we search the literature for diffuse radio detections of the clusters in our sample. Various authors claim to detect diffuse radio emission from four of the clusters: A 209, A 773, A 2218 and A 2219 (Moffet & Birkinshaw 1989; Giovannini et al. 1999; Govoni et al. 2001; Kempner & Sarazin 2001). All of these four clusters are classified as clumpy in our analysis, and are among the least relaxed clusters in our sample (Table 3.7). We therefore speculate that the dynamical immaturity that we identify in A 209, A 773, A 2218 and A 2219 may be sufficiently energetic to contribute to the diffuse radio emission observed in these clusters.

Summary

In summary, three of the four compact clusters (A 383, A 963 and A 1835) appear to be relaxed systems in hydrostatic equilibrium; two of these clusters (A 383 and A 1835) are also cooling flow clusters, as shown by their steep central temperature gradient. In contrast, the fourth compact cluster (A 267) appears to be dynamically active and has a large offset between its X-ray and mass peaks. The clumpy clusters all show evidence of being merging systems, although there is considerable scatter

in the detailed properties (mass, temperature, X-ray morphology) of these clusters. We interpret this diversity as a signature of the dispersion in how recently the observed merger activity commenced and the detailed cluster physics in the central region of each system.

Further progress in understanding all of these clusters, and in particular the merger histories of the clumpy ones will come from our weak lensing analysis of panoramic multi-colour CFH12k imaging data (Kneib et al., 2002a, in prep.) and our wide-field spectroscopic survey of these fields (Kneib et al., 2002b, in prep.), in addition to further deeper *Chandra* imaging, especially of A 1763, for which observations are currently not scheduled.

3.9 Summary and Conclusions

We have observed ten objectively selected X-ray luminous clusters at $z \sim 0.2$ through the F702W filter using the WFPC2 camera on board NASA/ESA's *Hubble Space Telescope*. This is the first study to exploit *HST* observations of a homogeneous sample of X-ray luminous clusters. Our survey therefore offers an unprecendented, high resolution view of the mass and structure of clusters at a single, well-defined epoch.

The *HST* data reveal numerous multiply- and singly-imaged background galaxies, including two spectacular new strong lenses (A 68 and A 383). We use optical and near-infrared spectrographs on both 4– and 10–m class ground-based telescopes to obtain spectroscopic redshifts for these multiple-image systems. Together with three other clusters, for which spectroscopic redshifts are available from the literature (A 963, A 2218 and A 2219), this gives a total of five clusters for which spectroscopic redshift constraints are available. None of the remaining five clusters (A 209, A 267, A 773, A 1763, A 1835) contain unambiguous multiple-image systems.

We exploit an extended version of the LENSTOOL modelling software (Kneib 1993; Kneib et al. 1993, 1995, 1996; §2) to construct a detailed lens model of each cluster. We constrain these models with a combination of the available multiple-image constraints and a careful analysis of the weakly-sheared background galaxies

in each cluster field. We estimate that mass measurements based on models constrained by multiple-image systems are accurate to $\sim$ 2–5% and based on those constrained by just their weak-shear signal are accurate to $\sim$ 10–25%

We use our models to measure the total mass, $M_{\rm tot}$, of each cluster within a fixed radius of $r = 500$ kpc; we also measure the mass in each cluster that lies outside the central dominant mass component (i.e. the amount of substructure, $M_{\rm sub}$) within the same outer radius. We classify four clusters as compact on the basis of their low sub-structure fraction ($M_{\rm sub}\,/\,M_{\rm tot} < 0.1$) and six as clumpy ($M_{\rm sub}\,/\,M_{\rm tot} \geq 0.1$). This large fraction of clumpy systems implies that slightly more than half of this sample of X-ray luminous clusters are potentially growing and therefore are probably not in hydrostatic equilibrium on projected scales of $r \lesssim 500$ kpc. This result indicates that it may be dangerous to assume that all massive clusters are relaxed systems when attempting to constrain their properties with X-ray data (see also Allen 1998).

To investigate the impact of the cluster substructure on the global properties of the clusters, we compare cluster mass with X-ray luminosity. Overall, the mass dispersion is 2.5$\times$ greater than predicted by the self-similar scaling relations that assume clusters to be equilibrium systems. This large dispersion is dominated by the clumpy clusters (3$\times$ larger mass dispersion than self-similar); the compact clusters are a more homogeneous sub-sample and the scatter in their masses is consistent with $L_{\rm X} \propto {M_{\rm tot}}^2$.

The compact and clumpy clusters also form two distinct sub-samples in mass-temperature space. We find that the mean masses of the two classes are consistent within the uncertainties, however on average the clumpy clusters are $\sim$ 25% hotter than the compact clusters at a fixed mass. We also compare our mass-temperature data with the empirical relationship recently derived by ASF for a sample of six massive cooling flow clusters. We find that the two cooling flow clusters in our sample (A 383, A 1835) agree with the ASF relation and the majority of the non-cooling flow clusters are hotter than this. The two exceptions to this picture are A 773 and A 2218 both of which contain significant substructure. We attribute the relative coolness of A 773 to a much larger three-dimensional separation of the dominant mass components than their separation on the sky (Fig. 3.5), which

in combination with observing this cluster at an early stage in the merger process would allow the observed temperature to be more representative of relaxed clusters. In contrast, the temperature of A 2218 appears to arise from the deposition of cool gas from the infalling material into the cluster core. We also note that Macheck et al. (2002) find no evidence of strong shock-heating of the ICM, and weak evidence for cold gas in the central regions of this cluster, in support of this interpretation.

In summary, our analysis reveals that the X-ray temperature and luminosity of galaxy clusters are strongly influenced by their dynamical maturity. One's perspective on these massive systems depends fundamentally on the selection function used to construct the sample and the analysis methods used. Specifically, samples of cooling flow clusters ($t_{\rm cool} \lesssim 10^9$ years and emission line central galaxy) appear to form a well-defined sub-set of clusters which are more regular than the general cluster population and appear to follow scaling relations that are based on equilibrium models. Non-cooling flow clusters are more numerous and significantly more diverse than their cooling flow siblings. This diversity stems from the dynamical immaturity of the general X-ray luminous cluster population.

Other elements of the overall survey will probe these issues on larger spatial scales (weak lensing analysis of our CFH12k imaging data) and using complementary techniques (dynamical studies of the cluster galaxy populations). In the next chapter, we exploit our detailed lens models to investigate the following questions:

- What constraints can be put on the inner slope of the cluster density profile using radial arcs?
- What can we learn about the detailed physics of dark matter from the spatial distribution of matter in our lens models?
- What impact does a hotter normalisation of and broader scatter around the mass-temperature relation have on attempts to use galaxy clusters to constrain the normalisation of the matter power spectrum, σ_8?

We also exploit the magnifying power of the cluster lenses, and our detailed knowledge of the gravitational optics of these systems to probe the formation of massive elliptical galaxies in §5 and §6.

4 IMPLICATIONS FOR COLD DARK MATTER

4.1 Introduction

We now discuss the constraints from our previous analysis of the distribution of mass in ten X-ray luminous clusters (§3) on the properties of the dark matter, which is proposed to dominate these systems.

4.1.1 The Density Profile of Dark Matter Halos

The cold dark matter (CDM) paradigm proposes that the Universe is dominated by non-baryonic matter (Davis et al. 1985). Much theoretical effort has been invested in this very successful hypothesis, for example in large-scale numerical simulations of dark-matter-only universes (e.g. Jenkins et al. 1998). One prediction to emerge from such simulations is that dark matter halos can be described by a universal density profile that contains a central cusp described by $\rho \propto r^{-\alpha}$ with $\alpha \gtrsim 1$ (ρ is the three-dimensional density of the halo and r is the radial distance in spherical polar co-ordinates). The presence of this cusp in the simulations stems largely from the proposal that the dark matter that dominates the Universe principally comprises weakly-interacting particles (e.g. axions or photinos). Such dark matter is also sometimes referred to as "collisionless" dark matter which more graphically makes the point that in the absence of interactions, or "collisions", the density of dark matter is capable of reaching extraordinarily high levels in the centre of deep potential wells.

The simulations of galaxy cluster mass halos from different groups predict different values of α: Navarro, Frenk & White (1997) quote $\alpha \simeq 1$; Moore et al. (1998) find $\alpha \simeq 1.6$; Ghigna et al. (2000) claim $\alpha \simeq 1.4$. However, it has been suggested that the difference between these competing claims is due to numerical effects and not fundamental physics (Power et al. 2002). Unfortunately, none of these studies

attempt to estimate the scatter on their measurement of α, nor do they quantify the impact of their halo selection function on their analysis. It is therefore difficult to assess whether these apparently discrepant results do indeed conflict with each other. The clearest statement that can distilled from this theoretical pursuit of α is that cold dark matter halos are predicted to contain a central density cusp with a power law slope in the range $\alpha \sim 1$–1.6.

Observationally our view of the distribution of mass in galaxies and clusters is complicated by the presence of baryons. For example, the potential well of a typical cluster contains hot X-ray emitting gas and galaxies in addition to the dark matter that is studied in the numerical simulations. Globally, the baryon mass-fraction in a typical cluster is 20–30%, however this fraction rises significantly on radial scales of $r \lesssim 10$ kpc in many rich clusters due to the influence of the central galaxy. The density profile of Cl 0024+16 , a rich cluster at $z = 0.39$ has been proposed to provide a powerful test of CDM because it is not dominated by a single massive galaxy (instead the central region contains 4–5 bright galaxies, see Fig. 1.5), and thus the central density profile may be dark matter dominated even on small scales. Tyson et al. (1998) studied the gravitationally-lensed images in this cluster and concluded from their modelling that this cluster contains a flat core (i.e. $\alpha \sim 0$), apparently at odds with CDM. Cl 0024+16 is therefore often cited as a challenge to the CDM paradigm. However, recent dynamical studies of this cluster (Czoske et al. 2001, 2002) have complicated this interpretation. Czoske et al. show that Cl 0024+16 is a complex merging cluster that is viewed along the axis of the merger. They also use numerical simulation to show that the flat density profile of this cluster could be a natural consequence of this merger.

An alternative approach to constraining the inner slope of dark matter density profile of clusters is to search for clusters that contain a radial arc. In contrast to tangential arcs (which constrain the mass within the radius of the arc), radial arcs provide precise constraints on the slope of the density profile (§2.1.6), and should thus provide important insights into the shape of cluster density profiles.

Although the counter-CDM interpretation of Tyson et al.'s result now appears to be weakened, observational results from galaxy-scale halos continue to challenge

CDM. For example, the low density cores of dwarf irregular galaxies (Moore 1994; Flores & Primack 1994; De Blok & McGaugh 1997; Dalcanton & Bernstein 2000), the persistence of bars in high surface-brightness galaxies (Debattista & Sellwood 1998), and the small number (~ 100) of galaxies observed in the Local Group (Mateo 1998) compared with theoretical predictions of $\sim 1,000$ such galaxies (Press & Schechter 1974; Kauffmann et al. 1993; Moore et al. 1999; Klypin et al. 1999). These issues motivated Spergel & Steinhardt (2000) to propose that the dark matter particles are self-interacting, with a large scattering cross-section. Spergel & Steinhardt made several predictions about the properties of self-interacting dark matter (SIDM) halos, two of which are relevant here: SIDM halos have a constant density core and the centres of SIDM halos are spherical. Both of these predictions arise directly from the dark matter self-interactions, because these interactions are expected to lead to thermalisation, with heat being transferred from the high density central cusp to larger radii, resulting in flat, spherical cores. They also estimated that if SIDM is to be a viable solution to the problems described above, then the dark matter cross-section to self-interaction must be in the range ~ 0.45–$450\ \mathrm{cm^2\,g^{-1}}$.

4.1.2 Constraints on the Matter Power Spectrum

A second route to investigate the nature of dark matter in CDM universes is to constrain the amplitude of fluctuations in the matter power spectrum. This is commonly described by the parameter σ_8 (see §1), which measures the rms fluctuation of the linear theory matter density on co-moving scales of $8\ h^{-1}\mathrm{Mpc}$*. A variety of methods have been used to measure σ_8, including the abundance of massive galaxy clusters (e.g. Eke et al. 1996, 1998), cosmic shear statistics (see Mellier et al. 2002 for a recent review), weak lensing by X-ray luminous clusters in the Sloan Digital Sky Survey (Viana, Nichol & Liddle, 2002) and joint analysis of the 2dF Galaxy Redshift Survey (2dFGRS) data with constraints on the Cosmic Microwave Background anisotropies from recent balloon and ground-based experiments (Lahav et

*This scale is chosen to be that at which the fractional rms fluctuation in the density field is unity. Originally, it was found from analysis of optically selected Lick galaxy counts (Peebles 1980) that this condition is satisfied, at least for luminous matter, on scales of $8\ h^{-1}\mathrm{Mpc}$.

al. 2002 and references therein). These studies broadly polarise into two camps†: $\sigma_8 \sim 1$ and $\sigma_8 \sim 0.7$, each claiming $\lesssim 10\%$ uncertainty. The reason for this discrepancy is currently unclear, however many of the results that favour $\sigma_8 \sim 1$ use the cluster mass-temperature relation to relate constraints from the observed temperature function of X-ray clusters to a cluster mass function (e.g. Eke et al. 1998). Clearly, a robust understanding of cluster physics is essential for this approach to work. One tantalising possibility is that if the proponents of a low σ_8 are vindicated, then this result would reduce the predicted abundance of satellite halos in the local group, and thus help to reconcile CDM with observations (e.g. Moore et al. 1998) .

4.1.3 Key Questions

Our detailed gravitational lensing study of massive galaxy clusters is an ideal opportunity to investigate these issues. We exploit our suite of detailed lens models (§3) to investigate the following questions:

- Using the radial arcs detected in our cluster sample, what constraints can we put on the inner slope of the density profiles of dark matter halos (§4.2)?
- Do the spatial and dynamical parameters of the mass components in our lens models favour CDM or SIDM (§4.3)?
- What impact do our measurements of the normalisation of and scatter around the cluster mass-temperature relation have on σ_8 (§4.4)?

We summarise our conclusions in §4.5.

4.2 The Density Profile of Galaxy Clusters

Most multiple-image systems observed in galaxy clusters comprise tangentially amplified images (often called "giant arcs"); together with a spectroscopic redshift measurement, these images allow the projected mass enclosed by the various images

†We assume a fixed value of $\Omega_o = 0.3$ throughout this section. If this assumption is relaxed then σ_8 would vary as $\sigma_8 \propto \Omega_o^{-0.6}$; therefore σ_8 is approximately 50% lower in an $\Omega_o = 1$ universe than in an $\Omega_o = 0.3$ universe.

to be measured with high accuracy (§2 & §3). A small fraction of multiple-image systems include a radially amplified image, which in contrast to the tangential images constrains the local slope of the cluster density profile (§2.1.6). Radial arcs have been found in the very centres ($r \lesssim 20$ kpc) of a few cluster lenses, and they are very difficult to detect in ground-based observations, with only a single example known (MS 2137.3−23 – Fort et al. 1992; Mellier et al. 1993). In contrast, *HST* has uncovered several radial arcs in previously well-studied cluster lenses (e.g. A 370, Smail et al. 1996; AC 114, Natarajan et al. 1998) which enabled the first tests of the form of cluster mass profiles on scales of $\lesssim 100$ kpc (Williams et al. 1999).

We detect four radially oriented features that appear to be gravitationally-lensed in our cluster lens sample (§3.4): B0b and B1d in A 383, C0d in A 68 and K0 in A 1835. We select from this list the most robust identifications and use them to investigate the slope of the cluster density profile. We discard both C0d and K0 from our analysis because the identification of C0d is quite tentative and we do not know the redshift of K0. In contrast, both robust identifications and accurate redshifts ($\Delta z \leq 0.1$) are available for both B0b and B1d. We therefore exploit our lens model of A 383 (§3) to investigate the slope of the density profile in this cluster.

In §4.2.1 we briefly describe the observational data, their reduction and analysis, followed in §4.2.2 by a summary of the A 383 lens model, we then summarise our results and present our conclusions in §4.2.3.

4.2.1 Data and Analysis

HST Imaging

As described in §3, A 383 was observed with the WFPC2 camera on-board *HST* on January 25, 2000. Three exposures totaling 7.5 ks were taken through the F702W filter. The reduction and analysis of these data is described in detail in §3.2. The final *HST* frame (Fig. 4.1) reveals many previously unobserved strongly lensed features, including a giant arc and two radial arcs, making A 383 a striking new addition to the catalogue of cluster lenses at intermediate redshifts.

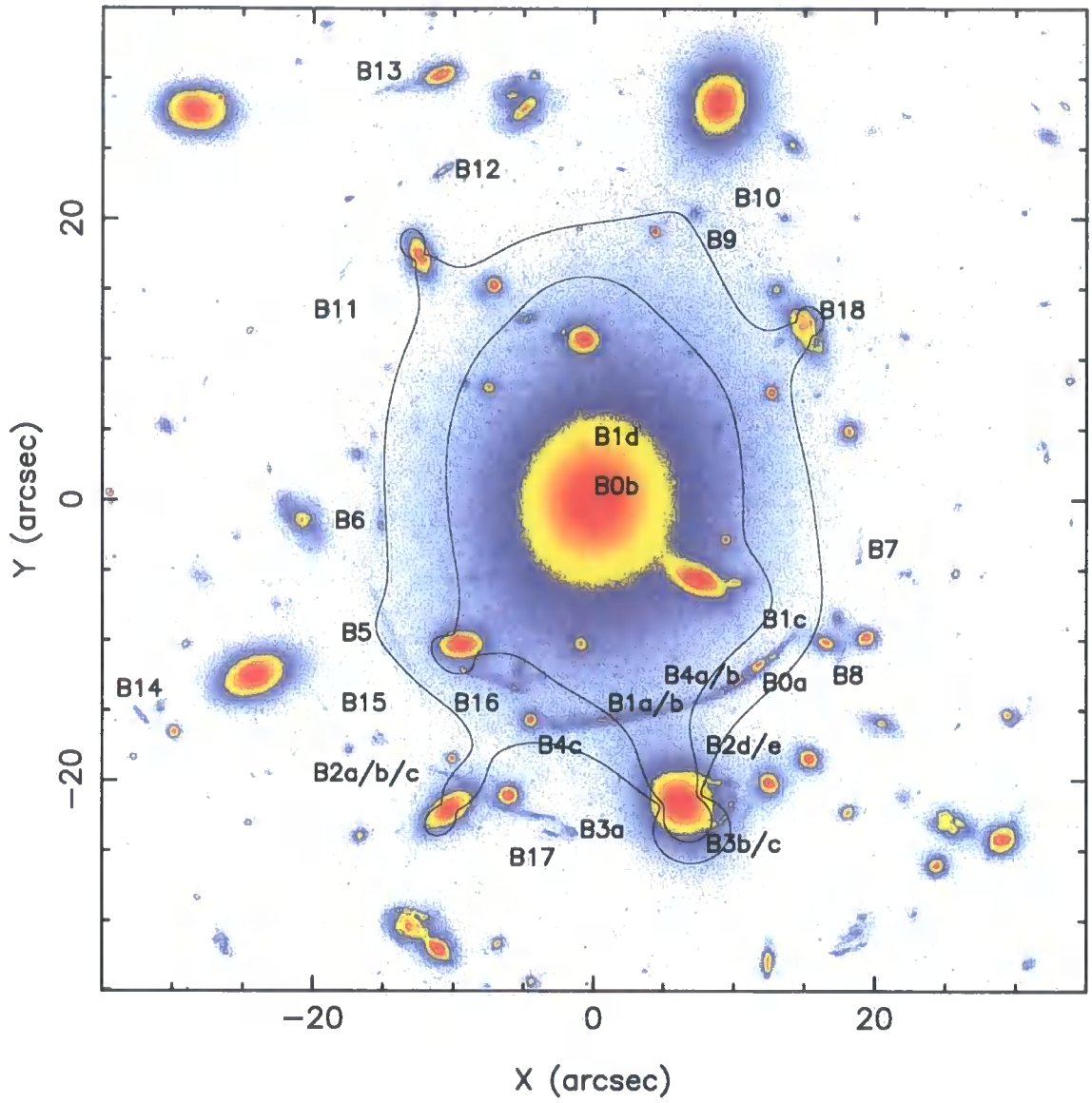

Figure 4.1: The central region of A 383 as observed with *HST*/WFPC2, overlaid with the z=1.1 (inner) and z=3.0 (outer) tangential critical lines from our lens model. The alpha-numeric labels identify the multiple images used to constrain the lens model and a number of other singly-imaged arclets. The detailed morphology of these arcs is further illustrated and analysed in Fig. 4–6. The spiral galaxy labeled B18 was included in our spectroscopic sample and has $z = 0.6560$.

Ground-based Imaging

We also used the 3.6–m Canada-France-Hawaii Telescope[‡] (CFHT) with the CFH12k camera to obtain panoramic images of A 383 on the nights of November 14–16, 1999. Total exposure times of 7.2 ks, 6.0 ks and 3.6 ks, accumulated at 6–10 dither positions, were acquired in the B, R and I bands respectively. Dr. Oliver Czoske reduced these data within IRAF using the MSCRED package including standard bias subtraction and flat-fielding using twilight flats. The dithered exposures were aligned with the Digital Sky Survey frame of the same field to an rms accuracy of 0.15″. More information on the reduction of these data is presented by Czoske (2002). Here we use the central regions of the B and I band frames to provide photometry of the lensed features in the cluster core (see Table 4.1). These two frames have seeing of 0.88″ and 0.71″ FWHM respectively.

In addition to the CFH12k imaging, we have obtained K-band images of the core of A 383 with the UFTI imager on the 3.8–m United Kingdom Infrared Telescope[§] (UKIRT), Mauna Kea, on October 14, 1999. The final frame was accumulated in 27 dithered sub-exposures of 90 s duration each to give a total on-source integration time of 2.4 ks, all in photometric conditions. The reduction of these data is described in detail in §5. The final frame has seeing of 0.42″ FWHM with 0.0908″/pixel sampling and an effective 5–σ depth of $K = 20.3$.

Arc Photometry

Arc photometry (Table 4.1) was performed on the *HST* frame and aligned, seeing-matched $BR_{702}IK$ frames. We first created a mask frame containing apertures corresponding to each observed arc in the *HST* frame. We then re-binned the *HST* mask to the CFH12k pixel scale (0.206″) and convolved it with the worst seeing of the ground-based imaging to produce a mask for use with the seeing-matched $BR_{702}IK$ frames. We also checked the seeing-matched frames to confirm that the arc morphology did not vary significantly between pass-bands. As some of

[‡]The Canada-France-Hawaii Telescope is operated by the National Research Council of Canada, the Centre National de la Recherche Scientifique de France and the University of Hawaii

[§]The United Kingdom Infrared Telescope is operated by the Joint Astronomy Centre on behalf of the Particle Physics and Astronomy Research Council

the lensed features are close to bright galaxies, we carefully excluded from the mask apertures any elements of the arcs that are not well resolved against the background of a neighbouring cluster elliptical.

The mask frames were then applied to the science frames and the sky background was estimated by median smoothing over the masked arcs. The sky frames were then subtracted from the science frames and the mask frames applied to the sky-subtracted frames to obtain a set of frames containing solely flux from the arcs. $BR_{702}IK$ photometry was then performed on these frames (Table 4.1). Uncertainties in the photometry were estimated by varying the smoothing length used to estimate the sky backgrounds.

Spectroscopy

On January 29, 2000 Dr. Harald Ebeling observed the brightest feature of the giant arc (B0a) with the LRIS spectrograph (Oke et al. 1995) on the Keck-II 10–m telescope[¶] in MOS mode, with a total exposure time of 3.6 ks in average seeing of 0.9″. Use of the 300/5000 grating centred at 7500 Å provided wide spectral coverage (5000–10,000 Å) at a spectral resolution of 2.55 Å/pixel. We show the spectrum of B0a in Fig. 4.2. We identify the strong emission line at 7493Å as [OII] λ3727 which places the galaxy at a redshift of $z = 1.0103 \pm 0.0001$. This interpretation is confirmed by the identification of FeII λ2600 and MgII λ2800 absorption features. The properties of this galaxy are discussed further in §4.2.2. Ten other galaxies were found to lie beyond the cluster redshift, including B18 at $z = 0.656$, which lies close to the cluster core (Fig. 4.1 and Table 4.1).

Gravitationally-lensed Features

In §3 we summarised the confirmed multiple-image systems that we used to constrain our lens model of this cluster. Here, we present a detailed discussion of the singly- and multiply-imaged faint galaxies that we detect in the core of A 383. The lensed features described in this section are identified in Fig. 4.1 and the multiple

[¶]The W.M. Keck Observatory is operated as a scientific partnership among the California Institute of Technology, the University of California and NASA

Table 4.1: Photometry and Spectroscopy of Lensed Features in A 383

Feature	R_{702}	$(B-R_{702})$	$(R_{702}-I)$	$(I-K)$	z	$R^d_{\rm source}$
B0a	21.74 ± 0.01	1.26 ± 0.01	0.50 ± 0.01	1.91 ± 0.03	1.0103 ± 0.0001^a	25.0 ± 0.5
B0b	21.71 ± 0.24	...	...	...		
B1a/b	21.26 ± 0.02	1.38 ± 0.03	0.83 ± 0.04	2.06 ± 0.14	1.1 ± 0.1	26.7 ± 0.6
B1c	22.79 ± 0.02	1.35 ± 0.03	0.76 ± 0.03	1.90 ± 0.07		
B1d	23.70 ± 0.07	...	...	...		
B2a/b	23.55 ± 0.06	...	...	...	3.0 ± 0.3	26.8 ± 0.7
B2c	23.66 ± 0.01	1.11 ± 0.03	0.05 ± 0.02	1.94 ± 0.08		
B2d/e	22.32 ± 0.21	0.99 ± 0.26	0.30 ± 0.23	< 2.3		
B3a	23.56 ± 0.02	1.07 ± 0.02	0.16 ± 0.02	< 1.9	3.0 ± 0.3	26.3 ± 0.5
B3b/c	22.38 ± 0.24	0.90 ± 0.27	0.35 ± 0.27	< 2.5		
B4a	22.87 ± 0.04	1.51 ± 0.08	0.78 ± 0.05	2.05 ± 0.15	1.2 ± 0.1	26.9 ± 0.5
B4b	22.09 ± 0.02	1.59 ± 0.05	0.72 ± 0.03	1.96 ± 0.09		
B4c	21.36 ± 0.03	1.62 ± 0.07	0.65 ± 0.06	1.99 ± 0.11		
B5	23.11 ± 0.03	...	...	...	$\gtrsim 2.4$	...
B6	23.18 ± 0.01	0.66 ± 0.03	-0.12 ± 0.15	< 3.5	$\lesssim 0.9^b$	...
B7	23.99 ± 0.02	0.87 ± 0.02	< 0.3	...	$\lesssim 1.3^b$	...
B8	24.44 ± 0.05	1.08 ± 0.14	0.57 ± 0.17	< 4.1	$\lesssim 2.0^b$	...
B9	24.96 ± 0.11	...	...	...	> 3.0	...
B10	24.24 ± 0.08	...	...	...	> 3.0	...
B11	24.61 ± 0.05	0.44 ± 0.03	0.33 ± 0.07	< 4.5	...	...
B12	22.68 ± 0.01	1.84 ± 0.01	0.78 ± 0.01	2.46 ± 0.01	...	...
B13	23.32 ± 0.02	...	...	...	...	...
B14	23.73 ± 0.01	1.69 ± 0.14	0.81 ± 0.16	2.19 ± 0.18	...	...
B15[c]	25.88 ± 0.02	> 1.4	< 1.8	> 4.0	$\lesssim 3.9$	...
B16	21.83 ± 0.01	1.18 ± 0.26	< 0.2	...	$\lesssim 1.0^b$	...
B17	23.62 ± 0.02	1.33 ± 0.03	0.26 ± 0.02	< 2.0	3.0 ± 0.3	
B18	19.84 ± 0.01	1.88 ± 0.02	0.73 ± 0.02	2.88 ± 0.02	0.6560 ± 0.0001^a	...
L^* E/S0	18.21	2.24	0.87	2.50	0.188	

a) Spectroscopic redshift;

b) Redshift assumes single image;

c) Extremely Red Object with $(R_{702} - K) = 5.8 \pm 0.1$ (§5.2.7);

d) Estimated R-band magnitude of the background galaxy, corrected for lens amplification.

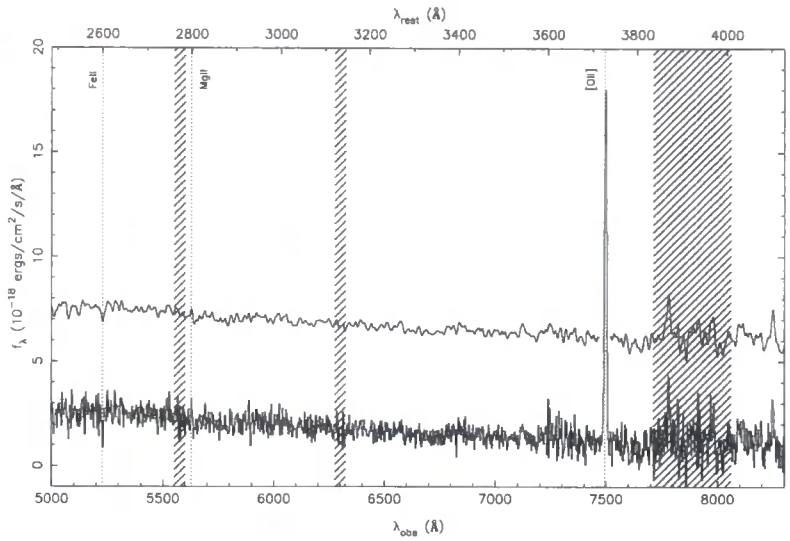

Figure 4.2: The spectrum of arc B0a in A 383 taken with the LRIS spectrograph on the Keck-II 10m telescope. The arc exhibits a blue continuum and we identify the strong emission line as [OII]λ3727 and confirm this with several UV absorption features (marked) to give a redshift of $z = 1.0103 \pm 0.0001$. The upper spectrum is smoothed to the nominal resolution of the spectrograph and offset vertically for clarity. The shaded regions show areas of the spectrum strongly affected by night sky lines.

images are further illustrated below in Fig. 4.3–4.5. The photometric and spectroscopic properties of the arcs are summarised in Table 4.1. We adopt the notation that, for example, B0 is the background galaxy that gives rise to the multiple images B0a and B0b and similarly B1 denotes the galaxy in the source plane that gives rise to images B1a, B1b, B1c and B1d in the image plane. We also denote arc substructure by extension of the numeric element of the arc label, for example, B2.1a, B2.1b, B2.1c, B2.1d and B2.1e are five images of one morphological feature of the background galaxy B2 (Fig. 4.5 and Table 4.1)

The Giant and Radial Arcs

We interpret the giant and radial arcs in A 383 as the lensed images of three background galaxies, B0, B1, and B4 at $z = 1.01$ (§4.2.1), $z \sim 1.1$ and $z \sim 1.2$ respectively. The images associated with each of these background galaxies are labeled B0a/b, B1a/b/c/d and B4a/b/c respectively in Fig. 4.1, 4.3 & 4.4. This interpretation is based on the following evidence:

(i) B0a has a spectroscopic redshift of z=1.01 (§4.2.1).

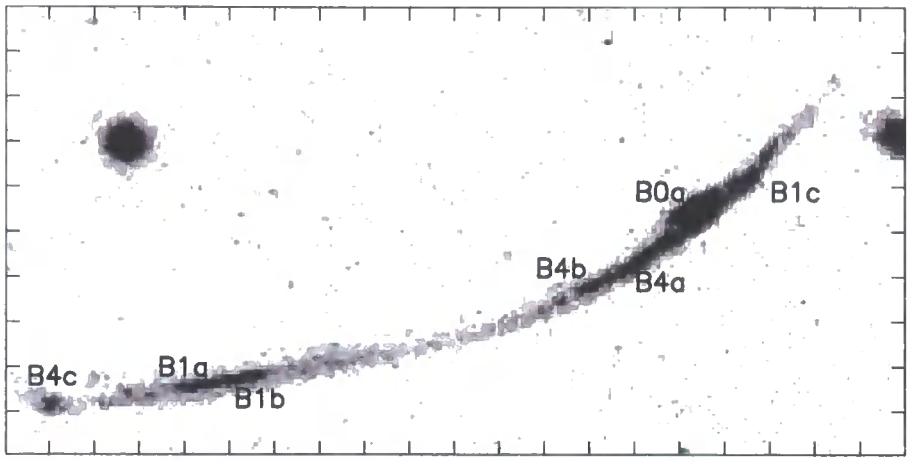

Figure 4.3: The giant arc in A 383 (see text for interpretation). Each tick mark represents 1″, and the orientation is as in Fig. 4.1. The path of the $z = 1.1$ critical line bisects the B1a/b image pair (Fig. 4.1).

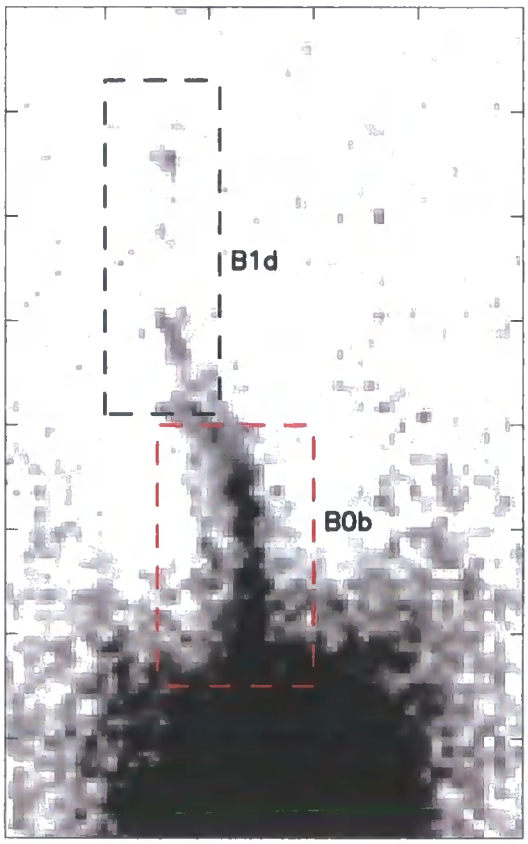

Figure 4.4: A view of the radial arcs as seen on the *HST* frame (enhanced by subtracting a median-smoothed frame from the science frame). Each tick mark represents 1″, and the orientation is as in Fig. 4.1.

(ii) The dip in the light profile of the giant arc between B1a and B1b and the symmetry of this image pair suggests that this is a pair of merging images (§2) straddling the $z \sim 1$ critical line as it traces a path away from the cluster centre towards the bright cluster elliptical south of the cluster centre.

(iii) The similarity of the optical and optical-infrared colours of B1a, B1b and B1c (Table 4.1) and their positions relative to the $z \sim 1$ critical line implies that B1c is a counter image of B1a/b.

(iv) B1c is $\sim 0.2''$ further away from the centre of the cluster than B0a, suggesting that B1 is at a slightly higher redshift than B0.

(v) The radially amplified image (Fig. 4.4) consists of two segments offset from each other by $\sim 1''$ in the tangential direction. This implies that the radial image consists of two radial arcs, the background galaxy relating to the outer arc lying at a higher redshift than that relating to the inner arc.

(vi) The tangential offset between B1c and B0a supports the above interpretation of the radial arcs and identifies the inner and outer radial arcs as probable counter images of B0a and B1a/b/c respectively.

(vii) When constrained by B0 and B1, the lens model predicts that $z \sim 1.2$ critical line bisects the image pair B4a/b, and that B4c is the counter image of this pair. This is supported by the photometry presented in Table 4.1.

Perturbations by Galaxy Halos

The lensing effect of neighbouring cluster galaxy halos on the B2/B3 system (Fig. 4.1 & 4.5) demonstrates how galaxy-scale masses measurably perturb the cluster potential. We interpret this complex group of blue arcs as being due to two background galaxies at a redshift of $z \sim 3$. This interpretation is based on the difference between the $R_{702} - I$ colours of B2c and B3a (Table 4.1), and the prediction of the lens model that the $z \sim 3$ tangential critical curve lies outside of the two cluster ellipticals adjacent to these arcs, bisecting each of the image pairs B2a/b, B2d/e and B3b/c (Fig. 4.1).

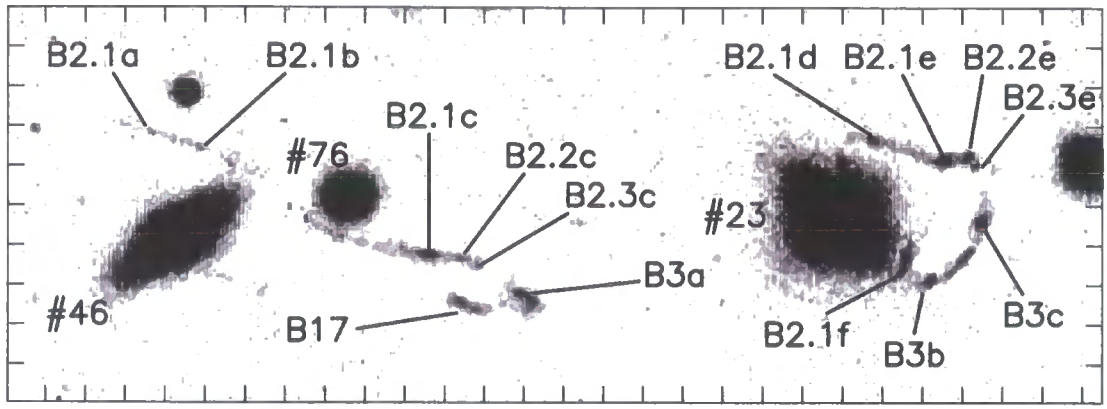

Figure 4.5: A view of the B2 and B3 multiple arc systems (enhanced by subtracting a median-smoothed frame from the science frame)). Cluster ellipticals #46, #76 and #23 are also labelled. Each tick mark represents 1″, and the orientation is as in Fig. 4.1. The path of the $z = 3$ critical line around these arcs is shown in Fig. 4.1.

This lens model also predicts the following counter images of the morphological features of the B2 / B3 system (Fig. 4.5):

(i) Six counter images of B2.1c coincident with B2.1a/b/d/e/f and the centre of cluster elliptical #23.

(ii) Two counter images each of B2.2c and B2.3c, one each coincident with B2.2e and B2.3e respectively, and the other one each under the halo of elliptical #23 to the left of B2.1d.

(iii) Two counter images of B3a coincident with B3b and B3c.

(iv) B17 is singly imaged, as it lies outside the $z \sim 3$ caustic.

The predictive power of this interim lens model is clear, however we restrict the multiple images used in subsequent iterations of the lens model to morphological details that are clearly detected against the halos of neighbouring cluster ellipticals. For example, B2.1f is not used to constrain subsequent lens models.

Faint Multiple Image Candidates

B5 (Fig.4.1) — B5 is a very faint arc lying in the saddle region between the central galaxy and the bright cluster elliptical South-East of the cluster centre. We interpret this arc as an image of a background galaxy which is magnified by this saddle and therefore constrain the redshift of the galaxy to be $z \gtrsim 2.4$.

B9/B10 (Fig. 4.1) — This is a pair of extremely faint arcs detected only because of the superb resolution and low sky background of the *HST* observations. Both arcs appear to comprise three images resulting from the magnifying effect of the saddle potential between the cluster centre and the cluster elliptical due North of the cluster centre. We estimate that they lie at a redshift of $z \gtrsim 3$.

4.2.2 Modelling and Results

In this section we summarise the gravitational lens modelling of A 383, based on our interpretation of the lensed features in this cluster. We then describe our lens model, and use this model to investigate the form of the density profile in the very centre of the cluster.

The Lens Model

We explained in detail how we constructed our lens model of A 383 and discussed our modelling assumptions in §2 and §3.6. Here we summarise the key features of the model.

The model consists of a single lens plane at $z = 0.188$, containing 25 mass components representing the cluster, the cD galaxy and 23 further individual cluster galaxies. The dynamical parameters ($r_{\rm core}$, $r_{\rm cut}$ and $\sigma_{\rm o}$) of the cluster and the cD galaxy were optimised in the χ^2 minimisation process. The dynamical parameters of the other 23 cluster ellipticals were scaled with their K–band luminosity following the scaling laws described in §2.2.3. The model parameters were constrained using both multiple-images and the weak shear field estimated from the shapes of the faint galaxies across the whole frame. The multiple-images used to constrain the model were: B0 (2 images), B1 (4 images), B2.1 (5 images), B2.2 (2 images), B2.3 (2 images), B3 (3 images) and B4 (3 images). We computed the best lens model by finding the combination of model parameters that produced the lowest value of χ^2. The fiducial parameters of this model (χ^2=0.8/dof) are presented in Table 4.2, together with the volume of parameter space for which $\Delta\chi^2 \leq 1$. These uncertainties were estimated by varying each dynamical parameter of the cluster halo and cD galaxy in turn while allowing the other parameters to find their

Table 4.2: Parameters of the Best Lens Model

	x_c ($''$)	y_c ($''$)	a/b	θ (deg)	r_{core} (kpc)	σ_o (km s^{-1})	r_{cut} (kpc)
Cluster	-0.3 ± 0.1	0.5 ± 0.1	$1.13^{+0.05}_{-0.05}$	129 ± 5	53 ± 2	920 ± 5	> 750
cD galaxy	-0.1 ± 0.1	-0.3 ± 0.1	$1.07^{+0.09}_{-0.03}$	98^{+15}_{-10}	$0.5^{+1.5}_{-0.4}$	250^{+30}_{-20}	> 10

optimum values.

We use the lens model to estimate the unlensed R–band magnitudes of the various multiply-imaged galaxies. We obtain $M_V \sim -19.3$, $M_V \sim -18.3$ and $M_V \sim -18.5$ for B0, B1 and B4 respectively (Table 4.1). Along with its blue optical-infrared colour, this suggests that B0 is a low luminosity star-forming galaxy. The redder colours of B1 and B4 suggest that these galaxies are undergoing lower rates of star formation than B0. We also estimate that in the source plane, B2 and B3 have $M_V \sim -22.0$ and $M_V \sim -22.4$ respectively, both also exhibiting the blue colours typical of star-forming galaxies (Table 4.1).

The Density Profile

The projected surface mass density of the best lens model is plotted as a function of projected distance from the centre of the cluster in Fig. 4.6. On scales $r \gtrsim 10$ kpc, the density profile is dominated by the cluster-scale mass component. The central galaxy mass component causes the density profile to steepen on scales of $r \lesssim 10$ kpc and further substructure is apparent at $r \sim 90$ kpc, coincident with the mass components associated with several bright cluster ellipticals. The shape of A 383's profile is however only constrained out to $r \sim 500$ kpc, this being the extent of the WFPC2 field of view. The mass profile is most accurately measured within $r \sim 100$ kpc where information from the multiple images is available.

The slope of A 383's density profile is constrained by the radial arcs, as their radial positions depend on the local gradient of the projected mass (§2.1.6). We estimate the slope of the projected density profile ($\Sigma \propto r^{-\beta}$) in the region $10 < r < 30$ kpc to be $\beta = 0.3 \pm 0.04$, where the uncertainty is estimated from the

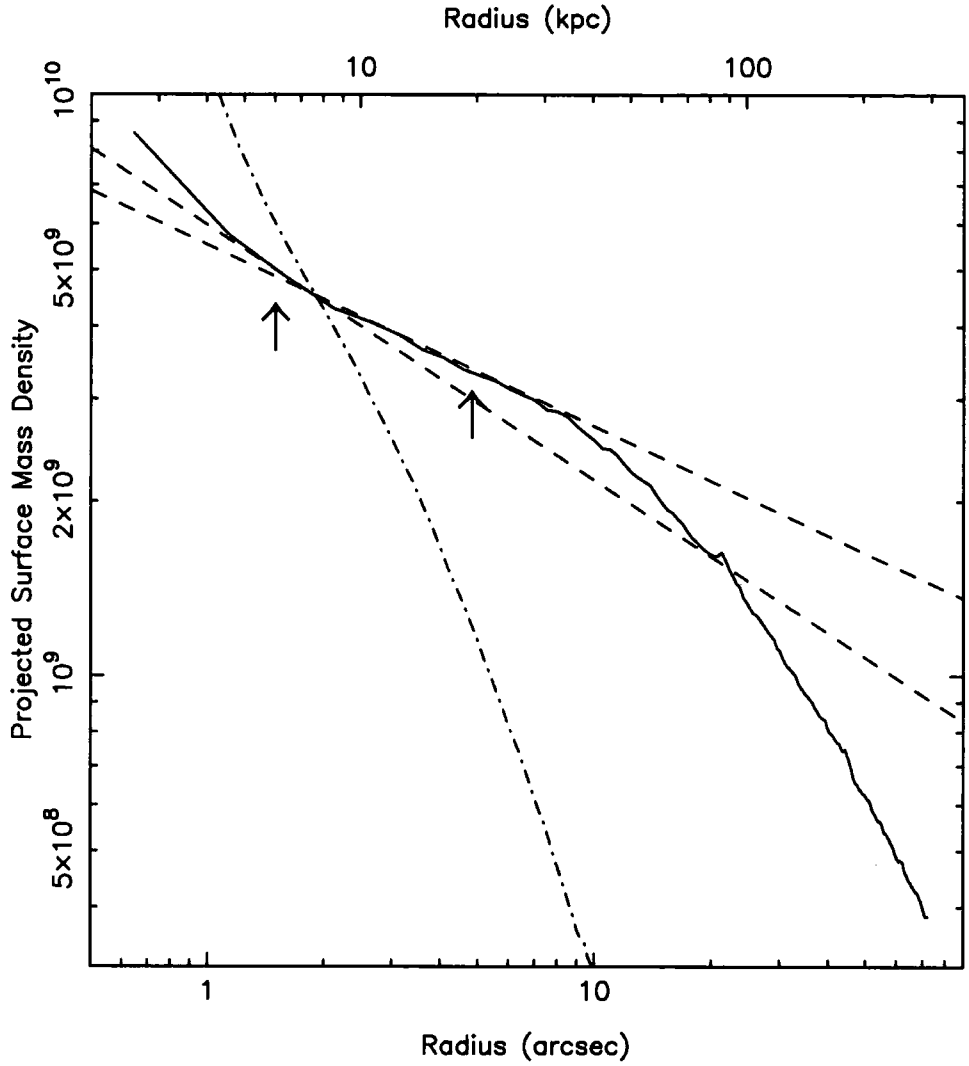

Figure 4.6: The solid line shows the projected surface mass density, Σ ($M_{\odot}kpc^{-2}$) of A 383 as a function of radius, obtained from the best lens model by measuring the mass density in concentric annuli. The dashed lines illustrate the difference between the profile slope at the positions of the two radial arcs (B0b and B1d), which are marked by arrows at 6 and 20 kpc respectively. The dot-dashed line shows the shape of the light profile of the cD galaxy (effective radius $\sim$ 25 kpc) for comparison purposes.

range of parameter values quoted in Table 4.2. We also note that there may be a systematic error term arising from our adoption of a given functional form for the mass components (§2). We return to this below, when we use a simple analytic model to estimate this systematic term. Deprojecting, assuming spherically symmetry, we estimate the slope of the three-dimensional density profile ($\rho \propto r^{-\alpha}$), to be $\alpha = 1.3 \pm 0.04$. We use the light profile of the cD galaxy to infer whether this slope could be due solely to the central galaxy or whether the dark matter halo also plays a role on these scales. Fig. 4.6 shows that the light profile falls off more steeply than the total projected mass density, implying that the steepness of the density profile at $r \gtrsim 10$ kpc is probably dominated by the dark matter.

Our modelling method does not include a parameter for the inner slope of the density profile. We therefore use analytic arguments to derive model independent estimates of α at the positions of the two radial arcs and thus to investigate the systematic uncertainty in our measurements of α that arise from our choice of model profile. We first use the projected density profile from our lens model (Fig. 4.6) to estimate α at the positions of the two radial arcs: $\alpha = 1.5 \pm 0.1$ and $\alpha = 1.3 \pm 0.04$ at $r \sim 6.0$ kpc (B0b) and $r \sim 20$ kpc (B1d) respectively. Independent slope estimates are obtained from analytical consideration of the positions of the radial and tangential images of B0 and B1 using: $\log(x_{\rm r} \,/\, x_{\rm t}) \sim (1/\beta) \log(1 - \beta)$, where $x_{\rm r}$ and $x_{\rm t}$ are the angular positions of the radial and tangential arcs respectively and $0 < \beta < 1$. We calculate $\log(x_{\rm r} \,/\, x_{\rm t})$ for B0 and B1 to be: -1.04 ± 0.07 and -0.51 ± 0.03 respectively, from which we estimate the de-projected density profile slopes to be $\alpha = 1.9 \pm 0.1$ and $\alpha = 1.3 \pm 0.1$ for the inner and outer radial arcs respectively. The former value is steeper than our lens model due to the non-singular mass profile adopted in the model (§4.2.2). It is however consistent with an isothermal peak in the centre of the cluster (i.e. on scales of $r \lesssim 10$ kpc) where physical processes are expected to be dominated by the baryonic content of the cD galaxy. The latter value is consistent with our lens model and strongly suggests that, although our modelling technique does not contain a slope parameter, it is sufficiently flexible to reproduce faithfully the cluster profile slope obtained from models that do explicitly include the profile slope as a free parameter. We also

use this analysis to estimate that the systematic uncertainty in our measurement of α at the position of B1d is of the order of ± 0.1, which in conjunction with the statistical uncertainties in our previous analysis gives an inner slope of $\alpha = 1.3 \pm 0.04(\text{statistical}) \pm 0.1(\text{systematic})$.

4.2.3 Discussion and Conclusions

The radial arcs detected in the core of A 383 ($z = 0.188$) provide a detailed view of the cluster mass distribution on scales of $r \lesssim 50\,\text{kpc}$. The morphologies and positions of these arcs have been used, in conjunction with ground-based multi-colour photometry and optical spectroscopy of the tangential counter-image of one of the radial arcs (B0b), to constrain the mass distribution and compute a precise mass density profile of this cluster.

We expect that the density profile of this cluster should be dark matter-dominated on scales of $r \sim$ 10–50 kpc, and we measure the slope of the three-dimensional density profile to be $\alpha = 1.3 \pm 0.04 \pm 0.1$ in this region. This result contrasts with the results of Tyson et al. (1998), who found a flat inner density profile in Cl 0024+16 at $z = 0.39$ (i.e. $\alpha \sim 0$). As we discuss in §4.1, dynamical studies of Cl 0024+16 have subsequently suggested that it may be currently undergoing a core-penetrating merger which may explain the flat density profile (Czoske et al. 2001, 2002). More recently, both strong and weak lensing have been used to measure the slope of the cluster density profile, α, in a number of clusters. For example, Dahle et al. (2002b) combined weak-lensing mass profiles from six X-ray luminous clusters (A 959, A 1351, A 1703, A 1722, A 1995, A 2537) and fitted a generalised halo density profile (Zhao 1996; Jing & Suto 2000) to this combined dataset. For a ΛCDM universe they found that $\alpha \sim 1.3$–1.6 (68% confidence), and could exclude $\alpha \lesssim 0.5$ at 95% confidence. In contrast Sand, Treu & Ellis (2002) used a joint strong-lensing and stellar velocity dispersion approach to model the mass distribution in the central region of MS 2137−23 which contains a radial arc. They found that $\alpha = 0.35^{+0.55}_{-0.3}$ (99% confidence) for a ΛCDM cosmology. Despite the variation between these results, they all exclude $\alpha = 0$ which was preferred by Tyson et al. (1998), it therefore appears that a central density cusp is present in at least a

fraction of massive galaxy clusters. Perhaps most interesting is the scatter in the measured values of α, which if the errors on individual measurements are robust, suggests significant diversity in the density profiles of dark matter halos. Clearly a much larger sample of clusters with radial arcs is required before the reasons for the discrepancies can be understood, and firm conclusions drawn. Nevertheless, observational studies are beginning to probe the dispersion in α, at least for clusters that are capable of producing radial arcs. However, we note that concentration on clusters that contain radial arcs may introduce a bias into the results. This possibility requires further investigation before the implications of current and future lensing measurements of α can be fully understood.

On the theoretical side, further progress will come with extension of Power et al.'s (2002) detailed numerical convergence study to higher mass systems including galaxy clusters. There is also an urgent need to quantify the scatter in α that such studies predict from a complete and representative sample of halos. As additional computing power becomes available it will also be important to include baryons in the highest resolution simulations to probe the impact of baryons on the slope of the density profile.

4.3 Self-interacting Dark Matter

Our suite of detailed lens models is a powerful tool to investigate the dynamical state of galaxy clusters, the most massive gravitationally-bound structures in the Universe. The distribution of mass in these clusters can also yield important clues about the physical properties of some of the smallest objects in the Universe – dark matter particles. We therefore use our lens models to test the predicted properties of SIDM (Spergel & Steinhardt 2000) and thus to place a new constraint on the collisional cross-section per unit mass of dark matter particles ($s_{\rm dm}$).

In §4.3.1 we review the tests that we could apply and the constraints available from our lens models to identify the most powerful constraint on $s_{\rm dm}$. We estimate a constraint on $s_{\rm dm}$ and compare it with other constraints from the literature, including both velocity independent and dependent models in §4.3.2. We discuss

our result and summarise our conclusions in §4.3.3.

4.3.1 Observational Tests and Constraints

We concentrate on Spergel & Steinhardt's (2000) predictions that SIDM halos will be spherical with a constant density core. On cluster scales, these predictions have so far been tested by Miralda-Escudé (2002) and Arabadjis et al. (2002). Miralda-Escudé (2002) argued that, if a dark matter halo is not spherical at a given radius, then one may obtain an upper limit on $s_{\rm dm}$ on the basis that the radius within which dark matter collisions are sufficiently common to thermalise (and thus circularise) the halo must be smaller than the radial position of the ellipticity constraint. As Miralda-Escudé showed, strong gravitational lensing is an ideal tool with which to constrain the ellipticity of dark matter halos, as the positions of multiple-images (both radial and tangential) provide very tight constraints on the geometry of the lens system. In contrast, Arabadjis et al. (2002) constrained $s_{\rm dm}$ using their analysis of *Chandra* observations of Cl 1358+62 to put an upper limit on the size of any constant density core in this cluster, and thus place a limit on $s_{\rm dm}$. We review the basic physics behind these two tests and then assess which of these predictions will yield the most stringent constraint on $s_{\rm dm}$ in the context of our cluster lens models.

The mean free path of particles in thermodynamic equilibrium is given by:

$$\lambda = \frac{1}{n\sigma\sqrt{2}} \tag{4.1}$$

where n is the number density of particles, and σ is their cross-section to collisions (e.g. Pendlebury 1985). The typical time between collisions of these particles, $t_{\rm coll}$, is therefore:

$$t_{\rm coll} = \frac{1}{n\sigma v\sqrt{2}} \tag{4.2}$$

where v is the typical speed of the particles. Applying this to SIDM, we can write the cross-section per unit mass of the dark matter particles, $s_{\rm dm}$ in the following form:

$$s_{\rm dm} = \frac{\sigma_{\rm dm}}{m_{\rm dm}} = \frac{1}{\rho\, t_{\rm coll} v\sqrt{2}} \tag{4.3}$$

where $m_{\rm dm}$ is the mass of the dark matter particle and ρ is the density of the dark matter in the region in which it is thermalised, and therefore also circularised.

If one of our detailed lens models is constrained to have a significantly non-circular mass distribution, then we can place a lower limit on $t_{\rm coll}$, because insufficient collisions will have taken place since the formation of the cluster to have thermalised the matter distribution: $t_{\rm coll} \lesssim t_{\rm clus}$ where $t_{\rm clus}$ is the age of the cluster. This lower limit on $t_{\rm coll}$ translates into an upper limit on $s_{\rm dm}$:

$$s_{\rm dm} \lesssim \frac{1}{\rho\, t_{\rm clus}\, \sigma_{\rm o}\, \sqrt{2}} \tag{4.4}$$

where ρ is now the density of the dark matter relevant to the strong lens model constraint, and $\sigma_{\rm o}$ is the velocity dispersion of the dark matter (e.g. Miralda-Escudé 2002). Alternatively, if our lens models reveal that the clusters have constant density cores, then we may convert Equation 4.4 into an equality and thus estimate $s_{\rm dm}$ (e.g. Arabadjis et al. 2002).

It is clear from this analysis that the most stringent limits on $s_{\rm dm}$ may be derived from lens model constraints that probe the highest density environments. The monotonic decrease of cluster density profiles with radius (e.g. Fig. 4.6) means that the closer the lensed feature is to the cluster centre, the tighter is the constraint on $s_{\rm dm}$. We therefore seek the constraint that lies at the smallest cluster-centric distance.

The core radius of the dominant central mass component in each of the cluster lens models is typically $r_{\rm core}$~50–100kpc (Table 3.5), and is constrained to better than $\sim$ 10% in the models that are constrained by multiple-image systems. As we have shown in our analysis of A 383 in §4.2, such a core radius does not reflect the presence of a flat central core in our models. Nevertheless, for convenience, we compare these "core radii" with other possible constraints. Tangentially amplified multiple-images (i.e. the majority of multiple-images) also lie at similar radii (Fig.s 3.1–3.10 & Table 3.2). Observational constraints on $s_{\rm dm}$ based on tangentially amplified multiple-images and possible flat cluster cores are therefore, in general,

of comparable strength. However, radial arcs lie much closer ($r \lesssim 20$ kpc) to the centre of lensing clusters than their tangentially magnified counterparts (Fig. 4.1). Constraints on $s_{\rm dm}$ based on the ellipticity of dark matter halos at the position of radial arcs should therefore deliver the tightest constraints on $s_{\rm dm}$ from strong lens models of galaxy clusters. However, care must be taken to ensure that the geometry of the cluster is dominated by dark matter and not by the high concentrations of baryons on the smallest scales in the cores of clusters ($r \lesssim 10$ kpc).

As discussed in §4.2, we observe four radially elongated features that are consistent with being radial arcs in our cluster sample: C0d (A 68), B0b (A 383), B1d (A 383) and K0 (A 1835). We discard K0 because the data currently available suggest that it is not multiply-imaged, and there are no other confirmed multiple-image systems in A 1835. Our detailed modelling and analysis of the density profile of A 383 in §4.2 indicates that the properties of B1d ($r \sim 20$ kpc) are dominated by the distribution of dark matter in this cluster. In contrast, B0b lies closer to the centre of the cluster ($r \sim 6$ kpc); consequently its properties are probably strongly influenced by the baryons associated with the central galaxy and the high central X-ray luminosity. We therefore discard B0b from our analysis, and retain B1d. Finally, we consider C1d in A 68, which lies at a similar cluster-centric distance as B1d. The properties of C1d are therefore probably also dominated by the distribution of dark matter in A 68. We therefore use the properties of the two radial arcs (C0d in A 68 and B1d in A 383) to constrain $s_{\rm dm}$.

4.3.2 A New Strong-lensing Constraint on $s_{\rm dm}$

The central cluster-scale mass component in both A 68 and A 383 have axis ratios of $a/b = 2.1 \pm 0.2$ and 1.13 ± 0.05 respectively (Table 3.5). We also compute the reduced χ^2 value for lens models of A 68 and A 383 that contain a circular central cluster-scale mass component, whilst allowing the other parameters to find their optimum values. We obtain $\chi^2 \gtrsim 30$ for these circular models, underlining the tightness of the constraints on a/b. Therefore the central dark matter halos of both A 68 and A 383 are both constrained to be non-circular at the positions of C0d and B1d respectively. We use A 383 to illustrate how the radial arc in this cluster

constrains the ellipticity of the cluster mass distribution: the offset in the position angle of the radial and tangential counter-images of B1 relative to the cluster centre (Fig. 4.1) can only arise if the mass distribution is elliptical. The example multiple-image configurations presented in Fig. 2.5 & 2.6 confirm that without this break in radial symmetry, a circular (in projection on the sky) cluster would produce images that are precisely aligned on opposite sides of the cluster centre.

We therefore measure the projected density of A 68 and A 383 at the positions of C0d and B1d respectively. To de-project these measurements, we adopt the density profile slope of $\alpha = 1.3$ at the position of B1d obtained in §4.2, which gives the simple relation $\rho = 0.3\Sigma/r$. We also measure the slope of the density profile of A 68 at the position of C0d, and confirm that this formula is also applicable to this cluster. To obtain an upper limit on $s_{\rm dm}$, we also need to know the age of each cluster. This is more straightforward to estimate for A 383 because it is a relaxed, compact cluster with a strong central cooling flow (§3 & Smith et al. 2001); this implies that gas in the centre of this cluster is cooling on timescales of $t_{\rm cool} \sim 10^9$ years, and thus the cluster must be older than this. We therefore adopt a cluster age of 5×10^9 years, which is identical to that used by Miralda-Escudé (2002), thus aiding comparison of our results. We note however, that this cooling-flow-based estimate is not strictly applicable to A 68 because it is a dynamically immature merging cluster (§3). We therefore adopt $\sim 5 \times 10^9$ years as a reasonable upper limit on the age of this cluster.

We substitute all of these ingredients into Equation 4.4 and derive an upper limit on $s_{\rm dm}$ based on the projected density of dark matter at the positions of C0d and B1d. We obtain: $s_{\rm dm} \lesssim 8 \times 10^{-3}$ cm^2 g^{-1} and $s_{\rm dm} \lesssim 7 \times 10^{-3}$ cm^2 g^{-1} from C0d and B1d respectively. Given the greater complexity of A 68 relative to the relaxed morphology of A 383 (§3), we adopt the latter constraint. This limit is a factor three lower than that obtained by Miralda Escudé (2002) ($s_{\rm dm} \lesssim 0.02$ cm^2 g^{-1}). The difference between these two results is probably caused by the higher density environment that we probe with our radial-arc-based test than Miralda-Escudé's reliance on the tangential arc in MS 2137−23.

We compare our result with the predictions of numerical simulations of SIDM

halos. Several authors (e.g., Davé et al. 2000; Hennawi & Ostriker 2002) find that $s_{\rm dm} \geq 0.45$ cm^2 g^{-1} (see also Spergel & Steinhardt 2000) is required to flatten dwarf galaxy and low-surface-brightness galaxy halos in their simulations, and thus to reconcile dark matter theory with observation. This is incompatible with the strong lensing constraints on $s_{\rm dm}$ described above.

One way to reconcile these discrepant views is to invoke a velocity dependent cross-section to dark matter self-interaction:

$$s_{\rm dm}\,(v) = s_{\rm dm,o} \left(\frac{v}{v_{\rm o}}\right)^{-a} \tag{4.5}$$

where $s_{\rm dm,o}$, $v_{\rm o}$ and a are determined by the fundamental physics of the interaction and if $a = 0$, then $s_{\rm dm} = s_{\rm dm,o}$. In this model, the constraint that we derive from A 383 translates to $s_{\rm dm,o} \lesssim 7 \times 10^{-3}$ cm^2 g^{-1}. For example, Firmani et al. (2001) have proposed a model with $a = 1$, based largely on the fact that their simulations produce dark matter halos with a scale-invariant density at the core-radius. They claim that this result matches the observations, however on cluster scales, they rely exclusively on Cl 0024+16, and so this agreement may be undermined by the recent identification of this cluster as a complex merging system (Czoske et al. 2001, 2002). Regardless of this uncertainty, we explore whether a velocity dependent cross-section can reconcile our upper limit on $s_{\rm dm}$ with the lower limit required to explain the properties of dwarf galaxies.

We adopt $v_{\rm o} = 100$ km s^{-1} (Arabadjis et al. 2002; Hennawi & Ostriker 2002) and plot $s_1 v_{100}^{-a}$ versus a in Fig. 4.7, where $s_1 \equiv (s_{\rm dm,o}\ /1{\rm cm}^2{\rm g}^{-1})$, $v_{100} \equiv (v/v_{\rm o})$ (i.e. v_{100} is v expressed in units of 100 km s^{-1}) and we equate v with the velocity dispersion of the central cluster-scale mass component in the lens model of A 383. We also plot a number of other constraints from the literature that are based on other predictions of SIDM: gravothermal core collapse (Hennawi & Ostriker 2002), flat cores in clusters (Arabadjis et al. 2001), and evaporation of satellite dark matter halos (Gnedin & Ostriker 2000). We identify a small region of parameter space that both satisfies the observational constraints, and solves the apparent discrepancies between observation and the CDM theory. For SIDM to be a viable solution, the parameters are constrained by the observations to lie in the ranges: $1.6 \lesssim a \lesssim 3.4$

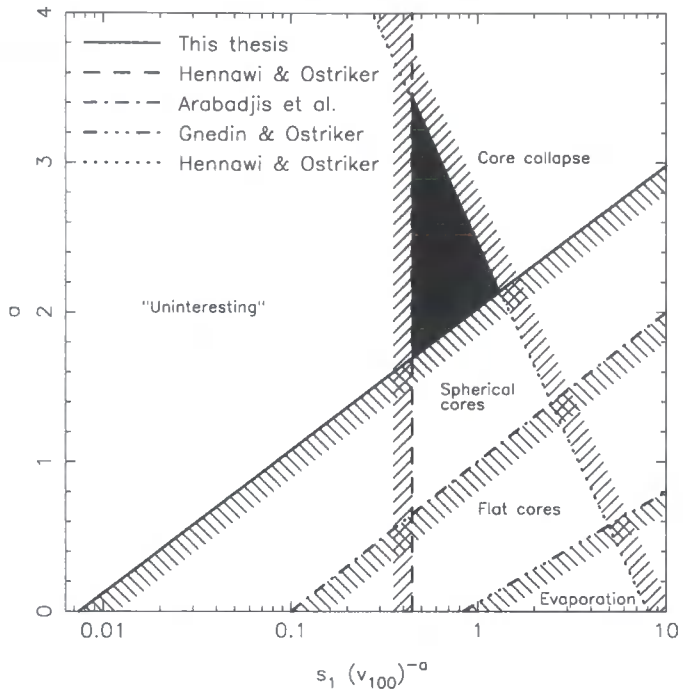

Figure 4.7: Constraints on the cross-section of dark matter particles to self-interaction. This figure is adapted from Henawi & Ostriker (2001), and shows our new constraint on $s_{\rm dm}$, obtained from the distribution of matter in the central $r \lesssim 20$ kpc region of A 383. The allowed region of parameter space is indicated by the black triangle.

and $0.45 \lesssim s_1 v_{100}^{-a} \lesssim 1.5$. In physical terms this means that the velocity dependence of $s_{\rm dm}$ must be strong enough that both the observed cusps in the centres of galaxy clusters (§4.2 & §3.6.3) are not destroyed by the interactions, but yet the density profiles of galaxy-scale halos are sufficiently flattened to match the observational data.

4.3.3 Discussion and Conclusions

We briefly discuss the uncertainties in our analysis and consider potential future avenues of investigation.

First, we consider the impact of baryons on our estimate of $s_{\rm dm}$. We have carefully selected the two radial arcs used in our analysis to ensure the minimum contamination from baryons (§4.3.1). Nevetheless, the clusters do contain baryons and this material presumably does have some affect on the shape of the cluster potential. Although the baryonic and non-baryonic material is assumed not to interact with each other, the baryons (specifically the hot intracluster gas) do interact with each other, and these interactions will act in the sense of thermalising and thus

circularising the gas distribution. We have been careful to restrict our analysis to radial arcs whose properties are dominated by the dark matter; we estimate that at a projected distance of $r = 20$ kpc from the centre of A 383, the baryons contribute $\lesssim 25\%$ to the total mass density. It seems unlikely that self-interaction between baryons may be biasing our result. However, if the baryons play a stronger role than we anticipate in determining the matter distribution at the positions of B1d and C1d, then this should have the effect of making the matter distribution more circular than it would otherwise be. Any low level contamination of our analysis by baryons would therefore cause us to over-estimate $s_{\rm dm}$. Our upper limit of $s_{\rm dm} \lesssim 7 \times 10^{-3}$ cm^2 g^{-1} therefore appears to be reasonably secure.

The recent simulations of Colín et al. (2002) are perhaps a more fundamental challenge to the results presented here. Colín et al. used high-resolution numerical simulations of both Milky Way and cluster mass collisionless and self-interacting dark matter halos to study the differences between the predicted properties of these two hypotheses. They concluded that the core of SIDM halos appear to be rounder than their collisionless counterparts, but they are not spherical. This suggests that Spergel & Steinhardt's prediction that the centres of SIDM halos are spherical may be an over-simplification, although it clearly does convey the sense of the comparison with collisionless dark matter. Unfortunately, Colín et al. did not quantify this effect, and so it is difficult to assess the impact of it on our results.

In summary, we have exploited our suite of detailed lens models (§3) to place a new upper limit on the cross-section of dark matter to self-interaction ($s_{\rm dm}$). Assuming that $s_{\rm dm}$ is independent of particle velocity, we obtain $s_{\rm dm} \lesssim 7 \times 10^{-3}$ cm^2 g^{-1}, which would exclude SIDM as a solution to the disagreement between collisionless dark matter predictions and observations of galaxy-scale halos. If we assume that $s_{\rm dm}$ depends on some power of the particle velocity (Equation 4.5), then we find that the allowed region of parameter space is quite small, and $1.6 \lesssim a \lesssim 3.4$ and $0.45 \lesssim s_1 v_{100}^{-a} \lesssim 1.5$. It therefore appears that a strong dependence of $s_{\rm dm}$ on particle velocity is essential to reconcile the presence of the central density cusps in and ellipticity of galaxy clusters with the conflicts between collisionless dark matter and observations on galaxy scales.

We have also discussed the principal uncertainties in our analysis and conclude that improved constraints on $s_{\rm dm}$ from cluster lensing require a larger number of well-constrained lens models plus more extensive high-resolution numerical simulations to aid in the interpretation of the observational results.

4.4 Normalisation of the Matter Power Spectrum

The amplitude of matter fluctuations in the Universe is an important constraint on theoretical models of large-scale structure formation (e.g. Press & Schechter 1974; Bond et al. 1991; Lacey & Cole 1993; Jenkins et al. 2001). One of the strongest observational constraints on this amplitude comes from the most massive clusters of galaxies, because they probe the most massive and thus rarest collapsed structures[‖].

In CDM models, the amplitude of the mass power spectrum is conventionally described by the linear-theory value of the rms fractional fluctuations in density averaged in spheres of 8 h^{-1}Mpc [**] radius, σ_8 . In principal, measurements of the cluster mass function, $n(>M)$, should yield a direct constraint on σ_8. However, it has not so far been possible to measure directly cluster masses with the precision and in the numbers required to construct directly a robust observed cluster mass function. In contrast, the local cluster X-ray temperature function, $n(>T)$, has proved more accessible (e.g. Edge et al. 1990; Henry & Arnaud 1991; Markevitch 1998; Blanchard et al. 2000; Pierpaoli et al. 2000; Ikebe et al. 2002). The X-ray temperature function in conjunction with a robust calibration between mass and X-ray temperature therefore offers an opportunity to constrain σ_8.

Attempts to calibrate the mass-temperature relation have so far concentrated on theoretical studies using both numerical simulations and analytic models (e.g. Evrard, Metzler & Navarro 1996; Voit 2000; Pearce et al. 2000; Thomas et al. 2002; Voit et al. 2002), analysis of X-ray observations of clusters under the assumption of circular symmetry and hydrostatic equilibrium (e.g. Markevitch 1998;

[‖]The predicted mass function decays exponentially at high mass – see for example Press & Schechter (1974).

[**]In this section we also express the Hubble parameter in terms of h, where $H_o = 100\,h^{-1}\,{\rm km\,s^{-1}Mpc^{-1}}$.

Nevalainen, Markevitch & Forman 2000; Finoguenov, Reiprich & Böhringer 2001; Allen, Schmidt & Fabian 2001; Reiprich & Böhringer 2002), and a lensing analysis of a sample of lensing clusters drawn from the literature (Hjorth et al. 1998). Superficially, these methods appear to be converging on a robust mass-temperature relation; for example, Voit et al. (2002) find agreement between the mass-temperature relation derived from their modified entropy model and the observed relations of Finoguenov, Reiprich & Böhringer (2001). However, despite the apparent excellent agreement between their analytic model and the X-ray data, Voit et al. voice the concern that both their model and the X-ray analyses assume that the hot X-ray emitting plasma is in hydrostatic equilibrium with the gravitational potential of the cluster. Our lensing analysis (§3) supports this view, as the clusters in our sample show many features of dynamical activity, suggesting that these assumptions may be invalid. There is therefore an urgent need to construct a cluster mass-temperature relation which is independent of this assumption. The simplest route to achieve this is to exploit gravitational lensing observations to measure the cluster masses. Hjorth et al. (1998) were the first to construct a lensing-based mass-temperature relation. Unfortunately this pioneering study relied on a heterogeneous sample of cluster drawn from the literature and consequently, their cluster selection function is poorly characterised and it is difficult to quantify robustly the uncertainties in their analysis. Nevertheless, the Hjorth et al. (1998) study was an important step in the right direction (see also Sheldon et al. 2002).

Our detailed *HST* lens models and analysis of *Chandra* data provide the most precise cluster mass and temperature measurements available thus far. Our objective selection criteria also give us confidence that our sample is free from gross biases to any particular sub-set of the overall cluster population. We are therefore presented with an opportunity to significantly improve the reliability of the mass-temperature calibration.

In §3 we compared the cluster masses derived from our lens models with the cluster temperatures based on archival *Chandra* observations (§3.7.3). We found that the normalisation of our lensing-based cluster mass-temperature relation is hotter than the cooling flow cluster relation of ASF (§3.7.3; Fig. 3.18). We investi-

gate the impact of this new, hotter mass-temperature relation on the normalisation of the matter power spectrum using a simple model and the observed temperature function (Edge et al. 1991).

In the next section we describe a model (Dr. Vincent Eke, priv. comm.) to translate our mass-temperature normalisation into a constraint on σ_8; we investigate the possible systematic effects that may bias our results in §4.4.2. We then discuss our result and summarise our conclusions in §4.4.3.

4.4.1 Modelling and Analysis

We parameterise the mass-temperature relation:

$$T_{\rm X,tot}\ ({\rm keV}) = A(M_{2500}/10^{14}\,h^{-1}\,{\rm M}_\odot)^\alpha \tag{4.6}$$

where $T_{\rm X,tot}$ is the cluster temperature measured within a projected radius of $r \leq 2$ Mpc, M_{2500} is the projected mass[††] within the radius at which the cluster density falls to $2,500\times$ the critical density required to close the Universe. We use a mass-dependent concentration index following Eke, Navarro & Steinmetz (2001) to convert the Jenkins et al. (2001) mass function, which gives the total halo mass, to M_{2500}, and we equate M_{2500} with our measurements of $M_{\rm tot}\,(\Sigma > 2.9\times10^8\ {\rm M}_\odot{\rm kpc}^{-2})$ presented in Table 3.6 and §3.7.3. For a given mass-temperature normalisation and scatter we then convert this M_{2500} function into a predicted temperature function and compare this with the observed cluster temperature function (Edge et al. 1991). Our model uses the following parameter set: $\{\Omega_{\rm o},\ \Lambda_{\rm o},\ \Gamma,\ \sigma_8,\ A,\ \sigma_T,\ \alpha\}$ where $\Omega_{\rm o}$ and $\Lambda_{\rm o}$ are the matter density and vacuum energy density of the Universe at $z = 0$, Γ is the spectral shape parameter for the power spectrum, σ_8 is the power spectrum normalisation discussed above, A is the normalisation of the cluster mass temperature relation, σ_T is the scatter in $\log(T_{\rm X,tot})$ at a fixed mass and α is the slope of the mass-temperature relation. We focus our attention on the behaviour of σ_8, A and to a lesser extent σ_T; we therefore adopt nominal "concordance" values for the

[††]When projecting three-dimensional masses to two-dimensional masses, we assume that on average the projected mass within a given radius is $1.5\times$ the three-dimensional mass within the same radius (Hjorth et al. 1998).

remaining input parameters: Ω_o= 0.3, Λ_o= 0.7, Γ = 0.2, α = 2/3 (e.g. Efstathiou et al. 2002; ASF).

We begin by converting the normalisation of ASF's mass-temperature relation for relaxed cooling flow clusters into the form required for our model (A = 2.6, $\sigma_T \sim 0.03$) and find that σ_8= 0.9 gives a reasonable agreement with the observed temperature function (Fig. 4.8). We then re-compute the model temperature function using our hotter normalisation (A = 4.4), whilst keeping σ_T and σ_8 fixed at 0.03 and 0.9 respectively. This temperature function over-predicts the amplitude of the observed temperature function by a factor of ~ 10. We re-run the model with progressively lower values of σ_8 and find that we need $\sigma_8 = 0.75 \pm 0.05$[‡‡] (i.e. $\sim$ 20% lower) in order to reconcile our mass-temperature normalisation with the observed temperature function. Finally, we increase the scatter in temperature to that found in our survey (σ_T = 0.1), and conclude that this higher scatter decreases σ_8 by $\lesssim 5\%$.

Taken at face value, this result implies that when a mass-temperature normalisation derived from relaxed, cooling-flow clusters is applied to the entire cluster population, the normalisation of the matter power spectrum is over-estimated by $\sim$ 20%. We identify the cause of this discrepancy as the dynamical activity present in our cluster sample (70% of our sample display evidence of dynamical immaturity) which boosts the temperature of clusters relative to relaxed clusters of similar mass, thus boosting the normalisation of the mass-temperature relation.

We test this interpretation by splitting the Edge et al. temperature function into dynamically relaxed and unrelaxed systems. There is no overlap between the Edge et al. sample and our sample, and so we are unable to use detailed lens model results to split their sample. Instead, we use the strong observational correlation between line emission from the cluster central galaxies and short cooling timescales ($t_{\rm cool} \lesssim 10^9$ years - Edge et al. 1991; Peres et al. 1998; Crawford et al. 1999) as a good indicator of a relaxed mass morphology. We plot the emission-line and non-emission-line temperature functions in Fig. 4.8 together with the respective model

[‡‡]The uncertainty quoted on this estimate of σ_8 the 1–σ statistical error estimated from the χ^2 fit of the model to the observed temperature function.

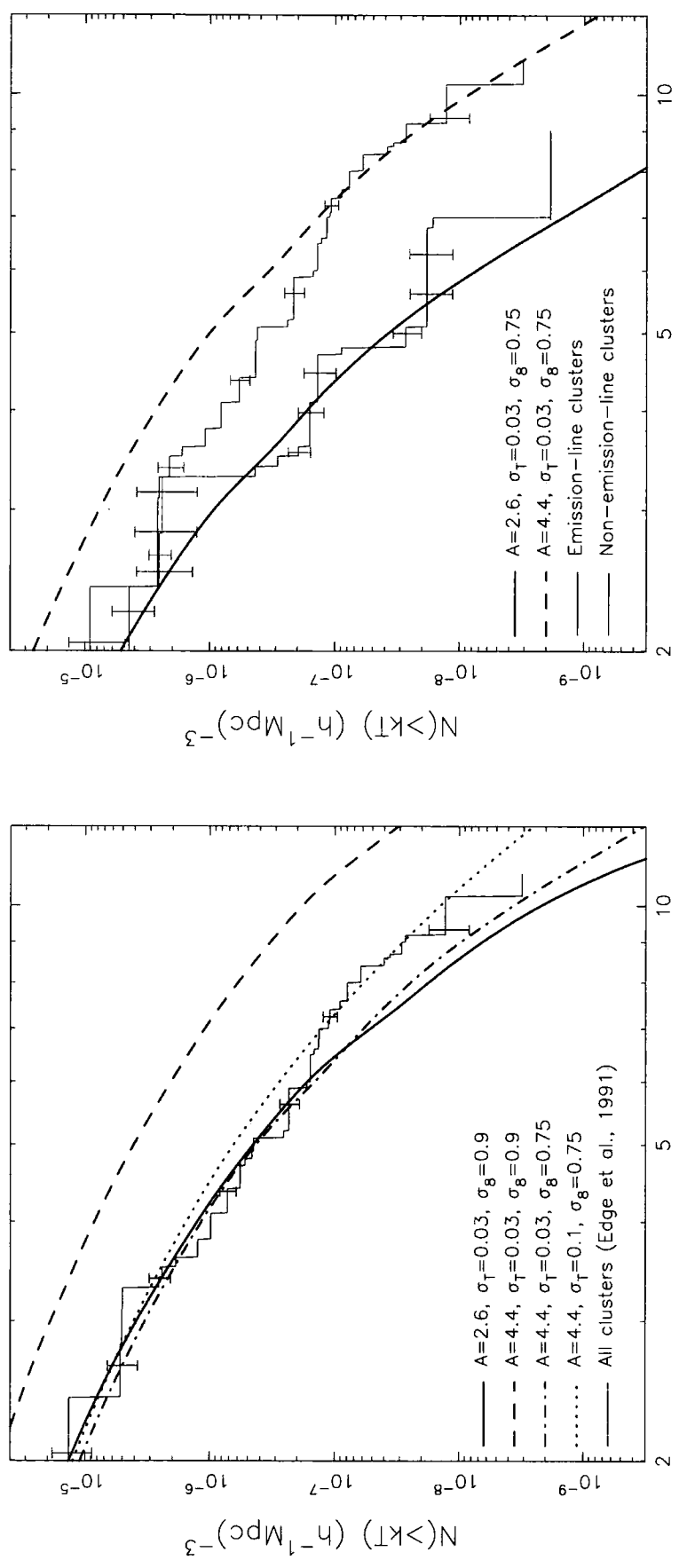

Figure 4.8: LEFT – The curves show model temperature functions based on the Jenkins et al. (2001) mass function and normalisations of the cluster mass-temperature relation taken from §3 and Allen, Schmidt & Fabian (2001). We compare these models with the observed temperature function of Edge et al. (1991). This panel shows the compares the model with the temperature function of the full Edge et al. sample. RIGHT – This panel splits the Edge et al. temperature function into clusters with central galaxies from which line emission has or has not been detected.

temperature functions. Looking at the overall picture, we find that a single (low) value of σ_8 matches the observed temperature function of both emission-line (relaxed) and non-emission-line (dynamically active) clusters when mass-temperature normalisations appropriate to each sub-sample are used in the calculations.

We note that for temperatures below $\sim$ 5 keV, the Edge et al. non-emission-line temperature function lies $\sim$ 20–50% below the model in Fig. 4.8. This may be due to incompleteness in the non-emission-line sub-sample because if merging systems have a lower flux and central surface brightness than the emission-line systems, then they will be preferentially missed in a flux limited sample. There may also be a systematic trend towards incompleteness at the cool end of the temperature function.

4.4.2 Systematic Uncertainties

Our results pinpoint and quantify merger-induced boosts to cluster temperatures as a major systematic uncertainty in the use of cluster abundances to constrain σ_8. Using our normalisation of the mass-temperature relation from our sample of ten X-ray luminous clusters at $z \sim 0.2$, we estimate that $\sigma_8 = 0.75 \pm 0.05$ where the quoted uncertainty is the 1–σ statistical uncertainty from our model fits. We now review our model and its inputs to identify further possible systematic uncertainties in our analysis. We identify the following systematic uncertainties:

- Conversion of our mass estimates within the small field of view of our *HST* observations to virial masses described the Jenkins et al. (2001) mass function.

- Potential systematic errors in the mass measurements of the clusters in our sample that are constrained by just their weak-shear signal.

- Possible projection effects that may lead us to over-estimate the mass of some clusters.

We discuss and attempt to quantify each of these effects below.

Conversion to Virial Mass Estimates

We explore whether the relatively small field of view of our *HST* observations and lens models could bias our result through its restriction of our analysis to the central $r \lesssim 500$ kpc of each cluster. This uncertainty manifests itself in our model when we convert the Jenkins et al. (2001) mass function from virial masses to the smaller aperture masses that we measure from our detailed lens models. However, from an empirical point of view, the crux of the issue is the level of uncertainty introduced into our model by effectively extrapolating our lens models out to the virial radius of each cluster. Kneib et al. (in prep.) will investigate this question in detail when they analyse the weak-shear signal in our panoramic ($28'' \times 42''$) CFH12k BRI–band imaging of our cluster sample. Prior to the completion of this wide-field analysis, we note that weak lensing analyses of individual clusters (e.g. King, Clowe & Schneider 2002) are unable to discriminate between isothermal ($\rho \propto r^{-2}$) and Navarro, Frenk & White (1997) ($\rho \propto r^{-3}$) profiles on large scales. We therefore exploit this lack of power in single-cluster weak-lensing studies to derive a conservative estimate on the systematic uncertainty in extrapolating our mass estimates for ten clusters out to the cluster virial radii. Specifically, we integrate both profiles over the radial range $0.5 \lesssim r \lesssim 3.0$ Mpc (i.e. the dynamic range over which we are extrapolating), and estimate that the uncertainty in profile shape introduces an uncertainty in the virial mass estimate for an individual cluster of $\sim 30\%$, which translates into an uncertainty in cluster temperature (assuming $M \propto {T_{\rm X}}^{3/2}$) of $\sim 20\%$. We use our model to estimate that this equates to an uncertainty in σ_8 of $\sim 10\%$.

Weak-shear Constrained Clusters

The reliance on just the weak-shear signal to measure the mass of five clusters in our sample may also bias the calibration of the cluster mass-temperature relation and thus our estimate of σ_8. We investigated this issue in §3.6.4 when we used the five clusters which contain multiple-images to estimate the systematic uncertainty in the mass measurements of the five clusters which do not contain multiple-images. We found that, although solely weak-shear constrained models agree with solely multiple-image constrained models within the statistical uncertainties, there was a

small systematic offset between the two mass determinations in the sense that mass estimates based on weak-shear constrained models appear to be $12 \pm 8\%$ lower than multiple-image constrained models of the same clusters. This systematic is probably caused by the contamination of the background galaxy catalogues by faint cluster galaxies (Fig. 3.11). Given that half of the clusters do not contain any multiple-images, this implies that we may have under-estimated the mean cluster mass of the whole sample by $\sim 6\%$, which gives a $\sim 4\%$ uncertainty in $T_{\rm X}$ in the mass-temperature normalisation and, from our model, a $\sim 2\%$ systematic uncertainty in σ_8.

Projection Effects

Finally, we discuss the possibility that projection effects that may cause us to over-estimate the three-dimensional mass associated with the cluster potential-wells in our sample. We discussed this issue in §3.8 and identified two clusters (A 773 and A 2218) whose mass estimates might be affected in this manner, although we favoured alternative explanations for their positions in mass-temperature space in both cases. Nevertheless, we conservatively adopt the most extreme picture described in §3.8, and quantify the impact of reducing the mass of these two clusters by 40%. The mean cluster mass would fall by $\sim 8\%$, leading to a $\sim 5\%$ uncertainty $T_{\rm X}$ in the mass-temperature normalisation and a systematic uncertainty of $\sim 3\%$ in σ_8.

Summary

We have investigated several potential systematic uncertainties that may affect our measurement of $\sigma_8 \sim 0.75$. We conclude that the overall systematic uncertainty on our measurement of σ_8 is $\sim$ 11–15%, depending on the degree of correlation between the different effects. We conservatively adopt the upper end of this range, and combine it with the statistical uncertainty to estimate that $\sigma_8 = 0.75 \pm 0.05({\rm statistical}) \pm 0.11({\rm systematic})$.

4.4.3 Discussion and Conclusions

Although the measurement of $\sigma_8 = 0.75 \pm 0.05 \pm 0.11$ is formally consistent with previous estimates of $\sigma_8 \sim 0.9$, the range of σ_8 encompassed by our result means that it joins a growing body of evidence for $\sigma_8 \sim 0.6$–0.8 (Viana, Nichol & Liddle 2002; Seljak 2001; Reiprich & Böhringer 2001; Borgani et al. 2001; Lahav et al. 2002) in contrast to the canonical value of $\sigma_8 \sim 0.9$–1 (e.g. Eke, Cole & Frenk 1996, 1998; Carlberg et al. 1997; Bahcall & Cen 1998; Pen 1998; Pierpaoli et al. 2001). Regardless of the relative merits of these previous works, each camp generally attributes the difference between these values of σ_8 to systematic effects in the various techniques and few proposals have been made for any physical processes which could cause the discrepancy. Also, few of these authors attempt to quantify the possible systematic uncertainties in their analysis, and we note that, with the exception of Viana, Nichol & Liddle's (2002) use of Sheldon et al.'s (2001) weak lensing results, none of these previous studies have used gravitational lensing to measure cluster masses.

In contrast, our result and interpretation of the differences between estimates of σ_8 in terms of a merger-driven temperature boost in the normalisation of the cluster mass-temperature relation flows naturally from our detailed lens modelling and precise cluster mass and substructure measurements. Independent confirmation of this physical interpretation comes from Randall et al. (2002) who used semi-analytic techniques to investigate the effect of cluster mergers on the observed luminosity and temperature functions, and thus on the inferred cluster mass function. Randall et al.'s results are strikingly similar to our own; they predict that merger boosts to the observed temperature function can cause σ_8 to be over-estimated by $\sim 20\%$ if hydrostatic equilibrium is assumed. We also review and estimate the magnitude of a number of sources of systematic error in our method.

Interestingly, cosmic shear studies which use the statistics of the multiple light-deflections by large-scale structure to constrain the cosmological parameters, find $\sigma_8 \simeq 0.9$ in a flat universe with $\Omega_o = 0.3$ (see Mellier et al. (2002) for a recent review). In contrast to studies of cluster lensing, cosmic shear studies therefore contradict the growing voice for a low value of σ_8. Whilst a cosmic shear signal appears to have

been convincingly detected by several groups (Bacon et al. 2000, 2002; Hoekstra et al. 2002; Kaiser, Wilson & Luppino 2000; Maoli et al. 2001; Refregier, Rhodes & Groth 2002; van Waerbeke et al. 2000, 2001, 2002; Wittman et al. 2000), a number of systematic uncertainties persist, including possible unidentified and/or poorly characterised instrumental effects and intrinsic alignment of galaxies due to effects other than lensing (e.g. Heavens et al. 2000; Catelan et al. 2001; Crittenden et al. 2001, 2002; Mackey et al. 2002; Brown et al. 2002). Such effects would generally lead to an artificial enhancement of the cosmic shear signal, and thus an over-estimate of σ_8.

Experiments that measure the anisotropy of the Cosmic Microwave Background (CMB) also provide independent constraints on σ_8 (e.g. Sievers et al. 2002). In fact, Bond et al. (2002) have recently suggested that the excess power detected in Cosmic Background Imager (CBI) maps of the CMB at multipoles of $\ell > 2000$ may be due to multiple Sunyaev-Zeldovich (1970 – SZ) scattering of CMB photons by hot electrons trapped in cluster potential wells along the integrated light-paths from the surface of last scattering. Bond et al. conclude that this is only a viable explanation of this CMB anisotropy if $\sigma_8 \sim 1$. However, Holder (2002) finds that this discrepancy could be resolved if the Universe was re-ionised at very early redshifts of ~ 25. Other plausible solutions including instrumental effects, a diffuse galactic foreground and residual point sources have all been highlighted by Mason et al. (2002), and have not been entirely ruled out. Attributing a fraction (or possibly all) of the $\ell > 2000$ excess to non-SZ effects would lower the value of σ_8 required to explain the excess. Perhaps the most persuasive evidence against Bond et al.'s high σ_8 interpretation of the $\ell > 2000$ excess is Lahav et al.'s (2002) joint analysis of data from the 2dF Galaxy Redshift Survey and three recent CMB anisotropy experiments (BOOMERANG, MAXIMA-1 and DASI). Lahav et al. find $\sigma_8 = 0.73 \pm 0.05$ in good agreement with our result.

In conclusion, much further work is needed to build a detailed understanding of the systematic uncertainties in the various methods used to measure σ_8. Our analysis is an important element of this endeavour as it quantifies for the first time the impact of cluster substructure on the use of cluster abundances to measure σ_8.

We also investigate the systematic uncertainties in our analysis and conclude from the current data that $\sigma_8 = 0.75 \pm 0.05$(statistical) $\pm$ 0.11(systematic).

4.5 Summary

We began by summarising the key observational challenges to the CDM paradigm (§4.1) and then exploited the density profile of A 383 (§4.2), the geometry of our lens models (§4.3) and our normalisation of the cluster mass-temperature relation (§4.4) to investigate the impact of our gravitational lensing experiment on these issues. We summarise our key results:

- The inner density profile of A 383 has a slope of $\alpha = 1.3 \pm 0.04$(statistical) $\pm$ 0.1(systematic) where $\rho \propto r^{-\alpha}$, ρ is the three-dimensional density and r is the three-dimensional radial coordinate. The density profile of A 383 is therefore consistent with the presence of a central cusp in the dark matter mass distribution predicted from simulations. Together with a number of other recent lensing studies (Dahle et al. 2002b; Sand, Treu & Ellis 2002) indicates that there is considerable scatter in the inner density profile of cluster-scale dark matter halos.

- Using the spatial distribution of mass in the central $\sim$ 20 kpc of A 383, constrained by radial arcs, we estimate a velocity independent dark matter cross-section t self-interaction of $s_{\rm dm,o} \lesssim 7 \times 10^{-3}$ cm^2 g^{-1}. This is significantly less than than the lower limit of $s_{\rm dm,o} > 0.45$ cm^2 g^{-1} estimated by Spergel & Steinhardt as required to reconcile CDM with the apparent observational challenges. We generalise our constraint on $s_{\rm dm,o}$ to a velocity dependent model $s_{\rm dm}\ (v) = s_{\rm dm,o}\ (v/v_{\rm o})^{-a}$ and combine it with other constraints from the literature to identify a small region of parameter space ($1.6 \lesssim a \lesssim 3.4$ and $0.45 \lesssim s_1\ v_{100}^{-a} \lesssim 1.5$*) that would resolve the galaxy-scale challenges to collisionless CDM.

*where $s_{\rm dm} = s_1\ v_{100}^{-a}$ and $s_1 = s_{\rm dm,o}$ /1 cm^2 g^{-1} and v_{100} is the particle velocity expressed in units of 100 km s^{-1}

- We use our new calibration of the cluster mass-temperature relation, to estimate that $\sigma_8 = 0.75 \pm 0.05(\text{statistical}) \pm 0.11(\text{systematic})$. We interpret the $\sim 20\%$ discrepancy between our estimate and the canonical value of $\sigma_8 \simeq 0.9$ as arising from the impact of the dynamical immaturity of most of the clusters in our sample on the ambient cluster temperatures, which gives rise to a hotter normalisation of the cluster mass-temperature relation. This is the first time that this systematic effect has been identified observationally, and is in agreement with the recent semi-analytic predictions of Randall et al. (2002).

In summary our survey appears to be good news for CDM. We find that cluster-scale halos probably do contain a central density cusp, and the alternative SIDM proposals appear to require a highly velocity-dependent cross-section to self-interaction. Regardless of these constraints on SIDM, our results support the growing body of evidence for a low value of σ_8. If true, this would reduce the overall normalisation of the matter power spectrum and thus should reduce the substructure predicted to occur on small scales. This would help to alleviate some of the galaxy-scale objections to CDM (e.g. Moore et al. 1999) and potentially remove the need to invoke SIDM in the first place.

5 A SEARCH FOR GRAVITATIONALLY LENSED EROs

Our lens models (§3) describe the detailed gravitational optics of our cluster sample. We therefore use the clusters to boost the sensitivity of our observations of faint high-redshift galaxies, using the lens models to relate our observations to "blank-field" studies and theoretical predictions of other groups.

We complement our *Hubble Space Telescope (HST)* imaging of the clusters with high-resolution ground-based near-infrared imaging (§5.1) and construct a sample of gravitationally-lensed EROs (§5.2). We discuss our results in §5.3 and compare the surface density of these galaxies with the predictions of various theoretical models. We list our main conclusions in §5.4. In contrast to the rest of this thesis, we assume H_o= 50 km s^{-1}Mpc^{-1}, Ω_o=0.3 and Λ_o= 0.7 because this makes comparison of our observational results with theoretical predictions more transparent.

5.1 Observations

5.1.1 *HST*/WFPC2 Optical Imaging

We describe the *HST* data used in this chapter and the reduction of these data in §3. We list these observations in Table 5.1.

We adopt the photometric system from Holtzman et al. (1995) and choose to convert the R_{702} photometry to Cousins R–band to aid in comparing our results with previous surveys. To achieve this we adopt a $(V-R)$ colour for an Sbc galaxy at z = 1–2 of $(V-R) \sim 1.1$, based on spectral templates derived from local galaxies. This translates into a correction of $R-R_{702} \sim 0.4$ with a systematic uncertainty of $\lesssim 0.1$ magnitudes arising from the likely presence of both more and less evolved galaxies than the adopted Sbc spectral type. The equivalent correction for galaxies with the $(V-R)$ colours of cluster ellipticals at $z \sim 0.2$, $(V-R) \sim 0.9$, is $R-R_{702} \sim 0.3$, with an estimated systematic uncertainty of $\lesssim 0.05$. Both of these

Table 5.1: Details of F702W and K–band Observations

Cluster	Redshift	$E(B-V)$	F702W	K–band							N_{ERO}	
				WF2		WF3		WF4		Depth	$(R-K) \geq$	
			T_{F702W} (ks)	T_K (ks)	FWHM ($''$)	T_K (ks)	FWHM ($''$)	T_K (ks)	FWHM ($''$)	$K(80\%)$	5.3	6.0
UKIRT Observations												
A 68	0.255	0.093	7.5	8.8	0.43	8.0	0.48	7.5	0.50	20.51	9	5
A 209	0.209	0.019	7.8	6.5	0.53	6.5	0.51	6.5	0.38	20.42	7	2
A 267	0.230	0.025	7.5	6.5	0.37	6.5	0.40	4.4	0.38	20.69	12	5
A 383	0.187	0.033	7.5	6.5	0.59	6.7	0.57	6.5	0.42	20.65	11	6
A 773	0.217	0.015	7.2	6.5	0.65	6.5	0.55	9.7	0.67	20.52	1	0
A 963	0.206	0.015	7.8	6.5	0.59	6.5	0.52	6.5	0.70	20.64	12	6
A 1763	0.228	0.009	7.8	6.5	0.58	6.5	0.55	6.5	0.69	20.65	5	2
A 1835	0.253	0.030	7.5	6.5	0.48	6.5	0.44	6.5	0.45	20.58	1	0
A 2219	0.228	0.024	14.4	6.5	0.60	9.7	0.60	6.5	0.51	20.67	2	0
WHT Observations												
A 2218	0.171	0.024	6.5			8.3 ks	0.75″			21.50	0	0

corrections are sufficiently accurate to define a sample of EROs in these fields. The final WFPC2 frames have a typical 3–σ detection limit within our 2″–diameter photometry aperture of $R \sim 26.6$.

5.1.2 Near-infrared Imaging

The near-infrared (K–band) imaging essential for identifying EROs was obtained for nine of the ten clusters with the UFTI imager on the 3.8–m United Kingdom Infrared Telescope (UKIRT)*. UFTI incorporates a 1024^2 Hawaii-1 detector providing a 92″ field of view with 0.0908″ pixel^{-1} sampling – necessary to sample the best seeing provided by UKIRT, $\lesssim$ 0.2–0.3″. The K–band imaging of these fields was obtained in two observing runs in 2000 April 4–7 and September 26–29. Conditions during both observing runs were good, with reasonable seeing and transparency. Each WFPC2 field was covered in three pointings (one per WFC chip: WF2, WF3 and WF4), although the different roll-angles for the various WFPC2 observations means that a particular near-infrared exposure may overlap more than one WFC chip. The individual pointings usually consist of 54×120–s exposures grouped into six sets of nine exposures, or occasionally 72×90–s exposures in eight sets of nine, each exposure being offset on a 3×3 grid with 10″ spacing, and the origin of each set was randomly moved by $\sim$ 3″. We list the total exposure times for the individual pointings (T_K) and the seeing for each in Table 5.1. The median seeing for these 2–hr integrations is 0.5″.

The data were reduced using the dedicated UFTI summit data pipeline (Currie et al. 1999) including dark subtraction, flat fielding using a local median sky, resampling onto an astrometric grid and combining to remove defects and cosmic ray events. A small amount of the data was re-reduced in Durham following a similar scheme and using standard IRAF tasks. Calibration was obtained from UKIRT Faint Standards (Casali & Hawarden 1992) interspersed throughout the science observations. We estimate that our absolute calibration is good to $\lesssim$ 0.05 mag. A reddening correction of $E(R-K) = 2.31E(B-V)$, was also applied to the $(R-K)$

*UKIRT is operated by the Joint Astronomy Centre on behalf of the Particle Physics and Astronomy Research Council of the United Kingdom.

colours following Schlegel et al. (1998). The final UFTI K–band images typically reach a median 80% completeness of $K \sim 20.6$ (Table 5.1). For comparison a passively evolving L^* elliptical will have $K \sim 18$–19 at $z = 1$. We show an example of one of our fields in Fig. 5.1.

The tenth cluster, A 2218, was observed in commissioning time with the new INGRID near-infrared imager (Packham et al. 2002) on the 4.2–m William Herschel Telescope (WHT)†. INGRID comprises a 1024^2 Hawaii-1 detector giving a 248″ field of view with 0.242″ pixel^{-1} sampling. These data comprise a 8.3 ks exposure of the whole WFPC2 field in A 2218 (Kneib et al. 1996) in the K_s–band. The seeing on the final stacked frame is 0.75″ and the frame reaches an 80% completeness limit of $K = 21.5$ for point sources. The reduction, calibration and analysis of these data are discussed in more detail in Smail et al. (2001). For uniformity in our analysis we restrict ourselves to a limit of $K \leq 20.6$ in A 2218.

In addition to the K–band imaging described above, a sub-set of the cluster fields were also observed in the J–band. We observed A 773, A 963, A 1763 and A 1835 with UKIRT/UFTI on the nights of 2001 February 16 and April 4 in non-photometric conditions and $\sim$ 0.6″ seeing, and A 68 A 267 and A 2219 with WHT/INGRID on the nights of 2001 June 27 and 2001 May 6, in $\sim$ 0.8″ seeing and photometric conditions (Table 5.2). All of these observations were reduced in a similar manner to the K–band images. The UFTI observations reach an 80% completeness limit of $J \sim 21$, whilst INGRID frames reach 80% depths of $J \sim$20–21. Finally, a J–band image of A 2218 is also available from the INGRID commissioning observations of that cluster (Smail et al. 2001), however, as we find no ERO sources brighter than $K = 20.6$ within that field, we do not discuss these data further.

5.1.3 Ground-based Optical Imaging

To study the spectral energy distributions of EROs between the R– and K–bands, we also make use of archival I–band imaging of the clusters in our sample. These

†Based on observations made with the William Herschel Telescope operated on the island of La Palma by the Isaac Newton Group in the Spanish Observatorio del Roque de los Muchachos of the Instituto de Astrofisica de Canarias

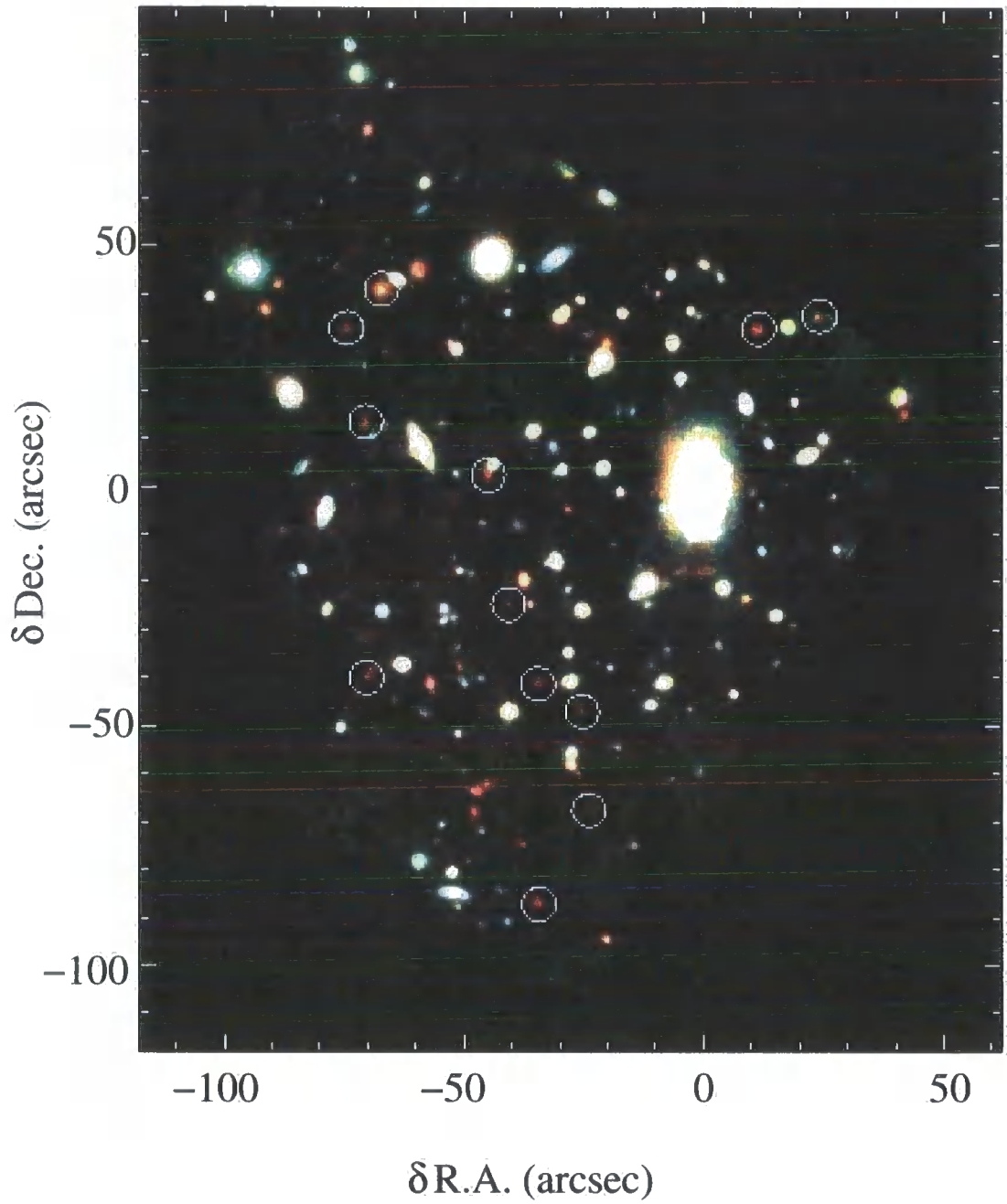

Figure 5.1: An example cluster field from our *HST*/UKIRT survey, showing a true colour *RIK* image of the core of A 963. The circles indicate the thirteen EROs with $(R-K) \geq 5.3$ detected in this field. The two EROs north-west of the cD appear to be elliptical galaxies with similar redshifts on the basis of their optical/near-infrared colours and morphology (§5.2). The field is centred on the cluster cD and has North top and East left. Note the very blue giant arc visible south of the cD.

Table 5.2: Summary of I– and J–band Observations

Cluster	I–band		J–band		
	T_I (ks)	FWHM (″)	T_J (ks)	FWHM (″)	Field(s) Observed[a]
A 68	3.6	0.7	3.2	0.8	WFPC2
A 209	3.6	0.7	...	...	...
A 267	0.9	0.7	1.3	0.8	WFPC2
A 383	3.6	0.7	...	...	...
A 773	0.9	1.4	3.2	0.6	WF4
A 963	0.6	1.1	3.2	0.6	WF2/3/4
A 1763	0.5	1.1	3.2	0.6	WF2/4
A 1835	1.0	1.1	3.2	0.6	WF2
A 2218	21.7	0.9	6.5	0.8	WFPC2
A 2219	0.5	1.1	2.2	0.8	WFPC2

(a) The I–band observations cover the whole WFPC2 field of view. For the J–band: WFPC2 denotes WHT/INGRID observations which cover the whole field; WF2/3/4 indicate UKIRT/UFTI imaging of a particular WFC chip.

observations come from a number of ground-based 4–m class telescopes and comprise 0.5–3.6 ks integration in 0.7–1.4″ seeing (Table 5.2), reaching $I \gtrsim 23$. We use panoramic imaging of A 68, A 209, A 267 and A 383 from the CFH12k camera on the 3.6–m Canada-France-Hawaii Telescope,[‡] taken on 1999 November 10–14. More details of their reduction and analysis can be found in Czoske (2002). For A 773 and A 963 we use I–band images taken on 1994 December 8–9 with PFCCD of the 4.2–m William Herschel Telescope[§]. Finally, we exploit imaging of A 1763, A 1835, A 2218 and A 2219 taken with the COSMIC imager spectrograph on the Hale 5–m[¶],

[‡]Based on observations made with the Canada France Hawaii Telescope, operated on the island of Hawaii by the Canada France Hawaii Telescope Corporation

[§]Based on observations made with the William Herschel Telescope operated on the island of La Palma by the Isaac Newton Group in the Spanish Observatorio del Roque de los Muchachos of the Instituto de Astrofisica de Canarias

[¶]This work is based on observations obtained at Palomar Observatory, which is owned and operated by the California Institute of Technology

more details of these observations and details of their reduction can be found in Smail et al. (1998) and Ziegler et al. (2001).

5.2 Analysis and Results

5.2.1 Source Detection and Photometry

The near-infrared images of each cluster were aligned and mosaiced together (if necessary) to create one K–band frame per cluster that covers the relevant WFPC2 field of view. The WFPC2 frames were rotated and aligned to the K–band frames with an rms tolerance of $\lesssim 0.01''$ and the whole field astrometrically calibrated using the APM catalogue to an absolute accuracy of $0.4''$.

To produce a catalogue of EROs in these fields we first analysed the K–band frames using the SExtractor package (Bertin & Arnouts 1996). All objects with isophotal areas in excess of 10 pixels ($0.082\,\mathrm{arcsec}^2$) at the $\mu_K = 23\,\mathrm{mag\,arcsec}^{-2}$ isophote ($1.5\sigma\,\mathrm{pixel}^{-1}$) and lying within the WFPC2 field of view were selected. Across the ten clusters, this survey covers a total area of 49 arcmin^2, excluding the PC chips, and these catalogues contain a total of 2,382 sources. We adopt the MAG_BEST magnitude computed by SExtractor as the total K–band magnitude of each source.

We perform extensive ($\sim 10^4$ realisations) Monte Carlo simulations to measure the completeness limits of these catalogues by suitably scaling and re-inserting a moderately bright ($K \sim 19$), compact ERO source into the science frames. The resulting 80% completeness limits (roughly equivalent to 5–σ detection limits) are presented in Table 5.1. We also re-perform these simulations using a more diffuse galaxy of similar magnitude, and find that the typical 5–σ limiting depth was $\lesssim 0.3$ magnitudes brighter than that for the compact source. This difference is not large enough to have a significant impact on the results presented in this chapter.

We measured the $(R-K)$ colour of all these sources using a $2''$ diameter aperture on seeing matched R– and K–band frames. As the image smoothing required to match the seeing reduces the pixel-to-pixel variation in the sky backgrounds, the noise estimates from the seeing-matched frames are compromised. We there-

fore exploited the overlap regions between the three UFTI pointings used to cover each *HST* field to compare independent photometry of sources as a function of magnitude, and so derive conservative estimates of the photometric uncertainties as a function of magnitude. We applied the same principle in the R–band, taking advantage of the six 2.4 ks exposures of A 2219 (§3.2), to make independent measurements on two frames, each derived from an independent sub-set of three exposures. This provides a reliable and conservative estimate of the photometric errors of sources in the R–band. We also estimate the 5–σ depth of the R–band imaging to be $R = 26.0$. However, for the purposes of our final photometry we adopt a 3–σ R–band detection limit of $R = 26.6$ to discriminate between $(R - K) \geq 5.3$ and $(R - K) \geq 6.0$ (§5.2.2) sources lying close to both detection limits.

We show the $(R - K)$–K colour-magnitude diagrams for the ten clusters in Fig. 5.2. The strong sequences of red galaxies identifiable in all the panels correspond to the evolved early-type cluster members. These provide a useful check of the calibration of the $(R - K)$ colours for sources in these fields. We estimate that the rms scatter in the colours of the cluster early-type sequences at a fixed luminosity as a function of redshift is ~ 0.08 mag, confirming that any field-to-field offset between our photometry of galaxies detected in each cluster field is $\lesssim 0.08$ mag.

Finally, we measure the $(I-K)$ and $(J-K)$ (where J–band imaging is available) colours of the ERO sample defined in §5.2.2 using a 2″ diameter aperture on seeing-matched frames, adopting a 3–σ detection limit when no I– or J–band counterpart is detected.

5.2.2 ERO Selection

We adopt the definition of an ERO as a galaxy with $(R - K) \geq 5.3$ as used by Daddi et al. (2000a), and also employ a more stringent definition of $(R - K) \geq 6$ (Thompson et al. 1999). These sample boundaries are shown for the individual cluster fields in Fig. 5.2, we list the numbers of galaxies in each class in the various clusters in Table 5.1 and give a catalogue of the sources in Table 5.3.

We show in Fig. 5.3 the composite $(R - K)$–K colour-magnitude diagram for

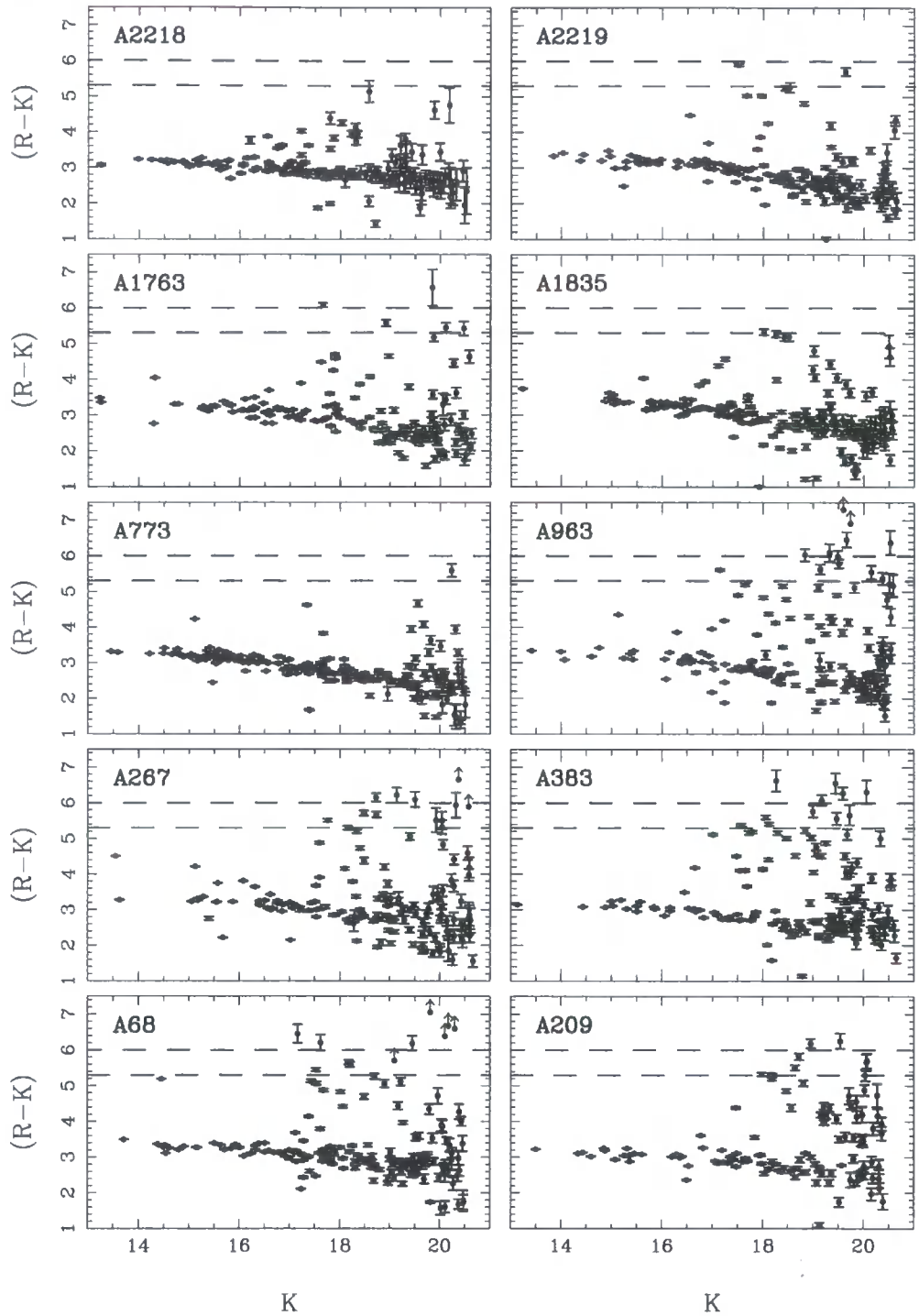

Figure 5.2: $(R-K)$–K colour-magnitude diagrams for the ten clusters in our survey, showing the order of magnitude field-to-field variation in ERO number counts. The K–band magnitudes in this figure are observed magnitudes (i.e. not corrected for gravitational amplification) and are plotted down to the 80% completeness limits listed in Table 5.1 (median 80% completeness limit is $K = 20.6$). The two dashed lines on each panel indicate the $(R-K) \geq 5.3$ and 6.0 ERO selection criteria respectively. Points marked by an upward pointing arrow are 3–σ limits in $(R-K)$.

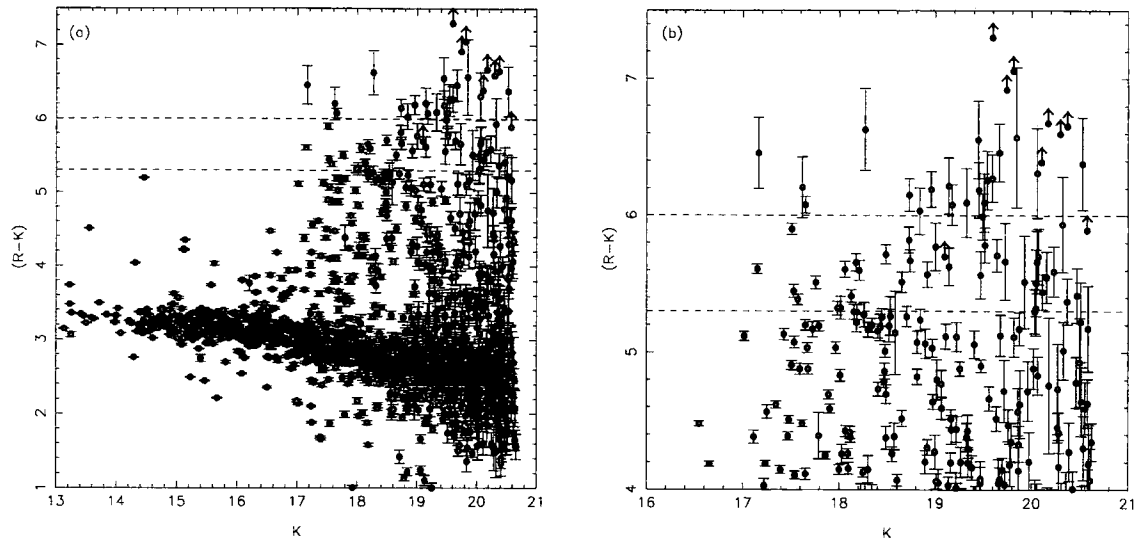

Figure 5.3: a) Composite $(R-K)$–K colour-magnitude diagram for the ten cluster fields in our survey. b) Zoom into $(R-K) > 4$ region of the composite $(R-K)$–K colour-magnitude diagram shown in (a). The two dashed lines in each panel indicate the $(R-K) \geq 5.3$ and 6.0 ERO selection criteria. Galaxies marked by an upward pointing arrow are 3-σ limits in $(R-K)$. We have co-added these objects and measure the typical R–band magnitude (in a 2″ diameter aperture) to be $R = 27.0 \pm 0.5$. This suggests that the galaxies not detected in the R–band are a continuation of the $(R-K) \geq 6.0$ population, rather than a distinct population of galaxies with much more extreme colours. Note, the K–band magnitudes plotted in this figure are observed magnitudes (i.e. not corrected for gravitational amplification).

all ten clusters, along with the sample boundaries. In total we find 60 sources with $(R-K) \geq 5.3$ in the ten fields (an image plane survey area of 49 arcmin^2) and 26 with $(R-K) \geq 6$ down to our median 80% completeness limit of $K = 20.6$.

In addition to the Monte Carlo simulations described in §5.2.1, we performed two further checks to verify the completeness of our ERO sample. First, we visually checked true-colour optical/near-infrared images of the clusters (e.g. Fig. 5.1) to guard against losing ERO candidates due to contamination of photometric apertures by nearby sources with less extreme colours. In two cases we re-calculated the colours of objects after masking the light from nearby galaxies to ensure a more reliable measurement. Second, we searched for EROs hidden under the halos of bright cluster ellipticals by subtracting a median-smoothed version of the each K–band frame from the original frame to produce a "difference" frame. This search revealed no further EROs.

These "difference" frames contain residual flux from the central regions of the bright cluster ellipticals, with the result that a fraction of each WFPC2 field of view remains obscured. We estimate this fraction, first thresholding the "difference"

frames at a level where the fainter EROs in our sample would not be detected. We then ray trace these thresholded frames back to the source plane (using our detailed lens models – §3). As the lens amplification is highest at the cluster centre and the centre of other bright cluster ellipticals, the transformation to the source plane results in the obscured fraction of each field of view being typically $\lesssim 5\%$.

We estimate contamination of the sample by red, low mass stars by visually comparing the K–band morphologies of the 19 EROs in our sample with a FWHM $\leq 0.8''$ to the images of morphologically-classified stars selected from the *HST* frames. Only one of these sources (ERO J024805−0330.2) has a star-like morphology; we therefore flag it as a possible star or AGN, but choose not to remove it from our analysis. This very low level of stellar contamination ($\leq 1.5\%$) is consistent with that determined by Daddi et al. (2000a) and Thompson et al. (1999).

A further potential bias in colour-selected surveys in gravitational lens fields is differential amplification across a galaxy image, causing separate regions of the galaxy with possibly different underlying colours to suffer different degrees of amplification. As the lens amplification only varies strongly with position close to critical lines, this bias is only a concern for multiply-imaged galaxies. Only one of our sample of 60 EROs is multiply imaged (§5.2.7 & §6.3). We therefore conclude that this bias has a negligible effect on our sample.

5.2.3 Surface Density of EROs

In a blank field survey, the surface density of sources brighter than a given limiting magnitude can be calculated by dividing the number of detected sources by the surveyed area. This simple calculation is more complicated in the field of a gravitational lens, due to the amplification of the source flux and the accompanying distortion of the background sky (source plane). Consequently, some regions of the source plane are observed to greater depths than others, even if the image plane is observed to a uniform depth. These effects can be quantified by constructing a detailed model of the gravitational lens. Such models are then used to compute the lens amplification as a function of image plane position. This knowledge of the lens amplification allows the surface density of sources to be estimated reliably as

described in more detail below.

We have constructed a detailed gravitational lens model of each cluster in our sample (§3) using the parametric lens inversion method described in §2. Our suite of detailed lens models characterises the gravitational optics of our cluster lens sample, and we therefore use these lens models to account for the effects of lens amplification on both the source counts and the surveyed area using the method described below, which is based on that first developed by Blain et al. (1999).

The amplification suffered by each background galaxy depends on its redshift ($z_{\rm S}$) and the redshift of the intervening lens ($z_{\rm L}$). This redshift dependence is weak if $z_{\rm S} \gg z_{\rm L}$, and as the cluster lenses all lie at $z_{\rm L} \sim 0.2$ and the background galaxies are all expected to lie at $z_{\rm S} \sim$ 1–2, this regime applies. We therefore adopt a single source plane of $z_{\rm S} = 1.5$ and use each model to compute a map of lens amplification as a function of image plane position for this value of $z_{\rm S}$ in each of the ten cluster fields. Adoption of a single value of $z_{\rm S}$ introduces an uncertainty of $\sim$ 10–20% into the final surface density values, which is comparable with the Poisson noise in the raw number counts.

We first use the amplification maps to de-amplify the image plane flux of each ERO in our sample and hence obtain their source plane K–band magnitudes. As gravitational lensing is achromatic, no correction is required to the $(R-K)$ colour. The number of EROs that are brighter than a source plane limiting magnitude $K_{\rm lim}$, $N_{\rm raw}$ ($<K_{\rm lim}$), can then be found by simply counting the number of sources brighter than $K_{\rm lim}$ in the source plane after correcting for lensing. A simple Poisson uncertainty is attached to this value.

We then calculate the area of the background sky within which each ERO is detectable in the following manner. An ERO with a source plane magnitude of $K_{\rm source}$ will appear in the image plane of any given cluster with a magnitude brighter than an image plane detection limit of $K_{\rm det}$ if it is magnified by a factor greater than $\mu_{\rm min} = 10^{-0.4(K_{\rm det}-K_{\rm source})}$. The area in the source plane within which such a galaxy would be detected in that cluster is thus $A_{>}(\mu_{\rm min})$, where $A_{>}$ is the area of the $z_{\rm S} = 1.5$ source plane behind the cluster that lies within the WFPC2 field of view and is magnified by a factor greater than $\mu_{\rm min}$ (Fig. 5.4). For each ERO we

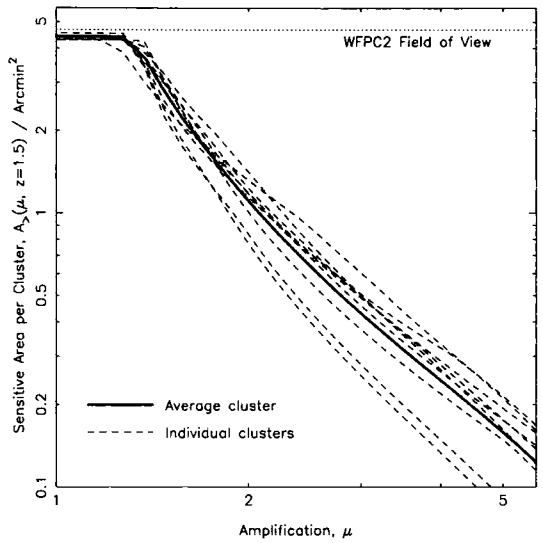

Figure 5.4: Cumulative area of the source plane in our survey, $A_>$, at $z = 1.5$, that experiences magnification greater than μ.

then sum over the ten cluster fields and compute the cumulative surface density $N(<K_{\rm lim})$ using the following equation:

$$N(<K_{\rm lim}) = \sum_{j=1}^{N_{\rm raw}(<K_{\rm lim})} \left\{ \sum_{i=1}^{10} A_{>,i}(\mu_{{\rm min},j}) \right\}^{-1} \tag{5.1}$$

where i runs over the ten clusters in our sample, and j runs over the number of galaxies brighter than $K_{\rm lim}$.

We present in Fig. 5.5 the cumulative surface density, $N(\leq K)$, of $(R-K) \geq 5.3$ and $(R-K) \geq 6.0$ EROs detected in our survey after correcting the source fluxes and source plane surface areas for lens amplification. We also show the results of recent shallower, wide-field surveys (Daddi et al. 2000a; Thompson et al. 1999). The three datasets agree in the region of overlap ($K \sim 17.5$–19.5). We estimate the cumulative surface density of EROs at $K \lesssim 21.6$ with $(R-K) \geq 5.3$ to be $(2.5 \pm 0.4)\,\mathrm{arcmin}^{-2}$ and with $(R-K) \geq 6.0$ to be $(1.2 \pm 0.3)\,\mathrm{arcmin}^{-2}$. We note that the $(R-K) \geq 6.0$ EROs appear to comprise a constant fraction of the overall $(R-K) \geq 5.3$ population at all magnitudes: $\sim 0.40 \pm 0.08$.

The slope of Daddi et al.'s (2000a) cumulative number counts for EROs with $(R-K) \geq 5.3$ is $\alpha = 1.05 \pm 0.05$ at $K < 19.5$, where $N(\leq K) = 10^{\alpha K}$. However, fainter than $K \sim 19.5$, we estimate the slope of our $(R-K) \geq 5.3$ cumulative number counts to be $\alpha = 0.30 \pm 0.01$, suggesting a break in the surface density of

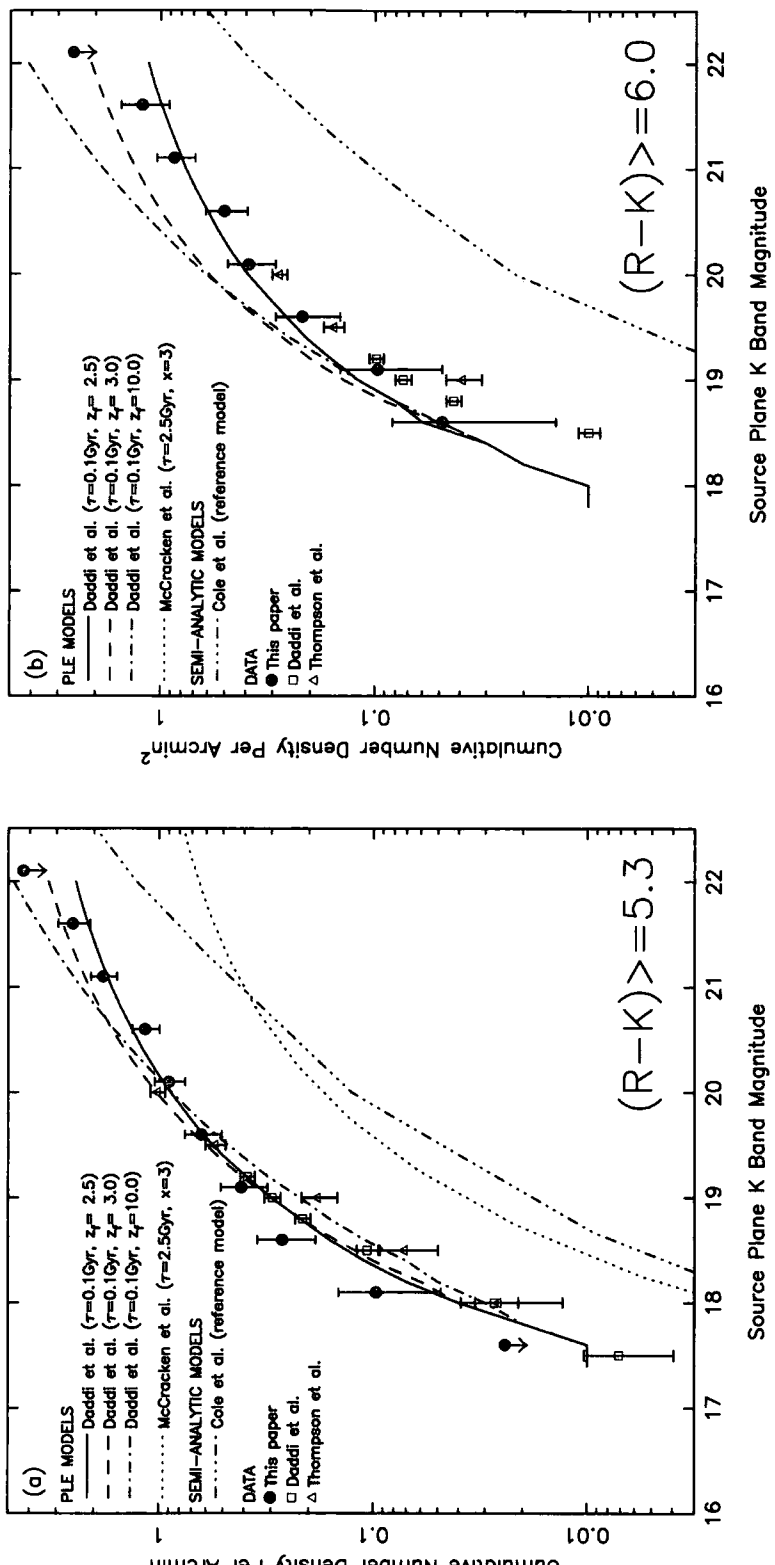

Figure 5.5: The cumulative surface density of (a) $(R-K) \geq 5.3$ and (b) $(R-K) \geq 6.0$ EROs detected through our cluster lens sample after removal of gravitational amplification, as a function of limiting source-plane K–band magnitude. The faintest two bins in both panels are plotted after allowing for the effects of incompleteness. We make no pass-band corrections between the different K–band filters used in the three surveys as such corrections are $\lesssim 0.1$ magnitudes (Cowie et al. 1994; Persson et al. 1998). The error bars are all Poissonian, and therefore generally underestimate the true error due to source clustering. We also plot the data of Daddi et al. (2000a) and Thompson et al. (1999), together with the PLE model predictions of Daddi et al. (2000b) and McCracken et al. (2000) and the semi-analytic model prediction of Cole et al. (2000). Note that the McCracken et al. model predicts zero surface density of EROs with $(R-K) \geq 6.0$. The Daddi et al. models assume ($\Omega_o = 0.3$, $\Lambda_o = 0.7$, $H_o = 50\ \mathrm{km\,s^{-1}Mpc^{-1}}$), McCracken et al. assume ($\Omega_o = 0.1$, $\Lambda_o = 0$, $H_o = 50\ \mathrm{km\,s^{-1}Mpc^{-1}}$) and Cole et al. assume ($\Omega_o = 0.3$, $\Lambda_o = 0.7$, $H_o = 70\ \mathrm{km\,s^{-1}Mpc^{-1}}$). Over the redshift range of interest ($z \sim 1$–2), the ΛCDM cosmology adopted by Daddi et al. and Cole et al. is very similar to McCracken et al.'s open cosmology (Peebles 1984 & McCracken et al. 2000). These differences in cosmological model therefore do not affect the conclusions drawn in §5.3.1 and §5.3.2.

$(R-K) \geq 5.3$ EROs at $K \sim 19$–20. Number counts of the $(R-K) \geq 6.0$ population reveal a similar break, with slopes of $\alpha = 1.43 \pm 0.25$ and $\alpha = 0.37 \pm 0.02$ for brighter and fainter EROs respectively.

5.2.4 Colour Distributions

We present the $(R-K)$–$(I-K)$ colour-colour diagram of our ERO sample in Fig. 5.6. We also plot in Fig. 5.6 the expected colours of passively evolving ellipticals as a function of redshift (for a formation redshift of $z_f = 2.5$ – see also §5.3.1). We begin by comparing the $(R-K)$ and $(I-K)$ ERO selection criteria. Of the $(R-K) \geq 5.3$ EROs, $\lesssim 10\,(15\%)$ have $(I-K) < 4$ and would therefore not be classified as EROs in an $(I-K)$ selected sample. Most of these galaxies are also blue in $(R-K)$, and given their proximity to the $z \lesssim 1$ portion of the evolutionary track, we suggest that they are probably early-type galaxies whose 4000–Å break lies between the R– and I–bands.

We also see that a substantial fraction of the $(R-K) \geq 6.0$ galaxies are redder than the passive evolutionary track. Whilst we treat this comparison with caution, due to uncertainties in both photometric measurements and calibration onto the models, this suggests that the $(R-K) \geq 6.0$ population may contain a sizeable fraction of starburst galaxies. We also measure the typical colour of those EROs for which we can only place a limit on their $(R-K)$ colour by co-adding the F702W–band images of these EROs. Using the same photometric approach as in §5.2.1, we obtain a typical R–band magnitude for these galaxies of $R = 27.0 \pm 0.5$, just 0.4 magnitudes fainter than the 3–σ limit of $R = 26.6$ determined in §5.2.2. This suggests that these galaxies are a continuation of the $(R-K) \geq 6.0$ population that is detected in R, rather than a distinct population of galaxies with much more extreme colours. The three galaxies with the most extreme $(R-K)$ colours are shown in Fig. 5.7.

Pozzetti & Mannucci (2000) propose a method for breaking the "age–dust" degeneracy between passive and starburst EROs. They explore the $(I-K)$–$(J-K)$ and $(R-K)$–$(J-K)$ planes, proposing a classification scheme based on the steepness of the spectral break between optical and near-infrared bands at $z = 1$–2. We

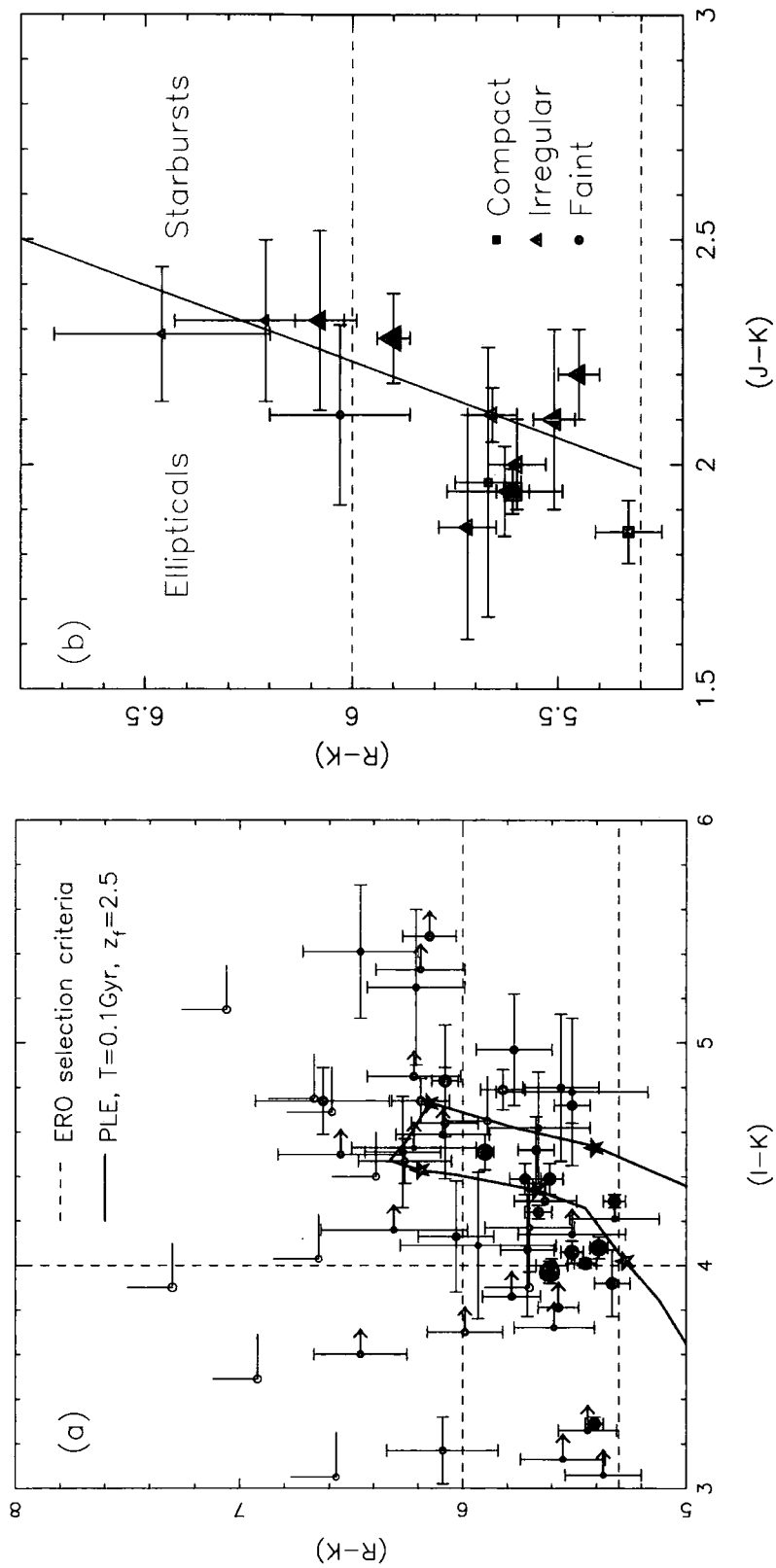

Figure 5.6: (a) $(R-K)$–$(I-K)$ colour-colour diagram showing our sample of EROs. The predicted evolution of an early type galaxy in the $z_f = 2.5$, $\tau = 0.1$ Gyr PLE model (Daddi et al. 2000b) is shown by the solid line. We mark redshift intervals of $\Delta z \sim 0.25$ by stars, starting with $z = 1$ at the lower left. The excess of galaxies with colours redder than the elliptical galaxy track suggests that the $(R-K) \geq 6.0$ ERO population may contain a significant fraction of dusty starburst galaxies. The open points represent galaxies for which only limits on both colours are available. (b) $(R-K)$–$(J-K)$ colour-colour diagram showing the EROs for which we have obtained J–band detections. The solid diagonal line shows $(J-K) = 0.34(R-K) + 0.19$ from Pozzetti & Mannucci (2000). The dashed lines mark our ERO selection criteria. The size of the filled points scale with source-plane K–band magnitude in both panels.

show the $(R-K)$–$(J-K)$ plane of those EROs for which we have obtained J–band detections in Fig. 5.6. We note that all of the morphologically classified "Compact" EROs (see §5.2.5) lie on the "Elliptical" side of the classification boundary. The situation is less clear for the "Irregular" galaxies, where the large photometric uncertainties mean that we cannot reliably state that the majority of these galaxies lie on the "Starburst" side of the classification boundary. More accurate J–band photometry and spectroscopic identifications of the brighter members are required before firm conclusions may be drawn from this analysis.

Whilst the foreground cluster lenses increase the chances of successful spectroscopic identifications, the same amplifying power allows us to observe yet fainter EROs ($K \sim 20$–21 in the image plane), for which spectroscopic observations will remain unfeasible. As a test of the capabilities of photometric redshift measurements for EROs we use HYPER-Z (Bolzonella et al. 2000) to estimate photometric redshifts for those EROs for which $RIJK$–band photometry is available. We use template spectra corresponding to 51 different ages for a $\tau = 0.1$ Gyr μ–model from Bruzual & Charlot (1993) to obtain a likelihood map in dust extinction–redshift (A_V–z) space for each galaxy. In most cases, valid solutions are possible for a wide range of redshifts, however the most likely solution is usually found around $0.8 \leq z \leq 1.5$–2.

Future spectroscopic observations (e.g. §6.2 & §6.3) will probe the redshift distribution and star formation histories of our ERO sample in significantly more detail.

5.2.5 Morphological Diversity

To gain further insight into the diversity of the ERO population we now attempt to quantify the morphologies of our sample. The optical imaging from *HST* has exquisite spatial resolution ($\sim 0.15''$), however EROs are optically faint ($R \gtrsim 24$), and therefore suffer from low signal to noise in optical pass-bands. In contrast, EROs are typically well detected in the near-infrared and our K–band imaging from UKIRT enjoys superb seeing ($\sim 0.5''$). We therefore exploit both datasets in the following analysis.

We first attempt to measure the scale-size of the EROs in our sample. We

fit a Moffatt profile to the K–band image of each ERO from which we estimate the FWHM, and then crudely correct for the effects of seeing by subtracting in quadrature the FWHM of the PSF on the frame (Table 5.3). These measurements reveal no trend in intrinsic FWHM versus colour or K–band magnitude, most likely due to uncertainties in the individual measurements.

We therefore attempt to measure the morphology (scale-size and central concentration) of a typical ERO in amplification-corrected magnitude bins: $K \leq 19$, $19 < K \leq 20$ and $K > 20$, by co-adding the K–band images of the EROs in these magnitude ranges to improve the signal-to-noise ratio of our measurements. Using $\eta(\theta) = I(\theta)/\langle I \rangle_\theta$ where $I(\theta)$ is the surface brightness at radius θ and $\langle I \rangle_\theta$ is the mean surface brightness within θ (Petrosian 1976; Kron 1980), we measure the angular size $\theta_{0.5}$ of the three co-added galaxies where $\eta(\theta_{0.5}) = 0.5$ (Bershady et al. 1998). We also measure the concentration of these composite galaxies, $C_\eta = F(< \theta_{0.5}) \,/\, F(< 1.5\,\theta_{0.5})$, i.e. the ratio between the flux within the radius $\theta_{0.5}$ and that within $1.5\,\theta_{0.5}$ (Saracco et al. 1999).

Despite the co-addition of the data in these broad magnitude bins, no discernible trend in scale-size or concentration with K–band magnitude or colour is found; for example, the concentration values differ by $\lesssim 0.01$ while the error bars are typically $\gtrsim 0.05$. It therefore appears that, although our K–band data enjoys both high signal to noise and good resolution, a detailed morphological analysis of these galaxies at near-infrared wavelengths is not possible. We therefore turn to the optical *HST* imaging, noting that at $z \sim 1$–2, the F702W filter samples the rest-frame ultra-violet. The following morphological classification is therefore sensitive to any ongoing unobscured star-formation in these galaxies, allowing us to identify easily starburst systems.

We classify our ERO sample on the basis of their appearance in the *HST* F702W frames (Table 5.3): "C", compact galaxies; "I", irregular galaxies, e.g. disk-like, clumpy or interacting morphology; "F", faint galaxies which are either not or only just detected in the *HST* frames. The $(R - K) \geq 5.3$ sample comprises: 18% (C); 50% (I); 32% (F). Considering just the Compact and Irregular galaxies, we find that $\sim 90\%$ of the $(R - K) \geq 6.0$ population are irregular, compared with

$\sim 65\%$ of those with $5.3 \leq (R-K) \leq 6.0$. This is another hint that the $(R-K) \geq 6.0$ population may be dominated by distant dusty starbursts, although the large fraction of irregular $5.3 \leq (R-K) \leq 6.0$ EROs, suggests that dusty starbursts may also make an important contribution to the less extreme ERO population.

These results, especially the large fraction of dusty starburst EROs in our sample, disagree with previous work on the classification of EROs on the basis of their morphology. For example, Moriondo et al. (2000) claim that only ~15–20% of EROs in their sample have an "irregular" morphology, while 50–80% are well fitted by an elliptical galaxy ($r^{1/4}$ law) profile. As noted by these authors, their data is heterogeneous, being drawn from the *HST* archive, and so the depth of their observations is not well defined, in contrast to our more homogeneous data set. Another difference between the two studies is that $\sim 65\%$ of Moriondo et al.'s EROs come from targeted searches in probable dense environments, such as high redshift clusters, and regions around radio galaxies and quasars, whereas we survey random fields in the $z \gtrsim 1$ universe. Moriondo et al.'s (2000) results may therefore be biased by their concentration on dense environments.

Finally, we illustrate the diversity of ERO morphology in Fig. 5.7, including candidate interacting galaxies and strongly lensed EROs.

5.2.6 Clustering of EROs

There is an order of magnitude variation in the number of EROs detected in each cluster field (Fig. 5.2 & Table 5.1), supporting previous claims that at least some component of the ERO population is strongly clustered (Daddi et al. 2000a). However, to confidently identify two or more EROs as lying at the same redshift and therefore as being physically associated with each other generally requires spectra of those galaxies. Here, we search our photometric catalogue for examples of two or more neighbouring EROs that exhibit similar K–band magnitudes and $(R-K)$ colours. The premise being that such systems may represent high-redshift galaxy associations and that the similar colours and magnitudes of such galaxies are analogous with the strong early-type galaxy sequences observed in lower redshift clusters and groups (e.g. Fig. 5.2 & 5.3a & b). We find two candidate ERO pairs, one each

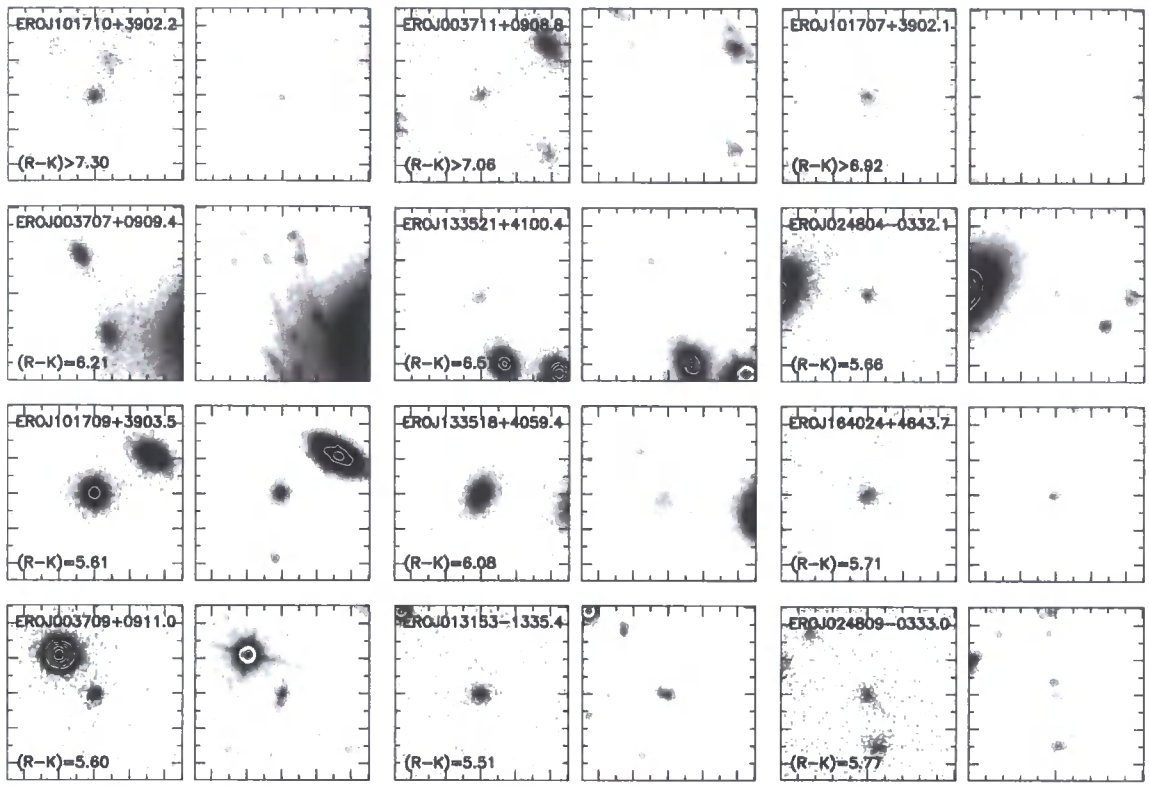

Figure 5.7: Images of a selection of EROs from the sample, showing the K–band to the left and the F702W–band (smoothed with a 0.2″ FWHM Gaussian) to the right in each case. The top row shows the most extreme EROs with $(R-K) \gtrsim 7$, the next row (upper middle) shows examples of strongly lensed EROs, the third row (lower middle) illustrates three of the more extended systems and the bottom row gives apparently interacting or morphologically complex systems. Each panel has North top and East left and is 10″ square. Note that we discuss ERO J003707+0909.4 in detail in §6.

in A 963 and A 1835.

EROJ101701+3903.4 & EROJ101703+3903.4 — These two EROs (Table 5.3) have $K \sim 19$ and $(R-K) \sim 6$ and lie north-west of the cD galaxy in A 963 in Fig. 5.1. They both have a regular K–band morphology and very faint, low-surface brightness R– and J–band morphologies. Within the photometric errors, the $(R-K)$ and $(J-K)$ colours of these two galaxies support the idea that these are two high redshift elliptical galaxies. However, ERO J101701+3903.4 is ∼0.5–1.0 magnitude bluer than its neighbour in $(I-K)$ (Fig. 5a & Table 3), indicating that it may be at a slightly lower redshift.

EROJ140057+0252.4 — This is one of two adjacent galaxies (separation $\sim 3''$) in the field of A 1835. The other galaxy falls just below the $(R-K) \geq 5.3$ criterion (Fig. 5.2), and is therefore not included in the ERO sample. Both galaxies have featureless K–band morphologies, as does the ERO in the R–band. The neighbour

however has a very diffuse and low surface brightness R–band morphology.

We conclude that there are no unambiguous examples of ERO associations in our sample.

5.2.7 Strongly Lensed EROs

The amplifying power of the cluster lenses becomes very high within $\lesssim 30''$ of the centre of the cluster. This is the region of the image plane in which rare, highly magnified giant arcs are detected in some clusters (e.g. A 383 – §4.2). In this same region of the image plane, we detect three strongly lensed EROs in our cluster sample, which we discuss below.

EROJ003707+0909.4 & EROJ003707+0909.5 — Three images of a single background galaxy are detected in the core of A 68. The two brighter images are adjacent to the central galaxy and are shown in Fig. 5.7, while the third image (ERO J0037006+0909.1) lies $\sim 20''$ south of the central galaxy and is considerably fainter. The optical morphology of these images reveals complex structure, containing what appears to be five bright knots within each image. In contrast the K–band shows a bright centrally concentrated source (K=17.2, 17.6 and 19.1 respectively). We obtain colours of $(R-K) \sim 6$, $(I-K) \sim 5$ and $(J-K) \sim 2.3$ for the central red region in both of the two brighter images (Table 5.3). The morphology and position of these arcs relative to the central galaxy suggest that they are three images of a single background disk galaxy.

We target this multiple-image system as part of our near-infrared spectroscopic follow-up of this sample of lensed EROs. We present and analyse these data in §6.3. In summary, ERO J003707 lies at $z = 1.60 \pm 0.03$ (we use this redshift as a constraint on the lens model of A 68 in §3) and our analysis reveals that this galaxy would still be an ERO in a blank-field observation. We therefore retain ERO J003707 in our sample, and refer the reader to §6.3 for the details of our source-plane analysis.

EROJ024804−0332.1 — This ERO was identified in our detailed analysis of A 383 in §4.2 and lies $\sim 25''$ south of the cD galaxy in this cluster and adjacent to a bright cluster elliptical. The ellipticity ($a/b \sim 7$) and position angle (tangential to the cD) of this ERO supporting the interpretation of this image as a lensed

background galaxy. We measure $(R-K) \sim 6$ and $(I-K) \gtrsim 5$, making this an extreme ERO under both $(R-K)$ and $(I-K)$ selection criteria. In §4.2 we estimated from our detailed lens model that this object's redshift is $z \lesssim 4$.

EROJ133521+4100.4 — This ERO is $\sim 20''$ north east of the central galaxy in A 1763 and is shown in Fig. 5.7. Its ellipticity ($a/b \sim 5$) and position angle with respect to the central galaxy indicate that it may be strongly lensed. We do not however detect any counter images which implies that this galaxy is either singly-imaged, or that the counter images fall below the detection threshold of our observations. The arclet has $K = 19.8$ and $(R-K) \sim 6.6$ and we place lower limits on its $(I-K)$ and $(J-K)$ colours of 3.5 and 1.5 respectively, suggesting that this may be a high redshift elliptical galaxy.

5.3 Discussion

In this section we compare the observed number counts of EROs with the theoretical predictions of pure luminosity evolution (Daddi et al. 2000b; McCracken et al. 2000 – hereafter M00) and semi-analytic (Cole et al. 2000 – hereafter C00) models of galaxy formation, and then summarise our conclusions. Our primary aim when comparing our observational results with the different model predictions is to investigate the suggestion that EROs comprise a mixture of evolved and dusty galaxy populations.

5.3.1 Comparison with PLE Models

In Fig. 5.5 we compare our observed number counts (§5.2.3) with Daddi et al.'s (2000b) PLE model down to $K \sim 22$. This model attempts to describe EROs as a single population of evolved galaxies using two free parameters: z_f, the initial redshift of star formation in these galaxies and τ, the e-folding time of the starburst. Daddi et al. adopt a Salpeter (1955) initial mass function (IMF), solar metallicity, no dust reddening and normalise the predicted number counts to the local luminosity function and rest frame colours of elliptical galaxies. Looking at the range of model parameters in this figure we see that at $K \sim 21$ the models diverge, enabling us to discriminate between them. For the $(R-K) \geq 5.3$ sample, the models with

$\tau = 0.1$ Gyr, $z_f = 2.5$ and $\tau = 0.3$ Gyr, $z_f = 3.5$, best match the data, with higher values of z_f predicting too many EROs at $K \gtrsim 20$. The same models are also the best match with the $(R-K) \geq 6.0$ sample.

However, as we showed earlier, EROs appear not to be a single population of galaxies, with the fraction of dusty starbursts possibly increasing towards redder optical/near-infrared colours and fainter K–band magnitudes (§5.2.3, §5.2.5). Agreement between the observations and these simple models should therefore deteriorate, at the faint, red limit. Unfortunately, comparison close to the faint limit is hampered by the cumulative nature of the data plotted in Fig. 5.5, fainter magnitudes being influenced by the brighter bins. Nevertheless, Fig. 5.5b suggests that the models have more difficulty in correctly predicting the surface density of $(R-K) \geq 6.0$ EROs, supporting the idea that this population contains a substantial fraction of dusty starbursts. We also note that although the best model lies within 1–σ (Poissonian) of our data, the very small number of these redder EROs in our sample, particularly at $K \sim 18$–19, implies that the disagreement between Daddi et al.'s (2000a) data and this model at $K \sim 18$–20 is a better test of the model at these magnitudes. Daddi et al. (2000b) also noticed this discrepancy between their $(R-K) \geq 6$ data and the models, and suggested that it was due to a possible deficit of $(R-K) \geq 6.0$ ellipticals at $K \lesssim 19.5$.

In summary, a simple model that assumes EROs comprise only passively evolving elliptical galaxies (with $\tau = 0.1$ Gyr and $z_f = 2.5$) succeeds fairly well in predicting the number density of the $(R-K) \geq 5.3$ population. This model is also the best match to observations of the $(R-K) \geq 6.0$ population, however the agreement is significantly worse, suggesting that the "single population" assumption may be a poor description of these more extreme EROs.

We also compare our observations with a more general PLE model which attempts to describe the whole galaxy population, and not just passive ellipticals. This more detailed model (M00) includes five galaxy populations (E/S0, Sab, Sbc, Scd, Sdm), each normalised to observed local galaxy parameters (i.e. luminosity function and rest frame colours). M00 also require their model to reproduce the shape and amplitude of Cowie et al.'s (1996) K–selected redshift distribution, which

contains very few $K < 19$ galaxies at $z > 1$. To achieve this, they adopt a dwarf dominated IMF ($x = 3$) in order to reconcile their PLE prescription with Cowie et al.'s observational results.

The M00 model (Fig. 5.5) under-predicts the surface density of $(R - K) \geq 5.3$ EROs by approximately an order of magnitude and predicts none with $(R - K) \geq 6.0$. We suggest that this is probably caused by M00 requiring their model to fit Cowie et al.'s (1996) K–selected redshift distribution, which contains comparatively few galaxies at $z > 1$. However, Cowie et al. (1996) were concerned that their optical follow-up of a small-field K–selected sample might be incomplete for the reddest (i.e. optically faintest – $R \gtrsim 24$) galaxies, and hence for galaxies at $z \gtrsim 1$. Recent wide field surveys have also discovered that EROs are strongly clustered (e.g. Daddi et al. 2000a: $\sim 700\mathrm{arcmin}^2$). In contrast, Cowie et al.'s spectroscopic survey covered just $26.2\,\mathrm{arcmin}^2$, raising the possibility that their survey targeted an under-dense patch of sky. We therefore suggest that near-infrared spectroscopy of wide field K–selected samples is necessary before the redshift distribution of such galaxies beyond $z \sim 1$ can be quantified reliably.

Most recently, Cimatti et al. (2002) have completed a near-infrared spectroscopy of a complete sample of $K_S < 20$ galaxies drawn from two independent fields that total $52\,\mathrm{arcmin}^2$. They find that $\sim 32\%$ of this sample lie at $z > 1$, and $\sim 9\%$ lie at $z > 1.5$. Whilst this survey addresses the need for near-infrared spectroscopy of K–selected samples, the relatively modest survey area means that concerns persist over the impact of clustering on the details of this result. Nevertheless, the Cimatti et al. result is a very important step towards achieving a robust redshift distribution of K–selected galaxies, and appears to confirm Cowie et al.'s concerns.

5.3.2 Comparison with Semi-analytic Models

We now return to the primary aim of our comparison with model predictions, that of investigating the suggestion that EROs comprise a mixture of evolved and dusty galaxy populations.

We compare our ERO number counts with the predictions of the "reference model" from C00. This is a semi-analytic model which calculates the formation

and evolution of galaxies in hierarchical clustering cosmologies, based on N-body simulations and simple parametrisation of physical processes. The model parameters are constrained by a number of local galaxy properties including the ratio of elliptical to spiral galaxies, the metallicity of local L^* ellipticals, B– and K–band luminosity functions, the fraction of gas in spiral and irregular galaxies and the size of galaxy disks. C00 assume a Kennicutt (1983) IMF, however they find that the optical/near-infrared colours of galaxies are insensitive to this choice. They also include dust extinction using a Milky Way extinction curve, however as the authors point out, they do not allow for clumping of the dust and stars, nor do they include the effects of dust emission. We note that the model predicts a much weaker colour-magnitude correlation for cluster elliptical galaxies than that observed in the Coma cluster, the predicted colour of cluster ellipticals being $\sim$0.1–0.4 magnitudes bluer than the observations.

The surface density of EROs predicted by the C00 reference model is shown in Fig. 5.5 (Dr. Carlton Baugh, priv. comm.). This model is very successful in reproducing the properties of local galaxies, however it under-predicts the surface density of EROs with $(R-K) \geq 5.3$ and 6.0 by approximately an order of magnitude. It would be inappropriate to modify this model to fit the ERO number counts if in doing so, it no longer agreed with the local observational constraints mentioned above. Nevertheless, this disagreement with observations may point to important opportunities to improve our understanding of galaxy formation and hence improve C00's semi-analytic model. We therefore briefly consider where these opportunities may lie.

As EROs appear to comprise galaxies containing both evolved and dust-reddened stellar populations (§5.2.3 and §5.2.5), C00's under-prediction of EROs suggests that their reference model contains insufficient old stars and/or dust at $z \sim 1$–2. It therefore appears that their reference model does not produce enough stars and/or dust at high-redshift ($z \gg 2$). One possible remedy would be to increase the fraction of stars formed in bursts, at the expense of quiescent star formation. This should reduce the level of ongoing star formation at $z > 1$ (which would otherwise make these galaxies too blue to be classed as EROs). Another possible remedy

would be to adopt a top heavy IMF as this would increase the quantity of dust produced through the formation of a larger fraction of massive stars, thus both making starburst galaxies redder and allowing more systems to go through a starburst ERO phase without altering dramatically the properties of the local galaxy population with which the current model agrees. Introducing dust clumping may also provide a more realistic description of the spatial distribution of dust in starburst systems.

EROs are not the only population of extragalactic objects that challenge the C00 model. The observed surface density of the sub-millimetre-bright population discovered with SCUBA (Holland et al. 1999) in the late 1990's (e.g. Smail et al. 2002) is also difficult to explain with the reference model. We note, however, that Lacey et al. (priv. comm.) have recently modified the C00 model to include a much more detailed treatment of dust, including a top heavy IMF. With these modifications, the model is able to reproduce the observed number counts of the sub-millimetre population. This is important progress for our understanding of galaxy formation, and prompts the question whether these modifications can also help to reconcile the model with the observed ERO number counts. Whilst a detailed analysis has yet to be performed, we understand (Baugh, priv. comm.) that the Lacey et al. modifications have made a negligible difference to the shortfall in the model ERO number counts. This suggests that the timing and duration of star formation may be more fruitful avenues for further investigation of the number counts of EROs.

Although the C00 reference model under-predicts the observed number of EROs, this model does provide a physically motivated framework to qualitatively interpret the relationship between the various classes of ERO. In the model the redshifts of galaxies predicted to have $5.3 \leq (R-K) \leq 6.0$ and $K \lesssim 22$ are $z \sim 0.8$–2.5, equally split between the $z \sim 0.8$–1.5 and $z \sim 1.5$–2.5 bins. The lower redshift bin is dominated by passively evolving galaxies ($\sim 90\%$ of the total) whose stars are sufficiently old to produce such red colours in the observed pass-bands, whilst the higher redshift bin is dominated by starburst galaxies ($\sim 95\%$ of the total), whose $(R-K)$ colours are reddened by dust. A similar analysis of the predicted $(R-K) \geq 6.0$ population reveals that almost all of these more extreme EROs are

predicted to lie at $z \sim 1.5$–2.5, with $\sim 70\%$ of these galaxies being dusty starbursts. The C00 reference model therefore appears to provide some theoretical basis for the observational evidence (§5.2) for both a predominance of distant dusty starburst galaxies in the $(R-K) \geq 6.0$ EROs, and passively evolving galaxies at $z \sim 1$ producing the bulk of the $(R-K) \sim 5.3$–6.0 population.

We now return to the break in the number counts of EROs identified in §5.2. Whilst the normalisation of the semi-analytic predictions falls an order of magnitude short of our observations, the qualitative properties of the predicted ERO population offers a plausible explanation of the break in the count slopes. At magnitudes brighter than the break, the counts may be dominated by lower redshift ($z \sim 0.8$–1.5), predominantly passively evolving galaxies, whereas faint-ward of the break, the counts could be dominated by the distant ($z \sim 1.5$–2.5), dusty starburst galaxies. We therefore speculate that the break may be due to a transition from an ERO population dominated by evolved galaxies at $z \sim 1$ ($K \lesssim 19.5$) to one dominated by distant dusty starburst galaxies (that may have experienced a recent merger) at $z \sim 2$ ($K \gtrsim 19.5$).

5.4 Conclusions

We have undertaken a deep optical/near-infrared survey of the 10 massive clusters in our lens survey. We find 60 EROs with $(R-K) \geq 5.3$, of which 26 have $(R-K) \geq 6.0$ in a total image plane survey area of 49 arcmin^2 down to $K = 20.6$.

We use the detailed models of the cluster lenses from §3 to quantify the lens amplification and thus to correct the observed number counts for the effects of gravitational lensing. After making these corrections, we estimate a surface density of $2.5 \pm 0.4\,(1.2 \pm 0.3)$ arcmin^{-2} for EROs with $(R-K) \geq 5.3\,(6.0)$ at $K \leq 21.6$. Our results agree with previous shallower wide-field surveys at $K \lesssim 19$ and probe the number density of EROs with $(R-K) \geq 5.3$ and 6.0 down to a source plane magnitude of $K \sim 22$ for the first time.

The number counts of both classes of ERO flatten significantly at magnitudes fainter than $K \sim 19$–20. We speculate that this is due to a transition from an

ERO population dominated by evolved galaxies at $z \sim 1$–2 ($K \lesssim 19$–20) to one dominated by distant dusty starburst galaxies at $z > 1$ ($K \gtrsim 19$–20). Analysis of the $(R-K)$–$(I-K)$ and $(R-K)$–$(J-K)$ planes also suggests that the $(R-K) \geq 6.0$ population may contain a substantial fraction of dusty starburst galaxies.

Approximately 50% of our sample contain morphological substructure including disk-like, clumpy or interacting morphologies. This is a larger fraction than found by previous studies (e.g. Moriondo et al. 2000) which claimed that only ~15–20% of EROs have such morphologies. The discrepancy may be due to a bias towards dense environments and the heterogeneity of Moriondo et al.'s dataset, compared with our unbiased and more homogeneous dataset.

We compare our observations with progressively more sophisticated models of galaxy formation, beginning with a two parameter (z_f and τ) PLE model that attempts to describe EROs as a single population of elliptical galaxies (Daddi et al. 2000b). The model parameters which best match the observations are $\tau = 0.1$ Gyr and $z_f = 2.5$, ruling out the very high formation redshifts ($z_f \sim 10$) that were allowed by Daddi et al.'s (2000a) shallower observations. However, this single population model matches the $(R-K) \geq 6.0$ EROs significantly worse than the $(R-K) \geq 5.3$ EROs, supporting the idea that the more extreme population contains a large fraction of distant dusty starbursts in addition to the elliptical galaxies contained within this model.

We then compared our observations with PLE models that attempt to describe the whole galaxy population, and not just passive ellipticals (M00). These models under-predict the surface density of $(R-K) \geq 5.3$ EROs by approximately an order of magnitude and predict none with $(R-K) \geq 6.0$. This deficit of EROs is probably caused by M00 requiring their model to fit the median redshift of Cowie et al.'s (1996) K–selected redshift distribution. We suggest that this confirms Cowie et al.'s (1996) concern that their optical follow-up of a small-field K–selected sample suffers from strong clustering of the faintest and reddest sources, as well as possibly being incomplete for the reddest (i.e. optically faintest – $R \gtrsim 24$) galaxies, and hence for galaxies at $z \gtrsim 1$. It therefore appears that near-infrared spectroscopy of wide field K–selected samples is necessary before the redshift distribution of

galaxies at $z \gtrsim 1$ can be reliably quantified (e.g. Cimatti et al. 2002).

Finally, we compare the observed number density of EROs with the semi-analytic predictions from the reference model of C00. This semi-analytic model under-predicts the number density of EROs at $K \sim 18$–22 by an order of magnitude, indicating that the current generation of semi-analytic models may not produce sufficient stars and/or dust at high redshift ($z > 2$). However, as the C00 reference model is physically well motivated, we look at the predicted properties of the ERO population, finding that their redshift distribution and the split between passive and dusty EROs appear to support our interpretation of the break in the slope of the number counts.

This is the first survey to exploit massive foreground galaxy clusters to amplify the flux of background EROs. The sample constructed from our deep, high resolution K– and R–band observations is therefore ideally suited to near-infrared spectroscopic follow-up on 10–m class telescopes, the lens amplification allowing us to probe ~ 1 magnitude beyond the normal reach of such observations.

Table 5.3: Catalogue of EROs

Source	α,δ (J2000)	K	$(R-K)$	$(I-K)$	$(J-K)$	FWHM ($''$)	Morphology (a)
A 68							
ERO J003703+0909.7	00 37 03.30 +09 09 44.4	20.10 ± 0.16	> 6.39	> 4.40	> 1.42	1.23	F
ERO J003706+0909.1	00 37 06.10 +09 09 08.7	19.10 ± 0.01	> 5.70	> 3.86	> 2.06	0.92	I, §5.2.7
ERO J003707+0909.4	00 37 07.25 +09 09 23.8	17.62 ± 0.03	6.21 ± 0.22	5.25 ± 0.35	2.32 ± 0.18	0.62	I, §5.2.7
ERO J003707+0909.5	00 37 07.37 +09 09 28.4	17.16 ± 0.03	6.46 ± 0.26	5.41 ± 0.30	2.29 ± 0.15	0.66	I, §5.2.7
ERO J003709+0909.6	00 37 08.84 +09 09 37.0	19.45 ± 0.10	6.19 ± 0.20	> 5.33	> 2.07	0.25	F
ERO J003709+0911.0	00 37 09.03 +09 11 01.8	18.21 ± 0.04	5.60 ± 0.07	4.00 ± 0.03	2.00 ± 0.10	3.86	I, Clumpy
ERO J003710+0908.9	00 37 09.57 +09 08 53.4	18.17 ± 0.03	5.66 ± 0.06	4.24 ± 0.03	2.11 ± 0.06	0.18	I
ERO J003710+0909.1	00 37 09.58 +09 09 08.4	17.53 ± 0.03	5.45 ± 0.05	4.01 ± 0.02	2.20 ± 0.10	0.45	I, Disk?
ERO J003711+0908.8	00 37 10.53 +09 08 46.8	19.81 ± 0.12	> 7.06	> 5.15	> 1.71	0.46	F
ERO J003711+0909.1	00 37 10.91 +09 09 09.8	20.17 ± 0.16	> 6.67	> 4.75	> 1.35	0.27	F
ERO J003711+0909.2	00 37 11.00 +09 09 10.1	20.30 ± 0.17	> 6.59	> 4.69	> 1.22	0.89	F
A 209							
ERO J013151−1335.5	01 31 50.78 −13 35 31.0	20.07 ± 0.15	5.70 ± 0.20	4.17 ± 0.20	...	0.34	C
ERO J013153−1335.4	01 31 52.82 −13 35 22.8	18.65 ± 0.05	5.51 ± 0.08	4.72 ± 0.08	...	0.39	I, Clumpy
ERO J013154−1336.3	01 31 54.14 −13 36 19.9	19.54 ± 0.11	6.26 ± 0.21	4.47 ± 0.10	...	0.42	F
ERO J013157−1336.6	01 31 56.98 −13 36 37.5	17.98 ± 0.03	5.32 ± 0.05	4.29 ± 0.03	...	0.50	I
ERO J013159−1336.2	01 31 58.60 −13 36 15.4	20.06 ± 0.15	5.66 ± 0.23	4.62 ± 0.25	...	0.31	C
ERO J013159−1336.3	01 31 59.36 −13 36 16.4	18.72 ± 0.06	5.82 ± 0.10	4.79 ± 0.09	...	0.33	I, Disk
ERO J013200−1336.5	01 31 59.66 −13 36 28.4	18.96 ± 0.09	6.19 ± 0.13	4.74 ± 0.10	...	0.36	F
A 267							
ERO J015238+0101.0	01 52 38.43 +01 02 02.8	17.76 ± 0.02	5.51 ± 0.05	4.06 ± 0.05	2.10 ± 0.20	0.42	I, Disk?
ERO J015238+0101.9	01 52 37.60 +01 01 51.6	18.73 ± 0.05	6.15 ± 0.12	> 5.48	> 1.85	0.67	C
ERO J015240+0101.2	01 52 40.08 +01 01 08.8	18.74 ± 0.05	5.67 ± 0.08	4.52 ± 0.15	1.96 ± 0.30	0.35	C

(a) "C", Compact; "I", Irregular; "F", Faint morphological classification, as discussed in §5.2.5.

Table 5.3: Catalogue of EROs – Continued

Source	α,δ (J2000)	K	$(R-K)$	$(I-K)$	$(J-K)$	FWHM ($''$)	Morphology (a)
A 267 (continued)							
ERO J015240+0101.6	01 52 39.55 +01 00 38.4	20.37 ± 0.17	> 6.65	> 4.03	> 0.20	0.57	F
ERO J015240+0101.7	01 52 39.88 +01 01 39.3	20.32 ± 0.15	5.93 ± 0.35	4.09 ± 0.33	> 0.26	0.34	C
ERO J015240+0101.8	01 52 39.82 +01 01 50.0	19.51 ± 0.10	6.09 ± 0.21	> 4.59	> 1.07	0.53	F
ERO J015241+0101.1	01 52 41.25 +01 02 07.4	19.14 ± 0.09	6.22 ± 0.21	> 4.85	> 1.44	0.68	F
ERO J015243+0101.5	01 52 42.80 +01 01 27.0	19.93 ± 0.11	5.51 ± 0.34	4.78 ± 0.33	> 0.65	1.30	C
ERO J015245+0101.8	01 52 44.53 +01 00 47.9	20.04 ± 0.16	5.32 ± 0.20	> 4.21	> 0.54	0.60	F
ERO J015247+0101.1	01 52 47.28 +01 01 04.8	18.48 ± 0.03	5.72 ± 0.07	4.39 ± 0.07	1.86 ± 0.25	0.29	I
ERO J015249+0100.6	01 52 48.93 +01 00 38.1	20.58 ± 0.16	> 5.89	> 4.65	> 0.03	0.51	F
ERO J015249+0101.6	01 52 49.10 +01 00 36.8	20.05 ± 0.11	5.51 ± 0.24	> 4.14	> 0.53	0.52	F
A 383							
ERO J024804−0332.1	02 48 04.12 −03 32 06.4	19.73 ± 0.07	6.22 ± 0.28	> 4.53	...	0.29	C, §5.2.7
ERO J024805−0330.0	02 48 04.55 −03 29 57.3	19.59 ± 0.09	6.27 ± 0.17	4.51 ± 0.25	...	0.46	I
ERO J024805−0330.2	02 48 04.56 −03 30 11.0	18.12 ± 0.02	5.41 ± 0.04	3.29 ± 0.03	...	0.00	C, Star?
ERO J024805−0330.3	02 48 04.82 −03 30 18.0	18.06 ± 0.04	5.61 ± 0.06	4.39 ± 0.07	...	0.47	I
ERO J024805−0330.3	02 48 04.90 −03 30 22.7	20.06 ± 0.11	6.31 ± 0.33	> 4.16	...	0.36	C
ERO J024805−0330.4	02 48 04.89 −03 30 24.7	19.18 ± 0.08	6.08 ± 0.15	4.64 ± 0.25	...	0.33	I
ERO J024806−0331.5	02 48 06.44 −03 31 27.3	18.27 ± 0.05	6.63 ± 0.30	4.74 ± 0.15	...	0.54	I
ERO J024808−0331.8	02 48 07.99 −03 31 47.5	19.44 ± 0.10	6.55 ± 0.28	> 4.50	...	0.63	I
ERO J024809−0332.9	02 48 08.79 −03 32 56.4	19.47 ± 0.11	5.56 ± 0.17	4.80 ± 0.33	...	0.62	F
ERO J024809−0333.0	02 48 08.58 −03 33 00.0	19.00 ± 0.05	5.77 ± 0.17	4.97 ± 0.25	...	0.61	I, Merging?
ERO J024810−0332.4	02 48 10.02 −03 32 25.8	17.57 ± 0.02	5.39 ± 0.04	4.08 ± 0.05	...	0.61	I
A 773							
ERO J091802+5143.1	09 18 02.50 +51 43 06.4	20.23 ± 0.11	5.59 ± 0.18	> 3.73	> 1.23	0.34	I, Disk

(a) "C", Compact; "I", Irregular; "F", Faint morphological classification, as discussed in §5.2.5.

Table 5.3: Catalogue of EROs – Continued

Source	α,δ (J2000)	K	$(R-K)$	$(I-K)$	$(J-K)$	FWHM ($''$)	Morphology (a)
A 963							
ERO J101701+3903.4	10 17 01.42 +39 03 24.6	19.32 ± 0.05	6.09 ± 0.25	3.17 ± 0.15	> 2.13	0.47	I
ERO J101703+3903.4	10 17 02.52 +39 03 22.0	18.84 ± 0.04	6.03 ± 0.17	4.13 ± 0.25	2.11 ± 0.11	0.58	F
ERO J101706+3901.7	10 17 05.69 +39 01 41.6	20.53 ± 0.15	6.38 ± 0.34	> 2.94	> 0.80	0.00	F
ERO J101706+3902.0	10 17 05.79 +39 02 02.3	20.16 ± 0.10	5.55 ± 0.19	> 3.13	> 1.04	0.57	F
ERO J101707+3901.4	10 17 06.61 +39 01 22.1	19.51 ± 0.08	5.78 ± 0.13	> 3.86	> 1.71	0.11	I
ERO J101707+3902.1	10 17 06.58 +39 02 08.3	19.74 ± 0.09	> 6.90	> 3.49	> 1.27	0.21	I, Clumpy
ERO J101707+3902.4	10 17 07.09 +39 02 25.0	20.37 ± 0.09	5.37 ± 0.17	> 3.06	> 0.96	0.28	I
ERO J101707+3902.9	10 17 07.43 +39 02 52.2	19.14 ± 0.04	5.63 ± 0.14	> 4.29	1.94 ± 0.10	0.46	I, Disk?
ERO J101709+3903.5	10 17 09.30 +39 03 31.4	17.15 ± 0.01	5.61 ± 0.04	3.97 ± 0.05	1.94 ± 0.05	0.56	C
ERO J101710+3902.2	10 17 09.66 +39 02 10.0	19.60 ± 0.08	> 7.28	> 3.90	> 1.65	0.64	I
ERO J101710+3903.0	10 17 09.61 +39 03 03.6	19.49 ± 0.07	5.99 ± 0.17	> 3.70	> 1.55	1.20	I
ERO J101710+3903.4	10 17 09.94 +39 03 23.3	19.66 ± 0.09	6.46 ± 0.21	> 3.60	> 1.47	0.85	F
A 1763							
ERO J133511+4100.3	13 35 11.46 +41 00 15.5	18.92 ± 0.06	5.57 ± 0.09	> 3.81	...	1.25	I
ERO J133517+4058.7	13 35 16.77 +40 58 43.0	20.11 ± 0.15	5.44 ± 0.13	> 3.26	> 1.57	0.63	I
ERO J133518+4058.8	13 35 17.82 +40 58 45.9	20.47 ± 0.16	5.42 ± 0.20	> 2.70	> 0.98	0.64	I
ERO J133518+4059.4	13 35 18.30 +40 59 25.8	17.65 ± 0.02	6.08 ± 0.06	4.83 ± 0.25	2.32 ± 0.20	0.76	I
ERO J133521+4100.4	13 35 21.16 +41 00 24.4	19.84 ± 0.10	6.57 ± 0.51	> 3.05	> 1.05	1.24	F, §5.2.7
A 1835							
ERO J140057+0252.4	14 00 57.13 +02 52 26.4	18.01 ± 0.02	5.33 ± 0.08	3.92 ± 0.15	1.85 ± 0.07	0.53	C
A 2219							
ERO J164023+4644.0	16 40 23.05 +46 44 02.3	17.51 ± 0.01	5.90 ± 0.04	4.51 ± 0.08	2.28 ± 0.10	0.51	I, Disk
ERO J164024+4643.7	16 40 23.95 +46 43 42.1	19.64 ± 0.05	5.71 ± 0.12	4.07 ± 0.30	> 1.76	0.68	I

(a) "C", Compact; "I", Irregular; "F", Faint morphological classification, as discussed in §5.2.5.

6 THE DIVERSITY OF EROs

6.1 Spectroscopy of EROs

Spectroscopic identification of Extremely Red Objects (EROs) is very challenging because the strong spectral features in the rest-frame optical that are used to study galaxies at lower redshifts (e.g. the [OII] and Hα emission lines and the 4000Å break) are shifted to the edge of and beyond optical pass-bands (i.e. $\lambda_{\rm obs} \gtrsim 1\mu$m). At the redshifts where these galaxies are typically seen, this situation is often complicated by poor red sensitivity of optical spectrographs and (in the case of dusty EROs) strong dust absorption in the rest-frame ultraviolet (including the [OII] line). Near-infrared spectroscopy offers a potential solution to these difficulties, allowing longer wavelengths to be probed. However the strong sky absorption and emission at wavelengths beyond $\sim 1\mu$m mean that only limited wavelength windows are accessible from the ground and the sensitivity of such observations is also undermined. A further complication of near-infrared spectroscopy is the lack of near-infrared multi-object spectrographs which severely limits the efficiency of these observations.

Our search for gravitationally lensed EROs (§5) was designed to increase the chances of successful spectroscopic follow-up by exploiting the natural magnification of our sample of ten foreground cluster lenses (§3). In this chapter we describe the near-infrared spectroscopic observations of two of the brightest sources in our ERO catalogue: ERO J164034+4644.0 and ERO J003707+0909.5. We selected ERO J164023 because it was the brightest source from our catalogue available on sky during a gap in the Keck/NIRSPEC observing schedule of Prof. Richard Ellis and Dr. Tommaso Treu of Caltech in April 2001. We also successfully applied for UKIRT/CGS4 time in 2001B and used this time to target ERO J003707 because a successful spectroscopic identification of this bright ($K = 17.2$) multiply-imaged ERO would also provide a tight constraint on our lens model of A 68 (§3). Although these 4–m class telescope observations were inconclusive, they were very valuable

when planning subsequent Keck/NIRSPEC observations of the same source following our successful Gemini community service proposal.

We present our observations, analysis and discussion of ERO J164023 and ERO J003707 in §6.2 and §6.3 respectively and we summarise our conclusions from the spectroscopic follow-up in §6.4.

6.2 ERO J164023: A Dusty Starburst-Seyfert ERO

We present the detailed follow-up of one source identified in our search for gravitationally lensed EROs (§5): ERO J164023+4644 (hereafter referred to as ERO J164023). This galaxy was previously associated with an *ISO* 15μm source by Barvainis et al. (1999), who tentatively identified a single optical emission line as [OII] at $z = 1.05$, although they did not realise that the galaxy is an ERO.

We describe our observations in §6.2.1 and present our results in §6.2.2. We compare ERO J164023 with HR10 and ISO J1324−2016 (the only other two dusty EROs for which detailed results have been published) in §6.2.3 and summarise our conclusions in §6.2.4. We adopt a lens amplification of 1.4 for ERO J164023 from the lens model of A 2219 presented in §3.

6.2.1 Observations

Imaging

The K−band data used to identify ERO J164023 was obtained in a 6.5-ks exposure using the UFTI imager on the 3.8−m UK Infrared Telescope* (UKIRT) in 0.5″ seeing on 2000 April 5. ERO J164023 lies at 16:40:23.05 +46:44:02.3 (J2000) and a K−band image of this galaxy is shown in Fig. 6.1. We describe the reduction of these data in §5.

In addition to the K−band imaging, we obtained a J−band image of ERO J164023 with INGRID on the 4.2-m William Herschel Telescope (WHT)† on 2001 May 6.

*The United Kingdom Infrared Telescope is operated by the Joint Astronomy Centre on behalf of the Particle Physics and Astronomy Research Council

†The William Herschel Telescope is operated by the Isaac Newton Group on behalf of Particle

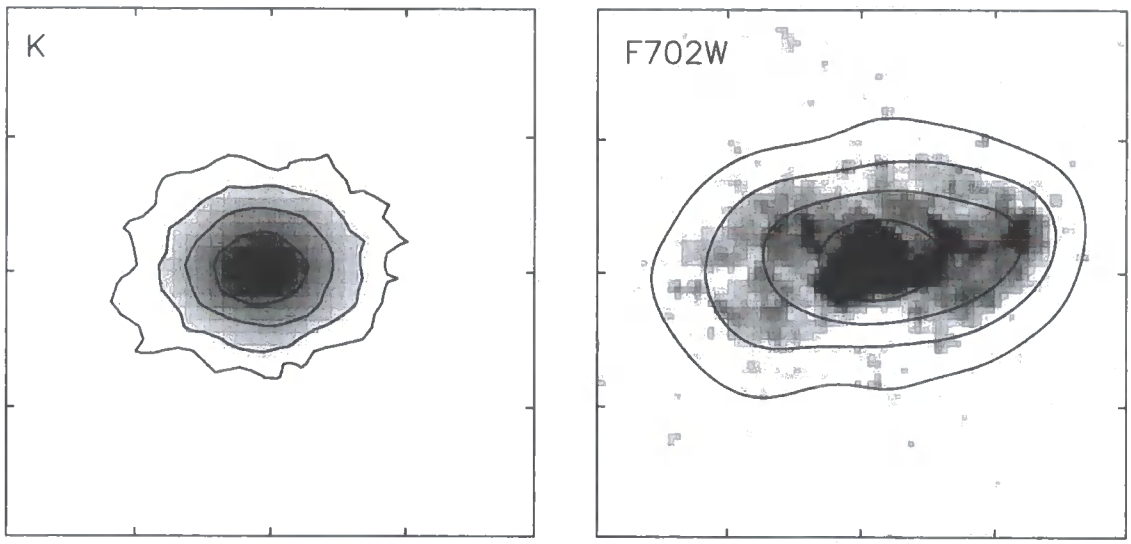

Figure 6.1: The UKIRT K–band (left) and *HST* F702W (right) images of ERO J164023. The resolution of these two images is $\sim 0.5''$ and $\sim 0.1''$ respectively. The contours on the left-hand panel are from the raw K–band image that also appears as the gray-scale in this panel and the contours in the right-hand panel are from the seeing-matched (i.e. $\sim 0.5''$ resolution) *HST* frame. The tick marks are $1''$ apart; North is up and East is Left.

This observation totalled 2.2 ks in $\sim 0.8''$ seeing, and was reduced in a similar manner to the K–band data. We also exploit H–band observations of this field from Gray et al. (2000) using the CIRSI imager on the WHT.

Morphological information on this ERO comes from *HST* imaging of the cluster. The field containing ERO J164023, A 2219, was observed with WFPC2 onboard *HST* for six exposures totalling 14.4 ks through the F702W filter (§3). We show the WFPC2 image of this galaxy in Fig. 6.1. To obtain optical photometry of the field we have also analysed archival $UBVI$–band imaging of A 2219 taken with COSMIC on the Hale 5-m[‡] and LRIS (Oke et al. 1995) on Keck[§] (Smail et al. 1995b, 1998).

Mid-infrared observations of the galaxy come from Barvainis et al. (1999) who observed A 2219 at 15μm with ISOCAM on-board ESA's *Infrared Space Observatory (ISO)*. They detected five sources, one of which (A2219#5) lies within $\sim 0.8''$ of ERO J164023.

At longer wavelengths, A 2219 was also observed by Chapman et al. (2000) using

Physics & Astronomy Research Council

[‡]The Hale Telescope at Palomar Observatory is owned and operated by the California Institute of Technology

[§]The W. M. Keck Observatory which is operated as a scientific partnership between Caltech, the University of California and NASA

Table 6.1: Photometry of ERO J164023

Observed Band	Flux Density[a,c] (μJy)	Magnitude[b,c]	Reference
U	< 0.10	> 25.6	Smail et al. (1998)
B	0.13 ± 0.02	26.2 ± 0.1	Smail et al. (1998)
V	0.19 ± 0.03	25.7 ± 0.2	Smail et al. (1995b)
R	1.32 ± 0.05	23.54 ± 0.04	§5
I	3.00 ± 0.24	22.15 ± 0.08	§5
J	20.4 ± 0.6	19.72 ± 0.06	§5
H	21.3 ± 0.7	19.20 ± 0.09	Gray et al. (2000)
K	63.0 ± 0.6	17.64 ± 0.01	§5
15μm	530 ± 110	...	Barvainis et al. (1999)
850μm	$< 6 \times 10^3$	...	Chapman et al. (2000)
28.5 GHz	< 780	...	Cooray et al. (1998)
4.9 GHz	< 300	...	Edge (priv. comm.)
1.4 GHz	< 100	...	Owen (priv. comm.)

[a] Errors quoted are 1-σ. Limits quoted are 3-σ detection limits.
[b] All magnitudes are measured in a 2″ diameter aperture.
[c] Flux density measurements and magnitudes in this table have not been corrected for gravitational amplification by the foreground cluster lens, A 2219, which amounts to a factor of 1.4.

SCUBA at 850μm (Holland et al. 1999) on the 15-m James Clerk Maxwell Telescope[¶]. They tentatively identified one of the sources in this field (SMM J16404+4644) with A2219#5 from Barvainis et al. (1999). However, as the 850μm source is $\gtrsim 6''$ away from ERO J164023, we suggest that this identification is probably incorrect and instead we adopt Chapman et al.'s 3–σ detection as a conservative upper limit on the 850μm flux from ERO J164023.

Finally, we obtain 3–σ detection limits in the radio from the 28.5 GHz, 4.9 GHz, 1.4 GHz maps of Cooray et al. (1998), Edge (priv. comm.) and Owen (priv. comm.). We list our optical, infrared, sub-millimeter and radio photometry in Table 6.1.

[¶]The James Clerk Maxwell Telescope is operated by the JAC on behalf of the Particle Physics & Astronomy Council, the Netherlands Organisation for Scientific Research and the National Research Council of Canada

Table 6.2: Emission Line Measurements of ERO J164023

Line	λ_{obs} (μm)	Flux [a] (10^{-17}erg s^{-1}cm^{-2})	FWHM[a,b] (km s^{-1})	$W^a_{\lambda,rest}$ (Å)
[OII]	0.7632	2 ± 1	< 320	30 ± 5
Hα	1.3441	27 ± 2	310 ± 50	60 ± 15
[NII]	1.3483	18 ± 2	330 ± 50	50 ± 20

[a] Fluxes, equivalent widths, and FWHMs are measured by fitting a Gaussian using SPLOT in IRAF and are not corrected for gravitational amplification.
[b] FWHM measurements are quoted after correcting for the instrumental resolution.

Spectroscopy

A near-infrared spectrum of ERO J164023 was obtained in the J–band with NIRSPEC on Keck-II on 2001 April 9 in photometric conditions and 0.6″ seeing. Three exposures of 600 s each were obtained, nodding along the 0.76″ × 42″ slit by 5″ between each exposure. The resolution of these observations was 10Å FWHM.

Wavelength calibration was achieved from the sky lines, using observations of a bright star to correct for geometrical distortion. An average sky spectrum was created by scaling and combining the individual spectra and this was then subtracted from each science observation before co-adding the spectra and extracting a one-dimensional spectrum. Flux calibration was achieved through observations of UKIRT standard stars, which were also used to correct for telluric absorption. No attempt was made to correct for slit losses. The flux-calibrated spectrum (Fig. 6.2) reveals two strong emission lines at 1.3441 and 1.3483μm, which we identify as Hα, and [NII]λ6583 respectively. This places the galaxy at a redshift of $z = 1.0480 \pm 0.0005$.

Barvainis et al. (1999) discuss an optical spectrum of A2219#5 obtained by Frye & Broadhurst using LRIS on Keck-I which we show in Fig. 6.3. This shows a strong emission line at 7634Å which Barvainis et al. tentatively identified as [OII]λ3727 at a redshift of $z = 1.048$, as confirmed by our near-infrared spectrum. The optical spectrum also appears to contain the Hθ absorption feature, although other members of the Balmer series and the Ca H & K lines are not convincingly

detected. We present the emission line measurements in Table 6.2.

6.2.2 Results and Discussion

Morphology

The *HST* frame ($\sim 0.15''$ resolution) suggests that ERO J164023 has a disk morphology in the rest frame UV (Fig. 6.1), with no obvious signs of strong dynamical disturbance. The disk component is sufficiently extended, $\sim$ 2–3″ (10–15 kpc), that it remains visible when the *HST* frame is degraded to the ground-based resolution (0.5″). In contrast, at this resolution the K–band emission shows less evidence of a disk and is more concentrated. The $(R-K) \sim 6$ colour of ERO J164023 (Table 6.1) is dominated by its central regions, with the outer regions displaying a more "modest" optical/near-infrared colour of $(R-K) \sim 5.3$.

Spectral Energy Distribution

We plot the rest-frame spectral energy distribution (SED) of ERO J164023 in Fig. 6.4. The SED of ERO J164023 rises steeply at optical/mid-infrared wavelengths and, although less well-constrained at sub-mm/radio wavelengths, the flux density probably peaks in the far-infrared/sub-mm.

The extreme redness of the SED at optical/near-infrared/mid-infrared wavelengths, suggests that the spectrum of ERO J164023 is heavily reddened by dust. We quantify this in two ways, first using the rest-frame far-infrared-to-blue luminosity ratio ($L_{\rm FIR}/L_B$). We estimate the (unlensed) far-infrared luminosity of ERO J164023, using the 850μm flux limit (Table 6.1) to scale the far-infrared luminosity of HR10 (Dey et al. 1999 – hereafter D99), obtaining $L_{\rm FIR} \lesssim 4 \times 10^{12}$ L$_\odot$, and we measure the (unlensed) rest-frame blue luminosity to be $L_B \sim 2 \times 10^{10}$ L$_\odot$ by interpolating between the observed I– and J–bands (Table 6.1). We therefore estimate $L_{\rm FIR}/L_B \lesssim 200$. Second, we use HYPER-Z (Bolzonella et al. 2000) to investigate the SED of ERO J164023 by fitting template star-forming model spectra for a range of star formation ages and dust extinction to the photometric data presented in Table 6.1. Assuming a starburst age of < 0.2 Gyr and adopting the spectroscopic

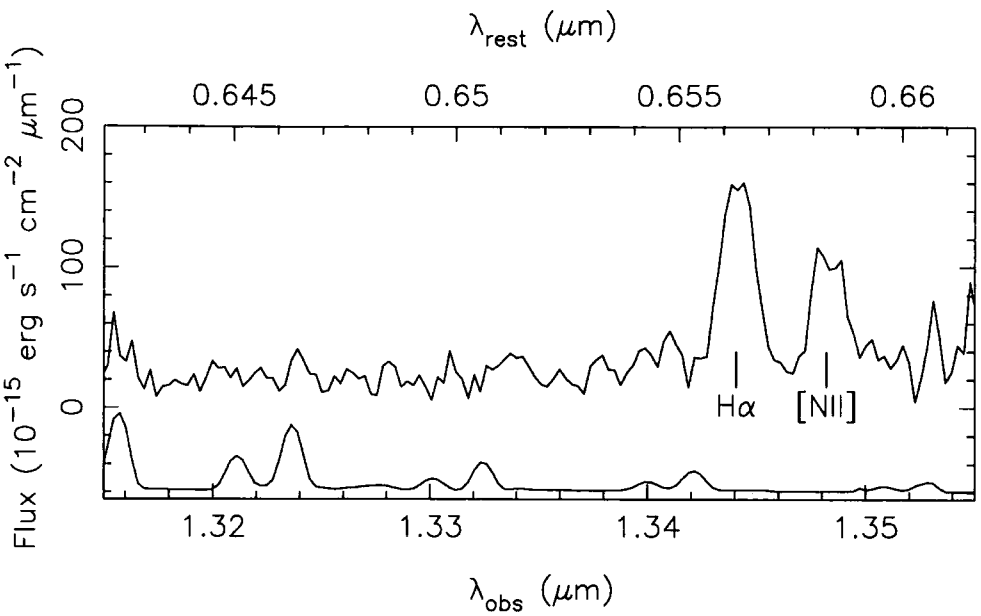

Figure 6.2: The near-infrared spectrum of ERO J164023. We identify the strong emission lines as Hα λ6563 and [NII]λ6583, giving a redshift of $z = 1.0480 \pm 0.0005$.

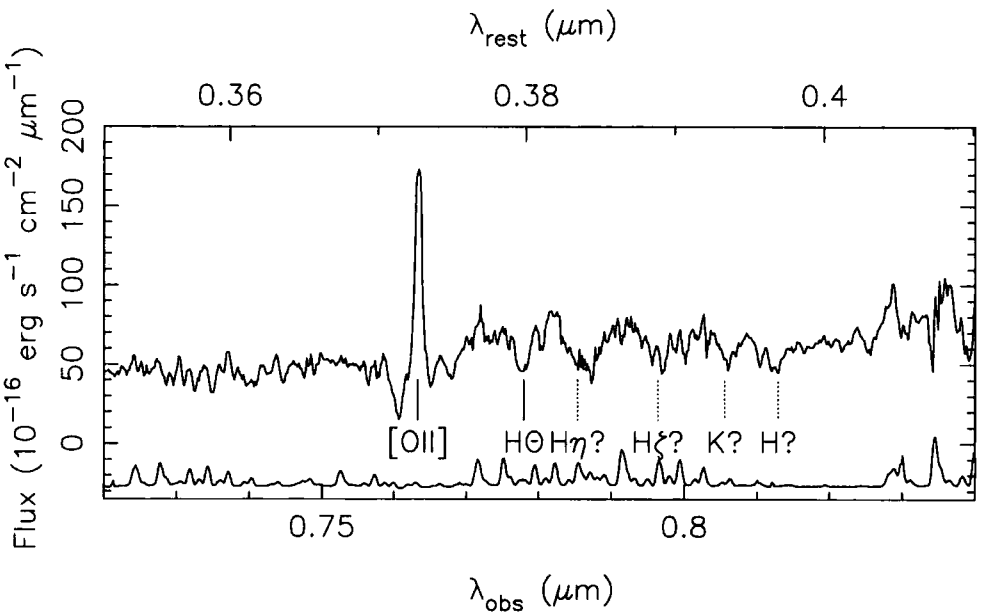

Figure 6.3: The optical spectrum of ERO J164023. We identify the strong emission line as [OII]λ3727 which is confirmed by the identification of the Hα and [NII] lines in the near-infrared spectrum (Fig. 6.2). The Hθ absorption feature is also tentatively detected, although other members of the Balmer series and the CaH and CaK features are not visible. The sky spectrum is also shown in arbitrary units below the science spectrum.

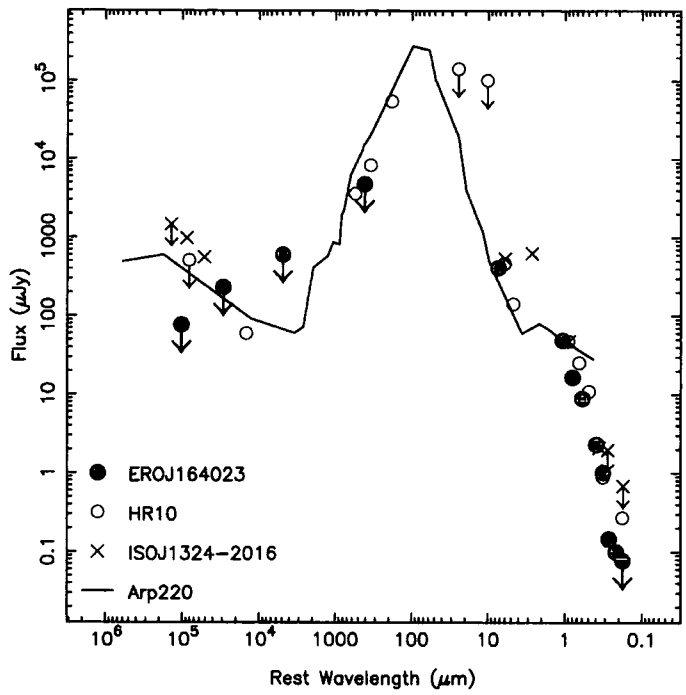

Figure 6.4: The rest frame spectral energy distribution (SED) of ERO J164023 from optical to radio wave-bands. For comparison, we show the SEDs of HR10 (D99; Elbaz et al. 2001), ISO J1324−2016 (Pierre et al. 2001) and Arp220 (Hughes et al. 1998) The flux densities of ERO J164023 have all been corrected for gravitational amplification. The SEDs of all four galaxies have been normalised to the observed K–band flux of ERO J164023.

redshift ($z = 1.048$) produces a solution of $A_V \sim 5$, confirming that ERO J164023 is heavily dust-obscured.

Starburst or AGN?

The spectra of ERO J164023 (Fig. 6.2 & 6.3) contain narrow [OII], Hα and [NII] emission lines (Table 6.2) and a weak Hθ absorption feature. These spectral features are all more typical of star forming galaxies than AGN (e.g. Liu & Kennicutt 1995).

However, the [NII] to Hα flux ratio, log([NII]/Hα) ~ -0.2 (Table 6.2), is higher than the typical value (-0.5) seen for star forming galaxies and suggests that the ERO may be a Seyfert 2 (Veilleux & Osterbrock 1987) or possibly, a composite starburst-Seyfert galaxy (Hill et al. 1999). Nevertheless, the nuclear activity in ERO J164023 may be quite weak, as an AGN contribution to the line emission of as little as 10 per cent appears to be sufficient to account for the [NII] to Hα ratio (Hill et al. 2001). We also note that ERO J164023 was not detected when A 2219 was observed at X-ray wavelengths by *ROSAT*/HRI, implying that any AGN is not

X-ray bright. The 3-σ detection limit from these observations is $< 5.7 \times 10^{-4} \mu$Jy [0.1–2.4 keV] (Edge, priv. comm.).

Assuming that star formation dominates the line emission, we estimate the star formation rate (SFR) of ERO J164023 from its lensing-corrected Hα luminosity: $L_{\mathrm{H}\alpha} = 3.3 \times 10^8$ L$_\odot$, obtaining SFR$_{\mathrm{H}\alpha} \sim 10$ M$_\odot$yr^{-1} for a Salpeter IMF (Kennicutt 1998). As we have made no corrections for dust extinction, this is probably a lower limit. Indeed, a suppression of the observed line fluxes due to dust is also suggested by the very low [OII] to Hα flux ratio of ERO J164023 (0.07±0.03, Table 6.2), which is far lower than the value seen in nearby spirals, 0.43 ± 0.27, and more typical of local dusty starburst galaxies (Poggianti & Wu 2000).

The constraints on the luminosity of the ERO at longer wavelengths can also be used to place an upper limit on the probable star formation rate. Based on the lensing-corrected far-infrared luminosity of $L_{\mathrm{FIR}} \lesssim 4 \times 10^{12} L_\odot$, we estimate SFR$_{\mathrm{FIR}} \lesssim 700$ M$_\odot$yr^{-1} (Kennicutt 1998). A similar upper limit to the SFR is obtained based on the 1.4 GHz flux limit (Table 6.1). We therefore can only constrain the SFR of ERO J164023 to lie within a broad range: $\sim$ 10–700 M$_\odot$yr^{-1}, although all of the estimates suggest that this is a strongly star forming galaxy. The factor of 70 difference between the far-infrared and Hα estimates of the SFR is consistent with that found by Poggianti & Wu (2000) for local starburst galaxies, indicating that the SFR could feasibly be as high as $\sim$700 M$_\odot$yr^{-1}.

6.2.3 The dusty ERO population

We now compare the properties of ERO J164023 with the only other spectroscopically-confirmed dusty EROs: the $z = 1.44$ starburst galaxy, HR10 (D99), and the dusty quasar ISO J1324−2016 at $z = 1.50$ (Pierre et al. 2001).

We start by classifying the EROs using the $(I-K)$–$(J-K)$ diagnostic diagram suggested by Pozzetti & Mannucci (2000). Unfortunately, there is no published J-band photometry for ISO J1324−2016, but using the $(I-K)$ and $(J-K)$ colours of ERO J164023 (4.5±0.1 and 2.1±0.1 – §5) and HR10 (5.8±0.1 and 2.6±0.1 – D99) we find that these galaxies both lie just on the starburst side of the proposed dividing line between evolved and starburst EROs on the $(I-K)$–$(J-K)$ plane. However,

due to the photometric uncertainties, neither ERO can be robustly classified as a starburst on the basis of these three photometric bands alone.

To compare the three EROs across a broader wavelength range we plot the SEDs of HR10 and ISO J1324−2016 in Fig. 6.4. Dealing first with HR10: the spectral shapes of ERO J164023 and HR10 at optical/near-infrared/mid-infrared wavelengths are very similar and both resemble the SED of Arp 220, implying that both galaxies are highly obscured. D99 estimate $L_{\rm FIR}/L_B \sim 300$ for HR10, suggesting that it may be more heavily obscured than ERO J164023. On the other hand, the crude estimates of dust obscuration from the V–band extinction and [OII]/Hα line ratio suggest that ERO J164023 and HR10 suffer comparable degrees of dust obscuration. The scatter seen in the estimates of the relative extinction in these two systems depending upon the diagnostic used supports the idea that the dust has a complex spatial distribution and produces different degrees of obscuration for the emission from the various stellar populations within the galaxies (e.g. Poggianti & Wu 2000).

There is some morphological support for differences in the spatial distribution of visible stars and dust in both HR10 and ERO J164023. *HST* imaging of HR10 through the F814W filter is discussed by D99, the higher redshift of this ERO means that these observations sample similar rest frame UV wavelengths to the F702W image of ERO J164023 ($\sim$ 3500Å). HR10 displays an "S"–shaped morphology, suggesting that it is a disk galaxy, although D99 propose that it may be dynamically disturbed. In contrast, the K–band morphology of HR10 is more symmetrical, suggesting that, like ERO J164023, it may either harbour a bulge of older stars, or more likely a central starburst that is more heavily dust-reddened than the outskirts of the galaxies.

D99 propose that HR10 is a dusty starburst-powered galaxy based on the lack of signatures of nuclear activity in both its emission line widths ($\sim 600\,{\rm km\,s^{-1}}$) and its emission line ratio: $\log([{\rm NII}]/{\rm H}\alpha) \sim -0.4$. Applying the same conversions as used in §6.2.2, we estimate the SFR in HR10 lies in the range ~ 40–$1200\,{\rm M_\odot yr^{-1}}$, where the lower bound again comes from the observed Hα flux (uncorrected for dust) and the upper bound is based on the far-infrared luminosity of the galaxy.

This range suggests that HR10 may be forming stars at a rate ∼2–3 times higher than ERO J164023.

Turning now to the comparison of ERO J164023 with ISO J1324−2016, we see that in contrast to the broad similarities between ERO J164023 and HR10, the galaxy shares few characteristics with ISO J1324−2016. The lack of *HST* imaging of ISO J1324−2016 precludes detailed analysis of its morphology, however Pierre et al. (2001) state that this source appears point-like in $\sim 0.5''$ seeing in the K–band, unlike ERO J164023 (and HR10) which is extended in similar seeing at these wavelengths (Fig. 6.1). The optical SED of ISO J1324−2016 also shows the precipitous decline in the UV characteristic of reddening by dust (Pierre et al. (2001) estimate $A_V \sim 4$–7 from the Balmer decrement in ISO J132402916), however the behaviour in the mid-infrared is very different from ERO J164023 (and HR10) with excess emission at 6.75 μm, which has been interpreted as evidence for a hot component, probably from circumnuclear dust around an AGN.

The identification of ISO J1324−2016 as a dusty quasar is confirmed by a strong, broad Hα emission line (~ 3000 km s^{-1}) and relatively strong radio emission ($P_{1.4\,\mathrm{GHz}} \sim 2 \times 10^{25}$ W Hz^{-1}). This contrasts markedly with the narrow line widths seen in both ERO J164023 and HR10. In addition, neither ERO J164023, nor HR10, have so far been detected at 1.4 GHz, although both appear to be at least an order of magnitude less luminous than ISO J1324−2016 in this band, with $P_{1.4\,\mathrm{GHz}} \lesssim 5 \times 10^{23}$ and $\lesssim 4 \times 10^{24}$ W Hz^{-1} respectively.

In summary: the properties of ERO J164023 suggest it shares many characteristics with the ultraluminous starburst HR10, although it is less extreme and also shows evidence of nuclear activity. However, the AGN component in ERO J164023 is dominated in most observations by the star formation in this galaxy and hence this system differs markedly from the dusty quasar, ISO J1324−2016.

6.2.4 Conclusions

We have obtained a secure spectroscopic identification of ERO J164023, a dusty starburst-Seyfert ERO at a redshift of $z = 1.05$. This brings the total number of spectroscopically identified dusty EROs for which detailed analysis is available in the

literature to three and adds a composite AGN/starburst system to the apparently pure starburst (HR10) and AGN-dominated systems (ISO J1324−2016) previously identified.

We complement this spectroscopy with deep *HST* optical imaging and infrared, sub-mm and radio data, enabling us to study the morphology and SED of this unusual galaxy. The main conclusions of our work are as follows:

(i) ERO J164023 is a disk galaxy, the central region of which dominates its optical/near-infrared colour of $(R - K) \sim 6$. The steep optical/infrared SED is consistent with this galaxy being heavily obscured by dust ($L_{\rm FIR}/L_B \lesssim 200$; $A_V \sim 5$).

(ii) The spectral line widths are consistent with the dust emission being powered by hot young stars. However, the [NII]/Hα line strength ratio suggests that this is a "composite" starburst-Seyfert galaxy. Assuming star formation to be the dominant power source, we constrain the SFR to lie in the broad range $\sim$ 10–700$\rm M_{\odot}yr^{-1}$ which is a factor of $\sim$2–3 times lower than HR10.

(iii) ERO J164023 and HR10 have strikingly similar rest frame optical/infrared spectral properties and both exhibit disk-like morphologies. The dominant role of the central region of these galaxies in producing their extremely red optical/near-infrared colours is consistent with them both containing an obscured, central starburst. Variation of the measured dust obscuration suffered by each galaxy from a number of diagnostics suggests that the dust and various stellar populations within dusty starburst galaxies differ in their spatial distributions.

(iv) Despite the photometric similarities of the three EROs, HR10 and ERO J164023 both differ from ISO J1324−2016 in that the latter's emission is primarily driven by an AGN, whereas star formation appears to be the dominant power source in HR10 and ERO J164023.

Overall, our work reveals that samples of dusty EROs contain the full range of power sources: dusty starbursts, AGNs and composite starburst-AGN systems. The broad wavelength range of our imaging (X-ray to radio) together with our optical and near-infrared spectroscopy allows us to identify which observations are required to accurately segregate active (i.e. dusty) and passive EROs and then to

classify active EROs into their different sub-classes.

Firstly, whilst the $(I-K)$–$(J-K)$ colour-colour plane (Pozzetti & Mannucci 2000) provides a rough classification between active and passive EROs, photometric uncertainties appear to undermine the accuracy of this method (a concern shared by Pozzetti & Mannucci 2000). Accurate separation of active and passive EROs therefore requires mid-infrared/far-infrared or sub-mm observations to search for the signature dust emission of active systems. The forthcoming launch of *SIRTF* should provide the opportunity for rapid progress in this respect.

However, near-infrared spectroscopy is also essential to further classify active EROs into their respective sub-classes on the basis of their detailed spectral properties. Spectral analysis of a statistically reliable sample of active EROs is therefore crucial to a better understanding of the evolution of dust-obscured star-formation and AGN-activity as a function of cosmic epoch. We anticipate that the forthcoming generation of near-infrared multi-object spectrographs will play a significant role in this activity.

6.3 ERO J003707: A Multiply-imaged Sa-ERO

In this section we present near-infrared spectroscopy of a second ERO identified in our UKIRT survey of the ten clusters in our sample. ERO J003707+0909.5 is one of three gravitational images of a single galaxy, produced by the foreground cluster lens A 68 ($z = 0.255$). We describe our observations in §6.3.1, describe our source-plane analysis in §6.3.2, discuss the diversity of passive EROs and speculate on the evolution of ERO J003707 in §6.3.3 and finally summarise our conclusions in §6.3.4.

6.3.1 Observations

ERO J003707 was first detected in *HST* imaging of A 68 as part of our lensing survey of X-ray luminous galaxy clusters (§3.2). A 68 was observed with *HST* /WFPC2 for 7.5 ks through the F702W filter and 8.8 ks using UFTI on the 3.8-m United Kingdom Infrared Telescope (UKIRT). We show a subset of these data in Fig. 6.5

and identify the three images of ERO J003707. We provide further details of these data and their reduction and analysis in §3 and §5.

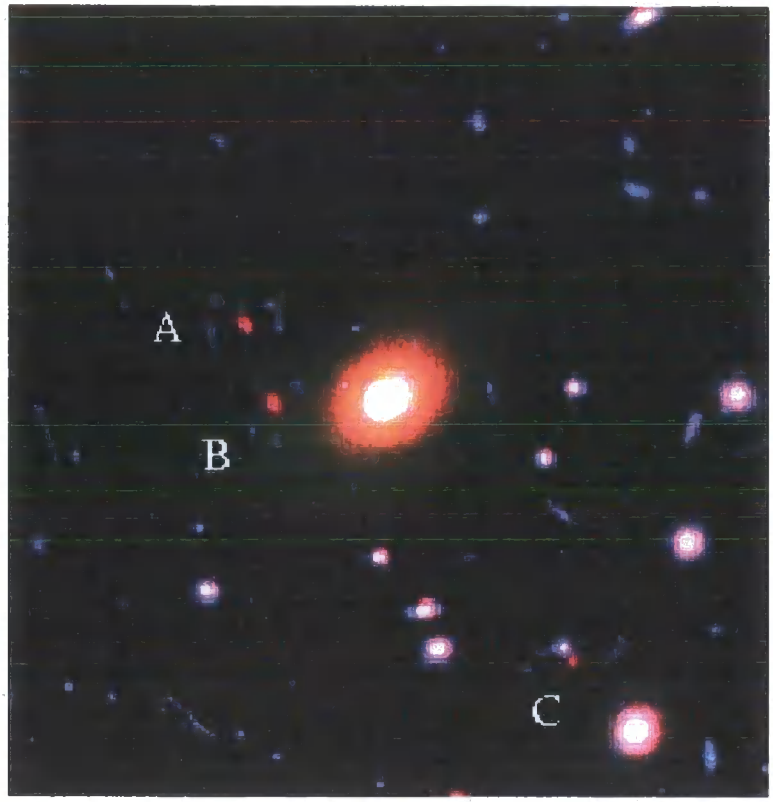

Figure 6.5: True colour *RK* view (50″ × 50″) of the core of the galaxy cluster A 68, exploiting the superlative resolution of both our optical *HST* and near-infrared UKIRT imaging data. The bright elliptical galaxy in the centre of the frame is the central galaxy of the cluster. Three images of ERO J003707 are clearly visible and are marked A,B and C. Each image comprises a central red "bulge", surrounded by numerous fainter blue knots of current or recent star formation. North is up and East is left.

Our near-infrared spectroscopy targeted specific spectral features based on the likely nature of ERO J003707, and a crude estimate of its redshift. We first examined our *RIJK*–band photometry of ERO J003707 (§5) and found that it does not discriminate between old stars and dust-obscuration as the origin of the extreme colours of this galaxy. For simplicity, we therefore fitted an elliptical galaxy spectral template (Coleman et al. 1980) to our photometry of the central red component (§5) using HYPER-Z (Bolzonella et al. 2000) and obtained $z_{\rm phot} \sim 1.7$. Assuming that the near-infrared emission is dominated by old stars, we searched for the 4000Å break and CaII H and K absorption lines in the z–band. However, since our photometry is not conclusive, and ERO J003707 appears to be a disk-galaxy (§6.3.2), we also observed in the J– and H–bands, searching for Hβ, [OIII], Hα and [NII] emission

lines in addition to [OII] which should appear in the z–band if ERO J003707 is a star-forming galaxy at $z \sim 1.7$.

We observed ERO J003707 with CGS4 (Mountain et al. 1990) on UKIRT on 2001 September 15–18 in non-photometric conditions and $\sim 1''$ seeing with the slit centered on the K–band emission from ERO J003707+0909.5 (α, δ (J2000) = 00 37 07.37 + 09 09 28.4). We adopted a slit position angle of 22° to ensure that the K–band emission from image B (Fig. 6.5) also fell on the slit, although this meant that the disk light was not well sampled. Nodding along the slit, we obtained total integrations of 7.2 ks and 21.6 ks in the J– and H–bands respectively. These data were reduced in a standard manner using IRAF tasks. The final reduced frames contained no strong spectral features, although a weak continuum was detected in the H–band. We also used the Keck-II 10–m telescope[‖] to obtain z– and H–band spectra of ERO J003707+0909.5 with NIRSPEC (McLean et al., 1998) on 2001 November 20–21. Using the same target co-ordinates and slit position angle, we integrated for 7.2 ks and 3.6 ks in the z– and H–bands respectively, in clear and photometric conditions (FWHM$\sim 0.8''$). These data were also reduced in a standard manner using IRAF tasks, including the WMKONSPEC package. These data confirm the absence of strong emission lines in the H–band. The z–band data also contain no strong emission lines, however they reveal a spectral break at $1.04 \pm 0.01 \mu$m. We show the z–band continuum in Fig. 6.6. Given the absence of strong emission lines in the zJH–bands and the fact that our observations primarily sample the central red component of this galaxy, we interpret the break in the z–band spectrum of ERO J003707 as the 4000Å break at a redshift of $z = 1.60 \pm 0.03$.

6.3.2 Source-plane Reconstruction and Analysis

We use our lens model of A 68 (§3) to reconstruct the source-plane properties of ERO J003707. We threshold the R– and K–band frames at 1.5–σ above the sky

[‖]Based on observations made at the W. M. Keck Observatory by Gemini staff, supported by the Gemini Observatory, which is operated by the Association of Universities for Research in Astronomy, Inc., on behalf of the international Gemini partnership. The W.M. Keck Observatory is operated as a scientific partnership among the California Institute of Technology, the University of California and the National Aeronautics and Space Administration.

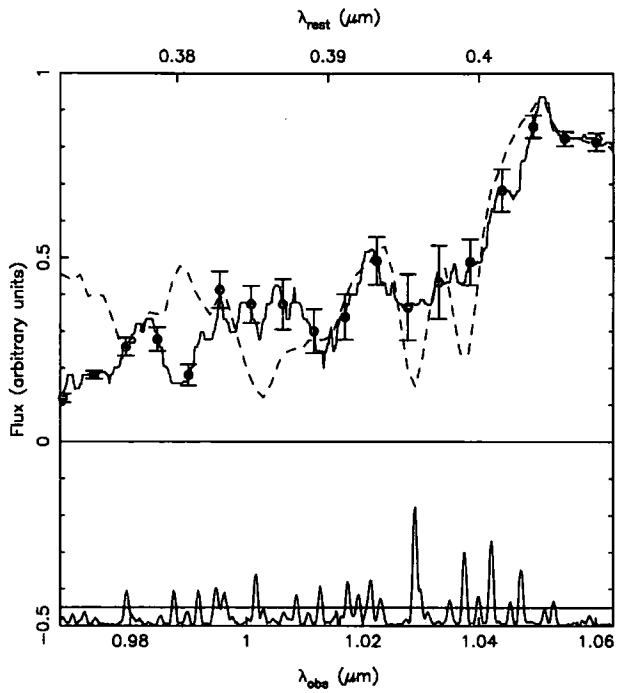

Figure 6.6: The NIRSPEC z–band continuum of the central red bulge of ERO J003707, produced by median filtering the spectrum, rejecting pixels dominated by strong night-sky emission i.e. those regions above the horizontal line in the lower spectrum, which shows the night sky spectrum (offset and scaled for clarity). The width of the median filter dominates the uncertainty in the redshift quoted in the text. We identify the discontinuity in the spectral shape at $\lambda = 1.04 \pm 0.01\mu$m as the 4000Å break. The continuum data are also plotted as filled circles at $\Delta\lambda = 50$Å intervals, and we estimate the uncertainties in these data points by bootstrap resampling within each median filter window. The dashed line shows a template spectrum of a passive galaxy from Mannucci et al. (2001).

background and ray-trace each pixel to the source plane at $z = 1.6$, thus creating R– and K–band source-plane maps of ERO J003707. We show, as an example, the source-plane reconstruction of ERO J003707+0909.5 (image "A" from Fig. 6.5) in Fig. 6.7b. We also simulate blank-field observations of ERO J003707 (i.e. without a magnifying gravitational lens) by adding the source reconstructions to noise maps from blank sky regions in the original science frames (Figs. 6.7c & 6.7d).

We measure the source-plane (i.e. "un-lensed") apparent K–band magnitude of ERO J003707: $K = 19.8 \pm 0.1$. This translates into $M_K \sim -25.0$ (Fioc & Rocca-Volmerange 1997), which suggests that the K–band luminosity of ERO J003707 is comparable to a present day $L^\star$ galaxy (adopting $M_K^\star = -24.8$ from Cole et al. 2001). We also measure the $(R - K)$ colour, using an aperture equivalent to a $2''$–diameter in the source-plane. We transform the F702W photometry to Cousins R–band and correct for interstellar extinction (see §5 for details), to give $(R -$

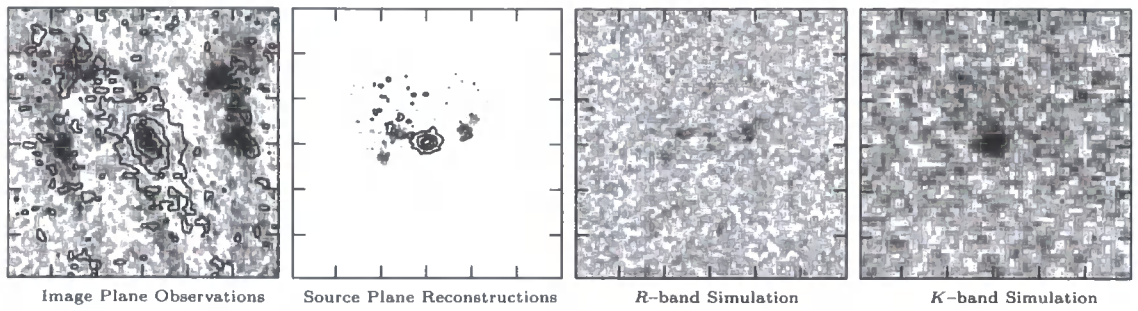

Figure 6.7: We illustrate the morphology of ERO J003707 using the most strongly amplified of its three gravitational images – image A from Fig. 6.5. (a) The image-plane morphology, showing the observed F702W morphology (FWHM$\sim$ 0.15″) as the grey-scale and the observed K–band morphology (FWHM$\sim$ 0.4″) as contours. The light from the central galaxy of A 68 had been subtracted from both the R– and K–band data in this panel. (b) The reconstructed F702W (grey-scale) and K–band (contours) source-plane morphology of ERO J003707; both reconstructions are displayed at the pixel-scale and resolution of the original *HST* observations. (c) A simulated blank-field 7.5–ks *HST*/WFPC2 observation of ERO J003707. (d) A simulated blank-field 8.8–ks UKIRT/UFTI (FWHM$\sim$ 0.4″) observation of ERO J003707. Each panel is 6″ on a side and North is up and East in left.

$K) = 5.4 \pm 0.1$. This is $\sim$ 1 mag bluer than we obtained in §5 because we did not correct the photometric aperture for lens amplification in the earlier work. We therefore measured the colour of the central red bulge in contrast to the source-plane photometry presented here that also samples the rest-frame ultraviolet emission from the disk. We also compare our photometry with spectral energy distributions of local galaxies using PEGASE (Fioc & Rocca-Volmerange 1997), and find that if a galaxy with an SED similar to a present-day Sa galaxy were placed at $z = 1.6$, it would have a similar $(R - K)$ colour to ERO J003707.

The *HST* frame reveals a complex and irregular rest-frame ultraviolet ($\sim$ 2700Å) morphology, comprising 5–6 knots indicating current or recent star formation (Fig. 6.7a). In contrast, the K–band morphology consists of a single centrally concentrated component, although there is some diffuse, low surface brightness K–band flux co-incident with the knots of rest-frame ultraviolet emission (Fig 6.7a). Together with our spectroscopy (§6.3.1) and the robustness of our classification of ERO J003707 as an ERO after correction for gravitational lensing, this suggests that ERO J003707 is a disk-galaxy with a passively evolving central bulge and a modestly star-forming disk. We quantify the morphology by measuring the source-plane concentration (C) and asymmetry (A) (Abraham et al. 1996) of the rest-frame ultraviolet and I–band emission from ERO J003707 using our R– and K–band data. We estimate:

$C(2700\text{Å}) = 0.13 \pm 0.02$, $C(8500\text{Å}) = 0.59 \pm 0.09$, $A(2700\text{Å}) = 0.79 \pm 0.05$ and $A(8500\text{Å}) = 0.56 \pm 0.04$. These measurements place ERO J003707 in the same region of C–A space as early-type spiral-galaxies in the local Universe when observed at ultraviolet and optical wavelengths (Burgarella et al. 2001; Kuchinski et al. 2001). We also measure the effective radius of the central bulge (r_e) and the exponential scale-length of the disk (r_d). At $z = 1.6$, the 4000Å break falls in the z–band (§6.3.1) and so our R– and K–band observations are dominated by the currently (or recently) star-forming and passively evolving components of the SED respectively. We crudely relate these two elements to the stellar disk and the central bulge respectively. We therefore use our R– and K–band source-plane reconstructions (Fig. 6.7b) to estimate $r_e \sim 0.6\,\text{kpc}$ and $r_d \sim 3.4\,\text{kpc}$. We compare these measurements with the observed r_e–r_d correlation for early-type disk-galaxies in the local Universe (e.g. Khosroshahi et al. 2000), and find that ERO J003707 is consistent with this correlation. Finally, we estimate that the rest-frame I–band bulge-to-total luminosity ratio, obtaining B/T ~ 0.8 – confirming that ERO J003707 is a bulge-dominated galaxy.

In summary, our source-plane photometric and morphological analyses reveal that ERO J003707 is a bulge-dominated early-type disk galaxy with an SED similar to a local Sa galaxy.

6.3.3 Discussion

Diversity of Passive EROs

Various authors (e.g. Kauffmann & Charlot 1998; Fontana et al. 1999; Daddi et al. 2000) have used observations of passive EROs and other K–selected samples to argue for or against monolithic collapse (e.g. Eggen et al. 1962; Larson 1975; Tinsley & Gunn 1976) or hierarchical assembly (e.g. White & Frenk 1991; Cole et al. 2000) theories of galaxy formation (see also §5). Regardless of the details of this debate, both arguments implicitly assume that *all* passive EROs are elliptical galaxies.

The extremely red colour of ERO J003707 is dominated by a central bulge of old stars, however ERO J003707 also appears to contain a weakly star-forming disk.

Contrary to the popular assumption, passive EROs therefore appear to comprise both elliptical galaxies and early-type spiral-galaxies at $z \gtrsim 1$ (Sa-EROs). Such Sa-EROs have probably not been identified in conventional blank-field ERO surveys (e.g. Daddi et al. 2000) due to the low surface brightness of the disk in these systems – the disk is only detected at $\lesssim 2$–σ in our simulated blank-field observation of ERO J003707 (§6.3.2).

We attempt to constrain the surface density of Sa-EROs. Our analysis of ERO J003707 reveals a colour gradient (§6.3.2); we therefore search for this signature in the other 59 members of our ERO sample (§5). We first quantify the expected gradient using our simulated R– and K–band blank-field observations of ERO J003707 to measure its seeing-matched (FWHM$\sim$ 0.4″) 1″ and 2″ diameter aperture $(R-K)$ colours. Although the 1″ colour is 0.6 ± 0.3 mag redder than the 2″ colour, the two colours are formally consistent within the uncertainties. We repeat this measurement ten times, each time using simulated images that incorporate different noise maps. These experiments confirm the $\lesssim 2$–σ significance of the colour gradient in our simulated observations. We measure the 1″ and 2″ diameter aperture $(R-K)$ colours of our ERO sample. We find that four EROs display statistically significant bluer colours at larger radii consistent with the simulations described above and we note that in §5 we classified all four of these galaxies as having an irregular morphology. We therefore suggest that ~ 10 per cent of EROs with $(R-K) \geq 5.3$ and $K \leq 21$ may be Sa-EROs, which translates into a surface density of $\sim 0.2\,\mathrm{arcmin}^{-2}$, based on the integrated number counts presented in §5.

Impact on Galaxy Formation Models

One of the primary objectives of studying EROs is to constrain the formation epoch of massive elliptical galaxies. To that end, we compared our ERO number counts with the predictions of several theoretical models, including the Cole et al. (2000) semi-analytic prescription (§5). In summary, the current generation of semi-analytic models under-predict the number density of EROs by approximately an order of magnitude (see also Firth et al. 2002). This is an important observational challenge to the hierarchical galaxy formation paradigm that underpins the Cole et al. model

(hereafter GALFORM). Whilst a detailed investigation of why hierarchical models fail to reproduce the observed ERO population is beyond the scope of this chapter, we briefly use ERO J003707 to shed some light on the issue.

Our discovery of a Sa-ERO, and the observational challenge of detecting the low surface brightness emission from the stellar disk of such systems raises important questions about our ability to compare observations with model predictions. The crux of the issue is that model predictions are based on the total light output of galaxies, taking no account of the spatial distribution and thus surface brightness of the emission. It is therefore possible that the low surface density of EROs predicted by GALFORM may be partly due to a relative blue-ening of galaxy colours relative to observed colours. We construct a simple test to investigate this hypothesis: if neglecting surface brightness effects in model predictions does causes significantly bluer model galaxy colours, then complete removal of this emission from the spectral energy distributions of the model galaxies should cause a significant reddening of galaxy colours. As GALFORM splits each galaxy into bulge and disk components, we therefore re-measured the predicted surface density of EROs in the Cole et al. (2000) reference model, using just the bulge light (i.e. we ignored the disk light, as it has a very low surface brightness in observed EROs). The resulting number counts are indistinguishable from those based on the total light output of the model galaxies (Baugh, priv. comm.). This suggests that the low numbers of EROs predicted by GALFORM is not due to a population of disk-galaxy EROs whose model colours are blue-ened by ignoring the low surface brightness of the disk emission when constructing colour-selected number counts. This result re-inforces our conclusion in §5 that the current implementation of semi-analytic models of galaxy formation appears to produce insufficient stars and/or dust at high-redshift.

Evolution of ERO J003707

We speculate on the evolution of ERO J003707. The rest-frame I–band luminosity of the central bulge is $\sim 4.3 \times 10^{10}$ $L_{\odot}$. The strong 4000Å break (§6.3.1) suggests that the bulge stars in ERO J003707 formed a few billion years prior to the epoch of observation (e.g. Dunlop et al. 1996). We estimate the age of these stars using the

D_{4000} index, which is defined as the ratio between the average flux density in the range $4050 \leq \lambda_{\rm rest} \leq 4250\,$Å and that in the range $3250 \leq \lambda_{\rm rest} \leq 3950\,$Å (Bruzual 1983). Unfortunately the useful wavelength range of our z–band spectroscopic data is limited by the night sky emission; we therefore are unable to measure the continuum flux beyond $\lambda_{\rm rest} \sim 4100\,$Å. We therefore use the available data, and use the template spectrum plotted in Fig. 6.6 to incorporate the limited wavelength range in the uncertainty in our measurement. We measure $D_{4000} = 2.4 \pm 0.5$, which translates into an age of $\geq 2.5\,$Gyr (Poggianti & Barbaro 1997; assuming solar metallicity), implying a formation redshift of $z_{\rm f} \gtrsim 3.7$ in a ΛCDM cosmology, and $z_{\rm f} \gtrsim 6.5$ in a standard CDM cosmology. This suggests that the bulge was formed in a short, but intense starburst at $z_{\rm f} \gg 2$. This event would have certainly disrupted and may have destroyed any existing disk. In contrast to its observed morphology, ERO J003707 was therefore probably a disk-less galaxy at $z \sim 3$.

Turning to the disk component, we estimate the rest-frame I–band disk luminosity to be $\sim 7.5 \times 10^9$ $L_\odot$ and the current star formation rate (SFR) to be SFR~ 6 $M_\odot$ yr^{-1} (Kennicutt's 1998; assuming a Salpeter (1955) IMF integrated over 0.1–100 $M_\odot$ and neglecting dust). Ignoring mergers, the future evolution of ERO J003707 will depend on the duration of star formation in its disk. If the gas becomes exhausted or expelled from the galaxy, then the star formation would cease and ERO J003707 would probably evolve into an E/S0 galaxy by the present day. On the other hand, semi-analytic models of galaxy formation (Baugh et al. 1996) predict that bulges and spheroids are formed from merging of disk-galaxies and subsequently may accrete gas, thus re-growing a disk component. We explore this "transvestite galaxy" hypothesis (Dr. Richard Bower, priv. comm.) by estimating the timescale ($\tau_{\rm eq}$) over which, at the current SFR, the disk stellar mass will become comparable with the bulge stellar mass. We convert the bulge luminosity to a stellar mass (assuming $M/L \sim 1$; Bell & de Jong 2001) and divide by the disk SFR to obtain $\tau_{\rm eq} \sim 6 \times 10^9\,$yrs which is roughly equal to the look-back-time from the present day to $z = 1.6$. This raises the intriguing possibility that the progenitors of a fraction of luminous spiral galaxies in the local Universe could have been EROs when observed at $z \gtrsim 1$.

6.3.4 Conclusions

We present near-infrared spectroscopy of ERO J003707+0909.5, the brightest of three gravitationally-lensed images of ERO J003707 in the field of the massive cluster A 68 ($z = 0.255$). Our near-infrared spectroscopy reveals a break at $\lambda_{\rm obs} = 1.04 \pm 0.01\mu$m in the spectral energy distribution of this galaxy. This feature arises from the redshifted 4000Å break of the old stellar population which dominates the central bulge-like component of this galaxy. We therefore conclude that ERO J003707 lies at $z = 1.60 \pm 0.03$. We use the detailed lens model of A 68 from §3 to reconstruct the source-plane properties of ERO J003707. Our main conclusions are as follows:

(1) The luminosity and $(R-K)$ colour of ERO J003707 are similar to those of an L^* galaxy with a SFR comparable to an Sa galaxy in the local Universe.

(2) Morphological parameters (C, A, $r_{\rm e}$, $r_{\rm d}$, B/T) based on rest-frame ultraviolet and I–band emission confirm that ERO J003707 is an early-type disk-galaxy.

(3) The unique association of passive EROs with elliptical galaxies is clearly too simplistic. We estimate that ~ 10 per cent of EROs with $(R-K) \geq 5.3$ and $K \leq 21$ may be Sa-EROs i.e. early-type disk-galaxies similar to ERO J003707.

(4) We estimate that the bulge stars in ERO J003707 formed ≥ 2.5 Gyr ago and speculate that, if the current disk SFR (~ 6 M$_\odot$ yr^{-1}) continues due to the cooling of gas onto ERO J003707 in the manner predicted by hierarchical galaxy formation models (Baugh et al. 1996), then ERO J003707 would evolve into a luminous spiral galaxy by the present day.

6.4 Summary

Our original motivation to search for EROs in the fields of the ten clusters in our *HST* lensing survey was to increase the chance of successful spectroscopic identification of these mysterious galaxies. The lack of efficient multi-object spectrographs on 10–m class telescopes continues to inhibit progress in this field. Nevertheless,

we have combined our unique sample of magnified EROs and long-slit near-infrared spectroscopy to identify two sources from the sample constructed in §5.

ERO J164023 is a dusty starburst-Seyfert galaxy at $z = 1.05$. This galaxy reveals that dusty EROs probably span the full range of power sources: starbursts (e.g. HR10, Dey et al. 1999), AGN (e.g. ISO J1324−2016, Pierre et al. 2001) and composite starburst-AGN systems such as ERO J164023.

ERO J003707 is a is a bulge-dominated early-type disk galaxy with an SED similar to a local Sa galaxy. We estimate that $\sim$ 10% of EROs may be similar systems and that the star-forming disk in these galaxies has probably not been detected due to the low surface brightness of the disk emission.

In contrast to the simple picture that EROs comprise simply passively evolving elliptical galaxies and a population of dusty starburst galaxies, our results indicate that EROs are considerably more diverse than previously thought. In addition to the ongoing quest to measure the fraction of passive and active EROs as a function of redshift, several new questions emerge:

- What is the relative fraction of AGN and starburst powered active EROs as a function of redshift?
- Given the existence of composite starburst-AGN systems, is there an evolutionary connection between pure AGN and pure starburst EROs?
- Can we place tighter constraints on the fraction of Sa-EROs using wide-field ERO surveys?
- What are the implications of Sa-EROs for galaxy evolution? Do galaxies reacquire a gaseous and stellar disk from their environment following merger activity as predicted by hierarchical models?

Answers to these questions will hopefully come with the next generation of wide-field ERO surveys and spectroscopic follow-up with wide-field near-infrared multi-object spectrographs and red-optimised optical spectrographs.

7 CONCLUSIONS

We describe an experiment to study the mass and structure of ten massive galaxy clusters at $z \sim 0.2$. In the absence of mass-selected cluster samples, we select ten of the most X-ray luminous clusters from the XBACs sample (Ebeling et al. 1996). The observational tools of choice to study the distribution of mass in galaxy clusters at intermediate redshift ($z \sim 0.1$–1) are (1) gravitational lensing, because it is free from assumptions about the physical nature and thermodynamic history of the cluster material and (2) *Hubble Space Telescope (HST)* imaging because the exquisite spatial resolution of such data significantly enhances the precision achievable in gravitational lensing studies. Gravitational lensing studies with *HST* therefore provides a detailed and direct view of the spatial distribution of the total (i.e. baryonic and non-baryonic) material content of these massive systems.

We present *HST* imaging of all ten clusters in our sample; we detect numerous previously unobserved gravitationally-lensed features, including two spectacular new strong-lensing clusters (A 68 and A 383). We employ optical and near-infrared spectrographs on 10–m class telescopes to secure spectroscopic identifications of the brighter multiple-image candidates. This information, together with the weakly-sheared background galaxies and published multiple-image spectroscopy enable us to constrain a detailed, analytic gravitational lens model of each cluster. We complement these models with analysis of archival *Chandra* observations of the same clusters. These X-ray data enable us to compare the similarities and differences between the total and baryonic mass distributions.

As well as studying the mass and structure of the galaxy clusters themselves, we use the lens models to investigate some of the key observational challenges to the Cold Dark Matter (CDM) paradigm. We also exploit the magnifying power of the lenses to construct a sample of gravitationally-lensed Extremely Red Objects (EROs). These faint, red galaxies are expected to harbour important clues about the formation epoch and mechanism of massive galaxies. We study the photometric, morphological and spectroscopic properties of this ERO sample in an attempt to

identify and decipher some of these clues.

We summarise the key results of this thesis under the headings: Cluster Mass and Structure, Implications for CDM and Gravitationally Lensed EROs.

7.1 Cluster Mass and Structure

The central region ($r \lesssim 500$ kpc) of six out of the ten clusters contain more than 10% substructure ($M_{\rm sub}\,/\,M_{\rm tot} \geq 0.1$). Based on this result alone, the prevalence of dynamical activity in X-ray luminous clusters at $z \sim 0.2$ is high. The *Chandra* data reveal a similar picture, with 70% of the clusters having an irregular or bi/multi-modal morphology. Six of these seven clusters also have $\geq$ 10% substructure in their lens models, and the seventh (A 267) has a highly elliptical mass morphology and a large offset between the mass and X-ray peaks (22 ± 1 arcsec) which is also strongly suggestive of dynamical activity.

We study the scatter of the clusters in the mass-$L_{\rm X}$ plane, and find that the mass dispersion of the compact ($M_{\rm sub}$ / $M_{\rm tot} < 0.1$) clusters is consistent with the self-similar scaling relations that assume hydrostatic equilibrium; the mass dispersion of the clumpy clusters ($M_{\rm sub}$ / $M_{\rm tot} \geq 0.1$) is 3$\times$ greater than self-similar. Turning to the mass-$T_{\rm X}$ plane, we see that on average, the clumpy clusters ($M_{\rm sub}$ / $M_{\rm tot} \geq 0.1$) are $\sim$ 25% hotter than the compact ($M_{\rm sub}$ / $M_{\rm tot} < 0.1$) clusters at a fixed mass; we interpret this as further evidence of the dynamical immaturity of the clumpy systems. Two of the compact clusters are classified as cooling flow clusters (A 383, A 1835); the mass and X-ray temperature of these two systems agree with the empirical mass-temperature relation for relaxed cooling flow clusters (Allen, Schmidt & Fabian 2001).

In summary the X-ray temperature and luminosity of the clusters are strongly influenced by their dynamical maturity. One's perspective on these massive systems depends fundamentally on the selection function used to construct the sample and the analysis methods used. Specifically, samples of cooling flow clusters ($t_{\rm cool} < 10^9$ years and emission line central galaxy) appear to form a well-defined sub-set of clusters which are more regular than the general cluster population and appear

to follow scaling relations that are based on equilibrium models. Non-cooling flow clusters are more numerous and significantly more diverse than their cooling flow siblings. This diversity stems from the dynamical immaturity of the general massive cluster population, indicating substantial in-fall into the central regions of clusters from the surrounding field during the last 2–3Gyr, i.e. since $z \sim 0,5$ for clusters at $z \sim 0.2$. We show how this in-fall affects the thermodynamics of the the intra-cluster medium, and also note that it will probably bring new galaxy populations into these high density regions.

7.2 Implications for CDM

We have also used our unique suite of detailed lens models to investigate some of the key observational challenges to CDM. Specifically, we studied the density profile of A 383, the geometry of our lens models and our normalisation of the cluster mass-temperature relation. We summarise our key results:

A 383 contains two radial arcs which enable us to place tight constraints on the slope of the dark matter density profile in the core of this cluster. We obtain an inner density profile slope of $\alpha = 1.3 \pm 0.04$(statistical) $\pm$ 0.1(systematic) where $\rho \propto r^{-\alpha}$, ρ is the three-dimensional density and r is the three-dimensional radial coordinate. Our model of A 383 is therefore consistent with the presence of a central cusp in the dark matter mass distribution. Other recent lensing studies (Dahle et al. 2002b; Sand, Treu & Ellis 2002) are also consistent with a central cusp, however there is a strong diversity between the values of α from these studies. There is therefore an urgent need to compare the range in profile slopes from observations with comparable results from simulations. It is already clear however, that the claimed "universal" profile may show large scatter.

We also investigate the proposal that a large cross-section to dark matter self-interaction may help to reconcile theory with a variety of challenges to CDM, primarily on galaxy-scales. We use the geometry of our lens model of A 383 to constrain the velocity independent dark matter cross-section to self-interaction to be $s_{\rm dm,o} \lesssim 7 \times 10^{-3}$ cm^2 g^{-1}. This is significantly less than than the lower limit

of $s_{\rm dm,o} > 0.45$ cm^2 g^{-1} estimated by Spergel & Steinhardt as required to reconcile CDM with the apparent observational challenges. We generalise our constraint on $s_{\rm dm,o}$ to a velocity dependent model $s_{\rm dm}\ (v) = s_{\rm dm,o}\ (v/v_o)^{-a}$ and combine it with other constraints from the literature to identify a small region of parameter space ($1.6 \lesssim a \lesssim 3.4$ and $0.45 \lesssim s_1\ v_{100}^{-a} \lesssim 1.5$*) that would resolve the galaxy-scale challenges to collisionless CDM.

Finally, we use our lensing based mass-temperature normalisation to investigate the systematic impact of cluster substructure on cluster abundance measurements of σ_8. In particular, we study the difference between the mass-temperature normalisations for compact and clumpy clusters. We estimate that $\sigma_8 = 0.75 \pm 0.05$(statistical) $\pm\ 0.11$(systematic), and interpret the $\sim 20\%$ discrepancy between our estimate and the canonical $\sigma_8 \simeq 0.9$ as arising from the impact of the dynamical immaturity in our cluster sample on the ambient cluster temperatures, giving rise to a hotter normalisation of the cluster mass-temperature relation. This is the first time that this systematic effect has been identified observationally, and agrees with the recent semi-analytic predictions of Randall et al. (2002).

7.3 Gravitational Lensed EROs

As well as revealing the detailed cluster morphology, our lens models describe the detailed gravitational optics of each system, and thus provide the crucial link between observations of magnified high redshift galaxies and robust measurement of their properties. We therefore exploit the magnifying power of the cluster lenses to construct a sample of gravitationally lensed Extremely Red Objects (EROs). These are a class of distant galaxies about which relatively little is known, but which are expected to harbour important clues about the formation epoch and mechanisms of the massive galaxies that we observe in the local Universe. We have therefore undertaken a deep near-infrared survey of the ten clusters in our *HST* lensing survey using the United Kingdom Infrared Telescope (UKIRT).

Our survey identifies 60 EROs with $(R-K) \geq 5.3$, of which 26 have $(R-K) \geq$

*where $s_{\rm dm} = s_1\ v_{100}^{-a}$ and $s_1 = s_{\rm dm,o}$ /1 cm^2 g^{-1} and v_{100} is the particle velocity expressed in units of 100 km s^{-1}

6.0 in a total image plane survey area of 49 arcmin^2 down to $K = 20.6$. After removing the effects of gravitational lensing using our detailed lens models, we estimate a surface density of 2.5 ± 0.4 (1.2 ± 0.3) arcmin^{-2} for EROs with $(R-K) \geq 5.3$ (6.0) at $K \leq 21.6$. Our results agree with previous shallower wide-field surveys at $K \lesssim 19$ and probe the number density of EROs with $(R-K) \geq 5.3$ and 6.0 down to a source plane magnitude of $K \sim 22$ for the first time. We also find that the number counts of both classes of ERO flatten significantly at magnitudes fainter than $K \sim 19$–20. We speculate that this is due to a transition from an ERO population dominated by evolved galaxies at $z \sim 1$–2 ($K \lesssim 19$–20) to one dominated by distant dusty starburst galaxies at $z > 1$ ($K \gtrsim 19$–20). Analysis of the $(R-K)$-$(I-K)$ and $(R-K)$-$(J-K)$ planes also suggests that the $(R-K) \geq 6.0$ population may contain a substantial fraction of dusty starburst galaxies. Visually classifying the EROs, we see that approximately 50% of our sample contain signs of morphological complexity including disk-like, clumpy or interacting morphologies. This confirms the presence of a large active population in our sample.

We compare a simple two parameter (z_f and τ) PLE model that attempts to describe EROs as a single population of elliptical galaxies (Daddi et al. 2000b) with our data. The model parameters which best match the observations are $\tau = 0.1$ Gyr and $z_f = 2.5$, ruling out the very high formation redshifts ($z_f \sim 10$) that were allowed by Daddi et al.'s (2000a) shallower observations. However, this single population model matches the $(R-K) \geq 6.0$ EROs significantly worse than the $(R-K) \geq 5.3$ EROs, supporting the idea that the more extreme population contains a large fraction of distant dusty starbursts in addition to the elliptical galaxies contained within this model. We also compare our observations with PLE models that attempt to describe the whole galaxy population, and not just passive ellipticals (M00). These models under-predict the surface density of $(R-K) \geq 5.3$ EROs by approximately an order of magnitude and predict none with $(R-K) \geq 6.0$. This deficit of EROs is probably caused by M00 requiring their model to fit the median redshift of Cowie et al.'s (1996) K-selected redshift distribution. We suggest that this confirms Cowie et al.'s (1996) concern that their optical follow-up of a small-field K-selected sample suffers from strong clustering of the faintest and reddest

sources, as well as possibly being incomplete for the reddest (i.e. optically faintest – $R \gtrsim 24$) galaxies, and hence for galaxies at $z \gtrsim 1$. It therefore appears that near-infrared spectroscopy of wide field K–selected samples is necessary before the redshift distribution of galaxies at $z \gtrsim 1$ can be reliably quantified.

In the final model comparison, we compare the observed number density of EROs with the semi-analytic predictions from the reference model of C00. This semi-analytic model under-predicts the number density of EROs at $K \sim 18$–22 by an order of magnitude, indicating that the current generation of semi-analytic models may not produce sufficient stars and/or dust at high redshift ($z > 2$). However, as the C00 reference model is physically well motivated, we look at the predicted properties of the ERO population, finding that their redshift distribution and the split between passive and dusty EROs appear to support our interpretation of the break in the slope of the number counts.

Our original motivation to search for EROs in the fields of the ten clusters in our *HST* lensing survey was to increase the chance of successful spectroscopic identification of these mysterious galaxies. The lack of efficient multi-object spectrographs on 10–m class telescopes continues to inhibit progress in this field. Nevertheless, we have combined our unique sample of magnified EROs and long-slit near-infrared spectroscopy to identify two sources from the sample.

- ERO J164023 is a dusty starburst-Seyfert galaxy at $z = 1.05$. This galaxy reveals that dusty EROs probably span the full range of power sources: starbursts (e.g. HR10, Dey et al. 1999), AGNs (e.g. ISO J1324−2016, Pierre et al. 2001) and composite starburst-AGN systems such as ERO J164023.

- ERO J003707 is a bulge-dominated early-type disk galaxy at $z = 1.60$ with an SED similar to a local Sa galaxy. We estimate that $\sim 10\%$ of EROs may be similar systems and that the star-forming disk in these galaxies has probably not been detected due to the low surface brightness of the disk emission.

In contrast to the simple picture that EROs comprise simply passively evolving elliptical galaxies and a population of dusty starburst galaxies, our results indicate that EROs are considerably more diverse than previously thought.

7.4 Summary

We summarise our conclusions by considering whether the outcome of this experiment is good or bad news for CDM. We divide our comments into two families of constraints: those based on the cluster lens sample at $z \sim 0.2$ and arising from the properties of massive galaxies at $z \sim 1$–2.

At $z = 0.2$, our results appear to be qualified good news for CDM. We find that cluster-scale halos probably do contain a central density cusp, and the alternative SIDM proposals appear to require a highly velocity dependent cross-section to self-interaction. However, there is significant scatter in the profile slopes obtained from recent lensing studies, suggesting that there may be a large dispersion around the claimed "universal" density profile (Navarro, Frenk & White 1997).

Our results support the growing body of evidence for a low value of σ_8. If true, this would reduce the overall normalisation of the matter power spectrum and thus should reduce the substructure predicted to occur on small scales. This would help to alleviate some of the galaxy-scale objections to CDM (e.g. Moore et al. 1999) and potentially remove the need to invoke SIDM.

The news is less good at $z \sim 1$–2, although it is not all doom and gloom. Hierarchical models under-predict the observed number counts of EROs by a substantial margin. However, the mix of those EROs that are produced by the models is in broad agreement with the observational mix, suggesting that the problem is more one of normalisation than fundamental flaws in the model framework. Further work is required observationally to quantify the mix, and these results will provide powerful constraints on current and future generations of galaxy formation models.

7.5 Further Study

Finally, we summarise some key elements of future study that will build on the results presented in this thesis.

- Extension of the detailed lens models using weak-lensing analysis of our panoramic multi-colour CFH12k data will probe the cluster density profiles out to the turnaround radii of the clusters ($r \sim 5$ Mpc).

- Detailed dynamical study of the cluster-galaxies will investigate the merger history of the clusters and provide the ideal complement to the cluster mass and structure analysis presented in this thesis.

- Construction of lensing-based cluster mass-temperature relations for larger samples and in a number of redshift slices (e.g. $z \sim 0.5$) would be a powerful probe of the evolution of dark matter in clusters and the thermodynamics of the intra-cluster medium.

- Exploitation of this and new cluster lens samples to study high-redshift galaxy populations, including Lyman-break galaxies, sub-millimetre sources, Lyman-α sources at $z \sim 3$–6 and EROs.

BIBLIOGRAPHY

The following abbreviations for the names of journals have been used:

A&A	Astronomy and Astrophysics
ApJ	Astrophysical Journal
ApJS	Astrophysical Journal Supplement
AJ	Astronomical Journal
ARA&A	Annual Reviews of Astronomy and Astrophysics
Astron. Nachr.	Astronomische Nachrichten
BAAS	Bulletin of the American Astronomical Society
Helv. Phys. Acta	Helvetica Physica Acta
MNRAS	Monthly Notices of the Royal Astronomical Society
New A.	New Astronomy
PASJ	Publications of the Astronomical Society of Japan
PASP	Publications of the Astronomical Society of the Pacific
Phil. Tran.	Philosophical Transactions of the Royal Society, London
Phys. Rev.	Physical Review
RvMP	Reviews of Modern Physics
SPIE	Proceedings of the Society of Photo-Optical Instrumentation Engineers
Z. Phys.	Zeitschrift für Physik

Abdelsalam H.M., Saha P., Williams L.L.R., 1998, MNRAS, 294, 734

Abell G.O., 1958, ApJS, 3, 211

Abell G.O., Corwin H.G., Jr., Olowin R.P., 1989, ApJS, 70, 1

Abraham R.G., van den Bergh S., Glazebrook K., Ellis R.S., Santiago B.X., Surma P., Griffiths R.E., 1996, ApJS, 107, 1

Adami C., Ulmer M.P., Durret F., Nichol R.C., Mazure A., Holden B.P., Romer A.K., Savine C., 2000, A&A, 353, 930

Afonso J., Mobasher B., Chan B., Cram L., 2001, ApJ, 559, L101

Alexander D.M., Vignali C., Bauer F.E., Brandt W.N., Hornschemeier A.E., Garmire G.P., Schneider D.P., 2002, AJ, 123, 1149

Allen S.W., Fabian A.C., Edge A.C., Bautz M.W., Furuzawa A., Tawara Y., 1996, MNRAS, 283, 263

Allen S.W., Fabian A.C., Kneib J.-P., 1996, MNRAS, 279, 615

Allen S.W., 1998, MNRAS, 296, 392

Allen S.W., Fabian A.C., 1998, MNRAS, 297, 57

Allen S.W., Schmidt R.W., Fabian A.C., 2001, MNRAS, 328, L37

Alpher R.A., Herman R.C., 1950, RvMP, 22, 153

Altieri B., Metcalfe L., Kneib J.-P., McBreen B., Aussel H., Biviano A., Delaney M., Elbaz D., Leech K., Lémonon L., Okumura K., Pelló R., Shulz B., 1999, A&A, 343, L65

Arabadjis J.S., Bautz M.W., Garmire G.P., 2002, ApJ, submitted, astro-ph/0109141

Aragón-Salamanca A., Ellis R.S., Schwartzenberg J.-M., Bergeron J.A., 1994, ApJ, 421, 27

Bacon D.J., Refregier A.R., Ellis R.S., 2000, MNRAS, 318, 625

Bacon D., Massey R., Refregier A., Ellis R.S., 2002, MNRAS, submitted, astro-ph/0203134

Bahcall N.A., Fan X., Cen R., 1997, ApJ, 485, L53

Bahcall N.A., Cen R., 1993, ApJ, 407, L49

Bahcall N.A., Ostriker J.P., Perlmutter S., Steinhardt P.J., 1999, Science, 284, 1481

Balogh M.L., Smail I., Bower R.G., Ziegler B.L., Smith G.P., Davies R.L., Gaztelu A., Kneib J.-P., Ebeling H., 2002a ApJ, 566, 123

Balogh M.L., Bower R.G., Smail I., Ziegler B.L., Davies R.L., Gaztelu A., Fritz A., 2002b MNRAS, submitted, astro-ph/0207360

Barger A.J., Cowie L.L., Trentham N., 1999, AJ, 117, 102

Barger A.J., Cowie L.L., Mushotzky R.F., Richards E.A., 2001, AJ, 121, 662

Barvainis R., Antonucci R., Helou G., 1999, AJ,118, 645

Baugh C.M., Cole S., Frenk C.S., 1996, MNRAS, 283, 1361

Beckwith S.V.W., Thompson D., Mannucci F., Djorgovski S.G., 1998, ApJ, 504, 107

Beijersbergen M., Hoekstra H., van Dokkum P.G., van der Hulst T., 2002, MNRAS, 329, 385

Bell E.F. & de Jong R.S., 2001, ApJ, 550, 212

Bennett C.L., Banday A.J., Gorski K.M., Hinshaw G., Jackson P., Keegstra P., Kogut A., Smoot G.F., Wilkinson D.T., Wright E.L., 1996, ApJL, 464, 1

Bernstein G.M., Nichol R.C., Tyson J.A., Ulmer M.P., Wittman D., 1995, AJ, 110, 1507

Bershady M.A., Lowenthal J.D., Koo D.C., 1998, 505, 50

Bertin E., Arnouts S., 1996, A&A, 117, 393

Blain A.W., Kneib J.-P., Ivison R.J., Smail I., 1999, ApJ, 512, L87

Blain A.W., Smail I., Ivison R.J., Kneib J.-P., 1999, MNRAS, 302, 632

Blanchard A., Sadat R., Bartlett J.G., Le Dour M., 2000, A&A, 362, 809

Blandford R.D., Kochanek C.S., 1987, ApJ, "Lectures on Gravitational Lensing", California Institute of Technology

Bolzonella M., Miralles J.-M., Pelló R., 2000, A&A, 363, 476

Bond J.R., Efstathiou G., Silk J., 1980, Phys. Rev. Letters, 45, 1980

Bond J.R., Cole S., Efstathiou G., Kaiser N., 1991, ApJ, 379, 440

Bond J.R., Contaldi C.R., Pen U.-L., Pogosyan D., Prunet S., Ruetalo M.I., Wadsley J.W., Zhang P., Mason B.S., Myers S.T., Pearson T.J., Readhead A.C.S., Sievers J.L., Udomprasert P.S., 2002, ApJ, submitted, astro-ph/0205386

Borgani S., Rosati P., Tozzi P., Stanford S.A., Eisenhardt P.R., Lidman C.,Holden B., Della Ceca R., Norman C., Squires G., 2001, ApJ, 561, 13

Bower R.G., 1991, MNRAS, 248, 332

Bradt H., Mayer W., Naranan S., Rappaport S., Spuda G., 1967, ApJ, 161, L1

Brainerd T., Blandford R., Smail I., 1996, ApJ, 466, 623

Bridle S.L., Hobson M.P., Lasenby A.N., Saunders R., 1998, MNRAS, 299, 895

Brown M.L., Taylor A.N., Hambly N.C., Dye S., 2002, MNRAS, 333, 501

Brusa M., Comastri A., Daddi E., Cimatti A., Vignali C., 2002, in X-ray Spectroscopy of AGN with Chandra and XMM-Newton, ed. Th. Boller, S. Komossa, S. Kahn, H. Kunieda (MPE Press, Garching), in press, astro-ph/0204251

Bruzual A.G., 1983, ApJ, 273, 105

Bruzual G., Charlot S., 1993, ApJ, 405, 538

Bryan G.L., Norman M.L., 1998, ApJ, 495, 80

Buote D.A., Tsai J.C., 1995, ApJ, 452, 522

Buote D.A., Tsai J.C., 1996, ApJ, 458, 27

Buote D.A., 2001, ApJ, 553, L15

Burgarella D., Buat V., Donas J., Milliard B., Chapelon, S., 2001, A&A, 369, 421

Byram E.T., Chubb T.A., Friedman H., 1966, Science, 152, 66

Cannon D.B., Ponman T.J., Hobbs I.S., 1999, MNRAS, 302, 9

Carlberg R.G., Yee H.K.C., Ellingson E., Morris S.L., Abraham R., Gravel P., Pritchet C.J., Smecker-Hane T., Hartwick F.D.A., Hesser J.E., Hutchings J.B., Oke J.B., 1997, ApJ, 485, L13

Carr B., 1994, ARA&A, 32, 531

Casali M.M., Hawarden T.G., 1992, The JCMT-UKIRT Newsletter, 4, 35

Casertano S., Wiggs M., 2001, "An Improved Goemetric Solution for WFPC2", *ISR WFPC2-2001-10*, [http://www.stsci.edu/instruments/wfpc2/Wfpc2_isr/wfpc2_isr0110.html]

Catelan P., Kamionkowski M., Blandford R.D., 2000, MNRAS, 318, L39

Cavaliere, A., Fusco-Femiano, R., 1978, A&A, 49, 137

Chapman S.C., McCarthy P.J., Persson S.E., 2000, AJ, 120, 1612

Chapman S.C., Scott D., Borys C., Fahlman G.G., 2002, MNRAS, 330, 92

Chowlson O., 1924, Astron. Nachr., 221, 329

Cimatti A., Villani D., Pozzetti L., di Serego Alighieri S., 2000, MNRAS, 318, 453

Cimatti A., Pozzetti L., Mignoli M., Daddi E., Menci N., Poli F., Fontana A., Renzini A., Zamorani G., Broadhurst T., Cristiani S., D'Odorico S., Giallongo E., Gilmozzi R., 2002, A&A, submitted, astro-ph/0207191

Cohen J., Kneib J.-P., 2002, ApJ, 573, 524

Colafrancesco S., 1999, in MPE Rep. 271, Proc. Workshop Diffuse Thermal and Relativistic Plasma in Galaxy Clusters, ed. H. Böhringer, L. Feretti, & P. Schuecker (Garching: MPE), 269

Coleman G.D., Wu C.-C., Weedman D.W., 1980, ApJS, 43 393

Cole S., Lacey C.G., 1996, MNRAS, 281, 716

Cole S., Lacey C.G., Baugh C.M., Frenk C.S., 2000, MNRAS, 319, 204, (C00)

Cole S., Norberg P., Baugh C.M., Frenk C.S., & the 2dFGRS team, 2001, MNRAS, 326, 255

Colín, P., Avila-Reese V., Valenzuela O., Firmani C., 2002, ApJ, submitted, astro-ph/0205322

Cooray A.R., Grego L., Holzapfel W.L., Joy M., Carlstrom J.E., 1998, AJ, 115 1388

Corbin M.R., Vacca W.D., O'Neil E., Thompson R.I., Rieke M.J., Schneider G., 2000, AJ, 119, 1062

Cowie L.L., Gardiner J.P., Hu E.M., Songaila A., Hodapp K.-W., Wainscoat R.J., 1994, ApJ, 434, 114

Cowie L.L., Songaila A., Hu E.M., Cohen J.G., 1996, AJ, 112, 839

Cowie L.L., Barger A.J., Bautz M.W., Capak P., Crawford C.S., Fabian A.C., Hu E.M., Iwamuro F., Kneib J.-P., Maihara T., Motohara K., 2001, ApJ, 551, L9

Crawford, C.S., Allen, S.W., Ebeling, H., Edge, A.C., Fabian,A.C., 1999, MNRAS, 306, 857

Crittenden R.G., Natarajan P., Pen U., Theuns T., 2001, ApJ, 559, 552

Crittenden R.G., Natarajan P., Pen U., Theuns T., 2002, ApJ, 568, 20

Currie M., Wright G., Bridger A., Economou F., 1999, adass, 8, 175C

Czoske O., 2002, PhD Thesis, Observatoire Midi-Pyrénées, Université Paul Sabatier, Toulouse, France

Czoske O., Kneib J.-P., Soucail G., Bridges T.J., Mellier Y., Cuillandre J.-C., 2001, A&A, 372, 391

Czoske O., Moore B., Kneib J.-P., Soucail G., 2002, A&A, 386, 31

Daddi E., Cimatti A., Pozzetti L., Hoekstra H., Roettgering H., Renzini A., Zamorani G., Manucci F., 2000a, A&A, 361, 535

Daddi E., Cimatti A., Renzini A., 2000b, A&A, 362, L45

Dahle H., Kaiser N., Irgens R.J., Lilje P.B., Maddox S.J., 2002a, ApJS, 139, 313

Dahle H., Hannestad S., Sommer-Larsen J., 2002b, ApJL, submitted, astro-ph/0206455

Dalcanton J.J., Bernstein R., 2000, AJ, 120, 203

Davé R., Spergel D.N., Steinhardt P.J., Wandelt B.D., 2001, ApJ, 547, 574

Davis M., Efstathiou G., Frenk C.S., White S.D.M., 1985, ApJ, 292, 371

de Blok W.J.G., McGaugh S.S., 1997, 290, 533

Debattista V.P., Sellwood J.A., 1998, ApJ, 493, L5

de Grandi S., Böhringer H., Guzzo L., Molendi S., Chincarini G., Collins C., Cruddace R., Neumann D., Schindler S., Schuecker P., Voges W., 1999, ApJ, 514, 148

Dey A., Spinrad H., Dickinson M., 1995, ApJ, 440, 515

Dey A., Graham J.R., Ivison R.J., Smail I., Wright G.S., Liu M.C., 1999, ApJ, 519, 610

Dickey, J.M., Lockman, F.J., 1990, ARA&A, 28, 215

Dressler A., Shectman S.A., 1988, AJ, 95, 985

Driver S.P., Phillipps S., Davies J.I., Morgan I., Disney M.J., 1994, MNRAS, 268, 393

Dunlop J., Peacock J., Spinrad H., Dey A., Jimenez R., Stern D., Windhorst R., 1996, Nature, 381, 581

Dunlop J.S., 2001, in UMass/INAOE Conference on Deep Millimeter Surveys, eds. Lowenthal J., Hughes D., (astro-ph/0011007)

Dye S., Taylor A.N., 1998, MNRAS, 300,23

Dye S., Taylor A.N., Greve T.R., Rögnvaldsson Ö.E., van Kampen E., Jakobsson P., Sigmundsson V.S., Gudmundsson E.H., Hjorth J., 2002, A&A, 386, 12

Dyson F.W., Eddington A.S., Davidson C.R., 1920, MNRAS, 62, 291

Eales S.A., Lilly S.J., Gear W.K., Dunne L., Bond J.R., Hammer F., Le Févre O., Crampton D., 1999, ApJ, 515, 518

Ebbels T.M.D., LeBorgne J.-F., Pelló R., Ellis R.S., Kneib J.-P., Smail I., Sanahuja B.,1996, MNRAS, 281, L75

Ebbels T.M.D., Ellis R.S., Kneib J.-P., Le Borgne J.-F., Pelló R., Smail I., Sanahuja B., 1998, MNRAS, 295, 75

Ebbels T.M.D., 1998, PhD Thesis, Institute of Astronomy, University of Cambridge, England

Ebeling H., et al., 1996, MNRAS, 281, 799

Ebeling, H., et al., 1998, MNRAS, 301, 881

Ebeling, H., et al., 2000, MNRAS, 318, 333

Ebeling H., Edge A.C., Henry J.P., 2000, in Large Scale Structure in the X-ray Universe, Proceedings of the 20-22 September 1999 Workshop, Santorini, Greece, eds. Plionis, M., Georgantopoulos, I., Atlantisciences, Paris, France, p.39

Ebeling H., Edge A.C., Henry J.P., 2001, ApJ, 553, 668

Eddington A.S., 1920, *"Space, time and Gravitation"* (Cambridge: University Press)

Edge A.C., Stewart G.C., Fabian A.C., Arnaud K.A., 1990, MNRAS, 245, 559

Edge A.C., Stewart G.C., 1991, MNRAS, 252, 414

Edge A.C., 2001, MNRAS, 328, 762

Efstathiou G., Moody S., Glazebrook K. & the 2fFGRS Team, MNRAS, 2002, 330, 29

Eggen O.J., Lynden-Bell D., Sandage A.R., 1962, ApJ, 136, 748

Einstein A., 1911, Annalen der Physik, 35, 898

Einstein A., 1915, Sitzungsber. Preuß. Akad.

Einstein A., 1936, Science, 84, 506

Eisenhardt P.R.M., Dickinson M., 1992, ApJ, 399, L47

Eisenhardt P.R.M., Elston R., Stanford S.A., Dickinson M., Spinrad H., Stern D., Dey A., 1998, in Proc. Xth Recontres de Blois, The Birth of Galaxies, ed. B. Guideroni, F.R. Bouchet, & T.X. Thuan (Paris: Editions Frontieres)

Eke V.R., Cole S., Frenk C.S., 1996, MNRAS, 282, 263

Eke V.R., Navarro J.F., Frenk C.S., 1998, ApJ, 503, 569

Eke V.R., Cole S., Frenk C.S., Henry J.P., 1998, MNRAS, 298, 1145

Eke V.R., Navarro J.F., Steinmetz , 2001, 554, 114

Elbaz D., Flores H., Chanial P., Mirabel I.F., Sanders D., Duc P.-A., Cesarsky C.J., Aussel H., 2002, A&A, 381, L1

Ellis R.S., Allington-Smith J., Smail I., 1991, MNRAS, 249, 184

Ellis R.S., 1997, ARA&A, 35, 389

Ellis R.S., Santos M.R., Kneib J.-P., Kuijken K., 2001, ApJ, 560, L119

Elston R., Rieke G.H., Rieke M.J., 1988, ApJ, 331, L77

Elston R., Rieke G.H., Rieke M.J., 1991, in ASP Conf. Ser. 14, Astrophysics with Infrared Arrays, ed. R. Elston (San Fransisco: ASP), 3

Elston R., Rieke M.J., Rieke G.H., 1989, ApJ, 341, 80

Evrard A.E., Mohr J.J., Fabricant D.G., Geller M.J., 1993, ApJ, 419, L9

Evrard A.E., Metzler C.A., Navarro J.F., 1996, ApJ, 469, 494

Fabian, A.C., 1994, AR&A, 32, 277

Fabian A.C., Mushotzky R.F., Nulsen P.E.J., Petereson J.R., 2001, MNRAS, 321, L20

Fahlman G., Kaiser N., Squires G., Woods D., 1994, ApJ,437, 56

Feretti L., 2001, in IAU Symp. 199, The Universe at Low Radio Frequencies, ed., A. Pramesh Rao(San Fransisco: ASP), in press (astro-ph/0006379)

Fernández-Soto A., Lanzettz K.M., Yahil A., 1999, ApJ, 513, 34

Finoguenov A., Reiprich T.H., Böhringer H., 2001, A&A, 368, 749

Fioc M.& Rocca-Vomerange B., 1997, A&A, 326, 950

Firmani C., D'Onghia E., Chincarini G., Hernández X., Avila-Reese V., 2001, MNRAS, 321, 713

Firth A.E., Somerville R.S., McMahon R.G., Lahav O., Ellis R.S., Sabbey C.N., McCarthy P.J., Chen H.-W., Marzke R.O., Wilson J., Abraham R.G., Beckett M.G., Carlberg R.G., Lewis J.R., Mackay C.D., Murphy D.C., Oemler A.E., Persson S.E., 2002, MNRAS, 332, 617

Fixsen D.J., Cheng E.S., Gales J.M., Mather J.C., Shafer R.A., Wright E.L., 1996, ApJ, 473, 576

Flores H., Hammer F., Thuan T.X., Ceśarsky C., Desert F.X., Omont A., et al., 1999, ApJ, 517, 148

Flores R.A., Primack J.A., 1994, ApJ, 427, L1

Fontana A., Menci N., D'Odorico S., Giallongo E., Poli F., Cristiani, S., Moorwood A., Saracco P., 1999, MNRAS, 310, L27

Fort B., Prieur J.L., Mathez G., Mellier Y., Soucail G., 1988, A&A, 200, L17

Fort, B., Le Fèvre, O., Hammer F., Cailloux, M., 1992, ApJ, 399, L125

Franx M., Illingworth G.D., Kelson D.D., van Dokkum P.G., Tran K.-V., 1997, ApJ, 486, L75

Freedman W.L., Madore B.F., Gibson B.K., Ferrarese L., Kelson D.D., et al., 2001, ApJ, 553, 47

Frenk C.S., White S.D.M., Efstathiou G., Davis M., 1990, ApJ, 351, 10

Friedmann A., 1922, Z. Phys., 10, 377

Friedmann A., 1924, Z. Phys., 12, 326

Fruchter A.S., Hook R.N., 1997, in Applications of Digital Image Processing, Proc. SPIE, 3164, ed. Tescher A., p120

Fruchter A.S., Hook R.N., 2002, PASP, 114, 144

Gamow G., 1949, RvMP, 21, 367

Gear W.K., Lilly S.J., Stevens J.A., Clements D.L., Webb T.M., Eales S.A., Dunne L., 2000, MNRAS, 316, 51

Geller M.J., Beers T.C., 1982, PASP, 94, 421

Ghigna, S., Moore, B., Governato, F., Lake, G., Quinn, T.,Stadel, J., 2000, ApJ, 544, 616

Gilmozzi R., Ewald S., Kinney E., 1995, "The Geometric Distortion Correction for the WFPC Cameras", *ISR WFPC2-95-02*, [http://www.stsci.edu/instruments.wfpc2/Wfpc2_isr/wfpc2_isr9502.html]

Gioia I.M., et al., 1990, ApJ, 356, L35

Giovannini G., Tordi M., Feretti L., 1999, NewA, 4, 141

Gnedin O.Y., Ostriker J.P., 2002, 561, 61

Golse G., Kneib J.-P., Soucail G., 2002, A&A, 387, 788

Goto T., Okamura S., McKay T.A., Annis J., Bahcall N.A., Bernardi M., Brinkmann J., Gomez P.L., Hansen S., Kim R.S.J., Sekiguchi M., Sheth R., 2002, PASJ, accepted, astro-ph/0205413

Govoni F., Feretti L., Giovannini G., Böhringer H., Reiprich T.H., Murgia M., 2001, A&A, 376, 803

Graham J.R., Dey A., 1996, ApJ, 471, 720

Graham J.R., et al., 1994, ApJ, 420, L5

Gray M.E., Ellis R.S., Refregier A., Beźecourt J., McMahon R.G., Beckett M.G., Mackay C.D., Hoenig M.D., 2000, MNRAS, 318, 573

Grossman S.A., Narajan R., 1989, ApJL, 324, 37

Gunn J.E., Gott J.R.III, 1972, ApJ, 176, 1

Gursky H., Kellogg E.M., Leong C., Tananbaum H., Giacconi R., 1971a, ApJ, 165, L43

Gursky H., Kellogg E., Murray S., Leong C., Tananbaum H., Giacconi R., 1971b, ApJ, 167, L81

Guth A., 1981, Phys. Rev. Letters, 23, 347

Hall P.B., Sawicki M., Martini P., Finn R.A., Pritchet C.J., Osmer P.S., McCarthy D.W., Evans A.S., Lin H., Hartwick F.D.A., 2001, AJ, 121, 1840

Hammer F., Rigaut F., 1989, A&A, 226, 45

Heavens A.F., Refregier A., Heymans C., 2000, MNRAS, 317, 965

Hennawi J.F., Ostriker J.P., 2002, ApJ, 572, 41

Henry J.P. & Arnaud K.A., 1991, ApJ, 372, 410

Herschel F.W., 1785, *"On the Construction of the Heavens"*, Phil.Trans., 78, 213

Herschel F.W., 1811, Phil.Trans., 101, 269

Hill T.L., Heisler C.A., Norris R.P., Reynolds J.E., Hunstead R.W., 2001, 121, 128

Hill T.L., Heisler C.A., Sutherland R., Hunstead R.W., 1999, AJ, 117, 111

Hoekstra H., Franx M., Kuijken K., Squires G., 1998, ApJ, 504, 636

Hoekstra H., Yee H.K.C., Gladders M.D., 2002, ApJ, submitted, astro-ph/0204295

Hogg D.W., Pahre M.A., McCarthy J.K., Cohen J.G., Blandford R., Smail I., Soifer B.T., 1997, MNRAS, 288, 404

Holder G.P., 2002, ApJ, submitted, astro-ph/0207633

Holland W.S., Robson E.I., Gear W.K., Cunningham C.R., Lightfoot J.F., Jenness T., et al., 1999, MNRAS, 303, 659

Holtzman J.A., Burrows C.J., Casertano S., Hester J.J., Trauger J.T., Watson A.M., Worthey G., 1995, PASP, 107, 1065

Hoyle F., Tayler R.J., 1964, Nature, 203, 1108

Hu E.M., Ridgway S.E., 1994, AJ, 107, 1303

Hubble E.P., 1925, The Observatory, 48, 139

Hubble E.P., Humason M.L., 1931, ApJ, 74, 43

Hubble E.P., 1936, "Realm of the Nebulae", Yale University Press

Hughes D.H., Dunlop J.S., 1998, in Carilli C., et al., eds, ASP Conf. Ser., Highly Redshifted radio lines. Soc. Pac. San Fransisco.

Hjorth J., Oukbir J., van Kampen E., 1998, MNRAS, 298, L1

Ikebe Y., Reiprich T.H., B'ohringer H., Tanaka Y., Kitayama T., 2002, A&A, 383, 773

Jenkins A., Frenk C.S., Pearce F.R., Thomas P.A., Colberg J.M., White S.D.M., Couchman H.M.P., Peacock J.A., Efstathiou G., Nelson A.H., 1998, ApJ, 499, 20

Jenkins A., Frenk C.S., White S.D.M., Colberg J.M., Cole S., Evrard A.E., Couchman H.M.P., Yoshida N., 2001, MNRAS, 321, 372

Jing Y.P., Suto Y., 2000, ApJ, 529, L69

Jones C., Forman W., 1999, ApJ, 511, 65

Kaiser N., 1986, MNRAS, 222,323

Kaiser N., Squires G., 1993, 404, 441 (KS93)

Kassiola A.,Kovner I., 1993, ApJ, 417, 450

Kauffmann G., White S.D.M., Guideroni B., 1993, MNRAS, 264, 201

Kauffmann G., Charlot S., White S.D.M., 1996, MNRAS, 283, 117

Kauffmann G., Charlot S., 1998, MNRAS, 297, L23

Kay S.T., Bower, R.G., 1999, MNRAS, 308, 664

Kant I., 1755, "Allgemeine Naturgeschichte und Theorie des Himmels"

Kellogg E., Gursky H., Tananbaum H., Giacconi R., Pounds K., 1972, ApJ, 174, L65

Kempner J.C., Sarazin C.L., 2001, ApJ, 548, 639

Kennicutt R.C., 1983, ApJ, 272, 54

Kennicutt R.C., 1998, ARA&A, 36, 189

Khosroshahi H.G., Wadadekar Y., Kembhavi A., 2000, ApJ, 533, 162

King L.J., Clowe D.I., Schneider P., 2002, A&A, 383, 118

Klypin A., Kravstov A., Valenzuela O., Prada F., 1999, ApJ, 522,82

Kneib J.-P., 1993, PhD Thesis, Université Paul Sabatier, Toulouse, France

Kneib J.-P., Mellier Y., Fort B., Mathez G., 1993, A&A, 273, 367

Kneib J.-P., Mellier Y., Fort B., Soucail G., Longaretti P.Y., 1994, A&A, 286, 701

Kneib J.-P., Mellier Y., Pelló R., Miralda-Escudé J., Le Borgne J.-F., Boehringer H., Picat J.-P., 1995, A&A, 303, 27

Kneib J.-P., Ellis R.S., Smail I., Couch W.J., Sharples R.M., 1996, ApJ, 471, 643

Kochanek C.S., 1990, MNRAS, 247, 135

Koekemoer A.M., et al., 2002, "*HST* Dither Handbook", Version 2.0 (Baltimore: STScI)

Kovner I., 1987, Nature, 327, 193

Kron R.G., 1980, ApJS, 43, 305

Kuchinski L.E., Madore B.F., Freedman W. L., Trewhella M., 2001, AJ, 122, 729

Lacey C.G., Cole S., 1993, MNRAS, 262, 627

Lahav O., Bridle S.L. & the 2dFGRS Team, 2002, MNRAS, 333, 961

Lambert J.H., 1761, *"Coßmologißche Briefe über die Einrichtung des Weltbaues"*, translated by Stanley L. Jaki, Scottish Academic Press, 1976

Larson R.B., 1975, MNRAS, 173, 671

Lavery R.J., Henry J.P., 1988, ApJ, 329, L21

Lemaître G., 1927, Ann. Soc. Sci. Bruxelles, 47, Ser. A, 103; English translation: 1931, MNRAS, 91, 483

Lewis, G.F., Babul, A., Katz, N., Quinn, T., Hernquist, L.,Weinberg, D.H., 1999, astro-ph/9907097

Liang H., Hunstead R.W., Birkinshaw M., Andreani P., 2000, ApJ, 544, 686

Liu C.T., Kennicutt R.C., 1995, ApJ, 450, 547

Liu M.C., Dey A., Graham J.R., Bundy K.A., Steidel C.S., Adelberger K., Dickinson M.E., 2000, AJ, 119, 2556

Luppino G.A., Gioia I.M., Hammer F., Le Fèvre O., Annis J.A., 1999, A&A, 136, 117

Lynds R., Petrosian V., 1986, BAAS, 18, 1014

Machacek M.E., Bautz M.W., Canizares C., Garmire G.P., 2002, ApJ, 567, 188

Mackey J., White M., Kamionkowski M., 2002, MNRAS, 332, 788

Madau P., Ferguson H.C., Dickinson M., Giavalisco M., Steidel C.C., Fruchter A., 1996, ApJ., 283, 1388

Majerowicz S., Neumann D.M., Reiprich T.H., 2002, A&A, submitted, astro-ph/0202347

Mannucci F., Basile F., Cimatti A., Daddi E., Poggianti B.M., Pozzetti L., Vanzi L., 2001, MNRAS, 326, 745

Maoli R., Van Waerbeke L., Mellier Y., Schneider P., Jain B., Bernardeau F., Erben T., Fort B., 2001, A&A, 368, 766

Markevitch M., 1997, ApJ, 483, L17

Markevitch M., 1998, ApJ, 504, 27

Markevich M., et al., 2000, CXC memo (http://asc.harvard.edu/cal "ACIS", "ACIS Background")

Markevitch M., et al., 2000, ApJ, 541, 542

Markevitch M., Vikhlinin A. 2001, ApJ, 563, 95

Markevitch M., 2002, ApJ, submitted, astro-ph/0205333

Marshall P., Hobson M.P., Gull S.F., Bridle S.L., 2002, MNRAS, in press, astro-ph/0112396

Mason B.S., Pearson T.J., Readhead A.C.S., Shepherd M.C., Sievers J.L., Udomprasert P.S., Cartwright J.K., Farmer A.J., Padin S., Myers S.T., Bond J.R., Contaldi C.R., Pen U.-L., Prunet S., Pogosyan D., Carlstrom J.E., Kovac J., Leitch E.M., Pryke C., Halverson N.W., Holzapfel W.L., Altamirano P., Bronfman L., Casassus C., May J., Joy M., 2002, ApJ, submitted, astro-ph/0205384

Mateo M., 1998, ARA&A, 36, 435

Mazzotta P., Fusco-Femiano R., Vikhlinin A., 2002, ApJ, 569, L31

McCarthy P.J., Persson S.E., West S.C., 1992, ApJ, 386, 52

McCracken H.J., Metcalfe N., Shanks T., et al., 2000, MNRAS, 311, 707, (M00)

McLean I.S., Becklin E.E., Bendiksen O., Brims G., Canfield J., Figer D.F., Graham J.R., et al., 1998, SPIE, 3354, 566

Mellier Y., Fort B., Soucail G., Mathez G., Cailloux M., 1991, ApJ, 380, 334

Mellier Y., Fort B., Kneib J.-P., 1993, ApJ, 407, 33

Mellier Y., van Waerbeke L., Bernardeau F., Tereno I., 2002, "Astronomy, Copsmology and Fundamental Physics", ESO-CERN-ESA Symposium, eds. Shaver A., Di Lella L., Gimenez A., in press, astro-ph/0206434

Menanteau F., Ellis R.S., Abraham R.G., Barger A.J., Cowie L.L., 1999, 309, 208

Messier C., 1784, *"Connaisance des Temps"*, Paris

Miralda-Escudé J., 1991, 370, 1

Miralda-Escudé J., 2002, 564, 60

Moffet A.T., Birkinshaw M., 1989, AJ, 98, 1148

Mohan N.R., Cimatti A., Röttgering H.J.A., Andreani P., Severgnini P., Tilanus R.P.J., Carilli C.L., Stanford S.A., 2002, A&A, 383, 440

Mohr J.J., Evrard A.E., Fabricant D.G., Geller M.J., 1995, 447, 8

Moore B., 1994, Nature, 370, 629

Moore B., Governato F., Quinn T., Stadel J., Lake G., 1998, ApJ, 499, L5

Moore B., Governato F., Quinn T., Stadel J., Lake G., 1999, MNRAS, 310, 1147

Moriondo G., Cimatti A., Daddi E., 2000, A& A, 364, 26

Mountain C.M., Robertson D., Lee T.J., Wade R., 1990, in Instrumentation in Astronomy, SPIE v1235, VII, 25

Moustakas L.A., Davis, M., Graham J.R., et al., 1997, ApJ, 475, 445

Mushotzky R.F., Scharf C.A., 1997, ApJ, 482, L13

Narayan R., Bartelmann M., 1996, *"Lectures on Gravitational Lensing"*, Proceedings of the 1995 Jerusalem Winter School; edited by A. Dekel and J.P. Ostriker; Cambridge University Press, astro-ph/9606001

Natarajan P., Kneib J.-P., Smail I., Ellis, R.S., 1998, ApJ, 499, 600

Navarro, J.F., Frenk, C.S., White, S.D.M., 1997, ApJ, 490, 493

Neumann D.M., Böhringer H., 1999, ApJ, 512, 630

Nevalainen J., Markevitch M., Forman W., 2000, ApJ, 532, 694

Newton I., 1704, "Opticks: A Treatise of the reflexions, refractions, inflexions and colours of light.", The Royal Society, London

Oke, J.B., et al., 1995, PASP, 107, 375

Packham C., Thompson K., Knapen J.H., Zurita A., Smail I., Greimel R., Folha D., Humphrey A., Rutten R., Ciardi D., Bec M., Bingham R., Broxterman M., Craig S., Dee K., Ives D., Jolley P., Moore P., Rees S., Talbot G., Worswick S., 2002, MNRAS, submitted

Paczyński B., 1987, Nature, 325, 572

Peacock J.A., 1999, *"Cosmological Physics"*, Cambridge University Press

Pearce, F.R., Thomas, P.A., Couchman, H.M.P., Edge, A.C., 2000, MNRAS, 317, 1029

Peebles P.J.E., 1980, *"Large Scale Structure of the Universe"*, Princeton University Press, Princeton

Peebles P.J.E., 1984, ApJ, 284, 439

Pelló R., Le Borgne J.-F., Sanahuja B., Mathez G., Fort B., 1992, A&A, 266, 6

Pelló R., Kneib J.-P., Le Borgne J.-F., Bzecourt J., Ebbels T. M., Tijera I., Bruzual G., et al., 1999, A&A, 346, 359

Pen U., 1998, ApJ, 498, 60

Pendlebury J.M., 1985, *"Kinetic Theory"*, Student Monographs on Physics, Adam Hilger Ltd

Penzias A.A., Wilson R.W., 1965, ApJ, 142, 419

Peres, C.B., Fabian, A.C., Edge, A.C., Allen, S.W., Johnstone,R.M., White, D.A., 1998, MNRAS, 298, 416

Persson S.E., Murphy W., Krzeminski W., Roth M., Rieke M.J., 1998, AJ, 116, 2475

Peterson J.R., Paerels F.B.S., Kaastra J.S., Arnaud M., Reiprich T.H., Fabian A.C., Mushotzky R.F., Jernigan J.G., Sakelliou I., 2001, A&A, 365, L104

Petrosian V., 1976, ApJ, 209, L1

Pierpaoli E., Scott D., White M., 2001, MNRAS, 325, 77

Pierre M., Lidman C., Hunstead R., Alloin D., Casali M., Cesarsky C., Chanial P., et al., 2001, A&A, 372, L45

Poggianti B.M. & Barbaro G., 1997, A&A, 325, 1025

Poggianti B.M., Wu H., 2000, ApJ, 529, 157

Power C., Navarro J.F., Jenkins A., Frenk C.S., White S.D.M., Springel V., Stadel J., Quinn T., 2002, MNRAS, submitted, astro-ph/0201544

Pozzetti L., Mannucci F., 2000, MNRAS, 317 L17

Press W.H., Schechter P., 1974, ApJ, 187, 425

Primack J.R., 2002, Proceedings of 5th International UCLA Symposium on Sources and Detection of Dark Matter, Marina del Rey, February 2002, ed. D. Cline, in press, astro-ph/0205391

Randall S.W., Sarazin C.L., Ricker P.M., 2002, ApJ, 577, in press (astro-ph/0206161)

Refregier A., Rhodes J., Groth E.J., 2002, ApJL, submitted, astro-ph/0203131

Reiprich T.H., Böhringer H., 2002, ApJ, 567, 716

Richstone D., Loeb A., Turner E.L., 1992, ApJ, 393, 477

Rizza E., Burns J.O., Ledlow M.J., Owen F.N., Voges W., Bliton M., 1998, MNRAS, 301, 328

Robertson H.P., 1936, ApJ, 83, 257

Roche N., Almaini O., Dunlop J., Ivison R.J., Willott C., 2002, MNRAS, submitted, astro-ph/0205259

Rowan-Robinson M., et al., 1997, MNRAS, 261, 513

Salpeter E.E., 1955, ApJ, 121, 161

Sand D.J., Treu T., Ellis R.S., 2002, ApJ, 574, L129

Saracco P., D'Odorico S., Moorwood A., Buzzoni A., Cuby J.-G., Lidman C., 1999, 349, 751

Schechter P., 1976, ApJ, 203, 297

Schlegel D.J., Finkbeiner D.P., Davis M., 1998, ApJ, 500, 525

Schmidt R.W., Allen S.W., Fabian A.C., 2001, MNRAS, 327, 1057

Schneider P., Bartelmann M., 1997, MNRAS, 286, 696

Schneider P., Ehlers J., Falco E.E., 1992, "Gravitational Lensing", Astronomy and Astrophysics Library, Springer-Verlag

Seitz C., Schneider P., 1995, A&A, 297, 287

Seitz S., Saglia R. P., Bender R., Hopp U., Belloni P., Ziegler B., 1998, MNRAS, 298, 945

Seljak U., 2001, MNRAS, submitted, astro-ph/0111362

Sheldon E.S., Annis J., Böhringer H., Fischer P., Frieman J.A., Joffre M., Johnston D., McKay T.A., Miller C., Nichol R. C., Stebbins A., Voges W., Anderson S.F., Bahcall N.A., Brinkmann J., Brunner R., Csabai I., Fukugita M., Hennessy G.S., Ivezic Z., Lupton R.H., Munn J.A., Pier J.R., York D.G., 2001, ApJ, 571, 85

Sievers J.L., Bond J.R., Cartwright J.K., Contaldi C.R., Mason B.S., Myers S.T., Padin S., Pearson T.J., Pen U.-L., Pogosyan D., Prunet S., Readhead A.C.S., Shepherd M.C., Udomprasert P.S., Bronfman L., Holzapfel W.L., May J., ApJ, submitted, astro-ph/0205387

Simard L., 1998, in Astronomical Data Analysis Software and Systems VII, ASP Conference Series, Vol. 145, 1998 Editors: R. Albrecht, R.N. Hook and H.A. Bushouse

Smail I., PhD Thesis, University of Durham, Durham, United Kingdom

Smail I., Hogg D.W., Yan L., Cohen J.G., 1995a, ApJ, 449, L105

Smail I., Hogg D.W., Blandford R., Cohen J.G., Edge A.C., Djorgovski S.G., 1995b, MNRAS, 277, 1

Smail I., Couch W.J., Ellis R.S., Sharples R.M., 1995c, ApJ,440, 501

Smail I., Ellis R.S., Fitchett M.J., Edge A.C., 1995d, MNRAS, 273, 277

Smail I., et al., 1996, ApJ, 469, 508

Smail I., Ivison R.J., Blain A.W., 1997a, ApJ, 490, 5

Smail I., Ellis R.S., Dressler A., Couch W.J., Oemler A., Butcher H., Sharples R.M., 1997b, ApJ, 470, 70

Smail I., Edge A.C., Ellis R.S., Blandford R.D., 1998, MNRAS, 293, 124

Smail I., Ivison R.J., Kneib J.-P., Cowie L.L.,Blain A.W., Barger A.J., Owen F.N., Morrison G.,1999a, MNRAS, 308, 1061

Smail I., Morrison G., Gray, M.E., Owen F.N., Ivison R.J., Kneib J.-P., Ellis, R.S., 1999, ApJ, 525, 609

Smail I., Ivison R.J., Owen F.N., Blain A.W., Kneib J.-P., 2000 ApJ, 528, 612

Smail I., Kuntschner H., Kodama T., Smith G.P., Packham C., Fruchter A.S., Hook R.N., 2001, MNRAS, 323, 839

Smail I., Ivison R.J., Blain A.W., Kneib J.-P., 2002a, MNRAS, 331, 495

Smail I., Owen F.N., Morrison G.E., Keel W.C., Ivison R.J., Ledlow M.J., 2002b, ApJ, accepted

Smith G.P., Kneib J.-P., Ebeling H., Csozke O., Smail I., 2001, ApJ, 552, 493

Soifer B.T., Matthews K., Neugebauer G., Armus L., Cohen J.G., Persson S.E., Smail I., 1999, AJ, 118, 2065

Soldner J., 1804, "Uber die ablenkung eines lichtsahls von seiner geraldlinigen bewegung durch die attrsktion eines weltkorpers, an welchem er nahe vorbeigeht", Berliner Astron. Jahrb., 161, 1804

Soucail G., Fort B., Mellier Y., Picat J.P., 1987a, A&A, 172, L14

Soucail G., Mellier Y., Fort B., Hammer F., Mathez G., 1987b, A&A, 184, L7

Soucail, G., Ota, N., Boehringer, H., Czoske, O., Hattori,M., Mellier, Y., 2000, A&A, 355, 433

Spergel D.N., Steinhardt P.J., 2000, Phys. Rev., 84, L3760

Spinrad H., Dey A., Stern D., et al., 197, ApJ, 484, 581

Squires G., Kaiser N., Babul A., Fahlman G., Woods D., Neumann D.M., Böhringer H. 1996, ApJ, 461, 572

Stanford S.A., Elston R., Eisenhardt P.R., Spinrad H., Sterm D., Dey A., 1997, AJ, 114, 2232S

Subramanian K., Cowling S.A., 1986, MNRAS, 219, 333

Teyssier R., Chiéze J.P., Alimi J.M., 1997, 480, 36

Thomas P.A., Muanwong O., Kay S.T., Liddle A.R., 2002, MNRAS, 330, 48

Thompson D., Beckwith S.V.W., Fockenbrock R., Fried J., Hippelein H., Huang J.-S., von Kuhlmann B., Leinhert C., Meisenheimer K., Phleps S., Roeser H.-J., Thommes E., Wolf C., 1999, ApJ, 523, 100

Tinsley B.M., Gunn J.E., 1976, ApJ, 203, 52

Trauger J.T., Vaughan A.H., Evans R.W., Moody D.C., 1995, "Geometry of the WFPC2 Focal Plane", in *Calibrating HST: Post Service Mission*, eds. A. Koratkar & C. Leitherer

Trentham N., 1998, MNRAS, 295, 360

Trentham N., Hodgkin S., 2002, MNRAS, 333, 423

Treu T., Stiavelli M., 1999, ApJ, 524, L27

Tyson J.A., Wenk R.A., Valdes F., 1990, ApJ, 349, 1

Tyson J.A., ochanski G.P., dell'Antonio I.P., 1998, ApJ, 498, L107

Vallée J.P., Bridle A.H., 1982, ApJ, 253, 479

van Dokkum P.G., Franx M., Fabricant D., Illingworth G.D., Kelson D.D., 2000, ApJ, 541, 95

van Kampen E., 1998, MNRAS, 301, 389

van Waerbeke L., et al., 2000, A&A, 358, 30

van Waerbeke L., et al., 2001, A&A, 374, 757

van Waerbeke L., Mellier Y., Pelló R., Pen U.-L., McCracken H.J., Jain B., 2002, A&A, submitted, astro-ph/0202503

Veilleux S., Osterbrock D.E., 1987, ApJS, 63, 295

Viana P.T.P., Liddle A.R., 1996, MNRAS, 281, 323

Viana P.T.P., Nichol R., Liddle A.R., 2002, ApJ, 569, L75

Vikhlinin A., Markevitch M., Murray S.S. 2001, ApJ, 551, 160

Voigt L.M., Schmidt R.W., Fabian A.C., Allen S.W., Johnstone R.M., 2002, MNRAS, accepted, astro-ph/0203312

Voit G.M., 2000, ApJ, 543, 113

Voit G.M., Bryan G.L., Balogh M.L., Bower R.G., 2002, ApJ, accepted, astro-ph/0205240

Walsh D., Carswell R.F., Weymann R.J., 1979, Nature, 279, 381

Walker A.G., 1935, MNRAS, 95, 263

Wang Q.D., Ulmer M.P., 1997, MNRAS, 292, 920

West M.J., Bothun G.D., 1990, ApJ, 350, 36

White S.D.M., Frenk C.S., Davis M., 1983, ApJL, 274, 1

White S.D.M., Frenk C.S., 1991, ApJ, 379, 52

White D.M., Jones C., Forman W., 1997, MNRAS, 292, 419

Williams L.L.R., Navarro J.F., Bartelmann M., 1999, ApJ, 527, 535

Williams R.W., et al., 1996, AJ, 112, 1335

Willott C.J., Rawlings S., Blundell K.M., 2001, MNRAS, 324, 1

Wilson G., Smail I., Ellis R.S., Couch W.J., 1997, MNRAS, 284, 915

Wittman D., et al., 2000, Nature, 405, 143

Wolf, R., 1865, Astronomisches Nachrichten, 65, 1

Wright, T., 1750, "An Original Theory of New Hypothesis of the Universe", London

Yamada T., Tanaka I., Aragón-Salamanca A., Kodama T., Ohta K., Arimoto N., 1997, ApJ, 487, L125

Zhao H., 1996, MNRAS, 278, 488

Ziegler B.L., Bower R.G., Smail I., Davies R.L., Lee, D., 2001, MNRAS, 325, 1572

Zwicky F., 1933, Helv. Phys. Acta 6, 10

Zwicky F., 1937a, Phys. Rev., 51, L290

Zwicky F., 1937b, Phys. Rev., 51, L679

Zwicky F., et al., 1968, *"Catalogue of Galaxies and of Clusters of Galaxies"*, Publ.: California Institute of Technology